

ABSTRACT

Mechanical and Thermal Property Prediction in Single Beads of Large Area Additive Manufactured Short-Fiber Polymer Composites

Timothy D. Russell, Ph.D.

Mentor: David A. Jack, Ph.D

The prediction of mechanical and thermal properties of 3D printed short-fiber reinforced polymers (SFRPs) are investigated in this study. Methods are demonstrated for predicting the internal spatially varying fiber orientation state and resulting internal spatially varying stiffness, coefficient of thermal expansion, and strength properties in a single bead of 13% carbon fiber filled acrylonitrile butadiene styrene. The methods allow determination of both the spatially varying microstructural properties and the effective, bulk properties in any direction by finite element analysis. The focus of this work is specifically on Large Area Additive Manufacturing, an extrusion-based process for manufacturing thermoplastic parts that are several feet long, but the methods are applicable to other SFRP processing methods as well. For the experimental validation portion of this dissertation, a large-scale 3D printing system was constructed to fabricate test specimens. Tensile, compressive, and flexural specimens were fabricated with this system and tested. It is demonstrated that correct order of magnitude predictions can be made for the effective stiffness, CTE, and strength of LAAM-printed SFRP beads using the presented computational methodology. In addition, the computational methodology lays a framework that lends itself to improvement by using more accurate modeling inputs as they are measured, and more accurate underlying equations as they are developed.

Mechanical and Thermal Property Prediction in Single Beads of Large Area
Additive Manufactured Short-Fiber Polymer Composites

by

Timothy D. Russell, B.S., M.S.M.E.

A Dissertation

Approved by the Department of Mechanical Engineering

Paul Ro, Ph.D., Chairperson

Submitted to the Graduate Faculty of
Baylor University in Partial Fulfillment of the
Requirements for the Degree
of
Doctor of Philosophy

Approved by the Dissertation Committee

David A. Jack, Ph.D, Chairperson

Douglas E. Smith, Ph.D.

Abhendra K. Singh, Ph.D.

Alexandre F. T. Yokochi, Ph.D.

Ronald B. Morgan, Ph.D.

Accepted by the Graduate School
December 2021

J. Larry Lyon, Ph.D., Dean

TABLE OF CONTENTS

LIST OF FIGURES	vii
LIST OF TABLES	xv
ACKNOWLEDGMENTS	xvi
DEDICATION	xvii
1 Introduction	1
2 Background Information	7
2.1 Additive Manufacturing of SFRPs	8
2.2 Large Area Additive Manufacturing	15
2.3 Fiber Orientation Modeling	18
2.3.1 Jeffery’s Model	21
2.3.2 Orientation Tensors	23
2.3.3 Fiber Interaction Models	33
2.3.4 Closures	35
2.4 Micromechanical Models	37
2.5 Strength Models	43
2.5.1 Simple Models	45
2.5.2 Failure Criteria	53
2.6 Other Models	62
2.6.1 Coefficient of Thermal Expansion	63
2.6.2 Coefficient of Moisture Expansion	64
2.6.3 Thermal Conductivity	65

2.6.4	Electrical Conductivity	66
3	Computational Methods and Results	67
3.1	Computational Methodology	67
3.1.1	Modeling the Fiber Orientation through a LAAM Nozzle . . .	72
3.1.2	Stiffness Prediction	75
3.1.3	Strength Prediction	77
3.1.4	CTE Prediction	80
3.2	Modeling Results	81
3.2.1	Fiber Orientation in a LAAM Bead	81
3.2.2	Spatially-Varying Stiffness and CTE in a LAAM Bead	88
3.2.3	Mesh Size Analyses	91
3.2.4	Effective Stiffness and CTE in a LAAM Bead	93
3.2.5	Strength Predictions	96
3.2.6	Laminate Analogy Approach to Stiffness	101
3.3	A Unified Methodology	103
4	Experimental Methods and Results	109
4.1	Experimental Methodology	109
4.1.1	Baylor LAAM System	110
4.1.2	Fiber Aspect Ratio Characterization	114
4.1.3	Strength Testing	123
4.2	Experimental Results	131
4.2.1	Fiber Aspect Ratio Characterization	131
4.2.2	Tensile Testing Results	136
4.2.3	Compression Testing Results	138
4.2.4	Flexural Testing Results	140
4.2.5	Additional TGA Testing Results	142

4.3	Modeling Modifications Based on Experimental Data	145
4.3.1	Considering a Realistic Tensile Bar Geometry	146
4.3.2	Considering Fiber Orientation Measurement Data	153
4.3.3	Considering Porosity	159
4.4	Comparison of Modeling and Experimental Results	163
5	Conclusions and Recommendations	168
APPENDICES		
A	Standard Operating Procedure for Baylor LAAM System	175
B	Tensile Testing Results	191
C	Compression Testing Results	194
D	Flexural Testing Results	197
E	Tensile Testing Results from SAMPE Study	202
F	Additional TGA Testing Results	204
	BIBLIOGRAPHY	212

LIST OF FIGURES

2.1	The unit vector \mathbf{p} from Equation 2.2 expressing the direction of a cylindrical fiber.	19
2.2	(a) Path of a cylindrical fiber in a simple shear flow predicted by Jeffery's equation. (b) Change in the components of \mathbf{p} over time. Used $a_r = 40$ ($r_e \approx 26$) and $L_{13} = 1$	22
2.3	Different representations of the same, highly x_1 -aligned orientation state: (a) a graphical representation of $\psi(\mathbf{p})$ as a shaded sphere, (b) individual fibers, (c) a graphical representation of \mathbf{A} as an ellipsoid.	24
2.4	Three orientation states: (a) uniaxial in x_1 , (b) random in $x_1 - x_2$ plane, and (c) completely random.	26
2.5	Orientation states with equivalent A_{11} and equivalent A_{22} , but different A_{12} . (a) Fibers oriented at $+\phi$, $A_{12} > 0$. (b) Fibers oriented at $-\phi$, $A_{12} < 0$	26
2.6	(a) $\psi(\theta, \phi)$ from Figure 2.3, (b) 2^{nd} order reconstruction of ψ , and (c) 4^{th} order reconstruction of ψ	29
2.7	An illustrative hypothetical micrograph of a fiber filled polymer like in [58] on which the method of ellipses could be performed.	31
2.8	(a) Definitions of angles (same as those in Figure 2.1). (b) Ambiguity problem; a fiber with major axis M oriented along ϕ has the same footprint as one oriented along $\phi + \pi$. Figures inspired by [58].	32
2.9	Assumed stress-strain behavior of fiber and matrix material for the rule of mixtures tensile strength equation. Figure recreated from Ref. [25].	46
2.10	Single fibers inside cracked polymer blocks being acted on by a force \mathbf{F} . (a) The fiber is perpendicular to the crack plane ($\beta = 0$). (b) The fiber is at an angle relative to the crack plane normal ($\beta \neq 0$).	48
2.11	The orientation distribution $g(\beta)$ with (a) $p = 1$, $q = 1$, (b) $p = 1$, $q = 2$, (c) $p = 2$, $q = 1$, (d) $p = 1/2$, $q = 2$, (e) $p = 2$, $q = 1/2$, and (f) $p = 1/2$, $q = 1/2$. Figure recreated from Fu and Lauke [94].	49

2.12	All figures recreated based upon results in [94]. (a) Fiber length factor χ_2 as a function of mean fiber length L_{mean} , showing tensile strength increases as L_{mean} increases. (b) Fiber length factor χ_2 as a function of critical fiber length L_c , showing steady decrease in tensile strength as L_c increases. (c) Fiber length factor χ_2 as a function of the mode fiber length L_{mod} , showing little change in χ_2 as L_{mod} increases. (d) Product of fiber length and orientation factors $\chi_1\chi_2$ as a function of mode fiber length L_{mod} , showing little change in tensile strength as L_{mod} increases.	51
2.13	Orientation distribution functions: (a) mostly aligned orientation; (b) an orientation symmetric about \mathbf{F} ; (c) completely random orientation; (d) nearly planar random orientation; (e) mostly aligned orientation but off-axis; (f) orientation with multi-axial bias. Figures a-c can be represented by $g(\beta)$ or $\psi(\theta, \phi)$ (or the orientation tensors). Figures d-f cannot accurately be represented by $g(\beta)$ but can be represented by $\psi(\theta, \phi)$ (or, equivalently, the orientation tensors).	62
3.1	Flow chart of the thermal property computational methodology. . . .	69
3.2	Flow chart of the stiffness and strength computational methodology. .	70
3.3	COMSOL planar deposition finite element flow model for the polymer melt at the tip of a LAAM-nozzle.	73
3.4	Finite element geometries with boundary conditions: (a) tensile specimen, (b) compression specimen, (c) flexural specimen.	76
3.5	Finite element geometry with boundary conditions for CTE specimen.	80
3.6	Planar orientation results. Used initial $A_{ij} = \frac{1}{3}\delta_{ij}$, $a_r = 38.8$, $C_I = 0.0019$, $\kappa = 0.125$, and $N = 31$	82
3.7	Orientation along streamline 15 predicted with (a) IRD model, and (b) RSC model.	84
3.8	Color scheme indicates velocity magnitude.	84
3.9	(a) $A_{ij}(x_1)$ at the nozzle exit predicted by the IRD model; (b) $A_{ij}(x_1)$ at the nozzle exit predicted by the RSC model; (c) $A_{ij}(x_2)$ at the bead end predicted by the IRD model; (d) $A_{ij}(x_2)$ at the bead end predicted by the RSC model. Used initial $A_{ij} = \frac{1}{3}\delta_{ij}$, $a_r = 38.8$, $C_I = 0.0019$, $\kappa = 0.125$, and $N = 61$	85

3.10	A_{11} (blue) and A_{22} (red) at the end of a LAAM-printed bead using 4 different initial orientation conditions: completely random (solid), steady state (dashed), highly aligned (dash-dot), and planar random (dotted). (a) IRD used with $a_r=38.8$, $C_I=0.0019$, $N=61$. (b) RSC used with $a_r=38.8$, $C_I=0.0019$, $\kappa=0.125$, $N=61$	88
3.11	Components of the contracted stiffness tensor, $\langle C \rangle_{ij}$, through the flow domain. (a) $\langle C \rangle_{ij}(x_1)$ at the nozzle exit, predicted by the IRD; (b) $\langle C \rangle_{ij}(x_1)$ at the nozzle exit, predicted by the RSC; (c) $\langle C \rangle_{ij}(x_2)$ at the bead end, predicted by the IRD; (d) $\langle C \rangle_{ij}(x_2)$ at the bead end, predicted by the RSC. Used initial $A_{ij} = \frac{1}{3}\delta_{ij}$, $a_r=38.8$, $C_I=0.0019$, $\kappa=0.125$, and $N=61$	89
3.12	Elastic moduli through the flow domain. (a) At the nozzle exit, predicted by the IRD; (b) At the nozzle exit, predicted by the RSC; (c) At the bead end, predicted by the IRD; (d) At the bead end, predicted by the RSC. Used initial $A_{ij} = \frac{1}{3}\delta_{ij}$, $a_r=38.8$, $C_I=0.0019$, $\kappa=0.125$, and $N=61$	90
3.13	Components of the CTE tensor, $\langle \alpha \rangle_{ij}$, through the flow domain. (a) $\langle \alpha \rangle_{ij}(x_1)$ at the nozzle exit, predicted by the IRD; (b) $\langle \alpha \rangle_{ij}(x_1)$ at the nozzle exit, predicted by the RSC; (c) $\langle \alpha \rangle_{ij}(x_2)$ at the bead end, predicted by the IRD; (d) $\langle \alpha \rangle_{ij}(x_2)$ at the bead end, predicted by the RSC. Used initial $A_{ij} = \frac{1}{3}\delta_{ij}$, $a_r=38.8$, $C_I=0.0019$, $\kappa=0.125$, and $N=61$	91
3.14	Non-uniform distribution of elements in x_2 direction for tensile, compressive, flexural, and CTE FE meshes. Note, $N_{x2} = N = 13$ for conciseness.	92
3.15	Tensile and compressive strength constants (σ_{LT} and σ_{LC} , respectively) through the flow domain. (a) At the nozzle exit, predicted by the IRD; (b) At the nozzle exit, predicted by the RSC; (c) At the bead end, predicted by the IRD; (d) At the bead end, predicted by the RSC. Note, σ_{LT} and σ_{LC} represent the tensile and compressive strengths in the x_1 (horizontal) direction. Furthermore, the following parameters were used: initial $A_{ij} = \frac{1}{3}\delta_{ij}$, $a_r=38.8$, $C_I=0.0019$, $\kappa=0.125$, and $N_{x2}=N=61$	98
3.16	Failure surface for (a) the tensile specimen (deformation scale factor=10, $N_{x2} = 31$, $N_{x1} = 121$), (b) the compression specimen (deformation scale factor=5, $N_{x2} = 31$, $N_{x1} = 121$), and (c) the flexural specimen (deformation scale factor=1.5, $N_{x2} = 31$, $N_{x1} = 13$). Used initial $A_{ij} = \frac{1}{3}\delta_{ij}$, $a_r=38.8$, $C_I=0.0019$, and $\kappa=0.125$. Color scheme indicates value of φ from Equation 3.16.	99

3.17	Effective longitudinal stiffness and strength predictions as functions of RSC modeling parameters, C_I and κ : (a) tensile stiffness, (b) tensile strength, (c) compressive stiffness, (d) compressive strength, (e) flexural stiffness, and (f) flexural strength. Used initial $A_{ij} = \frac{1}{3}\delta_{ij}$, $a_r = 38.8$, $N_{x2} = N = 31$, and $N_{x1} = 121$	100
3.18	(a) Effective longitudinal tensile, compressive, and flexural strengths as functions of the critical fiber length. (b) Effective longitudinal tensile, compressive, and flexural strengths as functions of the weight-average fiber length. (c) Effective longitudinal tensile, compressive, and flexural stiffnesses as functions of the weight-average fiber length. Used $N_{x2} = 31$ and $N_{x1} = 121$	102
3.19	Laminate analogy approach: effective longitudinal (a) tensile/compressive stiffness and (b) flexural stiffness as functions of the RSC modeling parameters, C_I and κ . Used initial $A_{ij} = \frac{1}{3}\delta_{ij}$, $a_r = 38.8$, and $N_{x2} = N = 31$	103
3.20	Custom COMSOL application for predicting anisotropic material properties of a 3D printed SFRP. An extremely fine mesh is used for the flow simulation, as shown.	104
3.21	(a) Velocity magnitude (m/s) and (b) u velocity along 31 streamlines.	105
3.22	Spatially-varying orientation state in a LAAM nozzle: (a) amount of fiber alignment in x_1 represented by A_{11} and (b) amount of fiber alignment in x_2 represented by A_{22} . Used RSC with $C_I = 0.0019$, $\kappa = 0.125$, and $a_r = 38.8$	105
3.23	Spatially-varying stiffness as a function of the orientation state in Figure 3.22: (a) $\langle C \rangle_{1111}$ and (b) $\langle C \rangle_{2222}$	107
3.24	Spatially-varying elastic moduli as functions of the orientation state in Figure 3.22: (a) E_{11} and (b) E_{22}	107
3.25	Spatially-varying CTE as a function of the orientation state in Figure 3.22: (a) $\langle \alpha \rangle_{11}$ and (b) $\langle \alpha \rangle_{22}$	107
3.26	Spatially-varying thermal conductivity as a function of the orientation state in Figure 3.22: (a) $\langle k \rangle_{11}$ and (b) $\langle k \rangle_{22}$	108
3.27	Spatially-varying strength constants as functions of the orientation state in Figure 3.22: (a) σ_{LT} and (b) σ_{LC}	108
4.1	Baylor LAAM System.	110

4.2	Mach3 standard user interface.	111
4.3	Custom Baylor-themed Mach3 user interface, designed in-house. . . .	112
4.4	Strangpresse interface (left) and Strangpresse Extruder Model 19 (right).	113
4.5	Upgraded Baylor LAAM System.	114
4.6	(a) TA Instruments Q50, TGA machine. (b) Typical pre-processed pellet of 13% CF-ABS. (c) Plot of TGA burn-off test data. The solid red curve indicates temperature change over time, the dashed blue curve indicates change in weight percent over time, and the black dash-dotted line indicates the point at which the environment was changed from nitrogen (N) to air.	117
4.7	(a) Individual beads printed with Baylor's LAAM system. (b) Dimensions of the 3D printed specimen to be burn-off tested.	118
4.8	Burn-off testing setup for 3D printed specimen. (a) Ney Vulcan 3-1750 box furnace. (b) Specimen enclosed in a petri dish with custom aluminum lid, sitting inside the furnace. (c) Specimen after burn-off test.	119
4.9	(a) Branson Digital Sonifier 450 used for dispersing fibers in a beaker of acetone. (b) Fiber-acetone mixture after sonication, in a petri dish. (The fibers are very small.)	120
4.10	(a) Keyence VR-3000 One-shot Measurement Macroscope used for imaging fibers. (b) Keyence micrograph showing a typical fiber length measurement. Circles highlight areas where distinguishing between different fibers can be difficult when using the Keyence system.	120
4.11	(a) JEOL JSM-6610LV Scanning Electron Microscope. (b) SEM micrograph with fiber diameter measurements.	121
4.12	Sampling for second fiber aspect ratio characterization study.	122
4.13	(a) MZ7 microscope used to capture micrographs of fibers in a petri dish. (b) Micrographs were stitched together in Adobe Photoshop CC 2017 to measure the fiber using a custom MATLAB code. The measurement data, shown in green, is saved from a previous measurement session, whereas the blue data is from the current measurement session.	123
4.14	Printed rectangle from which strength specimens were cut. Dimensions are shown in inches.	124

4.15 Strip of ABS taped with clear packing tape to 8020 aluminum for milling.	125
4.16 Buehler IsoMet TM Low Speed Precision Cutter used for cutting out specimens.	125
4.17 Warping of a tensile specimen after curing adhesive.	125
4.18 Tensile specimen tabbed, heat-treated, milled, and ready for testing: (a) 13% CF-ABS, (b) Neat ABS.	126
4.19 Test Resources 810 Series fatigue tester.	127
4.20 Tensile testing setup (a) without an extensometer and (b) with a 1 inch Epsilon 3542-0100-100-HT2 extensometer.	127
4.21 Compression testing setup (a) far view (b) close-up view of compression specimen inserted in the modified ASTM D695 compression test fixture (Boeing BSS 7260).	129
4.22 Flexural testing set up. (a) 100 Series Test Resources machine with a 1000 lbf load cell. (b) Close-up of testing specimen, ready for testing.	130
4.23 Fiber decomposition diagram.	132
4.24 Burn-off test of carbon fiber.	133
4.25 Study 1: fiber length distributions from, (a) the pre-processed pellet, and (b) the printed bead.	136
4.26 Study 2: fiber length distributions from, (a) the pre-processed pellet, (b) the extrudate (pre-deposition), and (c) the printed bead (post-deposition).	137
4.27 Tensile stress-strain plots: (a) Neat ABS and (b) 13% CF-ABS. . . .	138
4.28 Compression stress-strain plots: (a) Neat ABS and (b) 13% CF-ABS.	139
4.29 Flexural test results of Neat ABS, (a) load-deflection curve and (b) stress-strain curve, and of 13% CF-ABS, (c) load-deflection curve and (d) stress-strain curve.	141
4.30 Additional TGA burn-off test results showing the amount of highly volatile matter (<i>V</i>), medium volatile matter (<i>O</i>), combustible matter (<i>C</i>), and ash (<i>A</i>). Figure (a) is for a dried Neat ABS pellet sample, and figure (b) is for a dried 13% CF-ABS pellet sample.	143

4.31	Additional TGA burn-off test results for (a) a dried Neat ABS pellet sample, and (b) a dried 13% CF-ABS pellet sample.	145
4.32	(a) Baylor LAAM extruder, printing a strip (photograph filtered for better lighting). (b) Tensile specimens.	147
4.33	Cross-section of a tensile specimen: (a) photograph taken with an iPhone SE (model A1662) and (b) points captured along the edges of the specimen, used to define the cross-section of the tensile specimen geometry in COMSOL.	147
4.34	FE tensile specimen geometry in COMSOL with boundary conditions: (a) front view and (b) back view.	148
4.35	FE idealized rectangular tensile specimen geometry in COMSOL with boundary conditions: (a) front view and (b) back view.	148
4.36	FE meshes for (a) the realistic geometry and (b) the rectangular geometry.	149
4.37	Stiffness predictions for 3D FE COMSOL models: (a) used realistic tensile specimen geometry and (b) used rectangular tensile specimen geometry.	150
4.38	FE tensile simulations. Von Mises stress (deformation scale factor=6) for (a) the realistic geometry and (b) the rectangular geometry. Also, failure plots (deformation scale factor=6) for (c) the realistic geometry and (d) the rectangular geometry.	151
4.39	Tensile test setup: (a) MTS QTest/100 tensile testing machine with 100 kN load cell; (b) MTS 25 mm gage extensometer (Model 634.11F-24) mounted to a specimen.	152
4.40	Typical stress-strain response of a 6-bead tensile specimen like that shown in Figure 4.32b.	153
4.41	Printed bead cross section, divided into nine regions where the orientation has been found by Nargis [133]. The red dots indicate the centroids of each region.	154
4.42	Spatially varying components of A_{ij} across the cross section of a LAAM-printed bead. Measurement data from Nargis [133]: (a) A_{11} , (b) A_{22} , (c) A_{33} . RSC prediction using $a_r = 38.8$, $C_I = 0.0019$, $\kappa = 0.125$: (d) A_{11} , (e) A_{22} , (f) A_{33} . RSC prediction using $a_r = 38.8$, $C_I = 0.0019$, $\kappa = 0.05$: (g) A_{11} , (h) A_{22} , (i) A_{33}	155

4.43	3D finite element COMSOL flow model.	156
4.44	3D finite element COMSOL tensile simulation geometry.	156
4.45	Effective longitudinal stiffness and strength predictions, <i>corrected for void volume fraction</i> , as functions of RSC modeling parameters, C_I and κ : (a) tensile stiffness, (b) tensile strength, (c) compressive stiffness, (d) compressive strength, (e) flexural stiffness, and (f) flexural strength. Used initial $A_{ij} = \frac{1}{3}\delta_{ij}$, $a_r = 38.8$, and $N = 31$	161
4.46	Stiffness predictions for 3D FE COMSOL models, <i>corrected for void volume fraction</i> : (a) used realistic tensile specimen geometry and (b) used rectangular tensile specimen geometry.	162

LIST OF TABLES

2.1	Fiber Orientation Modeling Terms.	20
2.2	Voigt Order for Contracting Tensors.	39
2.3	Constants used in Tandon-Weng equations.	42
3.1	Properties of ABS Matrix and Carbon Fiber Used for Modeling. . . .	71
3.2	Summary of Effective Longitudinal Properties for All Flow Conditions.	94
4.1	Length and diameter measurements for fiber aspect ratio characteri- zation.	134
4.2	Corrected fiber aspect ratio measurements.	135
4.3	Tensile testing statistics.	138
4.4	Compression testing statistics.	140
4.5	Flexural testing statistics.	142
4.6	Tensile stiffness experimental results for tensile specimens made of 13% CF-ABS.	153
4.7	Measured vs. predicted A_{ij} data in a LAAM-printed bead. “Mea- sured” values are from Nargis [133]. Region numbers come from Fig- ure 4.41. Percentage errors are given in parentheses.	157
4.8	Tensile/Compressive Stiffness - Predictions.	164
4.9	Flexural Stiffness - Predictions.	165
4.10	Tensile Strength - Predictions.	165
4.11	Compressive Strength - Predictions.	165
4.12	Flexural Strength - Predictions.	166
4.13	Experimental Results Summary.	166

ACKNOWLEDGMENTS

First, I would like to thank my Saviour, Jesus Christ. I count all things to be loss in view of the surpassing value of knowing Him.

I would also like to sincerely thank my parents, Bradford and Ann Russell, who spent much effort in trying to raise me right and invested heavily in my education.

I am not sure if I ever would have gone to graduate school if it were not for my advisor and former Scoutmaster, Dr. David Jack. I am so glad we were able to reconnect. Thank you Dr. Jack for your relentless positivity and eagerness to help me all the way through my master's and Ph.D.!

I also extend thanks to all of my colleagues and professors for providing a positive atmosphere conducive to collaboration and growth. It has been a real blessing being able to be a part of the Sic'em Research group and it is exciting to see where it is headed!

I am also indebted to Dr. Blake Heller and Dr. Douglas Smith for letting me use their 2D finite element, shape-optimized flow model. Thank you!

Finally, I must also thank Luke Battershell and Baylor's machinist, Ashley Orr, for their extensive help in getting the LAAM system constructed and up and running. I could not have done it without you!

To my parents, Bradford and Ann Russell.

CHAPTER ONE

Introduction

Materials play a vital role in the development of human society. Advances in understanding have led to a desire to invent new materials by combining multiple distinct ones to form composites. Composite materials can be tailored to fit specific applications, offering unique, enhanced properties. Along with advancement in material selection has come improvement in the techniques and machinery used to build with these various materials. In turn, these improved manufacturing techniques motivate even more new materials to be developed. The present dissertation concerns both improving the current understanding of composite materials science, an ancient field, and the specific manufacturing method known as additive manufacturing, or 3D printing, which is a much more recent development.

Composite materials have been in existence since ancient times. Bricks made of earth and natural fiber like straw are a construction material dating back thousands of years [1]. Oftentimes composite materials are a combination of some sort of fiber reinforcement and a matrix material that acts as the glue holding all the fibers together. For example, in the case of bricks made of straw and clay, the straw is the fibrous constituent, and the clay is the matrix. Steel rebar and cement can also be used to make a modern-day composite material used in construction. These examples involve very large fibers, but some composite materials contain very small fibers that are difficult or impossible to distinguish from each other with the naked eye. For example, most glass fiber filled polymer composites contain glass fibers with diameters on the order of tens of microns or less. Carbon fiber filled polymer composites commonly contain carbon fibers with diameters around 7 microns. One advantage of small fibers is that their small size reduces the possible size of defects

in the fibers. This leads to very good material properties becoming achievable by composite materials science. Fiber filled polymer composites are the focus in the present dissertation.

One interesting feature with fibrous composite materials is that the material may exhibit directionally dependent properties, or anisotropic properties. This could be good or bad depending on what is needed. For example, since fibers are usually stronger than the matrix material they inhabit, a composite material is generally strongest in the direction the fibers are aligned in the most. Therefore, a composite part such as a laminated composite part could be designed to maximize its strength in the main load-bearing directions by preferentially aligning the fibers in those directions. This ability is attractive when combined with the fact that composites like glass fiber reinforced polymers and carbon fiber reinforced polymers (CFRPs) are also lightweight. In industries like the aerospace and automotive industries, lightweighting gets attention since reducing weight improves fuel economy and overall energy efficiency. If a lightweight part is needed for a particular application in which it would bear a load in only a couple of directions, the part could be tailor-made of lightweight fibers and polymer with the fibers preferentially aligned in the load bearing directions. If the same part were made of an isotropic metal though, although the metal may provide the needed strength in the load bearing directions, it would also likely be heavier and “waste” its strength in the non-load-bearing directions. Fiber filled polymer composites, therefore, provide an attractive substitute, offering good stiffness-to-weight and strength-to-weight ratios.

On the other hand, while composites with anisotropic properties can be used advantageously, the process of designing parts with them is more complicated. This is because their anisotropic properties are more complicated to predict. Furthermore, there are different ways of manufacturing them that can add difficulty to predicting the properties. Predicting the properties of a short fiber polymer composite (SFRP),

for example, can be much more complicated than predicting the properties of a continuous fiber laminated composite because the fiber orientation state is difficult to control. On the other hand, laminate manufacturing techniques like vacuum assisted resin transfer molding (VARTM) allow manufacturers to control the fiber orientation, so that it is known prior to attempting property predictions. VARTM involves stacking layers of weaved fibrous fabric and bonding them together with a neat polymer resin which is cured. The orientation of each layer can be chosen to optimize the properties of the entire laminate.

SFRP parts are often made with traditional polymer processing techniques like injection and compression molding. These processes can produce very complicated, spatially varying fiber orientation states inside SFRP parts, unlike in continuous fiber laminates. Thus, predicting the properties of SFRP parts oftentimes involves the problem of predicting their internal fiber orientation state first, then predicting the properties as functions of that orientation state. The advantage of SFRPs is that although they add complexity to property predictions, they reduce complexity in the manufacturing process. SFRPs can be processed relatively easily using most existing polymer processing methods and offer enhanced properties over their neat polymer counterparts. Furthermore, SFRPs made with thermoplastics can easily be recycled and processed again whereas thermoset laminates cannot.

Research on predicting the fiber orientation state in a fluid flow has its roots going back about a hundred years ago to George B. Jeffery. The works of Charles Tucker III and his students in the past few decades have contributed greatly to the current understanding of this topic as well. Tucker and his student Suresh Advani brought orientation tensors to light as a general but very compact way to describe orientation states. These have since become mainstream. Orientation tensors can also be used in predicting material properties. Thus, modern modeling techniques now give the ability to predict the final properties of SFRP parts based on the

processing conditions used to build said parts. In this way, SFRP parts can be evaluated prior to fabrication, saving time and money and improving an engineer's confidence level regarding the suitability of a particular part design.

However, fiber orientation modeling is quite a complex issue and research is ongoing. Since additive manufacturing has entered the limelight there is also a need to introduce fiber orientation modeling to the additive manufacturing industry to gain insights into how 3D printing processes can be improved.

Additive manufacturing (AM) began in the early 1980s and has gained much ground since, helped by the development of personal computers. AM involves building a 3D object from a Computer Aided Design (CAD) file, usually in a layer-by-layer fashion, stacking many 2D print patterns on top of each other. The AM process offers a designer the ability to design a part with little wasted material, easily add complexity to the part, iterate quickly through various designs of the part, and do all this while avoiding the need for expensive molds or tooling. All this saves time and money.

Naturally, AM started by using virgin build materials, but it has now developed enough that SFRPs have become of interest, such as for Large Area Additive Manufacturing (LAAM). LAAM, an extrusion-based 3D printing technology using thermoplastic build materials, provides the ability to print parts that are much bigger than what most 3D printers can print. These parts can be on the order of meters in width, height, and length. Adding short carbon fibers to the thermoplastic build material used by LAAM is extremely helpful in that it improves both the structural properties and the thermal properties of the parts that are fabricated. This has helped motivate the present dissertation to be written.

There are two main goals of this dissertation. The first is to advance the current understanding of microstructural property prediction. The first goal involves both fiber orientation modeling as well as property prediction. These topics

are surveyed in Chapter Two of this dissertation, which is more than just a literature review and includes examples and figures created by the author. As Advani noted in [2], many anisotropic properties can be predicted in terms of orientation tensors. However, a comprehensive list of the properties that can be determined by his techniques along with the explicit equations for these properties appears to be lacking in the literature. Therefore, one of the tasks associated with the first goal of this dissertation is to explicitly show the equations for many microstructural properties that can be obtained using Advani's methods. To demonstrate the versatility of Advani's techniques, Chapter Three ends with a presentation of an application made by the author in which the spatially varying fiber orientation state in a LAAM-printed SFRP bead can be predicted followed by predictions of the spatially varying mechanical and thermal properties. Several bulk, effective properties of LAAM-printed SFRP beads are also predicted and analyzed in Chapter Three using predicted microstructural properties and finite element analysis. Specific focus is given to predicting the effective anisotropic stiffness, coefficient of thermal expansion, and strength. Of course, predicting these properties for a single bead means the present work is just one step towards the greater goal of being able to predict the bulk response of entire LAAM-made parts.

The second goal of this dissertation is to advance the current understanding of extrusion-based, additively manufactured SFRPs, with a specific emphasis on LAAM. Some insights can be gained from the computational methods performed in Chapter Three. In addition to these, more insights can be gained in Chapter Four which covers the experimental portion of this dissertation. For fabricating the test specimens for the experiments, the author led the construction of a miniature LAAM system at Baylor University which has already served several researchers in the pursuit of their graduate degrees in addition to the author. The details of this system are discussed in Chapter Four. Chapter Four also includes a section on

making modeling modifications based on experimental results.

For this dissertation, many numerical analyses and finite element simulations have been performed. The software chosen to perform these operations was MATLAB® (R2019b; MathWorks) and COMSOL Multiphysics (Version 5.5; COMSOL Inc., Stockholm, Sweden). An advantage of using these is that COMSOL can be paired with MATLAB via LiveLink™, enabling a modeler to write functions in MATLAB and call them within the COMSOL environment. This is a powerful capability that is taken advantage of extensively. It should also be noted that although the computational methodology that is presented in this dissertation was developed with LAAM in mind, it can be applied to other SFRP processing techniques besides LAAM, including injection and compression molding. Therefore, the work presented here has value beyond the additive manufacturing industry.

CHAPTER TWO

Background Information

The amount of peer reviewed journal articles on additive manufacturing, SFRP processing, and mechanical property prediction of SFRPs is enough that extensive literature reviews could be written on any one of these topics alone. Thus, the challenge of compiling this chapter lies in deciding which topics and theories to address and which to exclude. Both additive manufacturing and important background information on microstructure analysis are reviewed. In addition, several figures have been included in this chapter as illustrative examples to clarify the concepts being discussed. All of the figures in this chapter were created or re-created by the present author.

The first section of this chapter gives an overview of additive manufacturing, including the build materials and types of additive manufacturing. This is followed by a focused section that discusses Large Area Additive Manufacturing (LAAM) in particular. While the computational methods in this dissertation can be applied to other SFRP processing techniques, the methods have been developed specifically with LAAM in mind. The next section discusses the fundamentals of predicting the internal spatially varying fiber orientation state in processed SFRPs. This is followed by a section on micromechanical models, which allow anisotropic stiffness properties to be predicted as a function of the internal, spatially varying fiber orientation state. The next section addresses strength prediction based on the internal, spatially varying fiber orientation state. Finally, a section on other properties that can be predicted as a function of the underlying orientation state, including thermal properties, is given.

2.1 Additive Manufacturing of SFRPs

Additive Manufacturing (AM) is defined by 3Dprinting.com as “a process of making three dimensional solid objects from a digital file” [3] and is also known as 3D printing. The additive approach to making parts differs from traditional subtractive machining and molding processes and more closely resembles the manufacturing process used by nature in constructing organic structures [4]. Charles Hull obtained the first patent on a 3D printing process in 1986 [5]. His stereolithography apparatus, now referred to as an SLA-type 3D printer, uses a process of curing layers of liquid polymer resin, building them up till a 3D object is formed. The company 3D Systems, which introduced this technology commercially, also developed the Standard Tessellation Language (.STL) file format which has become the industry standard for many types of AM [6]. Since the 1980s, most of the early patents on AM have expired and the number of AM types have multiplied, most using a variation of sectioning a digital 3D object into layers and building the object up one layer at a time.

Fey et al. [7] summarize five key advantages of AM. First, it is empowering in that virtually anyone with the proper build materials and a 3D printer can fabricate almost any part, anywhere. In addition, the processing of raw materials can be done more sustainably and parts made more energy-efficiently using AM. Thirdly, due to the nature of the AM process which builds the inside and outside structure of a part simultaneously, complicated parts can be fabricated and additional complexity can be added to them for free, enabling users to create parts that would be much more difficult or even impossible to fabricate using traditional manufacturing methods. The fourth advantage of AM given by Fey is that it has great flexibility in that a variety of completely different parts can be fabricated by a single 3D printer. The fifth advantage is that AM can cut lead times in product development. In fact, as noted in [4], the main initial market for AM was for prototyping since AM

enables designers to bypass tooling and fabricate parts quickly for testing, allowing designers to rapidly iterate through their designs. The five advantages given above by Fey et al. [7] imply that AM could have a great, positive impact in many areas including resource conservation, climate change, health care, and space exploration [7]. Another advantage of AM is that it is well suited for manufacturing low volumes of parts, especially ones with complex shapes (e.g., [8]).

There are plenty of journal articles reviewing the types of AM and the AM of composites (e.g., [6,8–11]). Broadly speaking, the types of AM can be divided up by the types of build materials they use and what state the build material is in prior to fabrication [8]. AM can be used to print a wide variety of materials including polymers, metals, ceramics, and composites (e.g., [8]). Both inorganic fiber-filled polymer composites, like those used in the work done by Oak Ridge National Laboratory researchers [12–16], and even metal powder-filled polymers composites (e.g., [17]) have been made. Some AM processes start with a liquid build material like a polymeric thermoset resin, some use a filament or paste that can be extruded, some a powder, and at least one even uses solid sheet material [8].

Some of the more common types of AM are described in [6] including SLA, digital light projection (DLP), continuous liquid interface production (CLIP), binder jetting, selective laser sintering (SLS), selective heat sintering (SHS), fused filament fabrication (FFF), and large area additive manufacturing (LAAM). SLA involves using a focused UV laser beam to selectively polymerize a liquid resin onto a build plate that is submerged in a tank of the liquid resin. DLP is similar, but projects light onto a build plate to fabricate an entire layer at a time, as opposed to tracing each layer with a concentrated laser as in SLA. CLIP is similar to SLA and DLP in that it also involves curing liquid resin held in a resin tank, but it does this in a continuous fashion as opposed to curing a layer at a time and incrementally increasing the height between the build plate and laser/light source. Binder jetting

uses a powder build material that is selectively bound together layer-by-layer using a liquid binder agent. SLS is similar to SLA in that it uses a concentrated laser beam, but uses a powdered build material like binder jetting. SHS is similar to SLS, but uses a thermal printhead instead of a laser. FFF additive manufacturing involves using a heated nozzle to melt and extrude a polymer filament. LAAM, or Big Area Additive Manufacturing (BAAM) such as that done by Oak Ridge National Laboratory, is similar to FFF in that it is a polymer, extrusion-based process but it is on a much bigger scale, able to print parts on the order of meters in every direction. A more in-depth discussion of LAAM will be given in Section 2.2. Another type of additive manufacturing mentioned in [6] is Laminated Object Manufacturing which involves cutting the layers of material out of sheets of build material and stacking and binding them together as described in [18].

The applications for AM abound. A few of the industries utilizing AM include the aerospace, automotive, energy, and biomedical industries [8]. In the aerospace industry, low-volume, complex parts made of advanced materials are often needed, which makes this industry very well suited for AM [8]. Examples of parts include turbine parts [19] and rocket parts [20]. Furthermore, development of new products is vital in the automotive industry, making AM helpful in that it can reduce the development time, the cost of manufacturing, and the final product cost [8]. Speeding up product development and reducing cost also make AM a good candidate for the energy industry [8]. In the biomedical industry, AM is a useful means of fabricating medical devices, tissue scaffolds, orthopedic implants, and artificial organs, as well as other devices [8]. In the architectural industry, AM serves as a means of making models [21] and even constructing full-size houses [22]. AM has also made inroads into education [23] and even fashion [24].

With the increasing demand for AM, there is an increasing demand for a wider material selection. Combining AM with composite materials opens up a wide

variety of design possibilities. A composite material is a mixture of multiple distinct materials that often offers superior properties (e.g., [25]). In addition, many types of composites can be 3D printed. The main three types of polymer composites for AM include nanocomposites, particle-filled polymers, and fiber-filled polymers [9]. Nanocomposites and particle-filled polymers can be produced using methods such as SLS, SLA, and FFF [9]. Fiber-filled polymers can also be printed by such methods and are the main focus in the present work.

In an excellent 2020 review article, van de Werken et al. [26] surveyed the cutting edge of 3D printing carbon fiber reinforced polymer composites (CFRPs) technology. This article demonstrates the idea that CFRPs are indeed a good route to promoting 3D printing technology from the prototyping space to functional, end-use part production [26]. Van de Werken et al. categorize CFRPs by matrix type, namely thermosets or thermoplastics, and fiber length, namely discontinuous or “short” fibers and continuous fibers [26]. The use of thermoset matrices is beneficial in that there is already a good knowledge base about how to achieve good fiber-matrix bonding due to their use in the aerospace industry [26]. On the other hand, thermoplastic matrices have comparatively low fiber-matrix bond strength and are expensive; however, thermoplastic matrices do not require prolonged curing times or complicated chemistry, they are relatively cheap to process, and they can be processed using many different existing manufacturing methods [26]. The carbon fibers used for CFRPs may be discontinuous, which includes milled fibers (on the order of hundreds of μm in length) and chopped fibers (on the order of a few mm long), or continuous fibers [26]. Continuous fiber CFRPs can achieve much better properties compared to discontinuous fiber CFRPs, however, CFRPs that have discontinuous fibers can be readily manufactured by nearly all types of 3D printing [26].

Van de Werken et al. support the idea that the fiber aspect ratio and fiber volume fraction can both significantly increase properties such as stiffness and strength

[26]. There is a trade-off though, because higher fiber volume fractions can be achieved with shorter fibers which have smaller aspect ratios, such as with milled fibers rather than with chopped fibers [26]. If the fibers can be forced to align though, higher volume fractions can be achieved [26]. Volume fractions of aligned chopped fiber composites can go up to about 25-40%, which is comparable to what is obtainable by random, milled fibers [26]. Chopped carbon fibers are restricted to volume fractions under 10% if they are randomly aligned [26]. It should also be noted that increasing the fiber volume fraction past a certain threshold can actually have a detrimental effect on mechanical properties due, possibly, to increased void content [26]. In addition, a fiber aspect ratio of 1000 can achieve over 80% of the theoretical maximum stiffness and strength of a composite but, for typical carbon fibers with diameter $\approx 7\mu\text{m}$, the fibers need to be at least $\approx 7\text{ mm}$ long which requires a low fiber volume fraction (assuming that alignment is not controlled) [26]. In addition, fibers with an aspect ratio this large are likely to bend. Modeling such fibers and the properties they help produce is complicated. In this dissertation though, much smaller fiber aspect ratios are considered such that it is safe to assume the fibers are rigid. This will be discussed more in Section 3.1.1.

One of the disadvantages of processing long, discontinuous fibers is fiber breakage during processing. Goris et al. of the University of Wisconsin-Madison's Polymer Engineering Center have obtained helpful findings after studying fiber breakage in the processing of long glass fiber filled polypropylene using a Couette rheometer [27]. They use the fiber attrition model of Shon et al. [28] (as cited in [27]), which says that fiber length will decrease exponentially over flow processing time

$$L(t) = (L_o - L_\infty)e^{-k_f t} + L_\infty \quad (2.1)$$

In the equation above, t is time, L_o is the initial fiber length, and k_f and L_∞ are fit to experimental data where L_∞ is an asymptotic value identified as the final fiber length.

In [27], Goris et al. found that the best combination of processing parameters led to a final fiber length of less than half of L_o . In the worst case scenario, the final fiber length was less than 10% of L_o . Goris et al. also found that a lower processing temperature, which increases the viscosity of a polymer melt and therefore increases the hydrodynamic stresses on the fibers, results in a reduced final fiber length. In addition, they found an increase in the fiber concentration (or fiber volume fraction), which leads to more fiber-fiber interaction and higher viscosity, also reduces the final fiber length [27]. Another finding is that, given enough processing time (they look at 3 minutes), the final fiber length will essentially be the same regardless of the initial fiber length. This last point leaves a gap in 3D printing technology. As revealed by Van de Werken et al. [26], there is 3D printing technology for short fiber composites and continuous fiber composites, but no one has developed a good method for the 3D printing of long, discontinuous fibers. Furthermore, aligned, continuous fiber 3D printing technology can produce materials with very attractive specific strength and stiffness properties comparable to metals, but this technology is costly [26].

Van de Werken et al. [26] also describe the pros and cons of the different kinds of 3D printing that can be used to fabricate CFRPs. Some of these include extrusion based processes, such as Fused Filament Fabrication (FFF), Direct Write, Reactive Extrusion, large-scale additive manufacturing, and large-scale Reactive Extrusion [26]. FFF produces parts that have weakness at the bead-to-bead interfaces and weakness due to voids both in the beads (intra-bead voids) and in between the beads (inter-bead voids) [26]. Better mechanical properties can be achieved by infrared heating, Z-pinning, and utilizing hot isostatic pressure [26]. High fiber alignment in the print direction is achieved due to the FFF process and typically, fiber volume fractions do not exceed 20% [26]. The FFF processing parameters, such as the processing temperature, layer thickness, and infill pattern, can make a difference on the final properties of a part as well [29] (as cited in [26]).

Direct Write 3D printing uses a thermoset resin that is pre-mixed with a catalyst before extrusion and cured during or after processing with heat or UV light [26]. A similar density to compression molded parts is achievable and even better mechanical properties can be attained since the fibers are more aligned [30]. Reactive Extrusion 3D printing is similar to Direct Write and also utilizes thermosets, but the thermoset resin and catalyst are fed separately into the extruder nozzle prior to deposition [26]. Reactive Extrusion printing can have much higher deposition rates than FFF [26].

Large-scale additive manufacturing technology also exists and is the focus of the present dissertation. Large Area Additive Manufacturing (LAAM) is an extrusion-based method similar in concept to FFF and will be discussed in more depth in the next section. Another promising large-scale additive manufacturing process is large-scale reactive extrusion, which is a more recent development and uses thermosets which form strong bonds at inter-bead interfaces [31, 32].

Stereolithography (or “SLA” for Stereolithography Apparatus) is another type of 3D printing that utilizes a thermoset resin, which is contained in a tank and selectively cured using light or heat, and has been used to print CFRPs using nonwoven carbon fiber mats [33]. However, there is little literature on SLA-printed CFRPs (e.g., [26]). Selective Laser Sintering (SLS) is another type of 3D printing that can be used to make CFRPs by selective laser-fusing of a powder material (e.g., [26]). Carbon nanofibers have been used in SLS and have been shown to increase storage modulus, but the process gives parts a rough surface [34]. Researchers of 3D printing composites have not paid much attention to SLS and the fact that the fibers are pulverized into a powder means that the fibers are very short and are limited in their ability to enhance mechanical properties [26].

2.2 Large Area Additive Manufacturing

Large Area Additive Manufacturing (LAAM), termed Big Area Additive Manufacturing (BAAM) by the developers at Oak Ridge National Laboratory, is an out-of-oven, extrusion-based additive manufacturing process which uses thermoplastic material to build parts on the order of meters in length, width, and depth [12]. The process is similar to FFF but uses pellet feedstock as opposed to filament, which decreases cost and opens up LAAM to a wide variety of potential build materials that are already produced in pellet form [12]. The LAAM process boasts the ability to deposit material that is 20 times cheaper over 200 times faster (up to 50 kg/hr) than typical FFF processes and it can produce parts that are about 10 times bigger as well [12]. Carbon fibers have proven to be crucial to LAAM-processed thermoplastics in order to maintain the dimensional stability of parts, which are built outside of an oven, while simultaneously enhancing their strength and stiffness [4]. The dimensional accuracy of the parts is affected by their thermal expansion and thermal conductivity properties. Since LAAM builds parts layer-by-layer and a layer starts to cool immediately after deposition before another hot layer is deposited on top of it, the parts fabricated by LAAM are prone to significant thermal gradients during printing and these can result in residual stress formation and warping. Carbon fiber mitigates thermal gradients by increasing the thermal conductivity of the deposited material and decreases dimensional change by decreasing the coefficient of thermal expansion (CTE) of the deposited material [4]. To address the temperature related problems of warping and delamination or cracking, which are issues in small-scale AM but even bigger issues as the scale is increased to LAAM-size, Compton et al. developed a transient, one-dimensional thermal model which can be used to predict the change in temperature of layers of LAAM-printed material over time [35].

Another issue effecting the dimensional accuracy of LAAM-printed parts is the size of the beads that are printed. LAAM beads are much bigger than those

generated with typical desktop FFF printers and typically have a cross-sectional area around 25-35 mm. For example, [12] reports typical dimensions of 8.4 mm wide by 4 mm thick, similar to the typical dimensions in works by the present author, which are about 9 mm by 3 mm [36,37]. Chesser et al. [38] developed methods to improve the dimensional accuracy of LAAM-made parts by incorporating the following: (1) a new nozzle design capable of printing two resolutions, the higher one selectively chosen when good resolution is more desirable than a high throughput; (2) a material diversion device that allows the extrusion flow rate to achieve steady state before printing and for the flow rate to be cut off after printing (this is helpful at areas in the print where the LAAM system must stop/resume extruding several times, such as at seams); (3) an empirical model for controlling extrusion rate around turns so that a more constant bead diameter is achieved.

LAAM combines the versatility of small-scale AM with large-scale part fabrication, which allows for interesting applications. One promising application is that of creating molds or tooling for Vacuum Assisted Resin Transfer Molding, which can be used for composite part fabrication [13]. In [13], a 20 wt% carbon fiber filled ABS was printed using LAAM to make a highly durable out-of-autoclave mold for fabricating composite laminate parts at room temperature. Since LAAM-made parts have a rough surface finish, Hassen et al. opted to print a slightly shrunken mold and then apply a coating which was machined and polished before another tooling gel was applied to the mold [13]. Despite the post-processing steps, Hassen et al. still concluded that transitioning from traditional tooling to LAAM-made tooling could reduce tooling costs by 10-100 times and concept-to-part time from months to weeks [13]. Kunc et al. also demonstrated the potential to fabricate in-autoclave tooling using LAAM with a 50 wt% carbon fiber Polyphenylene sulfide or LAAM with a 25 wt% carbon fiber filled Polyphenylsulfone [14]. Other parts that have been printed and demonstrate the potential of LAAM include: an automobile chas-

sis [15, 39], a mold for a helicopter blade [40], a mold for a yacht hull [40], a mold for a wind turbine blade [16], drill and trim fixtures [39], concrete formwork [39], furniture [39], foundry patterns [39], and functional prototypes and parts [39].

Finishing LAAM made parts can be done in multiple ways including applying a coat to the printed parts, machining the parts, or some combination of coating and machining. The company Thermwood has incorporated a post-processing machining ability into their LAAM system so that parts can be machined immediately after being printed [40]. Thermwood also prints parts on a bed of pellets made of the build material, which avoids adhesion problems and the need for a heated print bed. Since Thermwood’s machines can be used for machining, the rough bottom finish of a part as well as any warping that may have occurred on the bottom of the part is smoothed out after the part printed.

One issue plaguing LAAM is porosity, both between beads (inter-bead) and inside individual beads (intra-bead). Inter-bead porosity is an artifact of the LAAM process which produces beads with rounded cross-sections. This leads to triangular gaps in the printed structure. Duty et al. hypothesized that intra-bead porosity develops by the fibers effecting the flow field during processing by creating nucleation sites that are conducive to forming bubbles [12]. Tekinalp et al. [41] found that there were little to no intra-bead voids in neat-ABS samples printed using FFF, but that significant intra-bead porosity formed in carbon fiber filled ABS samples printed with FFF. On the other hand, the addition of carbon fiber decreased the size of inter-bead voids and this was attributed to the carbon fibers decreasing the die-swell and increasing the thermal conductivity of the processed material [41]. Compression molded samples in the same study did not suffer from porosity even in the carbon fiber filled ABS, but the significantly increased alignment and improved dispersion in the FFF-printed samples made their properties still comparable to the compression molded samples [41]. Interestingly, Tekinalp et al. also concluded that the FFF

process led to higher molecular alignment in printed ABS as opposed to compression molded ABS, as evidenced by the fact that in spite of porosity defects, they found the strength of printed ABS to be higher than that of compression molded ABS. They found the stiffness to be about the same for both the printed and compression molded ABS.

Reducing the porosity problem in FFF or LAAM-printed parts could result in superior material properties. A tamping mechanism was devised by Oak Ridge to flatten layers after they are deposited and still hot so that inter-bead voids can be reduced in size and so the layers are more level; this device also caused significant improvement in the in-plane stiffness and strength properties [12]. Until porosity in LAAM-printed material can be eliminated completely however, it should be accounted for when attempting to accurately predict the properties of printed SFRP material.

2.3 *Fiber Orientation Modeling*

The role of fiber orientation in determining the properties of additively manufactured SFRP parts can be studied at a macro or micro level. In general, the fibers will align *mostly* in the print direction (e.g., [41]) and thus, at the macro level the orientation state - and therefore the properties of a part - can be partially controlled by defining the print path with which the part is printed. Jiang et al., for example, found that carbon fiber could be used to increase the tensile stiffness and strength of several different polymers in the print direction [42]. Therefore, printing parts in the direction in which they bear the most load makes sense. However, the fibers do not align perfectly in the print direction. Therefore, the fiber orientation state must be quantified at a micro level as well to fully understand the fiber orientation effects on the properties a 3D printed SFRP. This latter point is the focus of this dissertation.

First, the orientation of an individual fiber within a matrix can be described by a unit vector,

$$\mathbf{p} = [\sin \theta \cos \phi \quad \sin \theta \sin \phi \quad \cos \theta]^T \quad (2.2)$$

where the angles θ and ϕ are shown in Figure 2.1. Most modern methods of modeling the internal fiber orientation state in a processed SFRP are built on Jeffery's model, which can be expressed as the time rate of change of \mathbf{p} . The next section will give a brief overview of Jeffery's model. Then a discussion of orientation tensors will be given followed by discussions of two of the more well known fiber orientation models. A final discussion on the *closure problem* will conclude the section on fiber orientation modeling. A summary of the fiber orientation modeling terms and operations used in this section is given in Table 2.1, where each term will be discussed fully in the following sections. In general, bold, lowercase letters refer to vectors, bold, uppercase letters refer to tensors, and non-bold letters with subscript indices refer to components of vectors and tensors. For example, x_i refers to the i^{th} component of the vector \mathbf{x} and A_{ij} refers to the (i, j) component of the tensor \mathbf{A} . Non-bold terms without subscripts are scalar parameters.

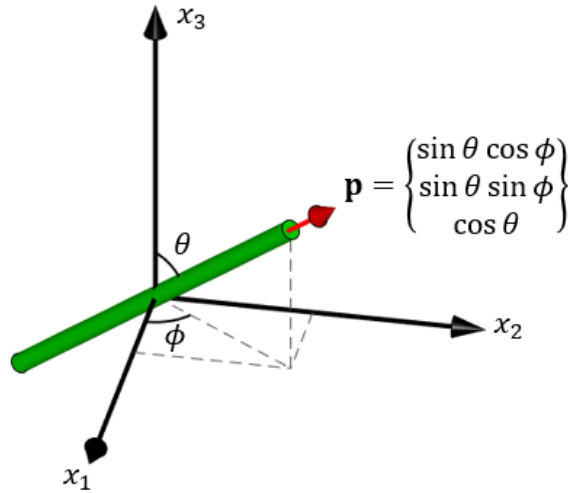


Figure 2.1: The unit vector \mathbf{p} from Equation 2.2 expressing the direction of a cylindrical fiber.

Table 2.1: Fiber Orientation Modeling Terms.

Term	Symbolic Notation	Index Notation
Orientation unit vector	\mathbf{p}	p_i
Position vector	\mathbf{x}	x_i
Velocity vector	\mathbf{v}	v_i
Velocity gradients	\mathbf{L}	$L_{ij} = \frac{\partial v_i}{\partial x_j}$
Vorticity tensor	$\mathbf{W} = \frac{1}{2}(\mathbf{L} - \mathbf{L}^T)$	$W_{ij} = \frac{1}{2}(L_{ij} - L_{ji})$
Rate of deformation tensor	$\mathbf{D} = \frac{1}{2}(\mathbf{L} + \mathbf{L}^T)$	$D_{ij} = \frac{1}{2}(L_{ij} + L_{ji})$
2 nd order orientation tensor	\mathbf{A}	A_{ij}
4 th order orientation tensor	\mathbf{A}_4	A_{ijkl}
6 th order orientation tensor	\mathbf{A}_6	A_{ijkl}
i^{th} eigenvalue of \mathbf{A}	λ_i	λ_i
i^{th} eigenvector of \mathbf{A}	\mathbf{e}_i	-
Function of λ_i and \mathbf{e}_i	$\mathbf{L}_4 = \sum_{i=1}^3 \lambda_i \mathbf{e}_i \mathbf{e}_i \mathbf{e}_i \mathbf{e}_i$	-
Function of \mathbf{e}_i	$\mathbf{M}_4 = \sum_{i=1}^3 \mathbf{e}_i \mathbf{e}_i \mathbf{e}_i \mathbf{e}_i$	-
Scalar magnitude of \mathbf{D}	$\dot{\gamma} = \sqrt{2\mathbf{D} : \mathbf{D}}$	$\dot{\gamma} = \sqrt{2D_{ij}D_{ij}}$
2 nd order identity tensor	\mathbf{I}	δ_{ij} (the Kronecker delta)
Fiber geometric term	$\xi = \frac{(r_e^2 - 1)}{(r_e^2 + 1)}$	-
Equivalent ellipsoidal aspect ratio [43]	r_e	-
Fiber interaction term	C_I	-
RSC slowness factor [44]	κ	-
Operators	Notation	Index Notation
Material derivative of \mathbf{p}	$\dot{\mathbf{p}} = \frac{d\mathbf{p}}{dt} = \frac{\partial \mathbf{p}}{\partial t} + \mathbf{v} \cdot \nabla \mathbf{p}$	$\dot{p}_i = \frac{dp_i}{dt} = \frac{\partial p_i}{\partial t} + v_j \frac{\partial p_i}{\partial x_j}$
Material derivative of \mathbf{A}	$\dot{\mathbf{A}} = \frac{d\mathbf{A}}{dt} = \frac{\partial \mathbf{A}}{\partial t} + \mathbf{v} \cdot \nabla \mathbf{A}$	$\dot{A}_{ij} = \frac{dA_{ij}}{dt} = \frac{\partial A_{ij}}{\partial t} + v_k \frac{\partial A_{ij}}{\partial x_k}$
Dot product	$\mathbf{X} \cdot \mathbf{Y}$	$X_{...ij} Y_{jk...}$ (sum on j)
Double dot product	$\mathbf{X} : \mathbf{Y}$	$X_{...ijk} Y_{jki...}$ (sum on j and k)

2.3.1 Jeffery's Model

Jeffery modeled the motion of a single, inertia-less, rigid, ellipsoidal fiber in a boundless flow domain in 1922 [45]. Given a velocity profile $\mathbf{v}(\mathbf{x})$ with velocity gradients $\mathbf{L}(\mathbf{x})$ for that flow domain, where \mathbf{x} is the position vector, Jeffery's model can be expressed as the time rate of change of the unit vector \mathbf{p} ,

$$\dot{\mathbf{p}} = \mathbf{W} \cdot \mathbf{p} + \xi (\mathbf{D} \cdot \mathbf{p} - \mathbf{D} : \mathbf{p}\mathbf{p}\mathbf{p}) \quad (2.3)$$

In Equation 2.3, the dot accent stands for the material derivative, the single dot between terms stands for the dot product (or *single contraction*), and the double dot between terms stands for the double dot product (or *double contraction*). In addition, ξ is a fiber geometric term (a function of the equivalent ellipsoidal aspect ratio discussed below), $\mathbf{W} = \frac{1}{2} (\mathbf{L} - \mathbf{L}^T)$ is the vorticity tensor, and $\mathbf{D} = \frac{1}{2} (\mathbf{L} + \mathbf{L}^T)$ is the rate of deformation tensor. Using index notation, we can alternatively express position as x_i , the velocity as v_i , the velocity gradients as $L_{ij} = \frac{\partial v_i}{\partial x_j}$, the vorticity as $W_{ij} = \frac{1}{2} (L_{ij} - L_{ji})$, and the rate of deformation as $D_{ij} = \frac{1}{2} (L_{ij} + L_{ji})$ as shown in Table 2.1, where i and j equal 1, 2, or 3. Both symbolic notation and index notation are given in Table 2.1. Whereas symbolic notation may look cleaner and simpler, index notation is more explicit and translates to programming well. Thus, since both notations are useful, both will be used in this dissertation. In index notation, Equation 2.3 can be expressed as

$$\dot{p}_i = W_{ij}p_j + \xi (D_{ij}p_j - D_{jk}p_jp_kp_i) \quad (2.4)$$

where the dot accent again denotes the material derivative i.e., $\dot{p}_i = \frac{dp_i}{dt} = \frac{\partial p_i}{\partial t} + v_j \frac{\partial p_i}{\partial x_j}$, and repeated indices indicate sums over the repeated indices i.e., $x_{ij}y_j = x_{i1}y_1 + x_{i2}y_2 + x_{i3}y_3$, for example.

Since Jeffery developed his model, it has been shown that his model can be applied to fibers of other axisymmetric shapes as well if an equivalent ellipsoidal aspect ratio is used [43, 46]. The equivalent ellipsoidal aspect ratio r_e for cylindrical

fibers is given in [43] as

$$r_e = 0.000035a_r^3 - 0.00467a_r^2 + 0.764a_r + 0.404 \quad (2.5)$$

where a_r is the geometric aspect ratio (fiber length divided by diameter). The fiber geometric term ξ in Equations 2.3 and 2.4 is given in terms of r_e as $\xi = \frac{r_e^2 - 1}{r_e^2 + 1}$.

Given a simple shear flow, Jeffery's equation predicts a periodic motion of a fiber as shown in Figure 2.2a. Figure 2.2 was generated using a cylindrical fiber with $a_r = 40$ ($r_e \approx 26$ according to Equation 2.5) and a simple shear flow with $L_{13} = 1$ (1/seconds) and all other components of \mathbf{L} being 0. The periodic path made by the end of the fiber is labeled a Jeffery orbit. This periodic motion can also be represented by graphing the components of \mathbf{p} over time as shown in Figure 2.2b. One can see in Figure 2.2b that the fiber tends to spend most of its time highly aligned in the flow direction x_1 as expected.

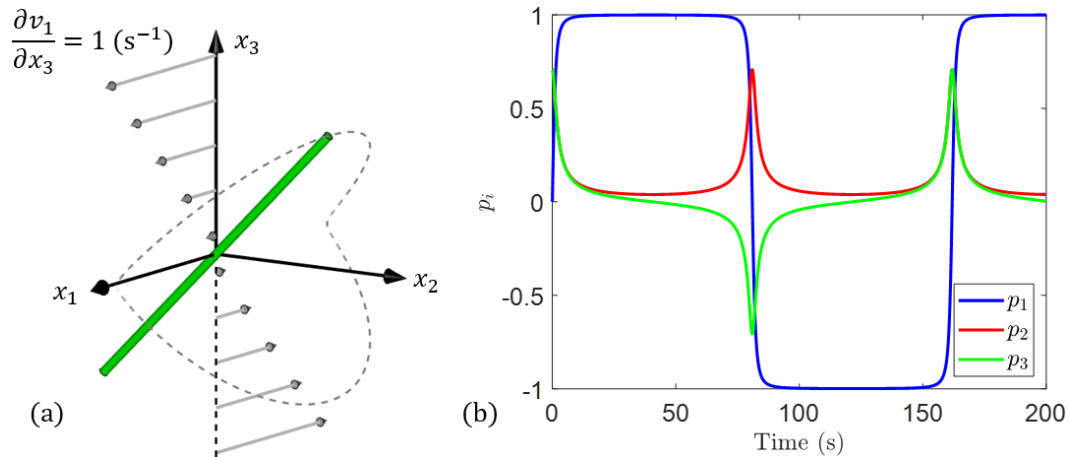


Figure 2.2: (a) Path of a cylindrical fiber in a simple shear flow predicted by Jeffery's equation. (b) Change in the components of \mathbf{p} over time. Used $a_r = 40$ ($r_e \approx 26$) and $L_{13} = 1$.

Jeffery's model was experimentally verified by Mason and colleagues ignoring fiber interaction effects and thereby validating its use only for dilute suspensions (e.g., [46, 47]). In [46], Trevelyan and Mason used a Couette apparatus which consisted of two concentric cylinders with particle-filled corn syrup in between. The

cylinders were rotated in opposite directions. This allowed Trevelyan and Mason to study the rotations of particles under a microscope while the particles' centers of mass remained mostly stationary. Their results give evidence of the need to use an equivalent ellipsoidal aspect ratio rather than a geometric aspect ratio if cylindrical fibers are being considered.

Jeffery's model does not account for fiber interaction and thus is not useful for predicting orientation states in most SFRP processing flows in which there are many fibers (a cubic millimeter of the 13 wt% carbon fiber filled acrylonitrile butadiene styrene considered later in this study will contain thousands of fibers). Thus, a probabilistic approach is often required for industrially relevant parts.

2.3.2 Orientation Tensors

The orientation probability density function, $\psi(\theta, \phi, \mathbf{x}, t)$ or $\psi(\mathbf{p}, \mathbf{x}, t)$, as discussed by Advani and Tucker (e.g., [48]) can be used to describe any physical orientation state where the probability of a fiber being oriented between θ' and $\theta' + d\theta$, and ϕ' and $\phi' + d\phi$ is

$$P(\theta' \leq \theta \leq \theta' + d\theta, \phi' \leq \phi \leq \phi' + d\phi) = \psi(\theta', \phi') \sin \theta' d\theta d\phi \quad (2.6)$$

The probability density function obeys the normalization property, $\int_0^{2\pi} \int_0^\pi \psi \sin \theta d\theta d\phi = 1$ where the integration is over the unit sphere [48]. In addition, it does not distinguish between a fiber pointing in the direction \mathbf{p} or $-\mathbf{p}$, so it is periodic, meaning $\psi(\mathbf{p}) = \psi(-\mathbf{p})$ or $\psi(\theta, \phi) = \psi(\pi - \theta, \pi + \phi)$ [48].

Graphically, ψ can be represented in multiple ways. One way is as a surface over ϕ - θ space [49, 50]. Another way is by a colored sphere [51, 52] or a shaded unit sphere like the one shown in Figure 2.3a, where a darker shade represents the direction where a fiber is more likely to be pointed. Figure 2.3a was generated using $\psi(\theta, \phi) = c \sin^{2n} \theta \cos^{2n} \phi$, where $c = 1 / \int_0^{2\pi} \int_0^\pi \sin^{2n} \theta \cos^{2n} \phi \sin \theta d\theta d\phi$ and $n = 2$. The directions of the fibers in Figure 2.3b were chosen psuedo-randomly from this dis-

tribution using the Accept-Reject Generation Algorithm (e.g., [50, 53]). Predicting $\psi(\mathbf{x})$ can be computationally expensive for real flow domains and thus, orientation tensors, which offer a more compact description of the orientation state, are preferable [2, 48].

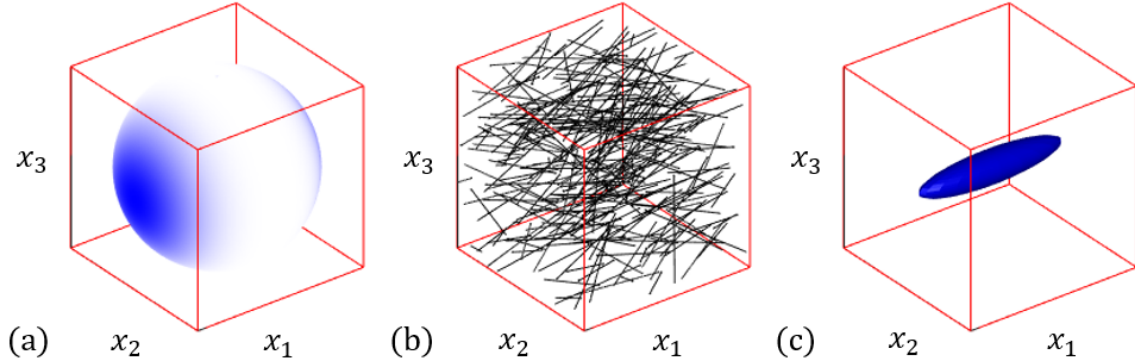


Figure 2.3: Different representations of the same, highly x_1 -aligned orientation state: (a) a graphical representation of $\psi(\mathbf{p})$ as a shaded sphere, (b) individual fibers, (c) a graphical representation of \mathbf{A} as an ellipsoid.

In his widely cited work, Advani expounded on the use of orientation tensors as a compact way to describe arbitrary orientation states in SFRPs [48]. The orientation tensors are defined in component form as

$$A_{ij\dots} = \int_0^{2\pi} \int_0^\pi p_i p_j \dots \psi(\theta, \phi) \sin \theta d\theta d\phi \quad (2.7)$$

where the integration takes place over the unit sphere and it is noted that odd-order orientation tensors are full of zeros [48]. The $\int_0^{2\pi} \int_0^\pi (\dots) \psi(\theta, \phi) \sin \theta d\theta d\phi$ operation is called *orientation averaging*, or *homogenization*, and will be referred to often in this work. It can also be represented by $\oint (\dots) \psi(\mathbf{p}) d\mathbf{p}$ or simply $\langle \dots \rangle$. The orientation tensors have several noteworthy properties as discussed by Advani [2, 48]:

- (1) They are completely symmetric:

$$A_{ij} = A_{ji}, \quad A_{ijkl} = A_{jikl} = A_{kijl} = A_{likj} = A_{klji}, \text{ etc.} \quad (2.8)$$

- (2) The trace of the second order orientation tensor always equals one. This is

easy to prove since the norm of \mathbf{p} is equal to one:

$$\begin{aligned}
\sqrt{p_i p_i} &= 1 \\
p_i p_i &= 1 \\
\langle p_i p_i \rangle &= \langle 1 \rangle \\
A_{ii} &= 1
\end{aligned} \tag{2.9}$$

where $\langle \cdots \rangle = \int_0^{2\pi} \int_0^\pi (\cdots) \psi(\theta, \phi) \sin \theta d\theta d\phi$.

- (3) An n^{th} order orientation tensor can be extracted from an orientation tensor of order $(n + 2)$:

$$A_{ijkk} = A_{ij}, \quad A_{ijklmm} = A_{ijkl}, \quad A_{ijklmnp} = A_{ijklmn}, \text{ etc.} \tag{2.10}$$

The n^{th} order orientation tensor has 3^n components but considerably less independent components due to the above properties. For example, \mathbf{A} has 5 independent components (rather than 9) due to Equations 2.8 and 2.9. Furthermore, \mathbf{A}_4 has $3^4 = 81$ total degrees of freedom but these reduce down to just 14.

The second-order orientation tensor also has a practical interpretation. The diagonal components, A_{11} , A_{22} , and A_{33} , represent the amount of fiber alignment in the x_1 , x_2 , and x_3 directions, respectively. Figure 2.4 illustrates this with three orientation states. $\mathbf{A}_{aligned}$ represents uniaxial alignment in the x_1 direction (Figure 2.4a), \mathbf{A}_{planar} , random alignment in the $x_1 - x_2$ plane (Figure 2.4b), and \mathbf{A}_{random} , completely random alignment (Figure 2.4c).

$$\mathbf{A}_{aligned} = \begin{bmatrix} 1 & 0 & 0 \\ 0 & 0 & 0 \\ 0 & 0 & 0 \end{bmatrix}, \quad \mathbf{A}_{planar} = \begin{bmatrix} 1/2 & 0 & 0 \\ 0 & 1/2 & 0 \\ 0 & 0 & 0 \end{bmatrix}, \quad \mathbf{A}_{random} = \begin{bmatrix} 1/3 & 0 & 0 \\ 0 & 1/3 & 0 \\ 0 & 0 & 1/3 \end{bmatrix}$$

The off-diagonal components of \mathbf{A} namely, A_{ij} where $i \neq j$, represent the amount of alignment between the x_i and x_j axes. For example, A_{12} is the amount of alignment between x_1 and x_2 . If A_{12} is positive, this indicates that the fibers are

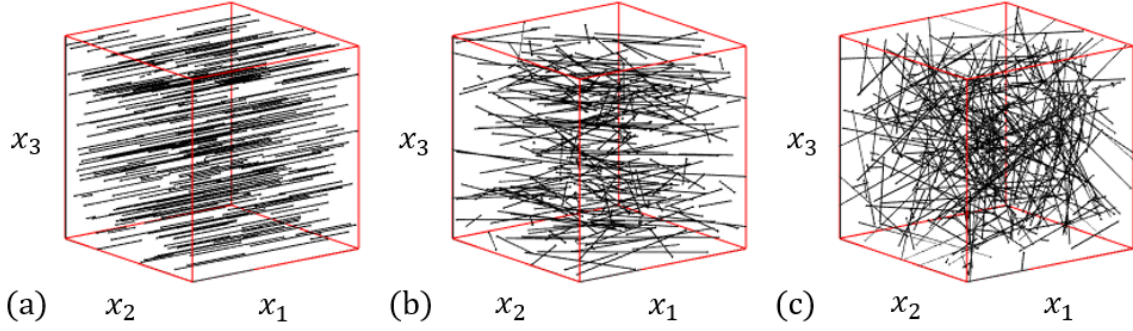


Figure 2.4: Three orientation states: (a) uniaxial in x_1 , (b) random in x_1-x_2 plane, and (c) completely random.

aligned more towards the first (or third) quadrant of the x_1-x_2 plane than they are towards the fourth (or second) quadrant, as shown in Figure 2.5a. If A_{12} is negative, the fibers are aligned more toward the fourth (or second) quadrant, as shown in Figure 2.5b. This resolves ambiguity about the orientation state. For example, a uniaxial orientation state aligned at $+\phi$ radians with respect to the x_1 axis in the x_1-x_2 plane will have the same A_{11} and A_{22} as an orientation state aligned at $-\phi$ with respect to the x_1 axis. The difference between these states is that A_{12} is positive for the $+\phi$ state and negative for the $-\phi$ state, as demonstrated by Figure 2.5. If A_{12} is 0, there is equal bias towards the first (or third) and fourth (or second) quadrants. Similar explanations can be given for A_{13} and A_{23} .

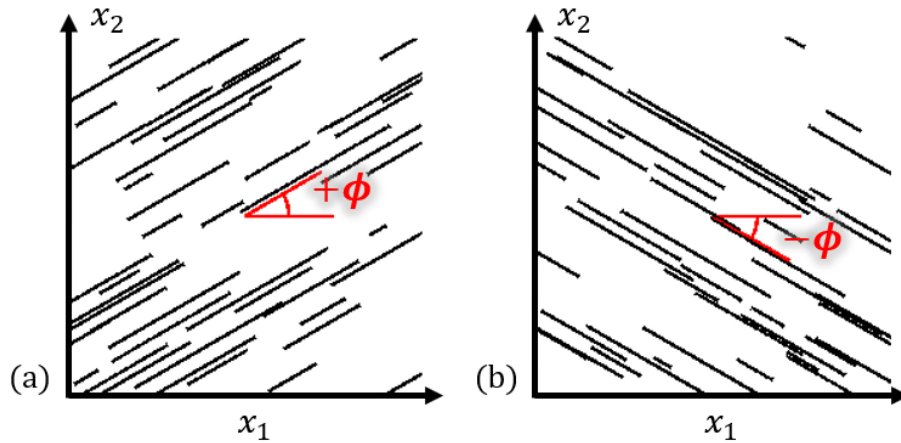


Figure 2.5: Orientation states with equivalent A_{11} and equivalent A_{22} , but different A_{12} . (a) Fibers oriented at $+\phi$, $A_{12} > 0$. (b) Fibers oriented at $-\phi$, $A_{12} < 0$.

The second-order orientation tensor \mathbf{A} can be represented graphically by an ellipsoid whose three axes are parallel to the eigenvectors of \mathbf{A} , namely \mathbf{e}_1 , \mathbf{e}_2 , and \mathbf{e}_3 , and scaled by the corresponding eigenvalues of \mathbf{A} , namely λ_1 , λ_2 , and λ_3 , where $\lambda_1 \geq \lambda_2 \geq \lambda_3$. This type of representation was inspired by a similar, 2D version given by Advani in his dissertation [2] and is displayed in Figure 2.3c for the orientation distribution shown in Figure 2.3a.

While orientation tensors can be stated in terms of ψ via Equation 2.7, conversely, ψ can be stated in terms of orientation tensors. Orientation tensors are connected to the coefficients of an infinite series expansion of ψ and thus, ψ can be approximately reconstructed given a finite number N of orientation tensors [2, 48–50, 54]. The N^{th} order reconstruction, $\hat{\psi}_N$, can be found using the following [49]:

$$\begin{aligned}\hat{\psi}_2(\mathbf{p}) &= f_o V_o + f_{ij}(\mathbf{p}) V_{ij} \\ \hat{\psi}_4(\mathbf{p}) &= f_o V_o + f_{ij}(\mathbf{p}) V_{ij} + f_{ijkl}(\mathbf{p}) V_{ijkl} \\ \hat{\psi}_6(\mathbf{p}) &= f_o V_o + f_{ij}(\mathbf{p}) V_{ij} + f_{ijkl}(\mathbf{p}) V_{ijkl} + f_{ijklmn}(\mathbf{p}) V_{ijklmn} \\ &\vdots\end{aligned}\tag{2.11}$$

where the basis functions, $f_{ij\dots}$, and Fourier coefficients, $V_{ij\dots}$, are given, respectively, by Equation 2.12 and 2.13,

$$\begin{aligned}f_o &= 1 \\ f_{ij} &= p_i p_j - \frac{1}{3} \delta_{ij} \\ f_{ijkl} &= p_i p_j p_k p_l - \frac{1}{7} (p_i p_j \delta_{kl} + p_i p_k \delta_{jl} + p_i p_l \delta_{jk} + p_k p_l \delta_{ij} + p_j p_l \delta_{ik} + p_j p_k \delta_{il}) \\ &\quad + \frac{1}{35} (\delta_{ij} \delta_{kl} + \delta_{ik} \delta_{jl} + \delta_{il} \delta_{jk}) \\ &\vdots\end{aligned}\tag{2.12}$$

$$V_{ij\dots} = \frac{1}{4\pi} \frac{1}{N!} \prod_{x=0}^N (2x+1) \int_0^{2\pi} \int_0^\pi \psi(\theta, \phi) f_{ij\dots} \sin \theta d\theta d\phi\tag{2.13}$$

The δ_{ij} in Equation 2.12 is the Kronecker Delta. Observe that the $V_{ij\dots}$ terms can be cast in terms of the orientation tensors. Inclusion of higher order terms in Equation 2.11 can lead to a more accurate reconstruction of ψ , which can be confirmed by using the error metric of [49],

$$\varepsilon_N = \sqrt{\int_0^{2\pi} \int_0^\pi \left(\psi(\theta, \phi) - \hat{\psi}_N(\theta, \phi) \right)^2 \sin \theta d\theta d\phi} \quad (2.14)$$

Figure 2.6 demonstrates this by using the ψ function from Figure 2.3 to get A_{ij} and A_{ijkl} by numerically integrating Equation 2.7 and then getting $\hat{\psi}_2$ and $\hat{\psi}_4$ by inserting A_{ij} and A_{ijkl} into Equations 2.11-2.13.

Figure 2.6 also demonstrates the need for many points in θ and ϕ to characterize ψ accurately. This is what makes ψ computationally expensive to calculate in realistic processing flows. To determine ψ at, say, 1000 spatial points in a flow domain using 20 points in θ and 40 points in ϕ at each spatial point amounts to solving for $1000 \times 20 \times 40 = 800,000$ variables. On the other hand, solving for A_{ijkl} , which has only 14 independent components, will lead to needing to solve for only $1000 \times 14 = 14,000$ variables. In addition, most of the accuracy of the solution is preserved as shown in Figure 2.6c. Solving for A_{ij} , while sacrificing a little accuracy but still being reasonably accurate, reduces the computational cost even further: only $1000 \times 5 = 5000$ variables need to be found in this case. Clearly, there is a computational advantage to using orientation tensors.

Using orientation tensors to quantify the orientation state in an SFRP is also advantageous for the purpose of material property prediction. For some n^{th} order tensor property \mathbf{T} , the corresponding orientation-averaged property can be found according to [2, 48]

$$\langle \mathbf{T} \rangle = \int_0^{2\pi} \int_0^\pi \mathbf{T} \psi(\theta, \phi) \sin \theta d\theta d\phi \quad (2.15)$$

where the right hand side of Equation 2.15 can be expressed in terms of the n^{th} order orientation tensor and lower order orientation tensors which, according to Equation

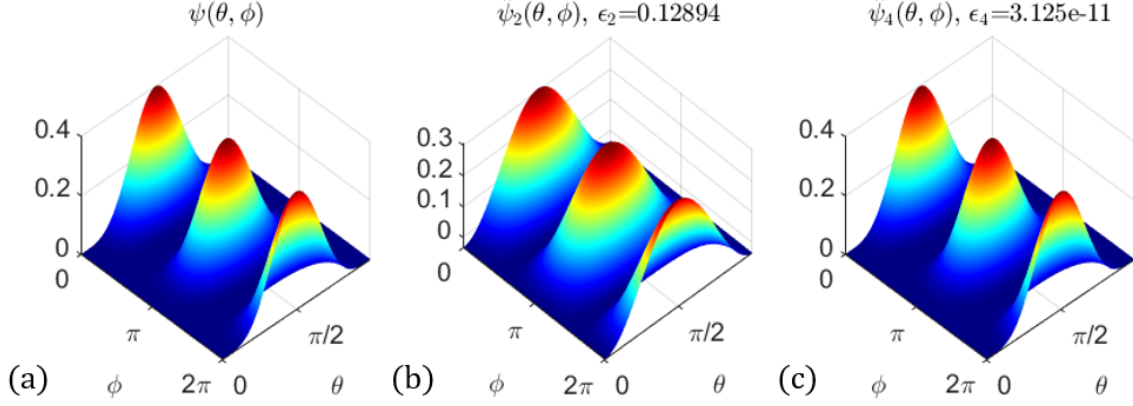


Figure 2.6: (a) $\psi(\theta, \phi)$ from Figure 2.3, (b) 2^{nd} order reconstruction of ψ , and (c) 4^{th} order reconstruction of ψ .

2.10, can be extracted from the n^{th} order orientation tensor [2, 48]. That is, all the orientation information from ψ that is needed to compute an n^{th} order tensor property comes from the n^{th} order orientation tensor [2, 48]. This is a foundational point for this dissertation. Advani and Tucker also give the forms of the orientation-averaged second order and fourth order tensor properties in terms of the components of the underlying transversely isotropic property tensors [48]:

$$\langle T \rangle_{ij} = A_1 A_{ij} + A_2 \delta_{ij} \quad (2.16)$$

$$\begin{aligned} \langle T \rangle_{ijkl} = & B_1 A_{ijkl} + B_2 (A_{ij} \delta_{kl} + A_{kl} \delta_{ij}) + B_3 (A_{ik} \delta_{jl} + A_{il} \delta_{jk} + A_{jl} \delta_{ik} + A_{jk} \delta_{il}) \\ & + B_4 (\delta_{ij} \delta_{kl}) + B_5 (\delta_{ik} \delta_{jl} + \delta_{il} \delta_{jk}) \end{aligned} \quad (2.17)$$

where A_{ij} is the second order orientation tensor, δ_{ij} is the Kronecker delta ($\delta_{ij} = 1$ when $i = j$, otherwise $\delta_{ij} = 0$), and the A 's and B 's are constant functions of the components of the underlying unidirectional property tensors, \bar{T}_{ij} and \bar{T}_{ijkl} , respectively. Jack and Smith [55] provide a method for deriving the forms of orientation-averaged properties such as those shown in Equations 2.16 and 2.17. As a result, it can be shown that the A 's and B 's come out to be (e.g., [56])

$$A_1 = \bar{T}_{11} - \bar{T}_{22}, \quad A_2 = \bar{T}_{22} \quad (2.18)$$

$$B_1 = \bar{T}_{1111} + \bar{T}_{2222} - 2\bar{T}_{1122} - 4\bar{T}_{1212}, \quad B_2 = \bar{T}_{1122} - \bar{T}_{2233},$$

$$\begin{aligned}
B_3 &= \bar{T}_{1212} + \frac{1}{2}(\bar{T}_{2233} - \bar{T}_{2222}), & B_4 &= \bar{T}_{2233}, \\
B_5 &= \frac{1}{2}(\bar{T}_{2222} - \bar{T}_{2233})
\end{aligned} \tag{2.19}$$

where the \bar{T}_{ij} 's are components of the underlying unidirectional second order tensor, \bar{T}_{ij} , and the \bar{T}_{ijkl} 's are components of the underlying unidirectional fourth order tensor, \bar{T}_{ijkl} .

Because the n^{th} order orientation tensor provides sufficient orientation information for predicting n^{th} order tensor properties, there is usually no need to predict anything higher than \mathbf{A}_4 in an SFRP melt flow as most tensor properties of interest are not higher than fourth-order. Furthermore, \mathbf{A}_4 is often approximated from the second-order orientation tensor \mathbf{A} using a closure method and thus, only \mathbf{A} needs to be predicted in these cases. An orthotropic closure [57] is used in this study to get \mathbf{A}_4 . A short discussion of orthotropic closures is given in Section 2.3.4.

Experimental measurement of the orientation tensors relies on being able to measure the orientation state of many individual fibers. There are several methods of doing this including acoustic, electromagnetic, irradiation, and optical [58]. Micro computed tomography (Micro-CT) systems can also be used to measure 3D orientation states [59], but these systems are expensive. Vélez-García et al. developed a cheaper optical method of characterizing 3D orientation states based on the 2D method of ellipses (MoE) [58, 60]. In their “VWB” methodology a cross-section of a fibrous sample is polished, plasma etched, and analyzed under a microscope. The cross-sections of the cylindrical fibers are elliptically shaped like those in Figure 2.7, unless they are perfectly perpendicular to the plane in which case they are circular. The orientation of a fiber, defined by the angles θ and ϕ in Figure 2.8, can then be found by using the major and minor axes of its elliptic cross section, M and m , respectively. The in-plane angle ϕ is determined as the angle between x_1 and M and

θ is found by

$$\theta = \cos^{-1} \left(\frac{m}{M} \right) \quad (2.20)$$

Once θ and ϕ are found, \mathbf{p} is found by Equation 2.2 and then \mathbf{A} is estimated by Equation 2.21 or Equation 2.22 (e.g., [58]),

$$A_{ij} = \frac{\sum_n (p_i p_j)_n L_n F_n}{\sum_n L_n F_n} \quad (2.21)$$

$$A_{ij} = \frac{\sum_n (p_i p_j)_n G_n L F_n}{\sum_n G_n L F_n} \quad (2.22)$$

The subscript n denotes a property of the n^{th} fiber, L_n is fiber length, and F_n is a weighting function. Velez-Garcia et al. use the weighting function of Konicek which he presented in his Master's thesis [61] (cited in [58]),

$$F_n = \frac{1}{L_n \cos(\theta_n) + d_n \sin(\theta_n)} \quad (2.23)$$

where d_n is fiber diameter. G_n in Equation 2.22 is the fractional area of a fiber footprint and allows for the quantification of orientation of fibers whose footprints are partially cropped out of the micrograph being studied. G_n helps prevent bias against larger ellipses which are more likely to be cropped. With $G_n = 1$, Equation 2.22 reduces to Equation 2.21.

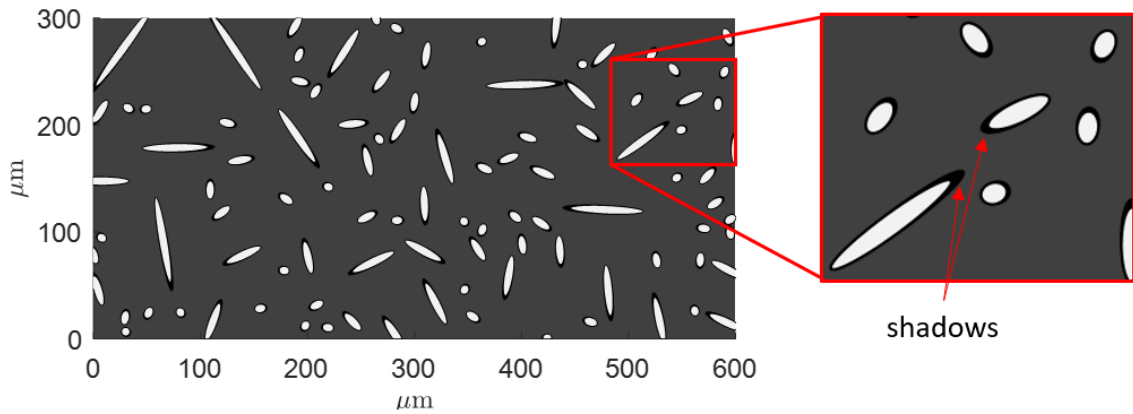


Figure 2.7: An illustrative hypothetical micrograph of a fiber filled polymer like in [58] on which the method of ellipses could be performed.

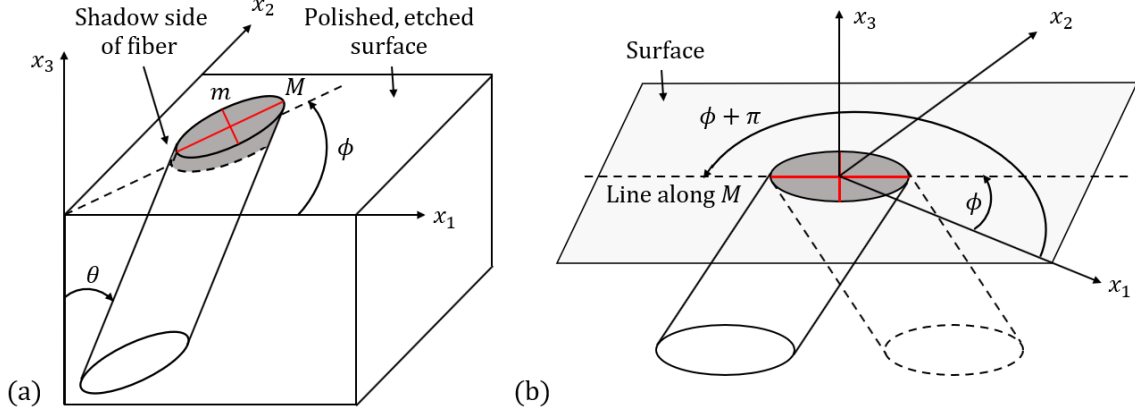


Figure 2.8: (a) Definitions of angles (same as those in Figure 2.1). (b) Ambiguity problem; a fiber with major axis M oriented along ϕ has the same footprint as one oriented along $\phi + \pi$. Figures inspired by [58].

The VWB method resolves two problems with the MoE. One is the inability to deal with non-elliptical footprints [58]. By being able to deal with non-elliptical footprints including the footprints at the edges of a micrograph that get cropped, the VWB method can more accurately characterize the orientation state over a given area. It also retains its accuracy better than the method of ellipses as the size of the required sampling area is decreased since the cropped footprints that would be thrown out by the MoE are retained by the VWB method. This ability to estimate \mathbf{A} with a finer resolution is important for studying flows in which there are quick changes in the orientation state.

Another issue with the MoE is the angle ambiguity problem [62] (as cited in [58]), which is that a fiber with an orientation of ϕ will have the same footprint as a fiber with orientation $\phi + \pi$ as illustrated in Figure 2.8b. The plasma etching step in the VWB method is critical to solving this ambiguity problem since it decomposes a thin layer of matrix material, leaving the fibers protruding out slightly so that a “shadow” effect is created. This effect (see Figures 2.7 and 2.8a) then enables one to detect whether the fiber is pointed along ϕ or $\phi + \pi$. Resolving this ambiguity problem means the VWB method can be used to get all of the components of the

orientation tensor including A_{13} and A_{23} , unlike the MoE which can only get A_{11} , A_{22} , A_{33} , and A_{12} .

2.3.3 Fiber Interaction Models

Jeffery's model is insufficiently accurate for predicting the orientation state in SFRPs with the fiber volume fractions required for most industrial use. Therefore, Folgar and Tucker developed a model for predicting the alignment of fibers in concentrated fiber suspensions by incorporating a fiber interaction term into their model [63]. Here, *concentrated suspension* refers to anything greater than dilute, such as the semi-concentrated case, where $(d/L)^2 < V_f < (d/L)$, and the highly concentrated case, where $V_f > (d/L)$ and d is the fiber diameter, L is the fiber length, V_f is the fiber volume fraction, and all the fibers are considered to be rigid cylinders of the same size [63]. For semi-concentrated SFRPs, the fibers are spaced apart by a distance between L and d and for highly concentrated SFRPs, the distance between them is comparable to d [63]. Dilute suspensions are defined by $V_f < (d/L)^2$ and have fibers spaced by a distance of more than L , but these are of minimal interest in industry due to their low fiber volume fractions [63].

The Folgar-Tucker Model, which will be referred to as the Isotropic Rotary Diffusion (IRD) model, can be expressed in terms of orientation tensors as

$$\dot{\mathbf{A}} = \mathbf{W} \cdot \mathbf{A} - \mathbf{A} \cdot \mathbf{W} + \xi (\mathbf{D} \cdot \mathbf{A} + \mathbf{A} \cdot \mathbf{D} - 2\mathbf{A}_4 : \mathbf{D}) + 2C_I \dot{\gamma} (\mathbf{I} - 3\mathbf{A}) \quad (2.24)$$

where $\dot{\gamma}$ is the scalar magnitude of \mathbf{D} and \mathbf{I} is the second order identity tensor. All the terms in Equation 2.24 are given in Table 2.1. C_I is the empirically-found fiber interaction coefficient, which adds an element of randomness to the orientation state. Typically, $C_I = 0.006-0.01$ according to [64]. Bay [65] developed the following empirical formula to calculate C_I in terms of fiber aspect ratio and volume fraction,

$$C_I = 0.0184 \exp(-0.7148 V_f a_r) \quad (2.25)$$

Unfortunately, the IRD model predicts that the steady state orientation state will occur more quickly than it does in reality [63]. While this does not inhibit the use of the IRD model in cases where steady state will be achieved, it is less than ideal for the transient solution. Thus, although the IRD has been useful to industry and has been used in much commercial injection molding software [64], a more accurate model is desirable.

The model of Wang, O’Gara, and Tucker, called the Reduced-Strain Closure (RSC) model, addresses the main issue of the IRD in which the steady orientation state was predicted too quickly [44]. The RSC model was built on the premise that the eigenvalues of \mathbf{A} could be decreased by use of a constant factor κ , while leaving the expressions of the rotation rate of the eigenvectors of \mathbf{A} alone [44]. The RSC model is given by

$$\begin{aligned}\dot{\mathbf{A}} = \mathbf{W} \cdot \mathbf{A} - \mathbf{A} \cdot \mathbf{W} + \xi \{ \mathbf{D} \cdot \mathbf{A} + \mathbf{A} \cdot \mathbf{D} - 2 [\mathbf{A}_4 + (1 - \kappa) (\mathbf{L}_4 - \mathbf{M}_4 : \mathbf{A}_4)] : \mathbf{D} \} \\ + 2\kappa C_I \dot{\gamma} (\mathbf{I} - 3\mathbf{A})\end{aligned}\tag{2.26}$$

where $\mathbf{L}_4 = \sum_{i=1}^3 \lambda_i \mathbf{e}_i \mathbf{e}_i \mathbf{e}_i \mathbf{e}_i$ and $\mathbf{M}_4 = \sum_{i=1}^3 \mathbf{e}_i \mathbf{e}_i \mathbf{e}_i \mathbf{e}_i$ where λ_i and \mathbf{e}_i are the i^{th} eigenvalue and eigenvector of \mathbf{A} . All the terms in Equation 2.26 are provided in Table 2.1. Typical values of the slowness factor are $\kappa = 0.05-0.2$ for SFRPs [44] (as cited in [64]). For $\kappa = 1$, the RSC model (Equation 2.26) is equivalent to the IRD model (Equation 2.24).

Other fiber interaction models for predicting the orientation tensors for concentrated fibrous suspensions also exist such as the anisotropic rotary diffusion model of Phelps and Tucker [64] and the anisotropic viscous constitutive model of Favaloro, Tseng, and Pipes [66] among others. Phelps and Tucker built their model on the previous works done by Fan et al. [67] and Phan-Thien et al. [68] in which the scalar fiber interaction factor C_I was substituted with a second order tensor to allow for anisotropic rotary diffusion [64]. Phelps and Tucker’s method gives better pre-

dictions for long-fiber composites that are injection molded but includes additional parameters that require tuning [64].

Whereas most models consider the flow and orientation to be decoupled, the model of Favaloro et al. [66] couples the orientation state with the flow by means of a scalar function for the anisotropic viscosity of the flow. VerWeyst and Tucker also demonstrated a method for coupling flow with orientation and concurrently solve continuity, orientation, and momentum equations [69]. Wang and Smith also studied coupled models [70,71]. Other researchers have investigated how to incorporate fiber flexibility into predictions of the fiber orientation state, an attractive capability for when it comes to more accurately predicting the orientation state and material properties of long fiber reinforced polymer composites (e.g., [72–76]). A recent model from 2018 by Bertevas et al. [77] used a smoothed particle hydrodynamics approach and predicted a skin/core/skin microstructure of an FFF-printed SFRP bead. This result will be corroborated later in this dissertation.

2.3.4 Closures

Many closures exist to approximate the fourth order orientation tensor as a function of the second order orientation tensor i.e., $\mathbf{A}_4 \approx f(\mathbf{A})$. Higher order closures also exist such that the sixth order orientation tensor is approximated in terms of the fourth i.e., $\mathbf{A}_6 \approx f(\mathbf{A}_4)$. If a higher order closure is used, \mathbf{A} can be recovered from \mathbf{A}_4 using Equation 2.10. Higher order closures (i.e., closures of sixth order or more) offer the opportunity for increased accuracy due to the increased number of terms that can be used in the reconstruction of ψ , but this does not necessarily imply that a higher order closure of one type will be more accurate than a second order closure of a different type. Breuer et al. counted 17 fourth order closures and 4 sixth order closures [51]. In practice, fourth order closures are more often utilized, since higher order closures require the solution of higher order equations of change for the

orientation state. For example, a sixth order closure for \mathbf{A}_6 requires knowledge of \mathbf{A}_4 , thus the IRD and RSC models as they are expressed in Equations 2.24 and 2.26 will be insufficient and instead an equation for $\dot{\mathbf{A}}_4$ must be solved, which will require more computational effort. In general, an n^{th} order closure requires the solution to the equation of change for the n^{th} order orientation tensor.

A few of the early closures include the quadratic, linear, and hybrid closures. The quadratic closure is exact for a unidirectional orientation state, and can be expressed simply as

$$A_{ijkl}^{quadratic} = A_{ij}A_{kl} \quad (2.27)$$

The linear closure is

$$\begin{aligned} A_{ijkl}^{linear} = & -\frac{1}{35} (\delta_{ij}\delta_{kl} + \delta_{ik}\delta_{jl} + \delta_{il}\delta_{jk}) \\ & + \frac{1}{7} (A_{ij}\delta_{kl} + A_{ik}\delta_{jl} + A_{il}\delta_{jk} + A_{kl}\delta_{ij} + A_{jl}\delta_{ik} + A_{jk}\delta_{il}) \end{aligned} \quad (2.28)$$

where all the terms are linear in A_{ij} (e.g., [2]). The linear closure is exact for a completely random (isotropic) orientation state [2]. The hybrid closure combines the linear and quadratic closures:

$$A_{ijkl}^{hybrid} = (1 - f) A_{ijkl}^{linear} + f A_{ijkl}^{quadratic} \quad (2.29)$$

where f is some scalar orientation factor ranging from zero to unity [2].

Orthotropic closures [57] are a highly accurate family of closures. These use the fact that \mathbf{A} has three principal axes which are in the directions of the eigenvectors of \mathbf{A} and that when rotated into the principal frame, many of the off-diagonal terms of the second order orientation tensor become 0. When some second orientation tensor \mathbf{A} is rotated into its principal reference frame, only the diagonal components remain

and these are termed the eigenvalues of \mathbf{A} [57]

$$\tilde{\mathbf{A}} = \begin{bmatrix} \lambda_1 & 0 & 0 \\ 0 & \lambda_2 & 0 \\ 0 & 0 & \lambda_3 \end{bmatrix} \quad (2.30)$$

Here, the tilde notation is used to identify the orientation tensor expressed in its principal reference frame. Using knowledge of the second order orientation tensor and the orientation tensor properties in Equations 2.8-2.10, the components of the fourth order orientation tensor in the principal reference frame can be reduced to just three independent values, which Cintra and Tucker choose to be \tilde{A}_{1111} , \tilde{A}_{2222} , and \tilde{A}_{3333} [57]. The problem of approximating \mathbf{A}_4 as a function of \mathbf{A} is then reduced to finding three functions such that

$$\tilde{A}_{1111} = f_1(\lambda_1, \lambda_2) \quad (2.31)$$

$$\tilde{A}_{2222} = f_2(\lambda_1, \lambda_2) \quad (2.32)$$

$$\tilde{A}_{3333} = f_3(\lambda_1, \lambda_2) \quad (2.33)$$

There are an infinite number of possible functions that could be chosen, some more accurate than others. Some methods fit the functions to experimental data to ensure accuracy in select situations. An orthotropic closure [57] detailed by Wetzel [78] and VerWeyst [79] (as cited in [69]) is used in this study to get \mathbf{A}_4 .

2.4 Micromechanical Models

The linear elastic behavior of a material can be described using Hooke's Law, which is given in tensor form as

$$\sigma_{ij} = C_{ijkl}\epsilon_{kl}, \quad \epsilon_{ij} = S_{ijkl}\sigma_{kl} \quad (2.34)$$

where σ_{ij} is the stress tensor, C_{ijkl} is the stiffness tensor, ϵ_{ij} is the strain tensor, and S_{ijkl} is the compliance tensor (e.g., [50]). The goal of this section is to determine

C_{ijkl} , which is also the inverse of S_{ijkl} . Most models for predicting C_{ijkl} for an SFRP with a misaligned fiber orientation state follow a two-step process (e.g., [2]): (1) determine the transversely isotropic stiffness tensor, \bar{C}_{ijkl} , of the underlying unidirectional SFRP; (2) take the orientation average of the transversely isotropic stiffness tensor to get the homogenized stiffness tensor, $\langle C \rangle_{ijkl}$. This section first presents methods to determine \bar{C}_{ijkl} and then transitions to determining the homogenized form of the stiffness, $\langle C \rangle_{ijkl} = \int_0^{2\pi} \int_0^\pi \bar{C}_{ijkl} \psi(\theta, \phi) \sin \theta d\theta d\phi$. In the following, the over bar on \bar{C}_{ijkl} distinguishes this term as a property of the underlying unidirectional composite. Furthermore, throughout this dissertation, the over bar will be used to denote other properties of the unidirectional composite.

For a unidirectional SFRP, \bar{C}_{ijkl} can be completely characterized by five independent constants (e.g., [80]). These constants could include, for example, the elastic moduli in the x_1 and x_2 directions, namely, \bar{E}_{11} and \bar{E}_{22} , the shear moduli \bar{G}_{12} and \bar{G}_{23} , and the Poisson's ratio $\bar{\nu}_{12}$. If these constants are known, the transversely isotropic stiffness for a unidirectional SFRP aligned along x_1 is found by (e.g., [80])

$$\bar{\mathbf{C}} = \bar{C}_{ij} = \begin{bmatrix} 1/\bar{E}_{11} & -\bar{\nu}_{12}/\bar{E}_{11} & -\bar{\nu}_{12}/\bar{E}_{11} & 0 & 0 & 0 \\ & 1/\bar{E}_{22} & -\bar{\nu}_{23}/\bar{E}_{22} & 0 & 0 & 0 \\ & & 1/\bar{E}_{22} & 0 & 0 & 0 \\ & & & 1/\bar{G}_{23} & 0 & 0 \\ & symmetric & & & 1/\bar{G}_{12} & 0 \\ & & & & & 1/\bar{G}_{12} \end{bmatrix}^{-1} \quad (2.35)$$

where the contracted form of the stiffness tensor has been used and we have let $\bar{\nu}_{23} = \frac{\bar{E}_{22}}{2\bar{G}_{23}} - 1$ (e.g., [50]). The stiffness tensor can be contracted since it is symmetric and it is contracted by using the Voigt order for index replacement as summarized in Table 2.2. This order will be used throughout this dissertation for describing the contracted forms of tensors. In addition, it should be noted that the matrix being

inverted in Equation 2.35 is simply the contracted compliance tensor, $\bar{\mathbf{S}}$ (or \bar{S}_{ij}), since the compliance and stiffness are inverses of each other.

Table 2.2: Voigt Order for Contracting Tensors.

Original Pair of Indices	Replacement Index
11	1
22	2
33	3
23 or 32	4
13 or 31	5
12 or 21	6

There are many micromechanics models for predicting the transversely isotropic stiffness $\bar{\mathbf{C}}$ of a unidirectional SFRP. Tucker and Liang review and evaluate several of them in [81]. The models reviewed by Tucker and Liang all make the following assumptions, taken verbatim from [81] as:

- *The fibers and the matrix are linearly elastic, the matrix is isotropic, and the fibers are either isotropic or transversely isotropic.*
- *The fibers are axisymmetric, identical in shape and size, and can be characterized by an aspect ratio l/d .*
- *The fibers and matrix are well bonded at their interface, and remain that way during deformation. Thus, we do not consider interfacial slip, fiber/matrix debonding or matrix micro-cracking.* [81]

Since it is difficult to fabricate a perfectly aligned SFRP to be experimentally tested, Tucker and Liang opted to compare the models they reviewed to finite element simulation results. One of the most well-known and accepted stiffness prediction approaches reviewed by Tucker and Liang is the set of Halpin-Tsai equations for getting the elastic constants (e.g., [82]). This set of equations can be stated for a

unidirectional SFRP aligned along x_1 in the form given by Advani [2]:

$$\bar{P}_c = P_m \frac{1 + \zeta \eta V_f}{1 - \eta V_f}, \quad \eta = \frac{P_f - P_m}{P_f + \zeta P_m} \quad (2.36)$$

where \bar{P}_c , P_m , and P_f are coinciding properties of the composite, matrix, and fiber, respectively, and a_r and V_f are the fiber aspect ratio and volume fraction, respectively. Moreover, $\zeta = 2a_r$ when $\bar{P}_c = \bar{E}_{11}$, $\zeta = 2$ when $\bar{P}_c = \bar{E}_{22} = \bar{E}_{33}$, and $\zeta = 1$ when $\bar{P}_c = \bar{G}_{12} = \bar{G}_{13}$ [2]. The classical Halpin-Tsai method of obtaining the Poisson's ratio is by a simple rule of mixtures, $\bar{\nu}_{12} = \nu_f V_f + \nu_m (1 - V_m)$ (e.g., [81]). An alternative expression for ζ when $\bar{P}_c = G_{12} = G_{13}$ is $\zeta = 1 + 40V_f^{10}$ which gives good results for composites with continuous fibers [83] (as cited in [81]).

Tucker and Liang [81] conclude that the Halpin-Tsai equations give reasonable results, but that the best models are the model of Lielens et al. [84] and the Mori-Tanaka model. The models of Lielens et al. and Mori-Tanaka give similar results for the fiber volume fraction considered by Tucker and Liang ($V_f = 0.20$), but Tucker and Liang's personal recommendation is the Mori-Tanaka as the best model for predicting the stiffness of unidirectional short-fiber composites. The Tandon-Weng version of the Mori-Tanaka approach is used in this dissertation, based on Tucker and Liang's recommendation.

According to Tandon and Weng [85], who used the Mori-Tanaka approach, four of the necessary five elastic moduli for a unidirectional SFRP aligned along x_1 are given by

$$\bar{E}_{11} = \frac{E_m}{(1 + V_f(A_1^{tw} + 2\nu_m A_2^{tw})/A^{tw})} \quad (2.37)$$

$$\bar{E}_{22} = \frac{E_m}{(1 + V_f[-2\nu_m A_3^{tw} + (1 - \nu_m)A_4^{tw} + (1 + \nu_m)A_5^{tw}]/2A^{tw})} \quad (2.38)$$

$$\bar{G}_{12} = G_m + \frac{G_m V_f}{G_m/(G_f - G_m) + 2(1 - V_f)S_{1212}^E} \quad (2.39)$$

$$\bar{G}_{23} = G_m + \frac{G_m V_f}{G_m/(G_f - G_m) + 2(1 - V_f)S_{2323}^E} \quad (2.40)$$

where matrix properties are designated with m subscripts, V_f is the fiber volume fraction, and the remaining constants are defined in Table 2.3. Tandon and Weng present two interdependent equations for the bulk modulus \bar{K}_{23} and the Poisson's ratio $\bar{\nu}_{12}$ that have to be solved by iteration. However, Tucker and Liang [81] gave the following closed form expression for $\bar{\nu}_{12}$ which will be used in this dissertation since it is more straightforward:

$$\bar{\nu}_{12} = \frac{\nu_m A^{tw} - V_f (A_3^{tw} - \nu_m A_4^{tw})}{A^{tw} + V_f (A_1^{tw} + 2\nu_m A_2^{tw})} \quad (2.41)$$

If desired, \bar{K}_{23} can also be determined from Equation 2.42 given by Tandon and Weng [85] but it is not necessary to determine \bar{C}_{ij} if \bar{E}_{11} , \bar{E}_{22} , \bar{G}_{12} , \bar{G}_{23} , and $\bar{\nu}_{12}$ are already known:

$$\bar{K}_{23} = \frac{(\lambda_m + G_m)(1 + \nu_m)(1 - 2\nu_m)}{1 - \nu_m(1 + 2\nu_{12}) + V_f \{2(\nu_{12} - \nu_m)A_3^{tw} + [1 - \nu_m(1 + 2\nu_{12})]A_4^{tw}\} / A^{tw}} \quad (2.42)$$

Once again, the constants in Equations 2.41 and 2.42 are given in Table 2.3.

Once the stiffness tensor of a unidirectional SFRP is found, it must be orientation averaged, or homogenized, to obtain the anisotropic stiffness tensor of a misaligned SFRP. Obtaining the orientation-averaged stiffness tensor, $\langle C \rangle_{ijkl}$, can be done using Equations 2.17 and 2.19. After obtaining the spatially varying $\langle C \rangle_{ijkl}$ in a processed SFRP part, the effective elastic modulus of the part in any direction can be found by performing a finite element tensile test simulation of the part where the stiffness properties of the part are defined by the spatially varying $\langle C \rangle_{ijkl}$.

An alternative approach to predicting the effective stiffness of an SFRP material is the laminate analogy approach. The laminate analogy approach can be used for predicting both the effective laminate moduli and flexural moduli. This method involves dividing the SFRP material into a discrete number of layers, each with its own orientation state. The effective elastic modulus E_{LT}^{lam} and flexural modulus E_{LF}^{lam}

Table 2.3: Constants used in Tandon-Weng equations.

Constant	Expression	Units
λ_f	$E_f \nu_f / [(1 + \nu_f)(1 - 2\nu_f)]$	Pa
λ_m	$E_m \nu_m / [(1 + \nu_m)(1 - 2\nu_m)]$	Pa
G_f	$E_f / [2(1 + \nu_f)]$	Pa
G_m	$E_m / [2(1 + \nu_m)]$	Pa
g	$\frac{a_r}{(a_r^2 - 1)^{3/2}} [a_r(a_r^2 - 1)^{1/2} - \cosh^{-1} a_r]$	-
S_{1111}^E	$\frac{1}{2(1 - \nu_m)} \left\{ 1 - 2\nu_m + \frac{3a_r^2 - 1}{a_r^2 - 1} - \left[1 - 2\nu_m + \frac{3a_r^2}{a_r^2 - 1} \right] g \right\}$	-
$S_{2222}^E = S_{3333}^E$	$\frac{3a_r^2}{8(1 - \nu_m)(a_r^2 - 1)} + \frac{1}{4(1 - \nu_m)} \left(1 - 2\nu_m - \frac{9}{4(a_r^2 - 1)} \right) g$	-
$S_{2233}^E = S_{3322}^E$	$\frac{1}{4(1 - \nu_m)} \left\{ \frac{a_r^2}{2(a_r^2 - 1)} - \left[1 - 2\nu_m + \frac{3}{4(a_r^2 - 1)} \right] g \right\}$	-
$S_{2211}^E = S_{3311}^E$	$-\frac{a_r^2}{2(1 - \nu_m)(a_r^2 - 1)} + \frac{1}{4(1 - \nu_m)} \left\{ \frac{3a_r^2}{a_r^2 - 1} - 1 + 2\nu_m \right\} g$	-
$S_{1122}^E = S_{1133}^E$	$-\frac{1}{2(1 - \nu_m)} \left[1 - 2\nu_m + \frac{1}{a_r^2 - 1} \right] + \frac{1}{2(1 - \nu_m)} \left[1 - 2\nu_m + \frac{3}{2(a_r^2 - 1)} \right] g$	-
$S_{2323}^E = S_{3232}^E$	$\frac{1}{4(1 - \nu_m)} \left\{ \frac{a_r^2}{2(a_r^2 - 1)} + \left[1 - 2\nu_m - \frac{3}{4(a_r^2 - 1)} \right] g \right\}$	-
$S_{1212}^E = S_{1313}^E$	$\frac{1}{4(1 - \nu_m)} \left\{ 1 - 2\nu_m - \frac{a_r^2 + 1}{a_r^2 - 1} - \frac{1}{2} \left[1 - 2\nu_m - \frac{3(a_r^2 + 1)}{a_r^2 - 1} \right] g \right\}$	-
D_1^{tw}	$1 + 2(G_f - G_m)/(\lambda_f - \lambda_m)$	-
D_2^{tw}	$(\lambda_m + 2G_m)/(\lambda_f - \lambda_m)$	-
D_3^{tw}	$\lambda_m/(\lambda_f - \lambda_m)$	-
B_1^{tw}	$V_f D_1 + D_2 + (1 - V_f)(D_1 S_{1111} + 2S_{2211})$	-
B_2^{tw}	$V_f + D_3 + (1 - V_f)(D_1 S_{1122} + S_{2222} + S_{2233})$	-
B_3^{tw}	$V_f + D_3 + (1 - V_f)(S_{1111} + (1 + D_1)S_{2211})$	-
B_4^{tw}	$V_f D_1 + D_2 + (1 - V_f)(S_{1122} + D_1 S_{2222} + S_{2233})$	-
B_5^{tw}	$V_f + D_3 + (1 - V_f)(S_{1122} + S_{2222} + D_1 S_{2233})$	-
A_1^{tw}	$D_1(B_4 + B_5) - 2B_2$	-
A_2^{tw}	$(1 + D_1)B_2 - (B_4 + B_5)$	-
A_3^{tw}	$B_1 - D_1 B_3$	-
A_4^{tw}	$(1 + D_1)B_1 - 2B_3$	-
A_5^{tw}	$(1 - D_1)/(B_4 - B_5)$	-
A^{tw}	$2B_2 B_3 - B_1(B_4 + B_5)$	-

Note: The λ and G terms are, respectively, the first and second Lamé parameters where a subscript f denotes a property of the fiber and a subscript m denotes a property of the matrix. The G terms are also known as the shear modulus. Furthermore, S_{ijkl}^E is the transformation tensor of Eshelby [86] (as cited in [81]).

of this “laminate” are

$$E_{LT}^{lam} = \frac{\mathcal{A}_{11}\mathcal{A}_{22} - \mathcal{A}_{12}^2}{t\mathcal{A}_{22}} \quad (2.43)$$

$$E_{LF}^{lam} = \frac{12(\mathcal{D}_{11}\mathcal{D}_{22} - \mathcal{D}_{12}^2)}{t^3\mathcal{D}_{22}} \quad (2.44)$$

where \mathcal{A}_{ij} and \mathcal{D}_{ij} are components of the 3×3 in-plane stiffness matrix \mathcal{A} and bending stiffness matrix \mathcal{D} from the laminate plate stiffness equations (e.g., [25]). Equations 2.43 and 2.44 assume that the thickness of the processed part is much smaller than its width and length, such that the shear strains γ_{12} and γ_{32} are negligible, and that the strain in the thickness direction is $\varepsilon_{22} \approx 0$ [25]. Equation 2.43 also assumes that the fictional laminate is balanced and symmetric and only experiences in-plane loads while Equation 2.44 is for a specially orthotropic, symmetric laminate [25].

2.5 Strength Models

One of the advantages of Advani’s orientation averaging technique is that it enables modelers to predict the material properties of an SFRP part based on the part’s processing conditions. Van Hattum and Bernardo explicitly showed how this technique could be used for the specific case of strength [87]. In this dissertation it will be revealed that their model can be taken further than they originally demonstrated in [87]. Before articulating Van Hattum and Bernardo’s model, however, relevant background information must be considered.

First, the concept of strength must be articulated. Ultimate strength refers to the stress at which a part fails completely, by fracturing through the entire thickness of the part. Yield strength refers to the stress at which a part begins to permanently deform. Thus, the yield strength signifies the point at the end of the linear elastic region on the stress-strain curve. Experimentally, it is often found using a 0.2% strain offset, as discussed in Section 4.2. The ultimate strength and the yield strength may coincide for one material system but not for another. In cases where they do coincide,

the ultimate/yield strength is oftentimes predicted using a linear relationship like a modified rule of mixtures (MROM) model. In cases where they do not coincide, it is easier to predict the yield strength than the ultimate strength since predicting the ultimate strength will require a non-linear relationship. However, when the stress state in a part exceeds its yield strength, the design of the part is often considered a “failed” design. So, in these cases, predicting the yield strength takes higher precedence over predicting the ultimate strength. Predicting the yield strength is the focus of this dissertation.

Furthermore, a material may fail at various stress levels depending on the manner in which it is loaded, whether it is under tensile, compressive, or bending forces. Therefore, the tensile yield strength of a material may differ greatly from its compressive or flexural yield strength. In Section 2.5.1, various models for predicting the longitudinal tensile and compressive yield strength of an SFRP will be discussed.

Although the tensile and compressive yield strength predictions are useful for quick comparison between different material systems, these properties only describe the behavior of an SFRP under simple uniaxial loading and are insufficient to describe the overall failure characteristics of a material that will be used for a part under a multi-axial loading scenario. Therefore, a failure criterion for multi-axial loading must be considered if the material is to be used in design. It will be seen in Section 2.5.2 that the strength model of Van Hattum and Bernardo is actually a tensor-based failure criterion that can be used to predict the effective longitudinal tensile, compressive, and even flexural yield strengths.

In this section, fiber properties are denoted by a subscript f and matrix properties are denoted by a subscript m . In addition, first subscripts L and T refer to longitudinal and transverse properties and second subscripts T , C , and F refer to tensile, compressive, and flexural properties, respectively. For example, E_{TT} is the transverse tensile stiffness of an SFRP and σ_{LC} is the longitudinal compressive

strength. Generally in this dissertation, the “longitudinal” direction refers to the direction in which the fibers are most aligned. The “transverse” direction is always perpendicular to the longitudinal direction. Furthermore, as in the previous section, terms with over bars are properties of the underlying unidirectional composite. For example, $\bar{\sigma}_{LT}$ is the longitudinal tensile strength of the underlying unidirectional composite whereas σ_{LT} is the longitudinal tensile strength of a composite with an arbitrary orientation state.

2.5.1 Simple Models

A simple rule of mixtures (ROM) can be used to predict the longitudinal tensile strength of an SFRP, as discussed in standard composites textbooks (e.g., [25])

$$\sigma_{LT} = \sigma_f V_f + \sigma'_m (1 - V_f) \quad (2.45)$$

where σ_{LT} is the yield tensile strength of the composite, V_f is the fiber volume fraction, σ_f is the yield strength of the fiber, and σ'_m is the stress in the matrix at the failure of the SFRP. Assuming that the material behaves linearly up to failure, Equation 2.45 can be used to predict the ultimate tensile strength of a continuous fiber composite in the direction in which the fibers are aligned, where the ultimate tensile strength is equal to σ_{LT} and σ_f is equal to the ultimate fiber tensile strength. Equation 2.45 also assumes all the fibers have equal strength and that they are stiffer and more brittle than the matrix. The reason for using σ'_m rather than σ_m in Equation 2.45 can be explained by using Figure 2.9. The composite is assumed to fail when the fibers fail, at a stress of σ_f and a strain of ϵ_f . Since $\sigma_f > \sigma_m$, once the fibers fail the matrix will not be able to sustain the load and will also fail. Thus, the matrix will only contribute σ'_m of its strength to the composite since this is the stress in the matrix at ϵ_f .

The ROM model does not account for varying fiber length and orientation. Therefore, to increase its accuracy, there have been multiple studies that have used a

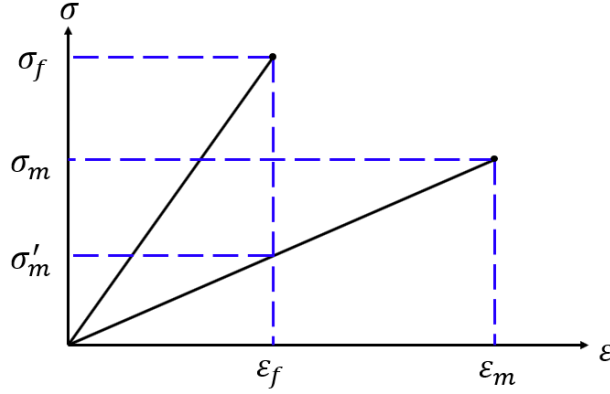


Figure 2.9: Assumed stress-strain behavior of fiber and matrix material for the rule of mixtures tensile strength equation. Figure recreated from Ref. [25].

modified ROM (MROM) model. Cox's work from 1951 is widely cited for predicting stiffness and strength of SFRPs [88]. His results indicate that the fiber contribution to the effective modulus of a short-fiber composite with a planar random orientation state is $1/3$ of the fiber modulus, or $1/6$ of the fiber modulus for a completely random distribution (e.g., [89]). These values have also been considered in strength prediction where, in [90], Bajracharya et al. used the multiplication factor $1/4$ (the average of $1/3$ and $1/6$) for a mostly aligned orientation state and got reasonable results for the tensile strength of a glass-fiber mixed polymer waste composite,

$$\sigma_{LT} = \frac{1}{4}\chi_2\sigma_f V_f + \sigma_m(1 - V_f), \text{ for mostly aligned state} \quad (2.46)$$

The above model also includes a fiber length factor χ_2 that takes into account a distribution of fiber lengths.

Another model for predicting tensile strength was presented by Chen in 1971, but he only looked at unidirectional and planar random orientation states [91]. Bowyer and Bader [92] (as cited in [89]) also predicted the tensile strength of an SFRP using the equation

$$\sigma_{LT} = \sigma_f V_f F\left(\frac{L_c}{L_{mean}}\right) C_o + \sigma_m V_m \quad (2.47)$$

where the function $F(\frac{L_c}{L_{mean}})$ and constant C_o account for non-uniform length and orientation, respectively.

In 1982, Fukuda and Chou [89] took a probabilistic approach, including fiber length and orientation distribution functions in their model. Their model has the form of Equation 2.47 and they were able to examine unidirectional SFRPs with a single fiber length, unidirectional SFRPs with a distribution of fiber lengths, randomly oriented SFRPs with a single fiber length, and partially aligned SFRPs with a single fiber length [89]. The original Fukuda-Chou model had an error in it that was corrected in [93]. Also, as Fu and Lauke [94] point out, Fukuda and Chou did not consider generalized formulas for their length and orientation distribution functions, so they could not study the effects of distributions on strength.

Fu and Lauke [94] developed an MROM model which enabled them to analyze the effects of critical length, L_c , mean length, L_{mean} , most probable length, L_{mod} , mean orientation, β_{mean} , and most probable orientation, β_{mod} , on the strength of an SFRP. Their model is similar to the Fukuda-Chou model, but seems to be more widely cited. The Fu-Lauke model [94] is

$$\sigma_{LT} = \chi_1 \chi_2 V_f \sigma_f + V_m \sigma_m \quad (2.48)$$

where χ_1 and χ_2 are the fiber orientation factor and fiber length factor, respectively. These take into account orientation and length distributions and $0 < \chi_1, \chi_2 \leq 1$. Their product is given as

$$\begin{aligned} \chi_1 \chi_2 = & \int_{\beta_{min}}^{\beta_{max}} \int_{L_{min}}^{L_{c\beta}} \frac{f(L)g(\beta)L^2 e^{\mu\beta}}{2L_c L_{mean}} dL d\beta \\ & + \int_{\beta_{min}}^{\beta_{max}} \int_{L_{c\beta}}^{L_{max}} \frac{f(L)g(\beta)L(1 - \mathcal{A} \tan \beta)}{L_{mean}} \left[1 - \frac{L_c(1 - \mathcal{A} \tan \beta)}{2L e^{\mu\beta}} \right] dL d\beta \end{aligned} \quad (2.49)$$

where L is the fiber length and β is the fiber orientation angle between the fiber's central axis and the force vector shown in Figure 2.10b i.e., the angle between \mathbf{p} and \mathbf{F} , where \mathbf{F} is parallel to the crack plane normal and in the direction in which the strength will be determined.

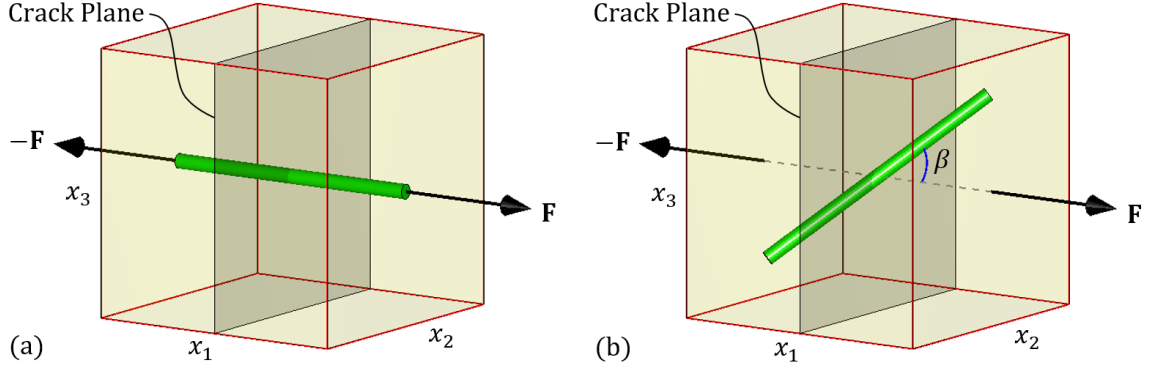


Figure 2.10: Single fibers inside cracked polymer blocks being acted on by a force \mathbf{F} . (a) The fiber is perpendicular to the crack plane ($\beta = 0$). (b) The fiber is at an angle relative to the crack plane normal ($\beta \neq 0$).

The other terms in Equation 2.49 include the minimum and maximum angles, β_{min} and β_{max} , respectively, where β_{max} is given by Equation 2.50; the minimum and maximum fiber lengths, $L_{min} = 0$ and $L_{max} = \infty$, respectively; the critical fiber length for an oblique fiber $L_{c\beta}$ (for $\beta \neq 0$) given by Equation 2.51; L_{mean} , the mean fiber length; and, finally, $f(L)$ and $g(\beta)$, the fiber length and fiber orientation probability density functions, respectively.

$$\beta_{max} = \arctan(1/\mathcal{A}) \quad (2.50)$$

$$L_{c\beta} = L_c(1 - \mathcal{A} \tan \beta)e^{-\mu\beta} \quad (2.51)$$

In Equations 2.50 and 2.51, \mathcal{A} is a parameter that takes into account fiber flexure and μ is the snubbing friction factor. Equation 2.51 accounts for a critical fiber length that depends on the angle of the fiber relative to the direction in which the strength will be determined. When $\beta = 0$, $L_{c\beta}$ is equivalent to L_c , the critical fiber length when the fiber is perpendicular to the crack plane. L_c is determined by

$$L_c = \frac{r_f \sigma_f}{\tau^i} \quad (2.52)$$

where, assuming the fibers are cylindrical in shape, the terms r_f , σ_f , and τ^i are the fiber radius, ultimate fiber tensile strength, and interfacial shear strength, respectively. The fiber length distribution, $f(L)$, can be approximated by a Weibull

distribution function as done by Fu and Lauke [94]. The fiber orientation distribution function they studied is

$$g(\beta) = \frac{\sin(\beta)^{2p-1} \cos(\beta)^{2q-1}}{\int_{\beta_{min}}^{\beta_{max}} \sin(\beta)^{2p-1} \cos(\beta)^{2q-1} d\beta} \quad (2.53)$$

which is shown in Figure 2.11 for several different parameter combinations.

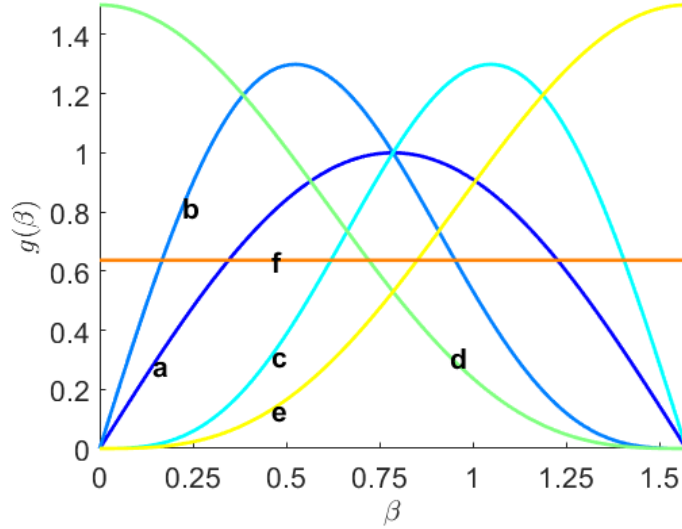


Figure 2.11: The orientation distribution $g(\beta)$ with (a) $p = 1, q = 1$, (b) $p = 1, q = 2$, (c) $p = 2, q = 1$, (d) $p = 1/2, q = 2$, (e) $p = 2, q = 1/2$, and (f) $p = 1/2, q = 1/2$. Figure recreated from Fu and Lauke [94].

Fu and Lauke [94] have several helpful conclusions from their study which can be drawn from Figures 2.12a-e which have been recreated from [94] for this dissertation. In these figures, the strength will increase or decrease as χ_1 , χ_2 , or $\chi_1\chi_2$ increases or decreases, thus these figures give insight into the behavior of the tensile strength. By letting $\chi_1 = 1$, Equation 2.48 is restricted to unidirectional orientation states and the effects of various fiber length constants can be studied as shown in Figures 2.12a, c, and d. When $\chi_1 = 1$, Equation 2.49 becomes

$$\chi_2 = \int_{L_{min}}^{L_c} \left(\frac{L^2}{2L_c L_{mean}} \right) f(L) dL + \int_{L_c}^{L_{max}} \frac{L}{L_{mean}} \left(1 - \frac{L_c}{2L} \right) f(L) dL \quad (2.54)$$

It should be stated that the critical fiber length designates if a fiber will pull-out or break when the SFRP fails. For a fiber of length L , if $L \geq L_c$ the fiber will

break. If $L < L_c$ the fiber will pull out of the matrix and thus, a higher L_c means more fibers will pull-out, decreasing the strength of the composite. Figures 2.12a, c, d, and e corroborate this fact by showing that as L_c increases, the strength decreases. Another conclusion from Fu and Lauke that can be gathered from Figure 2.12a is that when L_{mean} is close to L_c and increasing, the strength of the SFRP grows dramatically, but when L_{mean} is already large ($> 5L_c$) and increasing, the strength starts plateauing. Interestingly, Figure 2.12d shows that as the most common fiber length i.e., the mode L_{mod} , increases, χ_2 from Equation 2.54 hardly changes but decreases slightly. Furthermore, even when considering the effects of both length and orientation distributions, L_{mod} still does not effect the tensile strength significantly as can be seen in Figure 2.12e. Another interesting finding from Fu and Lauke is that when L_{mod}/L_c and L_{mean}/L_c are constant for a specific SFRP, the strength is constant no matter how small or large L_c , L_{mod} , or L_{mean} are. It was also found that μ has little effect on the tensile strength, that $\chi_1\chi_2$ decreases as \mathcal{A} increases, and that taking the orientation of the fiber into account has considerable effect on the predicted tensile strength of the SFRP.

Fu and Lauke’s method was initially pursued in this work as a means of predicting strength in single beads of LAAM-printed SFRP material. For example, it is possible that χ_1 be cast as a function of the orientation tensors. After a more thorough review of the literature, however, a tensor-based failure criterion was ultimately selected for strength prediction since it fits well with the fiber orientation modeling methodology and can be used to readily predict tensile or compressive yield strength properties in *any* direction. Nevertheless, the study of Fu and Lauke’s model gives valuable insights into the key factors effecting the strength of SFRPs.

A more recent tensile strength model is from Kuriger and Alam [95], where they predict strength using the following equation

$$\sigma_{LT}(\beta) = 2 \int_0^{\pi/2} g(\beta) \left[\frac{\cos^4 \beta}{\bar{\sigma}_{LT}^2} + \left(\frac{1}{\bar{\tau}_{12}^2} + \frac{1}{\bar{\sigma}_{LT}^2} \right) \sin^2 \beta \cos^2 \beta + \frac{\sin^4 \beta}{\bar{\sigma}_{TT}^2} \right]^{-1/2} d\beta \quad (2.55)$$

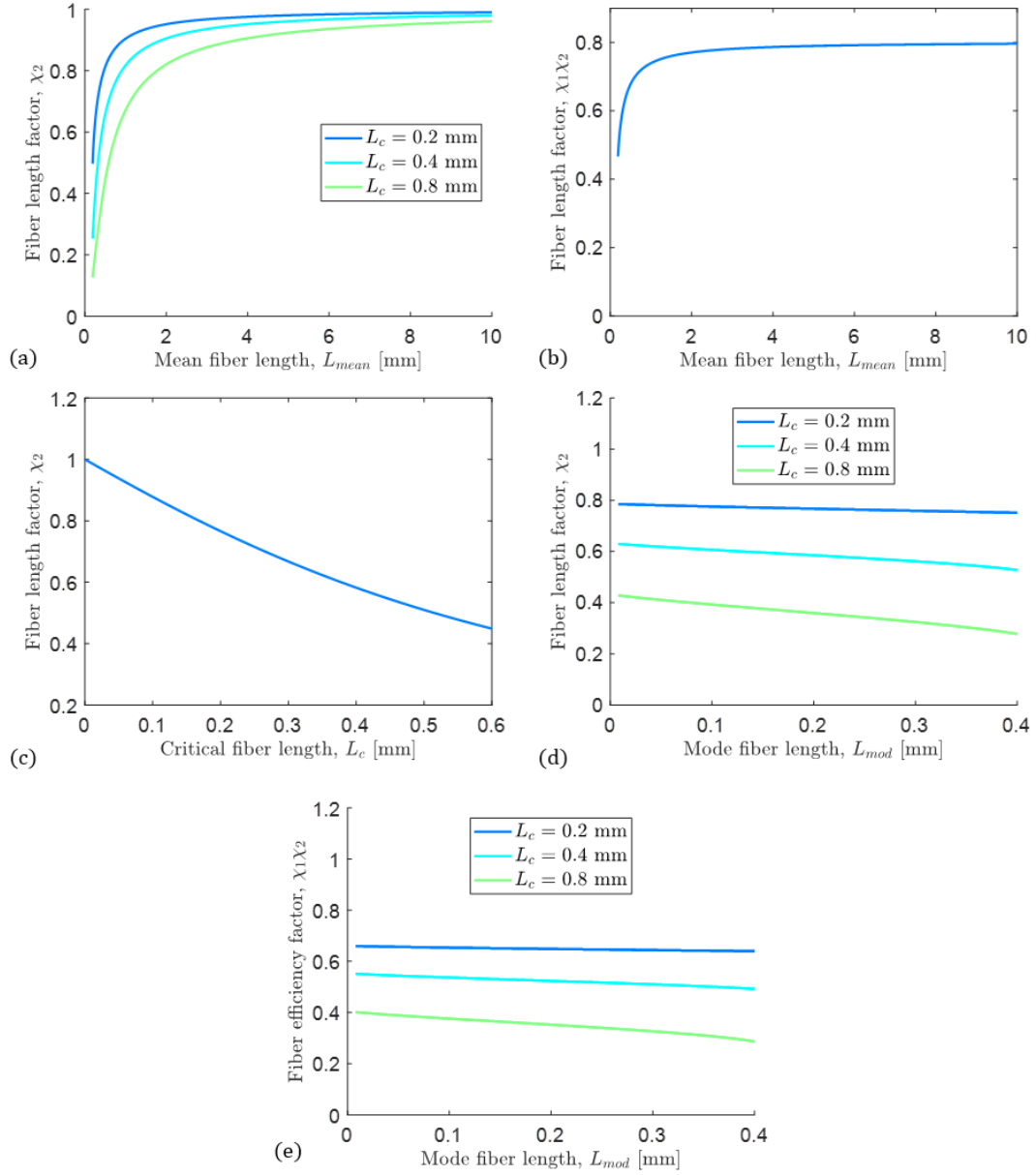


Figure 2.12: All figures recreated based upon results in [94]. (a) Fiber length factor χ_2 as a function of mean fiber length L_{mean} , showing tensile strength increases as L_{mean} increases. (b) Fiber length factor χ_2 as a function of critical fiber length L_c , showing steady decrease in tensile strength as L_c increases. (c) Fiber length factor χ_2 as a function of the mode fiber length L_{mod} , showing little change in χ_2 as L_{mod} increases. (d) Product of fiber length and orientation factors $\chi_1\chi_2$ as a function of mode fiber length L_{mod} , showing little change in tensile strength as L_{mod} increases.

where $g(\beta)$ is a Gaussian orientation distribution function found from experimental data collected by x-ray diffraction. The term $\bar{\tau}_{12}$ is the in-plane shear strength. Unlike the Fu-Lauke model, Equation 2.55 does not take into account a fiber length distribution.

The longitudinal compressive strength, σ_{LC} , can also be predicted using an MROM model. The Hayashi-Koyama compressive strength model [96] (as cited in [90]) is

$$\bar{\sigma}_{LC} = E_f \epsilon_m^* V_f + E_m \epsilon_m^* (1 - V_f) \quad (2.56)$$

where E_f and E_m are the elastic moduli of the fiber and matrix, respectively, and the ϵ_m^* term is the strain at which the matrix material yields. Bajracharya et al. [90] modified Equation 2.56 to

$$\sigma_{LC} = \chi_1 \chi_2 E_f \epsilon_m^* V_f + (1 - V_f) \sigma_m^* \quad (2.57)$$

where $\sigma_m^* = E_m \epsilon_m^*$, and χ_1 and χ_2 are the fiber orientation and lengths factors. From Fu and Lauke [94], $\chi_2 = L/(2L_c)$ if the fibers have uniform length L and $L < L_c$, so Bajracharya et al. [90] let χ_2 be a constant in Equation 2.57 such that

$$\chi_2 = \frac{L_w}{2L_c} \quad (2.58)$$

where L_w is the weight-average fiber length and L_c is the critical length. Note, that Equation 2.57 predicts σ_{LC} rather than strictly $\bar{\sigma}_{LC}$ since it takes an orientation distribution into account through χ_1 .

Another compressive strength model is that of Rosen [97] (as cited in [90])

$$\bar{\sigma}_{LC} = 2V_f \left[\frac{V_f E_m E_f}{3(1 - V_f)} \right]^{1/2} \quad (2.59)$$

but Bajracharya et al. found this model to be less accurate than Equation 2.57. One final compressive strength model stated in this dissertation is [25]

$$\bar{\sigma}_{LC} = \bar{G}_{12} \left[1 + 4.76 \left(\frac{\bar{G}_{12} s_\alpha}{\bar{\tau}_{12}} \right)^{-0.69} \right] \quad (2.60)$$

where s_α is the standard deviation of $g(\beta)$, which has been included to account for small amounts of misalignment introduced by imperfections in the manufacturing process, and \bar{G}_{12} and $\bar{\tau}_{12}$ are the shear stiffness and strength in the x_1 - x_2 plane.

2.5.2 Failure Criteria

The most basic failure criteria are the maximum stress and maximum strain criteria. These define hypercubes in the stress and strain space, respectively (e.g., [25]). A material under a stress/strain state defined by a point on the edge or outside of the hypercubes is predicted to fail. For the maximum stress criterion, the sides of the hypercube will be defined by the yield strengths of the composite i.e., σ_{LT} , σ_{LC} , σ_{TT} , σ_{TC} , $\tau_{23} = \tau_{32}$, $\tau_{13} = \tau_{31}$, and $\tau_{12} = \tau_{21}$. Thus, if a stress equals or exceeds its corresponding strength value, failure will be predicted. The sides of the strain hypercube are defined by failure strains and if an applied strain exceeds its corresponding failure strain, failure will be predicted. The maximum strain criterion is still, today, a favorite in industry [25]. However, in general, the failure envelope should not be restricted to the shape of a hypercube.

Much work has been done over the last 60 years to establish a general failure criterion [98]. One research team took it upon themselves to undertake the years-long World Wide Failure Exercise, whereupon researchers across the globe analyzed many of the major failure criteria [99] (as cited in [100]). Unfortunately, there was no failure theory that clearly rose above the rest and no theory that matched the experimental data perfectly [100]. There are also concerns, even conceptual discrepancy, amongst the research community over how a failure theory should be defined. Some of these concerns have to do with whether the failure envelope should be allowed to be open or if it is required to be closed (e.g., [99] as cited in [100]), whether the failure theory identifies the mode of failure (e.g., [101]), and how many parameters are acceptable (e.g., [98]).

While there are still concerns over the best approach, one of the early and most well-known failure criterion for anisotropic materials is that of Tsai and Wu [102]. The Tsai-Wu failure criterion [102] in terms of stress σ_i and strain ε_i is given, respectively, in Equations 2.61 and 2.62:

$$f_i \sigma_i + F_{ij} \sigma_i \sigma_j = 1 \quad (2.61)$$

$$g_i \varepsilon_i + G_{ij} \varepsilon_i \varepsilon_j = 1 \quad (2.62)$$

where $i, j = 1, 2, 3, 4, 5, 6$. The stress and strain tensors are in contracted 6×1 form following Voigt order i.e., $\boldsymbol{\sigma} = \sigma_i = [\sigma_{11}, \sigma_{22}, \sigma_{33}, \sigma_{23}, \sigma_{31}, \sigma_{12}]^T$ and $\boldsymbol{\varepsilon} = \varepsilon_i = [\varepsilon_{11}, \varepsilon_{22}, \varepsilon_{33}, 2\varepsilon_{23}, 2\varepsilon_{31}, 2\varepsilon_{12}]^T$. Note that in this dissertation, the term τ_{ij} has been reserved to refer to shear strengths, whereas σ_{ij} with $i \neq j$ refers to a shear stress. The terms f_i and g_i are contracted, second-order strength tensors and F_{ij} and G_{ij} are contracted, fourth-order strength tensors, which are related by the contracted, fourth-order stiffness tensor C_{ij} by

$$g_i = f_m C_{mi} \quad (2.63)$$

$$G_{ij} = F_{mn} C_{mi} C_{nj} \quad (2.64)$$

where $i, j = 1, 2, \dots, 6$.

The Tsai-Wu failure criterion defines a smooth, enclosed, ellipsoidal-shaped failure surface in 3D stress space (e.g., [102]). In 2D, when projected into the $\sigma_i \sigma_j$ -plane ($i = j$), the failure envelope will be an enclosed ellipse. One key advantage of the Tsai-Wu criterion is that, unlike the maximum stress criterion, it accounts for interaction between different types of stresses. This is good because certain failure modes will interact with each other. For example, a shearing force σ_6 (or σ_{12} in non-contracted notation) will effect the amount of stress in the x_2 direction, namely σ_2 , that a material will be able to withstand. A downside of the Tsai-Wu model is that it tends to over-inflate the amount of interaction between stresses

because it imposes interaction between all of the modes at once and cannot be used to identify the mode in which the material failed [25]. Hashin [101] proposed an alternative model that distinguishes between the failure modes, specifically, fiber tension, fiber compression, matrix tension, and matrix compression. The result is a failure envelope that is *piecewise* smooth [101]. However, despite its limitations, the Tsai-Wu model has still enjoyed a large amount of attention and success for decades [103]. In addition, a key advantage of the Tsai-Wu model is that it uses a tensor approach and since tensor transformations are well known, this allows for off-axis properties to be readily characterized and studied [87, 102]. Finally, the Tsai-Wu model also has a simple and compact definition that is relatively easy to implement.

In the case of a transversely isotropic material with x_1 as the axis of symmetry, several components of the strength tensors in the Tsai-Wu model will vanish, leaving the forms [102]

$$\bar{f}_i = \begin{bmatrix} \bar{f}_1 \\ \bar{f}_2 \\ \bar{f}_2 \\ 0 \\ 0 \\ 0 \end{bmatrix}, \quad \bar{F}_{ij} = \begin{bmatrix} \bar{F}_{11} & \bar{F}_{12} & \bar{F}_{12} & 0 & 0 & 0 \\ & \bar{F}_{22} & \bar{F}_{23} & 0 & 0 & 0 \\ & & \bar{F}_{22} & 0 & 0 & 0 \\ & & & \bar{F}_{44} & 0 & 0 \\ & & & & \bar{F}_{55} & 0 \\ & & & & & \bar{F}_{55} \end{bmatrix} \quad (2.65)$$

where the components are given by

$$\begin{aligned} \bar{f}_1 &= \frac{1}{\bar{\sigma}_{LT}} - \frac{1}{\bar{\sigma}_{LC}}, & \bar{f}_2 &= \frac{1}{\bar{\sigma}_{TT}} - \frac{1}{\bar{\sigma}_{TC}}, & \bar{F}_{11} &= \frac{1}{\bar{\sigma}_{LT}\bar{\sigma}_{LC}}, \\ \bar{F}_{22} &= \frac{1}{\bar{\sigma}_{TT}\bar{\sigma}_{TC}}, & \bar{F}_{44} &= 2(\bar{F}_{22} - \bar{F}_{23}), & \bar{F}_{55} &= 1/\bar{\tau}^2 \end{aligned} \quad (2.66)$$

Note that the interaction terms F_{12} and F_{23} still need to be defined in Equations 2.65 and 2.66. Tsai and Wu assumed they could be found experimentally [102], but this is challenging since biaxial loading of a sample to failure is difficult to control [103].

Tsai and Wu did, however, provide the following stability condition:

$$F_{ii}F_{jj} - F_{ij}^2 \geq 0 \quad (2.67)$$

where $i, j = 1, 2, \dots, 6$ and no summation is performed on the repeated indices. Equation 2.67 gives bounds to the interaction terms i.e., $F_{12} \leq \pm\sqrt{F_{11}F_{22}}$ and $F_{23} \leq \pm\sqrt{F_{22}F_{33}}$.

Various analytic forms for the interaction terms have been proposed. Li et al. [103] summarizes some of them. Wu [104] (as cited in [103]) found F_{12} to be close to 0. Narayanaswami and Adelman [105] (as cited in [103]) also suggested letting $F_{12}=0$. Tsai and Hahn [106] (as cited in [103]) suggested $F_{12} = -\frac{1}{2}\sqrt{F_{11}F_{22}}$. Li et al. let $F_{23} = F_{22} - \frac{1}{2}F_{44}$ and $F_{44} = \frac{1}{\bar{\tau}_{23}}$ where the shear strength $\bar{\tau}_{23}$ is assumed to be determinable by experiments [103]. Li et al. furthermore find $F_{12} = -\frac{1}{2}\sqrt{F_{11}(4F_{22} - F_{44})}$ by allowing the failure envelope to be open [103], a condition which was previously not allowed by Tsai and Wu whose failure surface is an enclosed ellipsoid [102]. Van Hattum and Bernardo appear to take $F_{12} = -\frac{1}{2}F_{11}$ and $F_{23} = \frac{1}{2}F_{11} - F_{22}$ [87]. In the work of DeTeresa and Larsen [107], they also do away with the closed failure surface requirement and assume the composite will not fail due to typical hydrostatic stress states or equal transverse compressive stresses. With these assumptions, which are reasonable for the carbon fiber composite they studied, they derive $F_{12} = -\frac{1}{4}F_{11}$ and $F_{23} = -F_{22}$ which they hypothesize will also work for other composites with high stiffness [107].

One of the advantages of the Tsai-Wu failure criterion is that the strength tensors can be rotated using tensor rotation relations to investigate the strength of an anisotropic material in any direction [102]. Van Hattum and Bernardo [87] preserved this capability when they combined the Tsai-Wu theory with Advani's orientation averaging technique to predict the strength of SFRPs with arbitrary fiber orientation states. Van Hattum and Bernardo also experimentally validated their model for predicting the effective tensile strength of a 5%, 10%, and 15%

carbon-fiber-filled polypropylene, with their predictions falling within 10% of their experimental results [87]. To make these predictions, Van Hattum and Bernardo used the Hill criterion, which makes the constraint that $\sigma_{LC} = \sigma_{LT}$ and yields the following strength tensors for the underlying unidirectional, transversely isotropic SFRP:

$$\bar{f}_i \equiv \begin{bmatrix} 0 \\ 0 \\ 0 \\ 0 \\ 0 \\ 0 \end{bmatrix}, \quad \bar{F}_{ij} = \begin{bmatrix} \frac{1}{\bar{\sigma}_{LT}^2} & \frac{-1}{2\bar{\sigma}_{LT}^2} & \frac{-1}{2\bar{\sigma}_{LT}^2} & 0 & 0 & 0 \\ & \frac{1}{\bar{\sigma}_{TT}^2} & -\frac{1}{2} \left(\frac{2}{\bar{\sigma}_{TT}^2} - \frac{1}{\bar{\sigma}_{LT}^2} \right) & 0 & 0 & 0 \\ & & \frac{1}{\bar{\sigma}_{TT}^2} & 0 & 0 & 0 \\ & & & \left(\frac{4}{\bar{\sigma}_{TT}^2} - \frac{1}{\bar{\sigma}_{LT}^2} \right) & 0 & 0 \\ & & & & \frac{1}{\bar{\tau}^2} & 0 \\ & & & & & \frac{1}{\bar{\tau}^2} \end{bmatrix} \quad (2.68)$$

symmetric

Van Hattum and Bernardo let the composites's transverse and shear strength be given by $\bar{\sigma}_{TT} = \sigma_m$ and, assuming the matrix is isotropic, $\bar{\tau} = \sigma_m/\sqrt{3}$, where σ_m is the strength of the matrix material [87]. For the composite's longitudinal tensile strength, they use an MROM model based on the following equations

$$\bar{\sigma}_{LT} = V_f \sigma_f \frac{L}{2L_c} + \sigma'_m (1 - V_f) = V_f \frac{\bar{\tau} L}{d} + \sigma'_m (1 - V_f), \quad \text{for } L < L_c \quad (2.69a)$$

$$\bar{\sigma}_{LT} = V_f \sigma_f \left(1 - \frac{L_c}{2L} \right) + \sigma'_m (1 - V_f), \quad \text{for } L \geq L_c \quad (2.69b)$$

where V_f is the volume fraction of fibers, σ_f is the strength of a single fiber, L is the fiber length, σ'_m is the stress in the matrix at the strain where a fiber fails, and L_c is the critical fiber length from Equation 2.52 where, assuming a strong fiber-matrix bond, τ^i is limited by the matrix and therefore $\tau^i = \tau_m$ [87]. It can also be assumed that the shear strength of the composite is controlled by τ_m , and therefore $\tau^i = \tau_m = \bar{\tau}$. Thus, Equation 2.52 becomes

$$L_c = \frac{\sigma_f r_f}{\bar{\tau}} \quad (2.70)$$

Van Hattum and Bernardo not only consider SFRPs with a distribution of fiber orientations, but also consider a distribution of fiber lengths in their model.

Since longer fibers tend to have more defects and, consequently, a lower strength than short fibers, Van Hattum and Bernardo express the strength of a fiber as a function of fiber length using a Weibull distribution function [87]:

$$\sigma_f = \sigma_f(L) = \sigma_o \Gamma(1 + 1/m) L^{-\gamma/m} \quad (2.71)$$

In the above equation, σ_o and m are the Weibull scale and shape factors, Γ is the gamma function, and γ is a constant [87]. Inserting $\sigma_f = \sigma_f(L_c)$ into Equation 2.69b, now gives the longitudinal tensile strength of the unidirectional composite as [87]

$$\bar{\sigma}_{LT} = V_f \frac{\bar{\tau} L}{d} + \sigma'_m (1 - V_f), \quad \text{for } L < L_c \quad (2.72a)$$

$$\begin{aligned} \bar{\sigma}_{LT} &= V_f \sigma_f(L_c) \left(1 - \frac{L_c}{2L}\right) + \sigma'_m (1 - V_f) \\ &= V_f \sigma_o \Gamma(1 + 1/m) L_c^{-\gamma/m} \left(1 - \frac{L_c}{2L}\right) + \sigma'_m (1 - V_f), \quad \text{for } L \geq L_c \end{aligned} \quad (2.72b)$$

Ultimately, Van Hattum and Bernardo take the length-average of the above equations using a fiber length distribution $f(L)$ characterized by a log-normal distribution [87]:

$$\bar{\sigma}_{LT} = \int_{L=0}^{L_c} \bar{\sigma}_{LT}(L) f(L) dL + \int_{L=L_c}^{L_{max}} \bar{\sigma}_{LT}(L) f(L) dL \quad (2.73)$$

It should be noted, however, that Van Hattum and Bernardo found that their consideration of $f(L)$ did not change their results significantly compared to when they simply used an average fiber length [87].

The fiber strength equation, Equation 2.71, is dependent on the type of fiber being studied. For Van Hattum and Bernardo, they used TENAX PAN-based HTA 5131 carbon fibers and found the following equation

$$\sigma_f(L) = 4940.1/L^{0.1554} \quad (2.74)$$

where L is in millimeters and gives σ_f in MPa [87]. The critical fiber length for a carbon fiber composite with this grade of carbon fiber can be found using

$$L_c = \frac{\sigma_f(L_c) d_f}{2\tau} \quad (2.75)$$

which is a roots problem that involves inserting Equation 2.74 with $L = L_c$. To consider a type of fiber other than that used by Van Hattum and Bernardo (whether carbon or not), alternative single-fiber tensile testing data would need to be referred to or generated from experiments so that a new equation for $\sigma_f(L)$ could be fit to it.

Once all the terms in Equation 2.68 have been defined, the strain-related strength tensors are found according to Equations 2.63 and 2.64 i.e., $\bar{g}_i = \bar{f}_m \bar{C}_{mi}$ and $\bar{G}_{ij} = \bar{F}_{mn} \bar{C}_{mi} \bar{C}_{nj}$. Next, \bar{g}_i and \bar{G}_{ij} are inserted into Equation 2.62 which must be orientation averaged to get the strength of a misaligned SFRP. Thus,

$$\begin{aligned}\bar{g}_i \varepsilon_i + \bar{G}_{ij} \varepsilon_i \varepsilon_j &= 1 \\ \langle \bar{g}_i \varepsilon_i + \bar{G}_{ij} \varepsilon_i \varepsilon_j \rangle &= \langle 1 \rangle \\ \langle g \rangle_i \varepsilon_i + \langle G \rangle_{ij} \varepsilon_i \varepsilon_j &= 1\end{aligned}\tag{2.76}$$

with $i, j = 1, 2, \dots, 6$. Since Van Hattum and Bernardo use the Hill Criterion, Equation 2.76 simplifies even further to

$$\langle G \rangle_{ij} \varepsilon_i \varepsilon_j = 1\tag{2.77}$$

where $\langle G \rangle_{ij}$ is found in the same manner as the orientation-averaged stiffness i.e., through using Equations 2.17 and 2.19. The next step is to solve for a strain state ε_i , such that Equation 2.77 holds true. This will signify the moment at which the SFRP material yields. Finding ε_i at the yield point can be accomplished by performing displacement-prescribed finite element analyses of the SFRP part under consideration, where a displacement is applied in the direction in which the strength is desired and is increased or decreased until Equation 2.77 is true (or sufficiently close to being true). The resulting stress in the direction of the applied displacement can then be taken to be the yield strength of the SFRP in that direction.

Furthermore, the strength constants of the SFRP can also be determined by extracting them from $\langle F \rangle_{ij}$ [87]. That is, the contracted, fourth-order, stress-related

strength tensor can be determined by rearranging Equation 2.64:

$$\langle F \rangle_{ij} = \langle G \rangle_{mn} \langle S \rangle_{mi} \langle S \rangle_{nj} \quad (2.78)$$

where $\langle S \rangle_{ij} = \langle C \rangle_{ij}^{-1}$ is the orientation-averaged compliance tensor [87]. Then, using Equation 2.68, the strength constants can be determined by $\sigma_{LT} = \sqrt{1/F_{11}}$ and $\sigma_{LC} = \sqrt{1/F_{22}}$.

If Equation 2.76 is used rather than the Hill criterion and Equation 2.77, $\langle g \rangle_i$ must be determined in addition to $\langle G \rangle_{ij}$. The second order tensor is obtained by Equations 2.16 and 2.18 (e.g., [56]), which results in

$$\langle \mathbf{g} \rangle = \langle g \rangle_i = \begin{bmatrix} (\bar{g}_1 - \bar{g}_2) A_{11} + \bar{g}_2 \\ (\bar{g}_1 - \bar{g}_2) A_{22} + \bar{g}_2 \\ (\bar{g}_1 - \bar{g}_2) A_{33} + \bar{g}_2 \\ (\bar{g}_1 - \bar{g}_2) A_{23} \\ (\bar{g}_1 - \bar{g}_2) A_{13} \\ (\bar{g}_1 - \bar{g}_2) A_{12} \end{bmatrix} \quad (2.79)$$

where contracted notation has been used.

Van Hattum and Bernardo's technique enabled them to obtain strength predictions within 10% of their experimental results for a carbon fiber filled polypropylene [87]. In addition, Andersons et al. [108] found the Van-Hattum-Bernardo model to be better than the modified Fukuda-Chou model at capturing the difference in strength of two flax fiber composites made with different thermoset matrices.

In summary, Van Hattum and Bernardo [87] demonstrate how to predict the tensile strength of an SFRP under any loading scenario and as a function of a fiber length distribution and a spatially varying, arbitrary orientation distribution. The only information that is needed to do this is the transverse and longitudinal tensile strength and the shear strength of the underlying perfectly aligned composite, namely $\bar{\sigma}_{TT}$, $\bar{\sigma}_{LT}$, and $\bar{\tau}$, respectively, the fiber length distribution function $f(L)$,

and the spatially varying orientation tensors \mathbf{A} and \mathbf{A}_4 [87]. The fact that the Van Hattum-Bernardo method accounts for an orientation distribution by using orientation tensors means that the Van Hattum-Bernardo method can be used directly with the fiber orientation information predicted by traditional fiber orientation models, like the IRD or RSC. Thus, the strength properties of an SFRP part can essentially be predicted from the processing conditions of the part. This is not the case with the MROM models discussed in Section 2.5.1. It would perhaps be feasible to replace $g(\beta)$ with $\hat{\psi}(\theta, \phi)$ in these MROM models or else express χ_1 as a function of the orientation tensors or a function of $\hat{\psi}$, but these routes would make the analysis significantly more complicated. The Van Hattum-Bernardo method is a more direct approach.

In addition, by using orientation tensors, generality is preserved. That is, the orientation tensors originate from and can be used to reconstruct ψ , which can be used to describe *any arbitrary* orientation state (e.g., [48]), whereas $g(\beta)$ can only accurately represent distributions that are symmetric about the direction in which the strength is being predicted. Figure 2.13 demonstrates this by using the shaded sphere representation of the orientation probability density function. Figures 2.13a-c can be represented by both $g(\beta)$ and $\psi(\theta, \phi)$, whereas Figures 2.13d-f can only be represented by $\psi(\theta, \phi)$ and not $g(\beta)$. Clearly, there is an advantage to using $\psi(\theta, \phi)$ (or the orientation tensors which can be used to reconstruct $\hat{\psi}(\theta, \phi)$) rather than $g(\beta)$ if generality is desired to be preserved, or if there is an interest in the off-axis properties.

There is a notable limitation with Van Hattum and Bernardo's model as they presented it in [87], however. Their use of the Hill criterion (Equation 2.68) is restrictive in that it does not allow different values of tensile strength and compressive strength to be predicted. Tensile and compressive strength can be significantly different from each other in SFRPs and therefore using a more general form of the

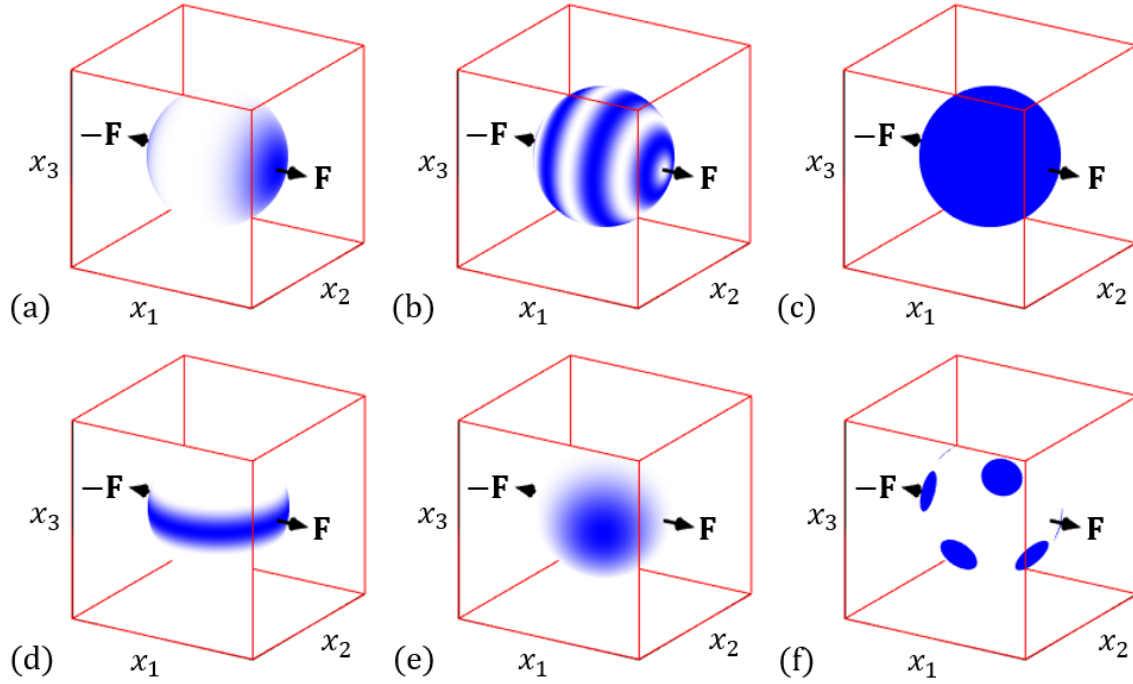


Figure 2.13: Orientation distribution functions: (a) mostly aligned orientation; (b) an orientation symmetric about \mathbf{F} ; (c) completely random orientation; (d) nearly planar random orientation; (e) mostly aligned orientation but off-axis; (f) orientation with multi-axial bias. Figures a-c can be represented by $g(\beta)$ or $\psi(\theta, \phi)$ (or the orientation tensors). Figures d-f cannot accurately be represented by $g(\beta)$ but can be represented by $\psi(\theta, \phi)$ (or, equivalently, the orientation tensors).

strength tensors, such as that in Equation 2.65, would be desirable so that the tensile and compressive strengths of an SFRP could be uniquely predicted. Doing so would require finding $\langle g \rangle_i$ in addition to $\langle G \rangle_{ij}$ for use in Equation 2.76. Van Hattum and Bernardo present the full form of $\langle g \rangle_i$ and $\langle G \rangle_{ij}$ in [56], but mainly focus on just flexural strength in this paper.

2.6 Other Models

There are other models for transversely isotropic properties that can be homogenized using Advani's method to get the corresponding orientation-averaged property. These include models for the coefficient of thermal expansion (CTE), coefficient of moisture expansion, thermal conductivity, and electrical conductivity.

2.6.1 Coefficient of Thermal Expansion

The transversely isotropic coefficient of thermal expansion (CTE) tensor of an SFRP with fibers aligned uniaxially along x_1 is given as

$$\bar{\alpha} = \bar{\alpha}_{ij} = \begin{bmatrix} \bar{\alpha}_{11} & 0 & 0 \\ 0 & \bar{\alpha}_{22} & 0 \\ 0 & 0 & \bar{\alpha}_{22} \end{bmatrix} \quad (2.80)$$

where the assumption that the fibers and matrix are isotropic is made (e.g., [109]). Thus, $\bar{\alpha}_{ij}$ is fully determined by two independent constants, $\bar{\alpha}_{11}$ and $\bar{\alpha}_{22}$. Halpin [110] (as cited by [109]) gives $\bar{\alpha}_{11}$ and Wright [111] (as cited by [109]) gives $\bar{\alpha}_{22}$,

$$\bar{\alpha}_{11} = \hat{\alpha} + \left(\frac{\widehat{K\alpha}}{\hat{K}} - \hat{\alpha} \right) \frac{1/\bar{E}_{low} - 1/E_{11}}{1/\bar{E}_{low} - 1/\bar{E}_{up}} \quad (2.81)$$

$$\bar{\alpha}_{22} = (1 + \nu_f)\alpha_f V_f + (1 + \nu_m)\alpha_m(1 - V_f) - \alpha_{11}\nu_{12} \quad (2.82)$$

where \bar{E}_{low} and \bar{E}_{up} are Schapery's lower and upper bound on the modulus of the unidirectional SFRP [112],

$$\bar{E}_{low} = \left(\frac{V_f}{E_f} + \frac{1 - V_f}{E_m} \right)^{-1}, \quad \bar{E}_{up} = E_f V_f + E_m(1 - V_f) \quad (2.83)$$

The hat accents on the terms in Equation 2.81 indicate volume averages i.e.,

$$\begin{aligned} \hat{\alpha} &= \alpha_f V_f + \alpha_m(1 - V_f) \\ \hat{K} &= K_f V_f + K_m(1 - V_f) \\ \widehat{K\alpha} &= K_f \alpha_f V_f + K_m \alpha_m(1 - V_f) \end{aligned} \quad (2.84)$$

Once again, the properties of the fibers and matrix are assumed to be isotropic in the above equations.

Barbero [25] gives $\bar{\alpha}_{11}$ and $\bar{\alpha}_{22}$ for fibers with differing axial (denoted by a subscript A) and transverse (denoted by a subscript T) properties

$$\bar{\alpha}_{11} = (\alpha_A V_f E_A + \alpha_m(1 - V_f)E_m)/E_{11} \quad (2.85)$$

$$\bar{\alpha}_{22} = (1 + \nu_A)\alpha_T V_f + (1 + \nu_m)\alpha_m(1 - V_f) - \alpha_{11}\nu_{12} \quad (2.86)$$

Note, that Equation 2.86 is identical to Equation 2.82 if the fibers are isotropic i.e., $\alpha_A = \alpha_T = \alpha_f$ and $E_A = E_f$.

Camacho and Tucker give the orientation-averaged form of the CTE tensor in [113],

$$\langle \alpha \rangle_{ij} = \langle S \rangle_{ijkl} (D_1 A_{kl} + D_2 \delta_{kl}) \quad (2.87)$$

where

$$D_1 = A_1(B_1 + B_2 + 4B_3 + B_5) + A_2(B_1 + 3B_2 + 4B_3) \quad (2.88)$$

$$D_2 = A_1(B_2 + B_4) + A_2(B_2 + 3B_4 + B_5) \quad (2.89)$$

The A 's in the equation above are given by Equation 2.18,

$$A_1 = \alpha_{11} - \alpha_{22}, \quad A_2 = \alpha_{22} \quad (2.90)$$

and the B 's come from Equation 2.19 where the \bar{T}_{ijkl} terms are components of \bar{C}_{ijkl} .

2.6.2 Coefficient of Moisture Expansion

Moisture absorption can also cause a material to expand, changing its dimensions, and the orientation-dependent moisture expansion properties of an anisotropic SFRP can also be found using the proposed methodology. Moisture expansion happens much more slowly than thermal expansion [25]. For the prediction of the moisture expansion properties, the transversely isotropic moisture expansion tensor of the underlying unidirectional SFRP aligned along x_1 is defined as

$$\bar{\beta} = \bar{\beta}_{ij} = \begin{bmatrix} \beta_{11} & 0 & 0 \\ 0 & \beta_{22} & 0 \\ 0 & 0 & \beta_{22} \end{bmatrix} \quad (2.91)$$

To simplify the equations for β_{11} and β_{22} , the assumption that the fibers do not absorb moisture is made, which is valid for inorganic fibers like glass and carbon [25]. Equations 2.92 and 2.93 come from [114] (as cited in [25])

$$\beta_{11} = \beta_m(1 - V_f) \frac{E_m}{E_{11}} \quad (2.92)$$

$$\beta_{22} = \beta_m(1 - \sqrt{V_f}) \left[1 + \frac{\sqrt{V_f}(1 - \sqrt{V_f})E_m}{\sqrt{V_f}E_{22} + (1 - \sqrt{V_f})E_m} \right] \quad (2.93)$$

In the above, β_m is the moisture expansion coefficient of an isotropic matrix. The coefficient of moisture expansion tensor is orientation averaged using the same procedure as that for the CTE, using Equations 2.87-2.90 with the α 's replaced by β 's.

2.6.3 Thermal Conductivity

The transversely isotropic thermal conductivity tensor of a unidirectional SFRP aligned along x_1 is described in terms of two independent constants as given by (e.g., [115])

$$\bar{\mathbf{k}} = \bar{k}_{ij} = \begin{bmatrix} k_{11} & 0 & 0 \\ 0 & k_{22} & 0 \\ 0 & 0 & k_{22} \end{bmatrix} \quad (2.94)$$

Halpin [110] gives k_{11} and k_{22} as

$$k_{11} = \frac{k_m(1 + 2a_r\mu_1V_f)}{1 - \mu_1V_f}, \quad k_{22} = \frac{k_m(1 + 2\mu_2V_f)}{1 - \mu_2V_f} \quad (2.95)$$

where

$$\mu_1 = \frac{(k_f/k_m) - 1}{(k_f/k_m) + 2a_r}, \quad \mu_2 = \frac{(k_f/k_m) - 1}{(k_f/k_m) + 2} \quad (2.96)$$

and k_m and k_f are the isotropic thermal conductivity of the matrix and fiber, respectively. If the thermal conductivity of the fiber can be characterized by differing longitudinal and transverse thermal conductivities, k_{f1} and k_{f2} , then k_f can be replaced by k_{f1} in the equation for μ_1 and by k_{f2} in the equation for μ_2 . The thermal conductivity tensor can be orientation averaged by Equations 2.16 and 2.18.

2.6.4 Electrical Conductivity

Electrical conductivity can be computed in a like manner to the thermal conductivity. Here, the approach of Barbero [25] is presented, who used the ROM for k_{11} in the longitudinal direction, and the Halpin-Tsai form [116] for k_{22} in the transverse direction,

$$k_{11} = k_f V_f + k_m (1 - V_f), \quad k_{22} = k_m \left[\frac{1 + \xi \eta V_f}{1 - \eta V_f} \right] \quad (2.97)$$

$$\eta = \frac{(k_f/k_m) - 1}{(k_f/k_m) + \xi}, \quad \xi = \log^{-1} \sqrt{3} \log \frac{a}{b} \quad (2.98)$$

where a/b is the fiber cross section aspect ratio and $\xi = 1$ for fibers with a circular cross section. Equation 2.97 can be used for thermal conductivity and mass diffusivity in addition to electrical conductivity and work well for thermal and electrical conductivity predictions for carbon-epoxy composites with $V_f \leq 60\%$ [25]. The orientation-averaged tensor property can be obtained by Equations 2.16 and 2.18.

CHAPTER THREE

Computational Methods and Results

In this chapter, the computational methods for predicting the stiffness, strength, and thermal expansion properties of a LAAM-made, SFRP bead are discussed. The SFRP considered in the models is a 13% carbon fiber filled acrylonitrile butadiene styrene (CF-ABS). Section 3.1 details the steps of the methodology, devoting subsections to the prediction of the orientation, stiffness, strength, and CTE. This is followed by a presentation of results in Section 3.2, which are divided into three subsections for orientation results, stiffness and CTE results, and stiffness and strength results. Section 3.3 then discusses the computational methodology from a broader viewpoint, presenting a custom-made COMSOL application that combines much of the modeling work done in this dissertation. This section also demonstrates the prediction of thermal conductivity, stiffness, CTE, and strength to highlight the versatility and usefulness of the proposed methodology.

3.1 Computational Methodology

The computational methodology in this study can be broken down into four key steps: (1) modeling the flow and predicting the fiber orientation state, (2) predicting the tensor properties of the underlying unidirectional SFRP, (3) obtaining the orientation averaged tensor properties, and (4) obtaining the effective properties of the anisotropic SFRP by performing a finite element (FE) simulation. The first step is performed using the FE solver COMSOL. Next, the tensor properties, specifically, stiffness, thermal conductivity, CTE, and strength, of the underlying unidirectional SFRP are predicted using MATLAB functions written in-house. Step 3 is executed in MATLAB, while step 4 involves pairing COMSOL and MATLAB via LiveLinkTM so that COMSOL can call custom-written MATLAB functions.

Several constituent material properties are needed for modeling the stiffness, strength, and thermal properties of the SFRP. The properties needed by the models are shown in the computational flow charts in Figures 3.1 and 3.2 for the thermal and mechanical properties, respectively. Table 3.1 gives the values of the properties used and the references where the properties were obtained. These properties were chosen to match those of the SFRP that was used in the experimental portion of this dissertation, a 13% by weight carbon-fiber-filled acrylonitrile butadiene styrene (13% CF-ABS) from PolyOne (now known as Avient) [117]. Since the specific grade of carbon fibers and ABS in the PolyOne mixture is unknown, these properties were based on carbon fiber and ABS properties found from various sources which are listed in Table 3.1.

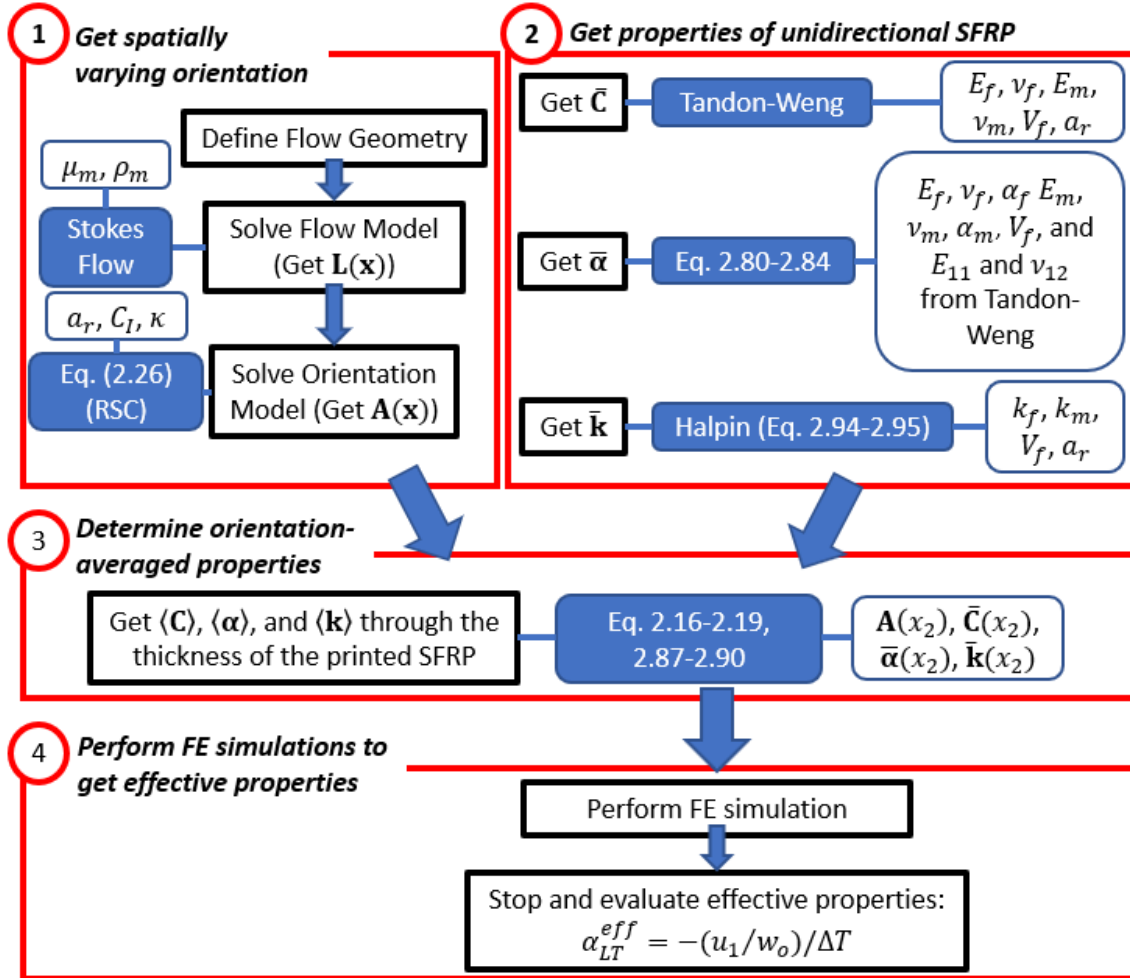


Figure 3.1: Flow chart of the thermal property computational methodology.

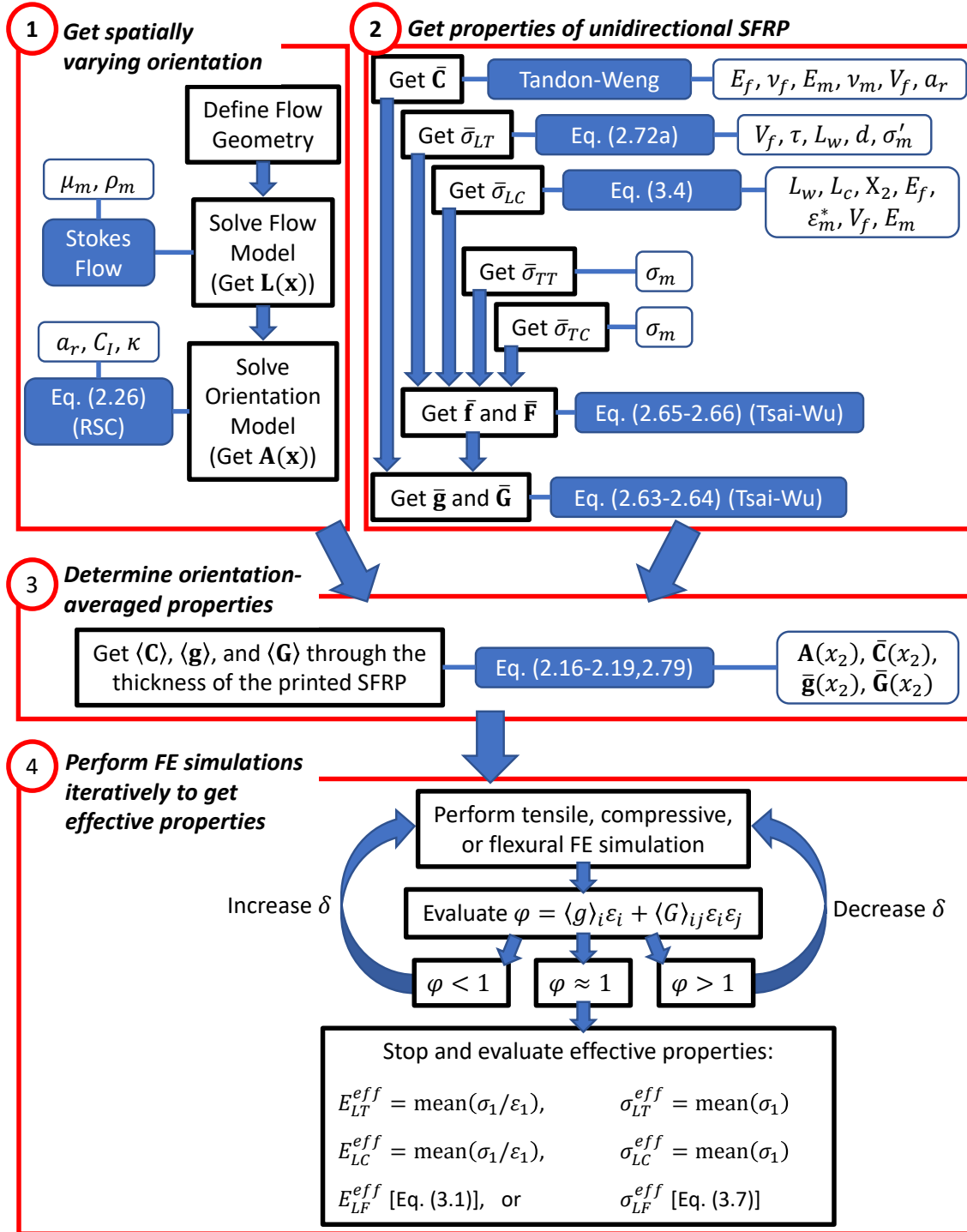


Figure 3.2: Flow chart of the stiffness and strength computational methodology.

Table 3.1: Properties of ABS Matrix and Carbon Fiber Used for Modeling.

Property	ABS Matrix	Ref.	Carbon Fiber	Ref.
Elastic Modulus (GPa)	$E_m = 2.41$	[118]	$E_f = 218$	[87]
Poisson's Ratio	$\nu_m = 0.35$	[119]	$\nu_f = 0.26$	[87]
Density (kg/m ³)	$\rho_m = 1040$	[118]	$\rho_f = 1760$	[120]
Dynamic Viscosity (Pa·s)	$\mu_m = 3200$	[121]	-	-
Linear CTE (10 ⁻⁶ /°C)	$\alpha_m = 90$	[121]	$\alpha_f = -2.6$	[109]
Thermal Conductivity ($\frac{W}{m \cdot K}$)	$k_m = 0.176$	[119]	$k_f = 8.00$	[120]
Tensile Yield Strength (MPa)	$\sigma_m = 37.9$	[118]	$\sigma_f = 6024$	[87] [*]
Compressive Yield Strain ($\frac{m}{m}$)	$\epsilon_m^* = 0.04$	[122]	-	-
Stress "at fiber failure strain" (MPa) [87]	$\sigma'_m = 24$	[87, 120, 123]	-	-
Shear Strength (MPa)	$\tau = 21.9$	[87] [*]	-	-
Fiber length (μm)	-	-	$L_f = 279$	4.2.1 ^{**}
Fiber Diameter (μm)	-	-	$d_f = 7.20$	4.2.1 ^{**}
Geometric Aspect Ratio	-	-	$a_r = 38.8$	4.2.1 ^{**}
Ellipsoidal Aspect Ratio	-	-	$r_e = 25.0$	[43] [*]
Critical Fiber Length (μm)	-	-	$L_c = 835$	[87] [*]
Fiber Weight Fraction	-	-	$w_f = 0.13$	[117]
Fiber Volume Fraction	-	-	$V_f = 8.11\%$	e.g. [25] [*]

^{*}These references are for the equations used to calculate the property, not necessarily for the property itself.

^{**}4.2.1 refers to Section 4.2.1 of this dissertation.

3.1.1 Modeling the Fiber Orientation through a LAAM Nozzle

The models chosen for predicting the fiber orientation are the IRD (Equation 2.24), since it has been well received in industry, and the RSC (Equation 2.26), because of its two-parameter ability to tune the orientation predictions. The anisotropic rotary diffusion model [64] could be used in the future but requires more tuning parameters to be determined and will thus not be pursued here. The assumption that the fibers are rigid in Jeffery-based models like the IRD and RSC is a reasonable assumption when dealing with “short” fibers (e.g., [63]). Here, a glass fiber with a diameter of $15\text{ }\mu\text{m}$ is considered “short” if it is less than 1 mm and “long” if it is greater than 1 mm (e.g., [124] as cited in [73]). In other words, “short” glass fibers have aspect ratios less than 67. The carbon fibers in this study have an aspect ratio of 38.8, which is less than 67, and are considerably stiffer than glass fibers. Thus, the rigid fiber assumption is acceptable to use in this dissertation.

The fiber orientation state within an SFRP affects the viscosity of an SFRP as it is being processed and therefore the velocity profile as well. Thus, the internal fiber orientation state within an SFRP that is being processed and the viscosity of that SFRP are coupled. While fully-coupled studies have been performed (e.g., [70, 71]) and have the potential to predict the orientation state more accurately, in practice, the coupling of the orientation and flow has often times been neglected to simplify the orientation analysis. Thus, in this section, the flow and orientation problems are decoupled. That is, the flow is first modeled as if the fibers do not exist, then the fiber orientation is calculated based on that flow profile.

To further reduce the computational efforts required, a two-dimensional planar flow model is considered rather than a three-dimensional model. The geometry is shown in Figure 3.3 and includes the tip of the LAAM nozzle as well as the deposition onto the print bed. The internal dimensions of the nozzle tip are based on the dimensions of a Strangpresse Model 19 extruder, the extruder on Baylor’s physical

LAAM system which is discussed in Section 4.1.1. The geometry for this model was generated by Heller using his die-swell shape optimization method given in [125].

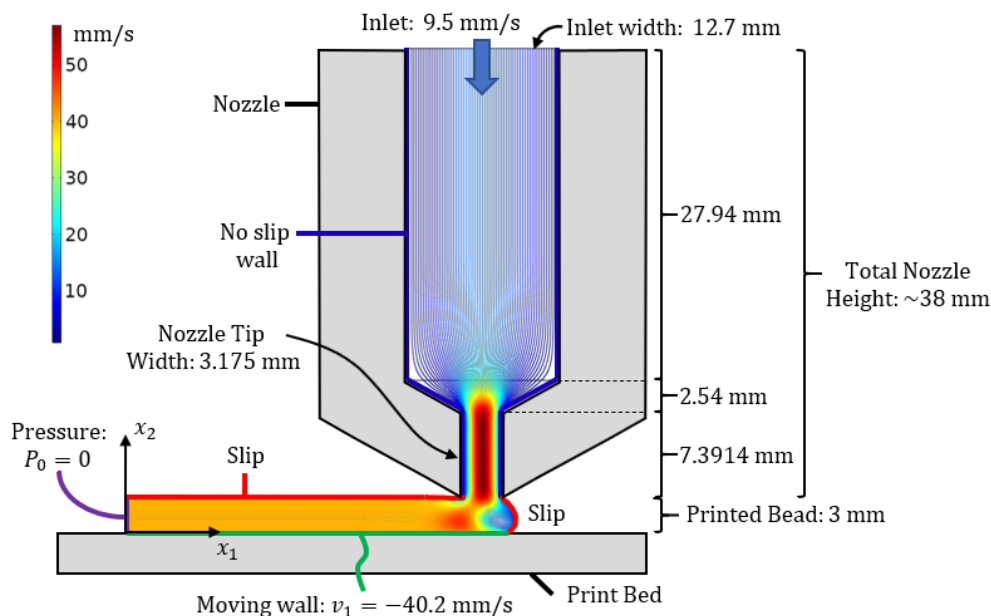


Figure 3.3: COMSOL planar deposition finite element flow model for the polymer melt at the tip of a LAAM-nozzle.

Wang and Smith [126] investigated using various rheology models for predicting the orientation state in a LAAM-nozzle flow, including viscoelastic, Newtonian, and generalized Newtonian models. When combined with the Tandon-Weng micromechanics model and an orthotropic closure, Wang and Smith's methods led to predictions of the elastic modulus in the flow direction that were within one standard deviation of the experimental average from a separate study [126]. This was true of all of the rheology models studied, including the Phan-Thien-Tanner, Carreau-Yasuda, Power law, Simplified Viscoelastic, and Newtonian models [126]. A Newtonian flow was considered for the model shown in Figure 3.3 since it is reasonably accurate and simple. However, although Wang and Smith did not experimentally validate the orientation state predicted by the various models they studied, it is possible that viscoelastic or generalized Newtonian models may lead to more accurate orientation predictions in future studies.

Thus, the flow in Figure 3.3 is modeled as a Newtonian fluid undergoing Stokes flow, ignoring inertial effects. The density and dynamic viscosity properties of the flow are taken from Table 3.1 to be $\rho_m = 1040 \text{ kg/m}^3$ and $\mu_m = 3200 \text{ Pa}\cdot\text{s}$. While these values affect the pressure in the flow domain, they have no bearing on the velocity field and thus do not make an actual difference in the predicted fiber orientation when using the IRD and RSC models.

The boundary conditions of the flow model include an average inlet flow velocity of 9.5 mm/s at the top of the flow domain, no slip walls inside the nozzle ($\mathbf{v} = \mathbf{0}$), slip walls on the exposed surface of the deposited bead except at the end ($\mathbf{v} \cdot \mathbf{n} = 0$, $2\mu \mathbf{Dn} - [(2\mu \mathbf{Dn}) \cdot \mathbf{n}] \mathbf{n} = \mathbf{0}$, where \mathbf{n} is the unit normal to the boundary), a moving wall at the base of the deposited bead moving at 40.2 mm/s (95 in/min) in the $-x_1$ direction, and a zero pressure outlet condition at the end of the deposited bead with normal flow and suppressed backflow constraints. Although the Baylor LAAM system has a stationary table and an extruder that moves in the x_1 , x_2 , and x_3 directions, the moving wall boundary condition for the print bed is acceptable since it specifies the speed at which the nozzle and print bed move *relative* to one another.

A mesh is generated by COMSOL's physics-controlled mesh generator for the FE simulation. This mesh consists of 15,961 domain elements including 15,400 triangular and 561 quadrilateral elements so that a dense solution can be obtained. Next the velocities and velocity gradients are plotted in COMSOL along a user-defined number of streamlines. The streamline paths in the COMSOL flow models in this dissertation are automatically generated by COMSOL. The plotting information i.e., the velocity data (v_1 and v_2) and velocity gradient data (L_{11} , L_{12} , L_{21} , L_{22} where $L_{ij} = v_{i,j} = \frac{\partial v_i}{\partial x_j}$) along the streamlines, is then exported so that it can be used in the IRD and RSC models to obtain the orientation state \mathbf{A} . The velocity gradient data enters these models through the vorticity, \mathbf{W} , and rate of deformation, \mathbf{D} , tensors as

discussed in Section 2.3.1 and the velocities are needed to calculate the time steps for the ordinary differential equation (ODE) solver. MATLAB’s “ode45” solver is used to solve the IRD (Equation 2.24) and RSC (Equation 2.26) models, programmed in-house as MATLAB functions.

3.1.2 *Stiffness Prediction*

The Tandon-Weng model [85] is used for modeling the stiffness of the underlying unidirectional SFRP, $\bar{\mathbf{C}}$, using Equations 2.35 and 2.37-2.41. Next, the spatially varying orientation-averaged stiffness $\langle \mathbf{C} \rangle$ is found as a function of the orientation tensors and space using Equation 2.17. At this point, the $\langle \mathbf{C} \rangle$ tensors can be inverted to obtain the spatially varying compliance, $\langle \mathbf{S} \rangle$, and then, using Equation 2.35, the spatially varying elastic moduli can be extracted and plotted.

While insight into the spatially varying stiffness behavior is interesting, these properties cannot be confirmed by simple experiments. The next step therefore is to obtain the effective stiffness properties of a printed SFRP bead by performing finite element simulations. The effective stiffness properties are also found using the laminate analogy approach in Section 3.2.6 for comparison purposes. The geometries and boundary conditions for three finite element models, one for tension, one for compression, and one for flexure/bending, are given in Figure 3.4. For each of these specimens, the fiber orientation state is assumed to vary only through the x_2 (thickness) direction and is equivalent to the orientation along the end of the printed bead shown in Figure 3.3. Thus, the orientation-averaged stiffness tensor properties only vary through the thickness of the specimens in Figure 3.4. It is worth noting that because of this, the lengths of the tensile and compressive specimens are inconsequential in predicting the properties of the printed material. Therefore, although the lengths were chosen based on anticipated experimental setups, the process of predicting the properties could potentially be expedited in the future by

using considerably shorter finite element geometries with less elements along the x_1 direction. For each of the models, a deformation of δ , in mm, is prescribed. In addition, only half of the flexural specimen is modeled since it is symmetric.

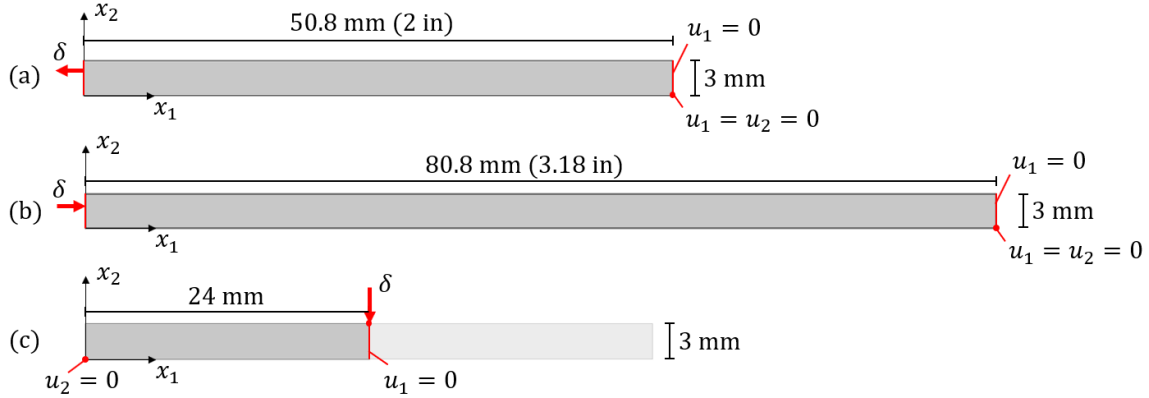


Figure 3.4: Finite element geometries with boundary conditions: (a) tensile specimen, (b) compression specimen, (c) flexural specimen.

After performing the displacement/deflection prescribed tensile, compressive, and flexural simulations, the effective stiffness properties are found according to the following post-processing methods. For the tensile simulations, the effective longitudinal tensile stiffness, E_{LT}^{eff} , is obtained by taking the average of σ_1/ϵ_1 along the right edge of the specimen. The effective longitudinal compressive stiffness, E_{LC}^{eff} , is found in an analogous manner for the compressive simulations. For the flexural/bending simulations, the maximum stress occurs in the center of the specimen in three-point bending. Although the specimen has regions dominated by tensile stresses and regions dominated by compressive stresses, the tensile stresses control the failure of the studied material system in the present configuration. Therefore, the effective flexural strength, σ_{LF}^{eff} , discussed in detail in the next section, is evaluated at the bottom, right corner of the symmetric FE flexural specimen. This corresponds to the bottom, center of the real flexural specimen. For simplicity, the effective flexural stiffness, E_{LF}^{eff} , is also evaluated at this point. Three-point bend testing according to ASTM D790-17 [127] is often performed to determine flexural

behavior of a composite. According to this standard,

$$E_{LF}^{eff} = \frac{L_s^3 m}{4wt^3} \quad (3.1)$$

where L_s is the length of the support span (48 mm), m is the slope of the elastic portion of the load-deflection curve, w is the width of the specimen (taken to be 9 mm), and t is the thickness of the specimen (3 mm). Assuming the load and deflection both start at 0, the slope m is determined by the load and deflection at failure, P and δ , (which are determined for the flexural strength calculation in the next section)

$$m = P/\delta \quad (3.2)$$

The above methods for predicting the effective stiffness properties are valid while the material is behaving elastically. Therefore, the stiffness properties are predicted for δ values less than or equal to the δ values that correspond to yield strain. It is also noted that the δ values that correspond to yield strain are found when predicting the effective yield strengths of the SFRP as discussed in the next section. In Section 3.2.3, an analysis on the proper mesh size for the finite element simulations is performed.

3.1.3 Strength Prediction

For the strength prediction, the Van Hattum-Bernardo method is used. However, rather than use the Hill criterion (Equation 2.68), the more general form for the strength tensors given in Equations 2.65-2.66 are used so that independent values of tensile and compressive strength can be predicted. As mentioned earlier, using this form requires obtaining the contracted strength tensors $\langle g \rangle_i$ and $\langle G \rangle_{ij}$. The second order tensor $\langle g \rangle_i$ is found by Equations 2.16 and 2.18 and $\langle G \rangle_{ij}$ is found by Equations 2.17 and 2.19. In addition, the fiber strength and critical fiber length are calculated using Equations 2.74 and 2.75.

The components of $\langle g \rangle_i$ and $\langle G \rangle_{ij}$ must also be defined. The interaction terms of DeTeresa and Larsen are chosen since they are simple forms and were found to be reasonable for a carbon fiber composite [107]:

$$F_{12} = -\frac{1}{4}F_{11}, \quad F_{23} = -F_{22} \quad (3.3)$$

This leaves five independent components in Equations 2.65-2.66, namely, $\bar{\sigma}_{LT}$, $\bar{\sigma}_{LC}$, $\bar{\sigma}_{TT}$, $\bar{\sigma}_{TC}$, and $\bar{\tau}$. It will be seen in the experimental section of this dissertation that the weight-average fiber length, L_w , in the 13% CF-ABS bead deposited by Baylor's LAAM system is considerably less than the critical fiber length, L_c . Also, since Van Hattum and Bernardo found that using a single average fiber length yields similar results to a fiber length distribution, Equation 2.72a with L replaced by L_w is appropriate for this study and is chosen to obtain $\bar{\sigma}_{LT}$. To get $\bar{\sigma}_{LC}$, we modify Equation 2.56 in a similar way as Bajracharya et al. [90], except without including the fiber orientation factor

$$\bar{\sigma}_{LC} = \chi_2 E_f \epsilon_m^* V_f + (1 - V_f) \sigma_m^* \quad (3.4)$$

where $\chi_2 = L_w / (2L_c)$. Similarly to the case for predicting $\bar{\sigma}_{LT}$, Equation 3.4 is valid if $L_w \leq L_c$ and all the fibers are assumed to have a uniform length of L_w . The assumptions of Van Hattum and Bernardo for the matrix dominated properties are made in this study as well, namely, $\bar{\sigma}_{TT} = \bar{\sigma}_{TC} = \sigma_m$, and, assuming the matrix is isotropic, $\bar{\tau} = \sigma_m / \sqrt{3}$.

All of the terms have been defined to now use the orientation-averaged Tsai-Wu failure criterion (Equation 2.76). The same finite element models used to determine the effective stiffness properties of the SFRP bead are used for determining the strength properties as well. However, determining the strength is not as easy as stiffness since a prescribed deformation δ must be found to satisfy Equation 2.76. If we let

$$\varphi(\epsilon) = \langle g \rangle_i \epsilon_i + \langle G \rangle_{ij} \epsilon_i \epsilon_j \quad (3.5)$$

where each of the terms in the above equation are functions of spatial location, \mathbf{x} , then employing the Tsai-Wu failure criterion involves finding a δ such that a strain state ε_i is produced that satisfies $\max[\varphi(\boldsymbol{\varepsilon}, \mathbf{x})] = 1$ at some spatial location \mathbf{x} . In this work, this is accomplished by performing a parameter sweep over δ until a δ value is found that leads to $1 \leq \max[\varphi] < 1.01$. A more sophisticated optimization algorithm could be employed in a future study if computational savings were a concern, but that is out of the scope of the current efforts. A reasonable guess for the initial displacement in the tensile and compressive simulations can be found by solving for the displacement as if all the strain was in the x_1 direction, i.e., solving $\langle g \rangle_1 \varepsilon_1 + \langle G \rangle_{11} \varepsilon_1 \varepsilon_1 = 1$ for δ_o where $\delta_o = L_s \cdot \varepsilon_1$ and L_s is the length of the specimen. This leads to

$$\delta_o = L_s \cdot \max \left(\frac{-\langle g \rangle_1 \pm \sqrt{\langle g \rangle_1^2 + 4 \langle G \rangle_{11}}}{2 \langle G \rangle_{11}} \right) \quad (3.6)$$

Once δ is found so that $\varphi \approx 1$ for the three loading scenarios, the effective strengths of the deposited bead can be evaluated. For the tensile test simulation, the average σ_1 along the right edge of the specimen is taken to be the effective longitudinal tensile strength, σ_{LT}^{eff} , of the deposited SFRP bead. For the compressive test simulation, the effective longitudinal compressive strength, σ_{LC}^{eff} , is found in the same manner. The flexural strength can be found using

$$\sigma_{LF}^{eff} = \frac{3PL_s}{2wt^2} \quad (3.7)$$

where, as before, P is the load at failure, L_s is the span width, w is the specimen width, and t is the specimen thickness (e.g., [127]). Equations 3.1 and 3.7 do not fully describe the complex, spatially varying stiffness and strength properties within the material, but they can be used to compare the flexural behavior of different material systems.

3.1.4 CTE Prediction

The effective longitudinal CTE, α_{LT}^{eff} , of a LAAM-made SFRP bead is also predicted using a FE simulation. Camacho and Tucker's form [113] for the orientation-averaged CTE tensor (Equation 2.87) is used to predict the CTE tensor through the thickness of the printed bead, assuming that the orientation state varies only through the thickness and that it is equal to that at the end of the printed bead shown in Figure 3.3. The FE geometry and boundary conditions used for predicting α_{LT}^{eff} are shown in Figure 3.5. As a post-processing step, the effective longitudinal CTE is evaluated using

$$\alpha_{LT}^{eff} = \text{mean} [-(u_1/w_o)/\Delta T] \quad (3.8)$$

where the mean is taken along the left edge of the specimen, u_1 is the resulting x_1 -displacement of the left side of the CTE specimen due to the temperature change (the negative sign ensures α_{LT}^{eff} is positive), w_o is the specimen length in the x_1 direction, and $\Delta T = 1^\circ\text{C}$ is the applied temperature.

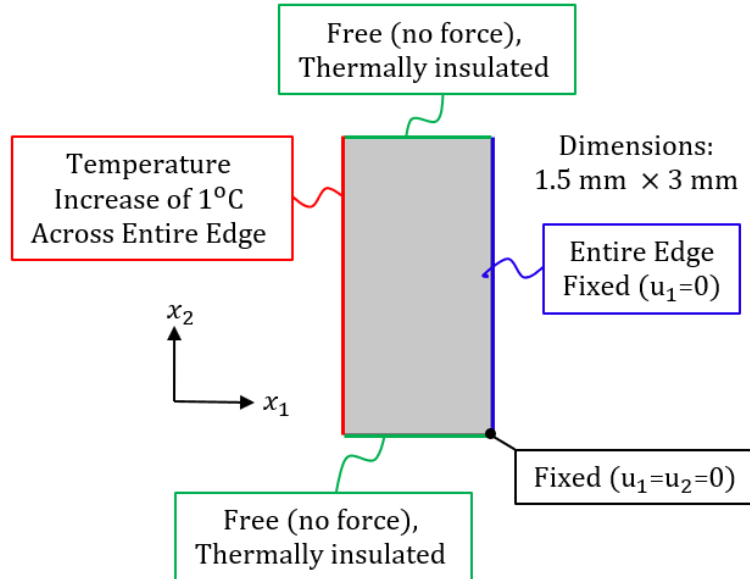


Figure 3.5: Finite element geometry with boundary conditions for CTE specimen.

3.2 Modeling Results

In this section, the results of the predicted fiber orientation state in the LAAM-made bead from the IRD and RSC models will be shown. This is followed by a study on the spatially-varying stiffness and CTE in a LAAM-printed bead. Next, a mesh size analysis is performed before analyzing effective stiffness, CTE, and strength properties in depth, in which a large amount of computational effort is required but can be mitigated by selecting a mesh that is course enough to save on computational time but fine enough to achieve reasonably refined predictions. A laminate analogy approach to predicting stiffness properties is also presented and compared to the presented methodology.

3.2.1 Fiber Orientation in a LAAM Bead

The spatially varying fiber orientation state throughout the flow domain is shown in Figure 3.6. Since typical values of the slowness parameter for short-fiber thermoplastics are $\kappa = 0.05\text{-}0.2$ [44] (as cited in [64]), the middle value of $\kappa = 0.125$ was used along with $C_I = 0.0019$ from Bay’s formula (Equation 2.25) to generate Figure 3.6 using the RSC model. In addition, the initial orientation state was chosen to be completely random, $A_{ij} = \frac{1}{3}\delta_{ij}$, and $a_r = 38.8$. To obtain these plots, A_{ij} was found along $N = 31$ streamlines. For Figures 3.6a and 3.6b, a course quadrilateral mesh was then constructed and values of A_{ij} were found at the centroids of each quadrilateral element by linearly interpolating the solution. The ellipsoidal representation of A_{ij} as discussed in Section 2.3.2 was used to create Figure 3.6a. The orientation representation of A_{ij} in Figure 3.6b involves directing a line segment parallel to the principal direction of A_{ij} and then scaling it by its corresponding eigenvalue. The orientation representations of A_{ij} in Figures 3.6a and b were both inspired by Advani [2]. An alternative approach to plotting the orientation state across a 2D surface is by plotting the components of A_{ij} as color plots as in Figures

3.6c and 3.6d. The color plots were generated in COMSOL by calling custom-made MATLAB functions.

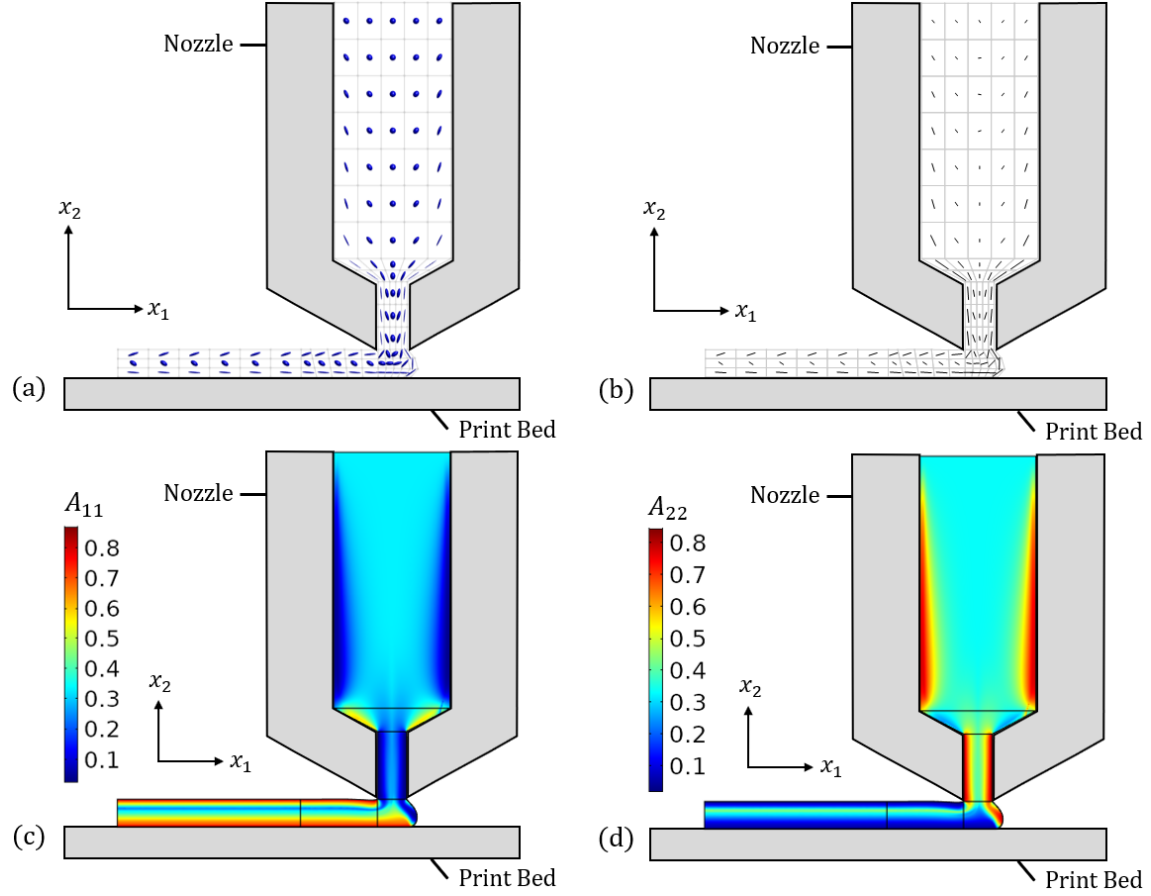


Figure 3.6: Planar orientation results. Used initial $A_{ij} = \frac{1}{3}\delta_{ij}$, $a_r = 38.8$, $C_I = 0.0019$, $\kappa = 0.125$, and $N = 31$.

The next analysis parallels work done by the author in [121], of which the present author retains the copyright under a Creative Commons CC BY 4.0 license, but some parameters have been updated to be more consistent with the other analyses in this dissertation. The analysis referred to compares results between the IRD and RSC models along a streamline, at the exit of the nozzle, and at the end of the deposited bead.

The second order orientation tensor was predicted along streamline 15 of $N = 61$ streamlines using both the IRD and RSC models with an initial random orientation state ($A_{ij} = \frac{1}{3}\delta_{ij}$), $a_r = 38.8$, $C_I = 0.0019$, and, for the RSC alone,

$\kappa = 0.125$. Figure 3.7 shows the results. Streamline 15 begins at the nozzle inlet, approximately half-way between the left edge and center of the nozzle. It is noteworthy that the random initial orientation state does not affect the IRD predictions in Figure 3.7a as much as the RSC predictions in Figure 3.7b. The RSC predictions are clearly dependent on the initial orientation state due to the slow rate of change in the alignment. This gives evidence that proper identification of the initial orientation state prior to the nozzle tip is important if the RSC model is to be used in industrial applications. This conclusion is corroborated again later in Figure 3.10.

Specific points of interest along the flow path have also been highlighted in Figure 3.7. Of special interest are when the flow reaches the nozzle exit and when it reaches the end of the bead. At the nozzle exit, the IRD model predicts a relatively high x_2 alignment and low x_1 alignment. After deposition at the bead end, however, the IRD model predicts relatively high x_1 alignment and low x_2 alignment, but the difference between A_{11} and A_{22} is not as extreme as it is at the nozzle exit. In other words, the tapered nozzle apparently induces rapid fiber alignment in the flow direction according to the IRD model, but after deposition, although the fiber alignment is still mostly in the flow direction, the alignment in the flow direction is not quite as high as it is at the nozzle exit. Thus, the incorporation of the die-swell and deposition in the flow model does make a difference for the IRD model. Similar trends in the changing orientation state are visible for the RSC model in Figure 3.7b as in Figure 3.7a, but the rate of alignment is clearly predicted to be slower than that of the IRD.

For obtaining the orientation at the nozzle exit, A_{ij} must be predicted along several streamlines and the values of A_{ij} at the end of each streamline collected. This is done using the FE flow domain shown in Figure 3.8. The boundary conditions for the flow domain in Figure 3.8 are the same as those from the planar deposition model in Figure 3.3, except that the deposited bead is missing, so the slip wall and

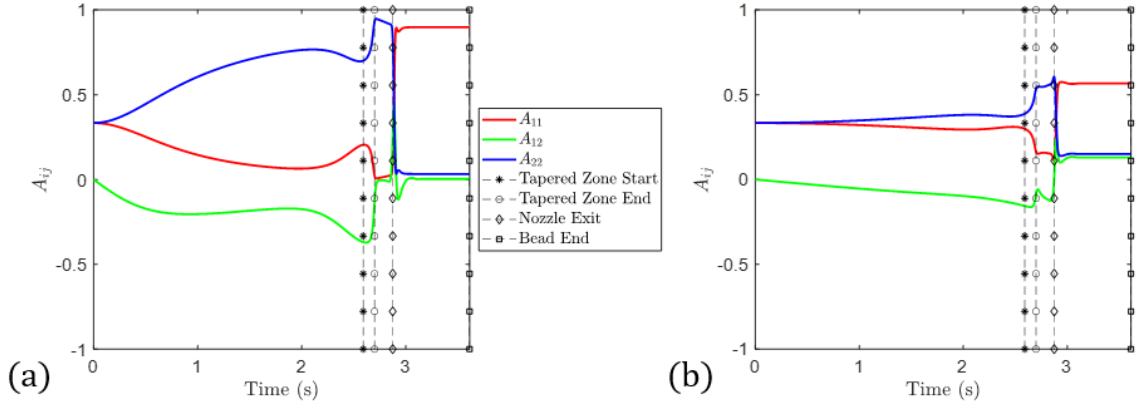


Figure 3.7: Orientation along streamline 15 predicted with (a) IRD model, and (b) RSC model.

moving wall boundary conditions are gone. In addition, a normal outflow condition is imposed at the nozzle exit in this model, thus, the results at the nozzle exit may differ from those that are obtained at the nozzle exit for the deposition model in Figure 3.3. The flow parameters are exactly the same as before i.e., initial $A_{ij} = \frac{1}{3}\delta_{ij}$, $a_r = 38.8$, $C_I = 0.0019$, $\kappa = 0.125$, and the number of streamlines $N = 61$. The resulting orientation states at the nozzle exit predicted using the IRD and RSC models are shown in Figures 3.9a and b, respectively.

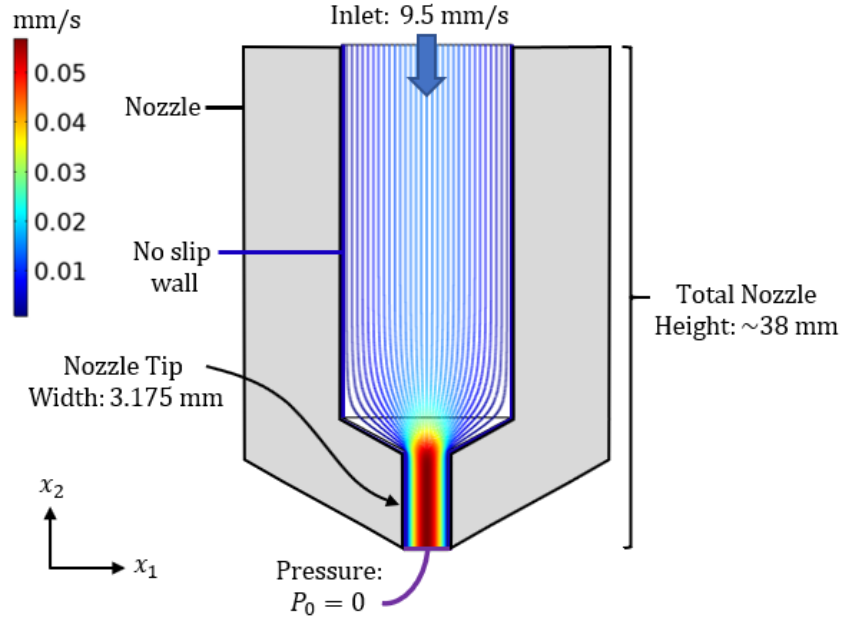


Figure 3.8: Color scheme indicates velocity magnitude.

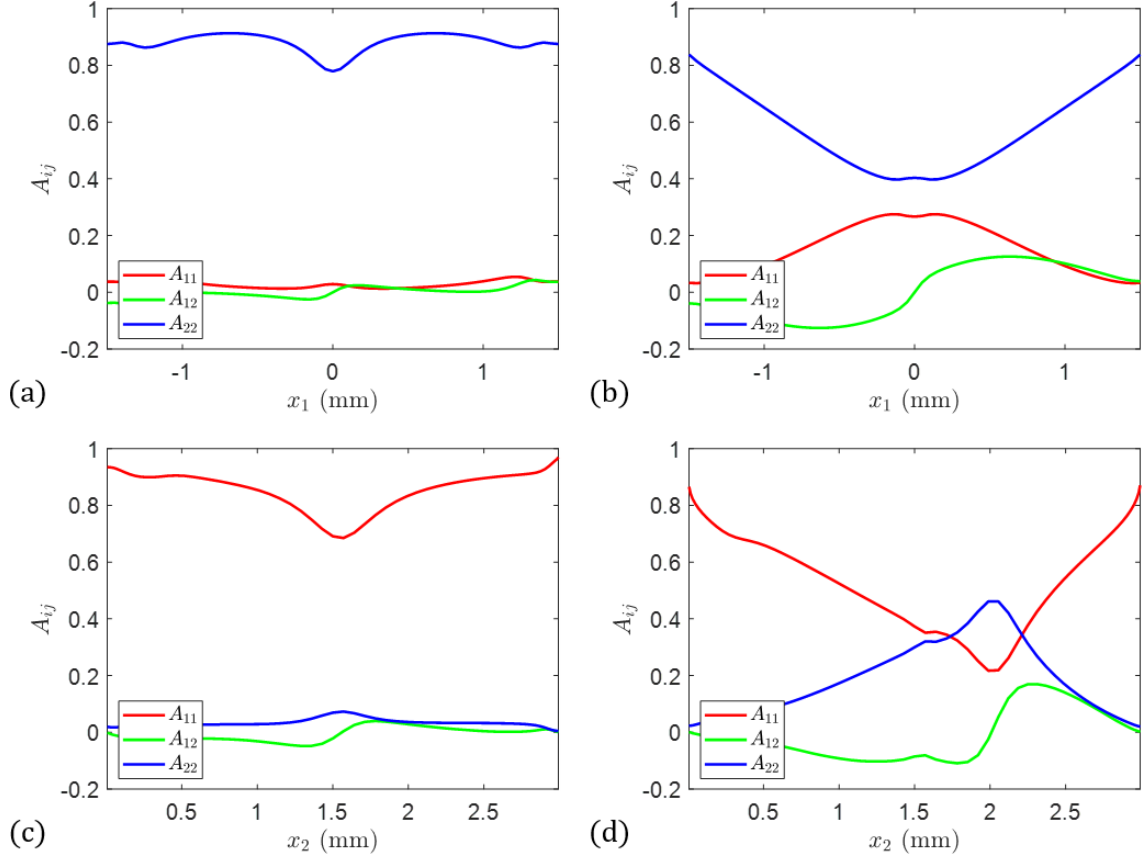


Figure 3.9: (a) $A_{ij}(x_1)$ at the nozzle exit predicted by the IRD model; (b) $A_{ij}(x_1)$ at the nozzle exit predicted by the RSC model; (c) $A_{ij}(x_2)$ at the bead end predicted by the IRD model; (d) $A_{ij}(x_2)$ at the bead end predicted by the RSC model. Used initial $A_{ij} = \frac{1}{3}\delta_{ij}$, $a_r = 38.8$, $C_I = 0.0019$, $\kappa = 0.125$, and $N = 61$.

Figures 3.9a and b show that A_{11} and A_{22} are predicted by both the IRD and the RSC models to be symmetric about x_2 at the nozzle exit. This should be expected since the nozzle is symmetric about $x_2 = 0$ up to the nozzle exit and the inlet condition is an average laminar inflow. A_{12} is not symmetric about $x_2 = 0$, however, since it contains the product of p_1 and p_2 according to Equation 2.7. This is consistent with the results shown in Figures 3.6a and b. The RSC model furthermore predicts much higher x_2 alignment along the sides of the nozzle as opposed to the center as shown in Figure 3.9b, which is due to the higher shear along the sides of the nozzle. Likely, the more random orientation state in the center of the nozzle is a result of the slowed orientation kinetics of the RSC model, as opposed to the faster

orientation kinetics predicted by the IRD model which appears to predict a more uniformly aligned orientation state as shown in Figure 3.9a.

Figures 3.9c and d show the orientation results for the IRD and RSC at the end of the deposited bead. These give evidence that inclusion of the die-swell and deposition sections of the flow model destroy the symmetry of the predicted orientation state. This effect is more pronounced when using the RSC model. Figures 3.9c and d do show that high alignment along the edges of the flow domain is preserved even after deposition though. Finally, Figures 3.9a-d demonstrate that while the average A_{22} through the thickness of the flow domain is higher than the average A_{11} through the thickness, after the polymer is deposited onto the build plate, the opposite is true: the average A_{11} is higher than the average A_{22} . This gives evidence that the orientation of the fibers tends to follow the flow direction of the extruded polymer. This is expected given the earlier analysis shown in Figure 3.7.

The next analysis was presented by the author in [128]. This analysis examines different initial conditions to see the effects of the initial orientation state on the orientation state that is predicted at the end of the printed bead. The first initial orientation condition considered is the completely random case,

$$\mathbf{A}_o = \frac{1}{3} \cdot \mathbf{I} = \begin{bmatrix} 1/3 & 0 & 0 \\ 0 & 1/3 & 0 \\ 0 & 0 & 1/3 \end{bmatrix} \quad (3.9)$$

where \mathbf{I} is the 3×3 identity tensor.

The second initial orientation is the “steady state” initial condition. This was found by defining an FE flow geometry that was a long (1 meter) channel with the same width as the nozzle inlet in Figure 3.3 and 3.8 (12.7 mm). The IRD model with $a_r = 38.8$, $C_I = 0.0019$, and $N = 61$ was then used to predict A_{ij} at the end of the channel, similarly to what was done to produce Figures 3.9a and b. The great length of the channel allows the orientation state to become steady before reaching the end,

thus giving a “steady state” orientation. This results in the following orientation tensor at the end of each streamline, except in the middle region,

$$\mathbf{A}_o = \begin{bmatrix} 0.0373 & A_{12} & 0 \\ A_{12} & 0.8748 & 0 \\ 0 & 0 & 0.0880 \end{bmatrix} \quad (3.10)$$

where $A_{12} = -0.0373$ on the left side of the nozzle, ≈ 0 in the center, and 0.0373 on the right. Heller used a similar approach to get a steady state initial orientation condition for a similar flow [115].

Two other initial orientation states considered are a highly x_2 -aligned state (Equation 3.11) and a state that is random in the x_1 - x_3 plane (Equation 3.12):

$$\mathbf{A}_o = \begin{bmatrix} 0.05 & 0 & 0 \\ 0 & 0.9 & 0 \\ 0 & 0 & 0.05 \end{bmatrix} \quad (3.11)$$

$$\mathbf{A}_o = \begin{bmatrix} 1/2 & 0 & 0 \\ 0 & 0 & 0 \\ 0 & 0 & 1/2 \end{bmatrix} \quad (3.12)$$

Figure 3.10 shows the results of using various initial orientation states. A_{11} and A_{22} are shown as functions of x_2 (the bead thickness direction) at the end of the printed bead for both the IRD and RSC models. Changing the initial orientation state has a more dramatic effect on the RSC predictions than the IRD predictions. Consequently, Figure 3.10 highlights the importance of using a correct initial orientation state in the fiber orientation evolution equation.

Measurement of the initial orientation state has not been performed in this dissertation, so an initially random orientation state is chosen for most of the modeling that is performed hereinafter. However, Wang and Smith have studied a 3D LAAM-nozzle flow model that takes into account upstream swirling effects induced

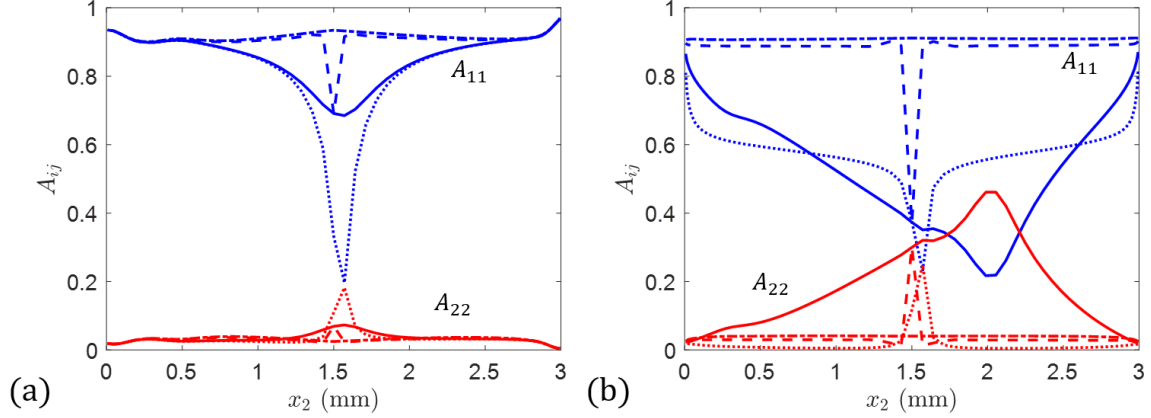


Figure 3.10: A_{11} (blue) and A_{22} (red) at the end of a LAAM-printed bead using 4 different initial orientation conditions: completely random (solid), steady state (dashed), highly aligned (dash-dot), and planar random (dotted). (a) IRD used with $a_r = 38.8$, $C_I = 0.0019$, $N = 61$. (b) RSC used with $a_r = 38.8$, $C_I = 0.0019$, $\kappa = 0.125$, $N = 61$.

by the extruder screw and found that the swirling effects make a significant difference, leading to higher stiffness in the flow direction [129]. Therefore, in future work, experimental verification of the actual orientation state prior to the tip of the LAAM-nozzle would be helpful so that \mathbf{A}_o might be chosen with more confidence.

3.2.2 Spatially-Varying Stiffness and CTE in a LAAM Bead

In this section, we discuss the results for the stiffness and CTE at the nozzle exit and the deposited bead, following the work of the author in [121]. These results are built on the orientation results given in Figure 3.9 which used an initial $A_{ij} = \frac{1}{3}\delta_{ij}$, $a_r = 38.8$, $C_I = 0.0019$, $\kappa = 0.125$, and $N = 61$. Select components of the fourth order, orientation-averaged stiffness tensor across the nozzle exit and across the deposited bead are shown in Figure 3.11.

There are noticeable similarities between Figures 3.9 and 3.11, with the stiffness in the x_1 and x_2 directions following the trends of the orientation in those directions i.e., $\langle C \rangle_{11}$ and $\langle C \rangle_{22}$ follow the trends of A_{11} and A_{22} , respectively. $\langle C \rangle_{22}$ is the dominant component of the stiffness tensor across the width of the nozzle at the nozzle exit on average, but $\langle C \rangle_{11}$ is the dominant component, on average, at the

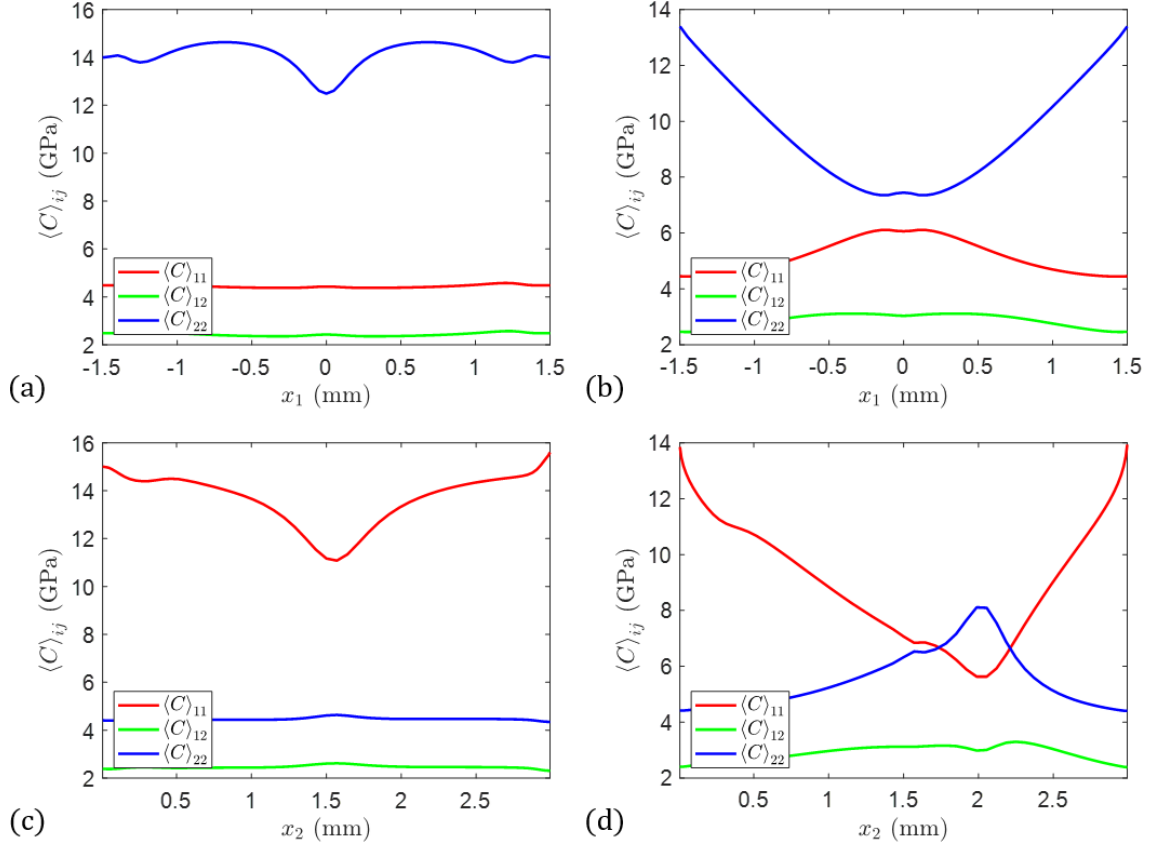


Figure 3.11: Components of the contracted stiffness tensor, $\langle C \rangle_{ij}$, through the flow domain. (a) $\langle C \rangle_{ij}(x_1)$ at the nozzle exit, predicted by the IRD; (b) $\langle C \rangle_{ij}(x_1)$ at the nozzle exit, predicted by the RSC; (c) $\langle C \rangle_{ij}(x_2)$ at the bead end, predicted by the IRD; (d) $\langle C \rangle_{ij}(x_2)$ at the bead end, predicted by the RSC. Used initial $A_{ij} = \frac{1}{3}\delta_{ij}$, $a_r = 38.8$, $C_I = 0.0019$, $\kappa = 0.125$, and $N = 61$.

end of the printed bead. Thus, the stiffness of the composite tends to be highest in the direction of the highest fiber alignment and lower in the transverse direction. Thus, it can be said that the direction of highest stiffness tends to be in the flow direction, like the fiber alignment.

Furthermore, the longitudinal elastic moduli, E_{11} and E_{22} , can be extracted from S_{11} and S_{22} of the compliance tensor, respectively, and are shown in Figure 3.12 through the thickness of the flow domain. These elastic constants follow similar but not identical trends as $\langle C \rangle_{11}$ and $\langle C \rangle_{22}$ in Figure 3.11 and, consequently, A_{11} and A_{22} in Figure 3.9.

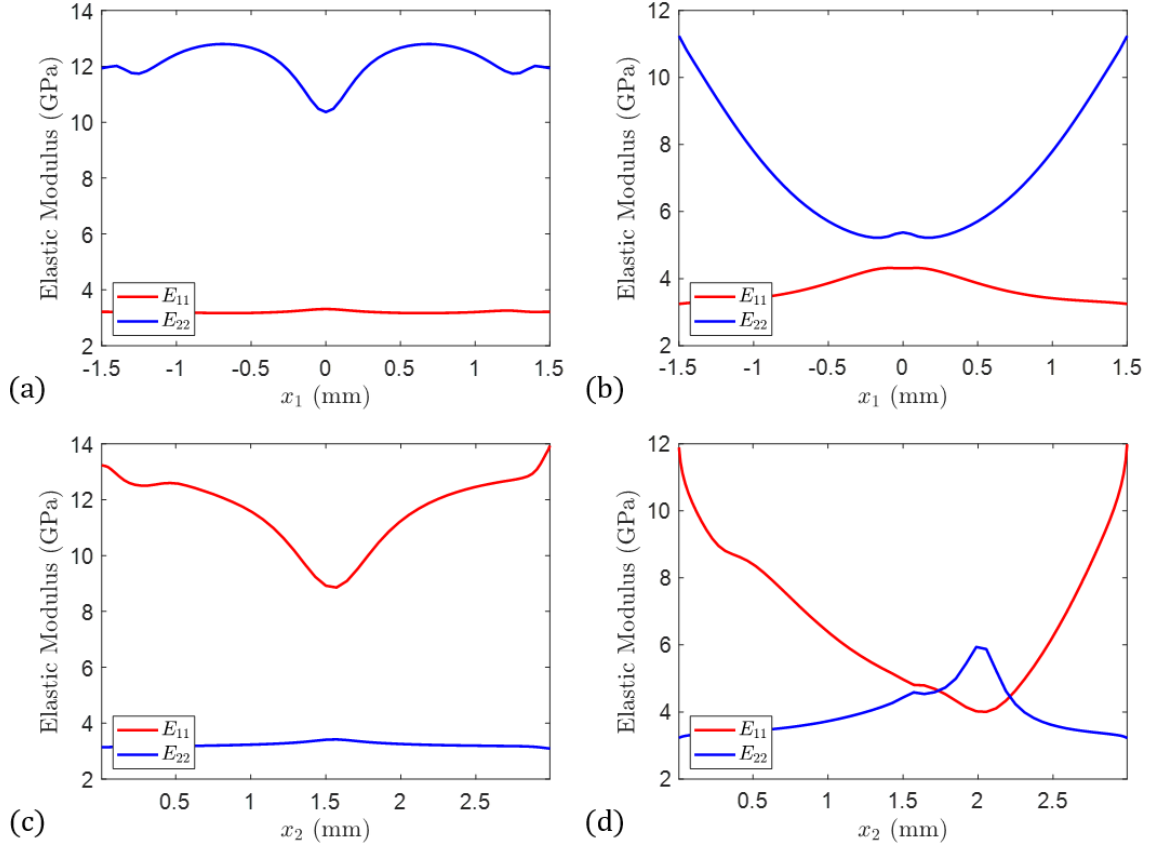


Figure 3.12: Elastic moduli through the flow domain. (a) At the nozzle exit, predicted by the IRD; (b) At the nozzle exit, predicted by the RSC; (c) At the bead end, predicted by the IRD; (d) At the bead end, predicted by the RSC. Used initial $A_{ij} = \frac{1}{3}\delta_{ij}$, $a_r = 38.8$, $C_I = 0.0019$, $\kappa = 0.125$, and $N = 61$.

The second order, orientation-averaged CTE tensor, $\langle \alpha \rangle_{ij}$, can also be determined across the width of the flow domain at the nozzle exit and the end of the printed bead. Figure 3.13 shows the results. Interestingly, $\langle \alpha \rangle_{11}$ is the dominant component of the CTE tensor at the nozzle exit and $\langle \alpha \rangle_{22}$ is the dominant component at the end of the deposited bead. Thus, the direction of highest fiber alignment is not the direction of highest CTE. This is due to the low CTE of the carbon fibers, which counteracts the higher CTE of the ABS matrix and decreases the overall CTE of the composite in the direction of highest fiber alignment. On the other hand, the direction transverse to the direction of highest fiber alignment has a relatively high CTE.

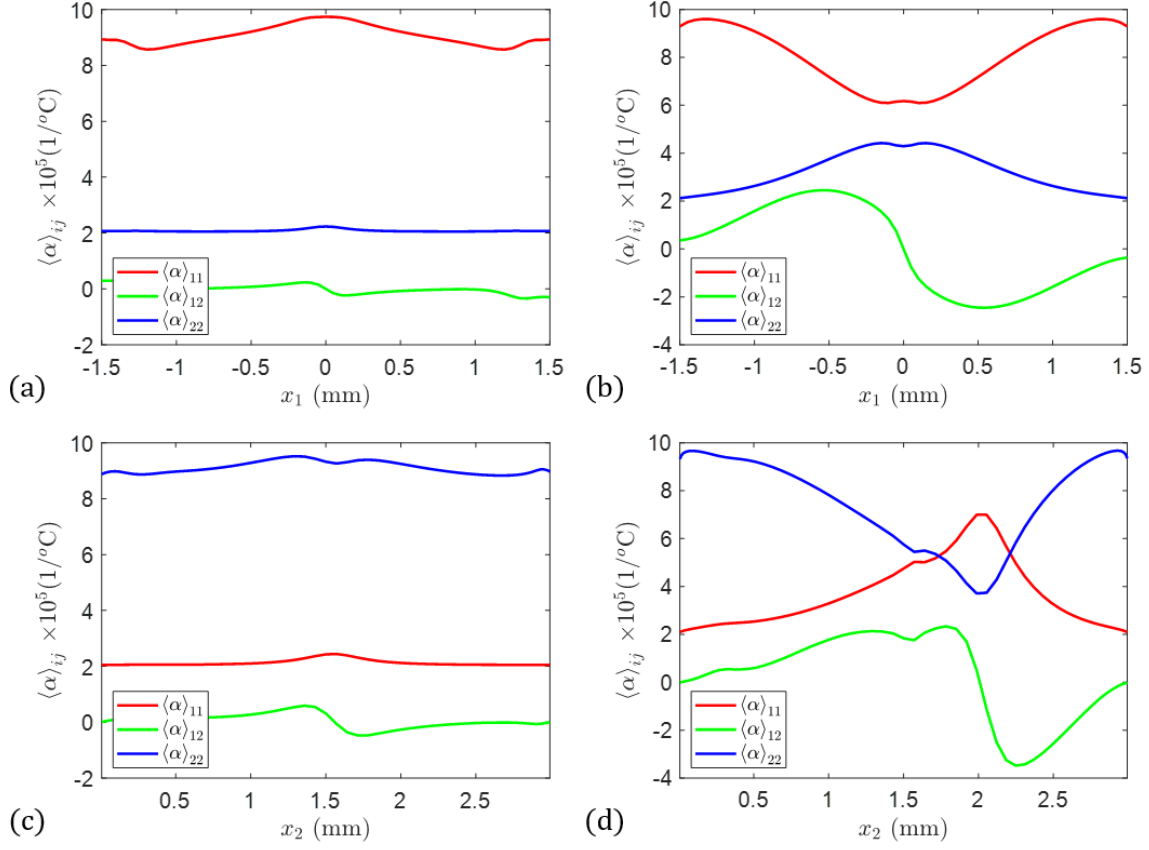


Figure 3.13: Components of the CTE tensor, $\langle \alpha \rangle_{ij}$, through the flow domain. (a) $\langle \alpha \rangle_{ij}(x_1)$ at the nozzle exit, predicted by the IRD; (b) $\langle \alpha \rangle_{ij}(x_1)$ at the nozzle exit, predicted by the RSC; (c) $\langle \alpha \rangle_{ij}(x_2)$ at the bead end, predicted by the IRD; (d) $\langle \alpha \rangle_{ij}(x_2)$ at the bead end, predicted by the RSC. Used initial $A_{ij} = \frac{1}{3}\delta_{ij}$, $a_r = 38.8$, $C_I = 0.0019$, $\kappa = 0.125$, and $N = 61$.

3.2.3 Mesh Size Analyses

Before moving on with analyzing the predicted properties of the printed bead, appropriate meshes for the tensile, compressive, flexural, and CTE specimens should be established. Since the geometries of each of the tensile, compressive, flexural, and CTE specimens are rectangles, rectangular elements are used for each of their FE models. In addition, the number of elements in the x_2 (thickness) direction should correspond to the number of streamlines, N , used in the flow analysis to utilize the full resolution of the flow solution. Thus, a flow simulation with N streamlines is conducted before simulating any tensile, compressive, flexural, or CTE

tests with $N_{x2} = N$ elements in the specimens' x_2 direction. The elements of each specimen are distributed in the x_2 direction such that their nodes are located halfway between where the streamlines are located in the flow simulation. This leads to thinner elements near the top and bottom of the bead as shown in Figure 3.14. The number of elements along the x_1 direction, N_{x1} , also needs to be determined for each specimen. These are distributed evenly along the length of each of the specimens.



Figure 3.14: Non-uniform distribution of elements in x_2 direction for tensile, compressive, flexural, and CTE FE meshes. Note, $N_{x2} = N = 13$ for conciseness.

The effective stiffness and strength properties for specimens with $N_{x2} \times N_{x1}$ meshes were evaluated for several combinations of N_{x2} and N_{x1} . The solutions for E_{LT}^{eff} , σ_{LT}^{eff} , E_{LC}^{eff} , σ_{LC}^{eff} , E_{LF}^{eff} , and σ_{LF}^{eff} showed little improvement beyond $N_{x2} \approx 30$ and $N_{x1} \approx 120$. In fact, there was less than 0.5% error for each of these values when the mesh was increased from 31×121 to 61×151 , where

$$\% error = \left| \frac{value_2 - value_1}{value_1} \right| \times 100\% \quad (3.13)$$

and $value_1$ is a property found using the finer mesh and $value_2$ is the corresponding property found using the courser mesh. For predicting α_{LT}^{eff} , $N_{x2} = 31$ and $N_{x1} = 11$ led to a solution with less than 0.1% error compared to the solution for $N_{x2} = 61$ and $N_{x1} = 121$. Therefore, $N_{x2} = 31$ and $N_{x1} = 121$ were chosen for the tensile, compressive, and flexural models and $N_{x2} = 31$ and $N_{x1} = 11$ were chosen for the CTE models. These mesh sizes were used for the remaining analyses in this chapter, unless otherwise noted.

3.2.4 Effective Stiffness and CTE in a LAAM Bead

The effective, longitudinal stiffness and CTE properties are predicted and studied as to their dependence on the following factors: the interaction model, the degree of fiber interaction C_I , the amount of slowness κ , and whether or not the die swell and deposition is included in the analysis. Results for these deterministic models are given in Table 3.2. The results for the deposited bead were found using the FE tensile test simulation depicted in Figure 3.4a with a displacement of $\delta = 0.01$ mm and the FE CTE test simulation depicted in Figure 3.5 with an applied temperature of 1°C . Similar models were used to obtain results for the nozzle exit, however, these models were oriented vertically and the sample widths were 3.175 mm rather than 3 mm to match the width of the nozzle. The work in this section follows that presented by the present author in [121], of which the present author retains the copyright. For comparison purposes, the present author experimentally determined $\alpha_{LT}^{eff} = 54.3 \times 10^{-6}/^\circ\text{C}$ for the 13% CF-ABS in [130] and experimental values for E_{LT}^{eff} are given in Chapter Four of this dissertation.

To help analyze the results, which are presented in Table 3.2, the percent relative difference (PRD) is defined as

$$PRD \equiv \frac{|value_1 - value_2|}{(value_1 + value_2)/2} \times 100\% \quad (3.14)$$

where $value_i$ is the material property under consideration. Considering the IRD results, the greatest PRD for E_{LT}^{eff} is between $E_{LT}^{eff} = 12.1$ GPa and $E_{LT}^{eff} = 9.59$ GPa and is evaluated to be 23.2%. It can be seen from Table 3.2 that E_{LT}^{eff} tends to decrease as C_I increases. The opposite trend is evident for α_{LT}^{eff} which tends to increase with increasing C_I . However, the α_{LT}^{eff} predictions from Table 3.2 are not as sensitive to C_I as E_{LT}^{eff} . The greatest PRD for α_{LT}^{eff} is between $20.8 \times 10^{-6}/^\circ\text{C}$ and $23.0 \times 10^{-6}/^\circ\text{C}$, which evaluates to 9.8%. Comparing the locations at which the predicted orientation state is taken to predict E_{LT}^{eff} and α_{LT}^{eff} , it is evident that the flow model of the nozzle by itself leads to over-predictions of E_{LT}^{eff} when compared to

Table 3.2: Summary of Effective Longitudinal Properties for All Flow Conditions.

Model	Location	C_I	κ	E_{LT}^{eff} (GPa)	$\alpha_{LT}^{eff} \times 10^{-6}/^{\circ}\text{C}$
IRD	Nozzle Exit	0.0019	1	12.1	20.8
	Nozzle Exit	0.003	1	11.7	20.9
	Nozzle Exit	0.01	1	10.1	22.1
	Deposited Bead	0.0019	1	11.6	21.2
	Deposited Bead	0.003	1	11.3	21.4
	Deposited Bead	0.01	1	9.59	23.0
RSC	Nozzle Exit	0.0019	1/30	5.70	42.8
	Nozzle Exit	0.0019	1/10	6.99	34.3
	Nozzle Exit	0.0019	1/8	7.37	32.2
	Nozzle Exit	0.003	1/30	5.68	42.8
	Nozzle Exit	0.003	1/10	6.94	34.4
	Nozzle Exit	0.003	1/8	7.31	32.3
	Nozzle Exit	0.01	1/30	5.60	43.1
	Nozzle Exit	0.01	1/10	6.67	34.9
	Nozzle Exit	0.01	1/8	6.97	32.9
	Deposited Bead	0.0019	1/30	5.31	46.3
	Deposited Bead	0.0019	1/10	6.44	37.0
	Deposited Bead	0.0019	1/8	6.73	35.3
	Deposited Bead	0.003	1/30	5.31	46.4
	Deposited Bead	0.003	1/10	6.42	37.1
	Deposited Bead	0.003	1/8	6.71	35.3
	Deposited Bead	0.01	1/30	5.28	46.5
	Deposited Bead	0.01	1/10	6.30	37.5
	Deposited Bead	0.01	1/8	6.55	35.8

predictions made with the flow model that includes the die-swell and deposition. The nozzle flow model also leads to under-predictions of α_{LT}^{eff} compared to the deposition flow model. Overall, E_{LT}^{eff} is more sensitive to the C_I parameter selection than α_{LT}^{eff} when using the IRD model.

The RSC results also indicate that when C_I increases, E_{LT}^{eff} decreases and α_{LT}^{eff} increases. Some changes in α_{LT}^{eff} are so small, however, that they are hidden when the results are rounded to the first decimal point. It can also be observed that κ has a greater effect than C_I on the E_{LT}^{eff} and α_{LT}^{eff} predictions and that the effect is significant. For example, for the deposited bead and $C_I = 0.0019$, E_{LT}^{eff}

increases from 5.31 GPa to 6.73 GPa when κ is increased from 1/30 to 1/8. This corresponds to a 26.8% increase in strength and a PRD of 23.6%. As is the case for the IRD predictions, the nozzle flow model also leads to over-predictions of E_{LT}^{eff} and under-predictions of α_{LT}^{eff} for the RSC when compared to results made using the deposition flow model. The greatest PRDs seen in the RSC results are between 5.28 GPa and 7.37 GPa for E_{LT}^{eff} and between $32.2 \times 10^{-6}/^{\circ}\text{C}$ and $46.5 \times 10^{-6}/^{\circ}\text{C}$ for α_{LT}^{eff} . These PRDs are 33.0% and 36.3%. Thus, the RSC results are more sensitive to the combination of factors considered in this study (the flow model, C_I , and κ) than the IRD.

For all of the factors considered in producing the results in Table 3.2, the predictions are most sensitive to the choice of the fiber interaction model, the IRD or RSC. For example, when the IRD is used with $C_I = 0.0019$, $E_{LT}^{eff} = 11.6$ GPa for the deposition model, but this number drops to 5.31 GPa when the RSC is used with $C_I = 0.0019$ and $\kappa = 1/30$. This is a drop of over 6 GPa or about 54.4%. On the other hand, for the RSC model, κ makes no more than a 2 GPa difference when increased from 1/30 to 1/8. In addition, for the RSC model, C_I makes a difference of no more than 0.4 GPa when increased from 0.0019 to 0.01. For the IRD, C_I makes a difference of no more than 2.1 GPa. Even the choice of flow model makes less of a difference for this study than the choice of fiber interaction model. The flow model makes less than a 0.7 GPa difference, for the IRD model and the RSC model.

Interestingly, C_I has little bearing on the final part behavior according to the RSC model. This observation stands in contrast to results for injection molded parts wherein there is a large amount of time that the fibers are subject to shear after passing the mold inlet. The flow through and out of the tip of a 3D printer nozzle experiences a shearing force for a comparatively short amount of time.

The inclusion of the die-swell and deposition have a noticeable effect on the internal fiber orientation state as well, but it should be noted that this effect is not

as strong as the effects of the combination of C_I and κ . Therefore, proper C_I and κ selection is highly important for this type of flow. A final note, as addressed in Section 3.2.1, is that accurate selection of the initial orientation condition for the IRD model is not very important since the orientation nearly reaches steady state prior to the tapered portion of the nozzle as shown in Figure 3.7a. However, the initial orientation condition makes a significant difference in the predictions made when using the RSC as shown in Figure 3.7b since the RSC retains more of the history of the flow due to slower fiber orientation kinetics. Therefore, accurate selection of the initial orientation state should be a priority if the RSC is to be used in industrial settings for this type of flow.

3.2.5 *Strength Predictions*

The next part of the computational methodology which will be discussed in Section 3.2.5 was developed by the present author in [131], of which the present author retains the copyright under a Creative Commons license. First, some ways of visualizing the spatially varying strength are demonstrated by means of plotting strength constants through the flow domain and creating failure plots. Secondly, the effective strengths of the composite are plotted as functions of fiber orientation modeling parameters to investigate the sensitivity of the methodology to the model inputs. The sensitivity analysis also examines the effect of the critical fiber length and weight-average fiber length on the predicted effective strength values of the printed SFRP.

3.2.5.1 Visualization plots. The strength constants σ_{LT} and σ_{LC} can be extracted from the homogenized strength tensors, similarly to how the elastic moduli were extracted from the homogenized compliance tensor to create Figure 3.12. Replacing \bar{F}_1 , \bar{F}_{11} , $\bar{\sigma}_{LT}$, and $\bar{\sigma}_{LC}$ with $\langle F \rangle_1$, $\langle F \rangle_{11}$, σ_{LT} , and σ_{LC} , respectively, in

Equation 2.66 and solving for σ_{LT} and σ_{LC} ,

$$\sigma_{LT} = \frac{2}{\langle F \rangle_1 + [\langle F \rangle_1^2 + 4 \langle F \rangle_{11}]^{1/2}}, \quad \sigma_{LC} = \frac{2}{[\langle F \rangle_1^2 + 4 \langle F \rangle_{11}]^{1/2}} \quad (3.15)$$

The strength constants σ_{LT} and σ_{LC} are plotted through the thickness of the bead in Figure 3.15 for the deposited bead's orientation state shown in Figure 3.9. One can see that the strength constants express similar trends as A_{11} and $\langle C \rangle_{11}$ shown, respectively, in Figures 3.9 and 3.11. The more dramatic dip in the compressive strength as compared to the tensile strength is related to a larger difference in the longitudinal and transverse compressive strengths. It is noteworthy that the compressive strength is substantially higher than the tensile strength at the end of the deposited bead with the greatest strength occurring in regions of highest fiber alignment i.e., along the top and bottom surfaces of the deposited bead.

Another helpful way of visualizing the properties of the printed SFRP is by creating failure plots. A failure parameter φ can be defined by using Equation 2.76,

$$\varphi(\boldsymbol{\varepsilon}) = \langle g \rangle_i \varepsilon_i + \langle G \rangle_{ij} \varepsilon_i \varepsilon_j \quad (3.16)$$

where the material does not fail when $\varphi(\boldsymbol{\varepsilon}) < 1$ but does when $\varphi(\boldsymbol{\varepsilon}) = 1$. By graphing $\varphi(\boldsymbol{\varepsilon}, \mathbf{x})$ as a function of space over the surface of a FE specimen under a load, one can gain insight into where the specimen's weak points are. Figure 3.16 shows $\varphi(\boldsymbol{\varepsilon}, \mathbf{x})$ for each of the three FE strength specimens considered. Figure 3.16a indicates weakness in the tensile specimen occurring on the top and bottom edges, with specific concern at the top and bottom corners on the right-hand side. On the other hand, the compressive specimen in general exhibits more weakness in the center of the bead than the top and bottom edges, with high weakness at the point of the applied load and in the top, right corner. The flexural specimen exhibits weakness in the bottom, right corner (corresponding to the bottom center of the full, real specimen which is symmetric) as is the case for an isotropic material.

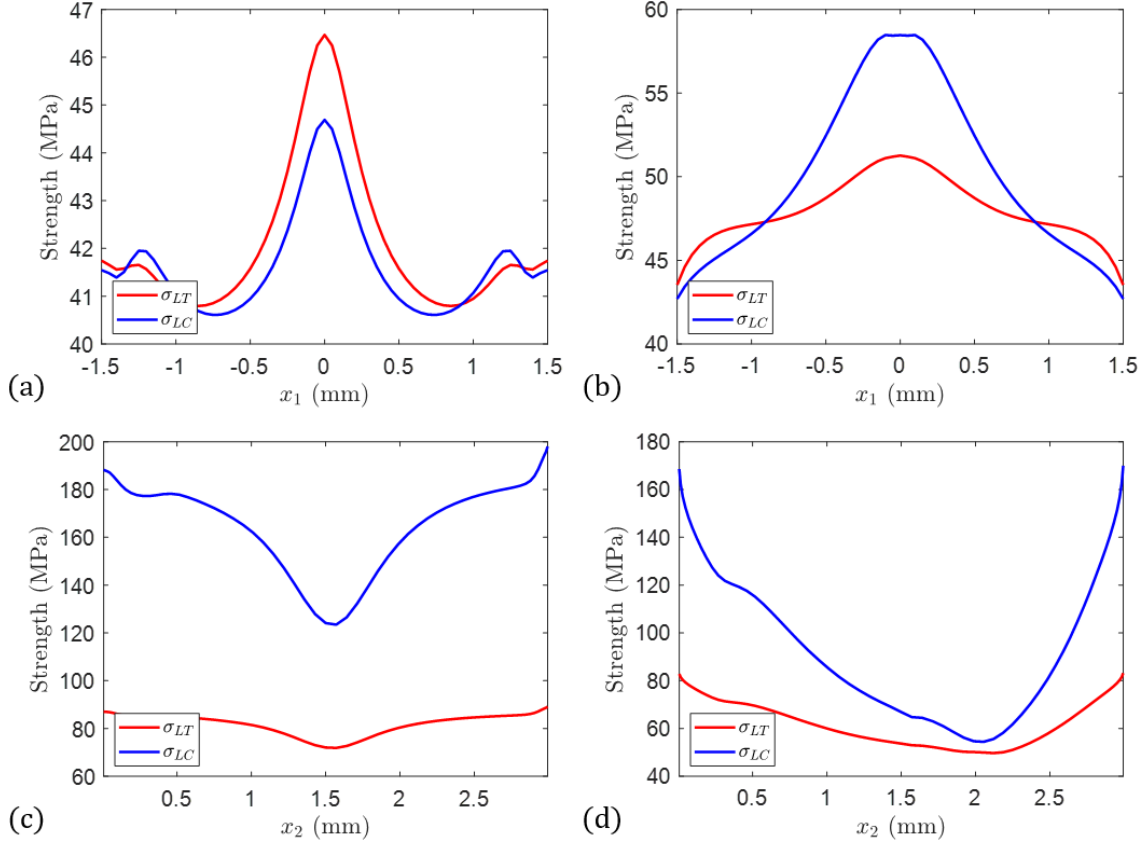


Figure 3.15: Tensile and compressive strength constants (σ_{LT} and σ_{LC} , respectively) through the flow domain. (a) At the nozzle exit, predicted by the IRD; (b) At the nozzle exit, predicted by the RSC; (c) At the bead end, predicted by the IRD; (d) At the bead end, predicted by the RSC. Note, σ_{LT} and σ_{LC} represent the tensile and compressive strengths in the x_1 (horizontal) direction. Furthermore, the following parameters were used: initial $A_{ij} = \frac{1}{3}\delta_{ij}$, $a_r = 38.8$, $C_I = 0.0019$, $\kappa = 0.125$, and $N_{x2} = N = 61$.

3.2.5.2 Sensitivity analyses. Typically for SFRPs, the fiber interaction coefficient is in the range $C_I = 0.006$ - 0.01 according to [64] and the slowness factor is in the range $\kappa = 0.05$ - 0.2 according to [44] (as cited in [64]). However, according to Bay's formula given in Equation 2.25 for the volume fraction and aspect ratio considered, the interaction coefficient is even lower, $C_I \approx 0.0019$. The results of the stiffness and strength predictions therefore were investigated for several C_I and κ combinations that encompass these ranges, to investigate the sensitivity of the stiffness and strength predictions to the modeling parameters. Stiffness and strength

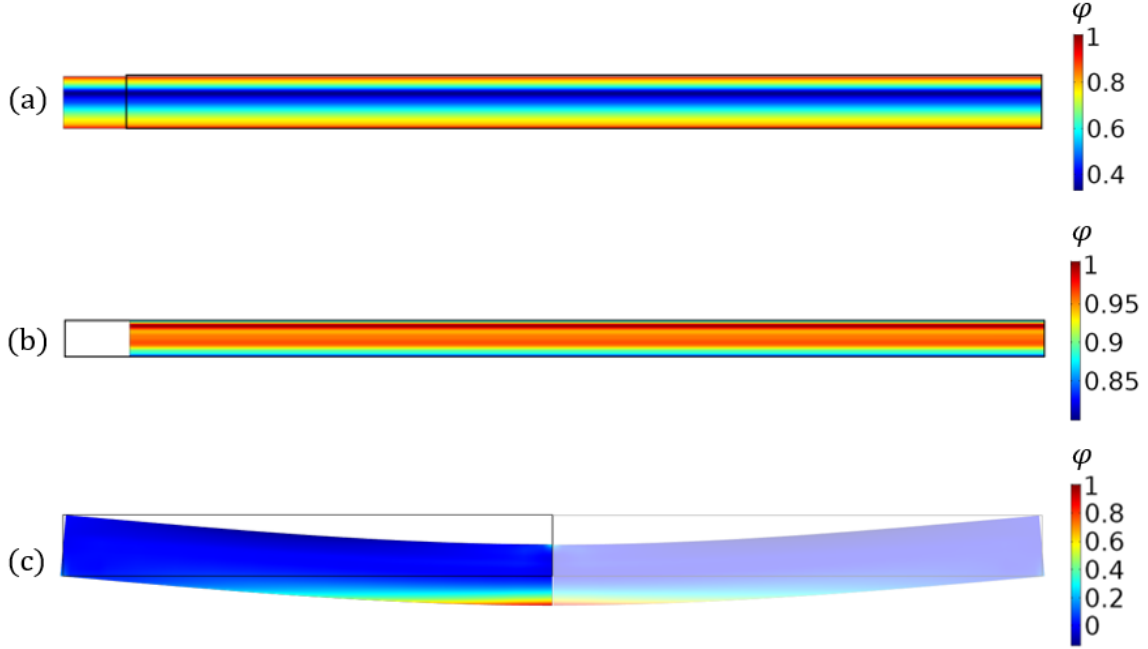


Figure 3.16: Failure surface for (a) the tensile specimen (deformation scale factor=10, $N_{x2} = 31$, $N_{x1} = 121$), (b) the compression specimen (deformation scale factor=5, $N_{x2} = 31$, $N_{x1} = 121$), and (c) the flexural specimen (deformation scale factor=1.5, $N_{x2} = 31$, $N_{x1} = 13$). Used initial $A_{ij} = \frac{1}{3}\delta_{ij}$, $a_r = 38.8$, $C_I = 0.0019$, and $\kappa = 0.125$. Color scheme indicates value of φ from Equation 3.16.

predictions made using the RSC model with the parameter ranges of $C_I = 0.0019$ -0.01 and $\kappa = 0.05$ -0.2 were found and are shown in Figure 3.17 for each of the three loading configurations investigated.

The fiber diffusion parameter κ has a clear impact on the stiffness and strength in Figure 3.17, but C_I does not as much. The stiffness and strength increase as κ increases. As C_I increases, the stiffness decreases slightly but the strength apparently does not strictly increase or decrease. In addition, since both the effective longitudinal tensile and compressive stiffness have the same mathematical relationship to the orientation state, their behavior will be identical, hence Figures 3.17a and b look the same. Summarizing all the predictions, E_{LT}^{eff} and E_{LC}^{eff} are both in the range 5.60-7.57 GPa, E_{LF}^{eff} is 6.44-8.95 GPa, σ_{LT}^{eff} is 41.0-51.7 MPa, σ_{LC}^{eff} is 75.3-99.7 MPa, and σ_{LF}^{eff} is 51.8-67.7 MPa. The sizes of these ranges highlight the importance

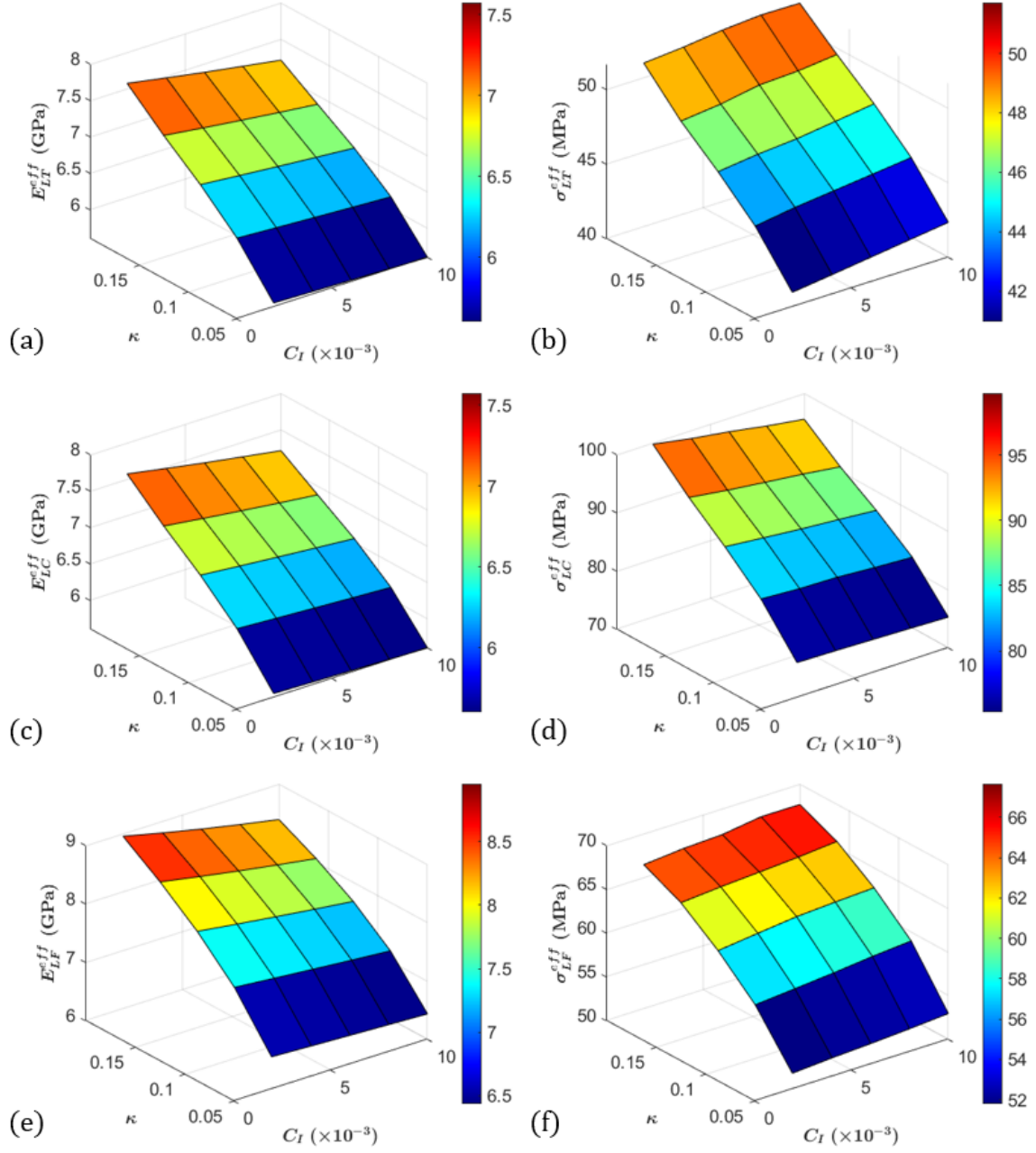


Figure 3.17: Effective longitudinal stiffness and strength predictions as functions of RSC modeling parameters, C_I and κ : (a) tensile stiffness, (b) tensile strength, (c) compressive stiffness, (d) compressive strength, (e) flexural stiffness, and (f) flexural strength. Used initial $A_{ij} = \frac{1}{3}\delta_{ij}$, $a_r = 38.8$, $N_{x2} = N = 31$, and $N_{x1} = 121$.

of accurate measurement of the modeling parameters, especially κ , so that accurate predictions can be made while using the RSC fiber orientation model.

Given the constituent properties of CF-ABS in Table 3.1, Equations 2.74 and 2.75 give $L_c \approx 835 \mu\text{m}$. However, the authors of [132] estimated $L_c \approx 640 \mu\text{m}$ for CF-ABS based on properties they found in the literature. This variability prompts an investigation of the sensitivity of the strength predictions to L_c . Figure 3.18a shows the strength predictions for each of the three specimens considered as functions of L_c over the range $300 \mu\text{m} \leq L_c \leq 1100 \mu\text{m}$. The most notable impact is on σ_{LC}^{eff} which has a 15.7% decrease from 98.3 to 82.9 MPa as L_c increases. From $L_c = 640 \mu\text{m}$ to $L_c = 835 \mu\text{m}$ there is a 4.6% drop in the compressive strength, σ_{LC}^{eff} , from 93.3 to 89.0 MPa. The tensile strength, σ_{LT}^{eff} , stays fairly constant, dropping 0.8% from 46.8 to 46.4 MPa as L_c increases from $300 \mu\text{m}$ to $1100 \mu\text{m}$. The flexural strength, σ_{LF}^{eff} , also stays fairly constant from $L_c = 300$ - $1100 \mu\text{m}$, dropping 1.4% from 62.0 MPa to 61.1 MPa. Thus, the critical fiber length does have an impact on the strength results, but the effect is nominal except on the longitudinal compressive strength.

The weight-average fiber length has a substantial effect on all the strength predictions as shown in Figure 3.18b and, unlike L_c , on all the stiffness predictions as well as shown in Figure 3.18c. Changing L_w changes a_r and therefore the predicted internal fiber orientation state in each of the samples, so this is accounted for in the predictions shown in Figures 3.18b and c. The stiffness and strength ranges over $L_w = 100$ - $1100 \mu\text{m}$ include the following: $E_{LT}^{eff} = E_{LC}^{eff} = 4.40$ - 8.33 GPa, $E_{LF}^{eff} = 4.86$ - 10.2 GPa, $\sigma_{LT}^{eff} = 31.3$ - 103 MPa, $\sigma_{LC}^{eff} = 61.0$ - 119 MPa, and $\sigma_{LF}^{eff} = 37.6$ - 167 MPa.

3.2.6 Laminate Analogy Approach to Stiffness

Results for the laminate analogy approach to predicting elastic modulus and flexural (bending) modulus are included in this section. The number of layers chosen for the analysis match the number of streamlines from the flow analysis ($N=31$) and

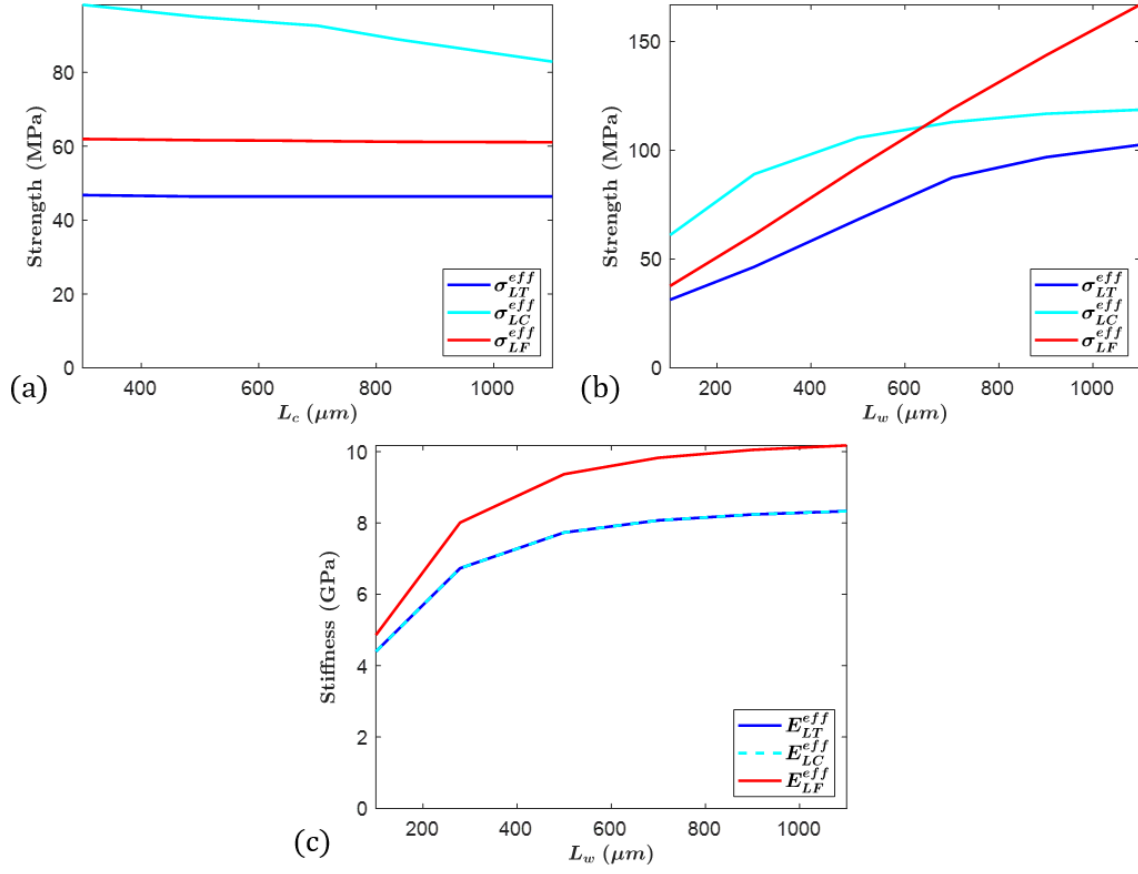


Figure 3.18: (a) Effective longitudinal tensile, compressive, and flexural strengths as functions of the critical fiber length. (b) Effective longitudinal tensile, compressive, and flexural strengths as functions of the weight-average fiber length. (c) Effective longitudinal tensile, compressive, and flexural stiffnesses as functions of the weight-average fiber length. Used $N_{x2}=31$ and $N_{x1}=121$.

the thicknesses of the layers match those of the elements in the FE simulations. The results, which are displayed in Figure 3.19, are very similar to what was obtained in the previous section over the ranges $C_I=0.0019$ -0.1 and $\kappa=0.05$ -0.2. The percent relative differences between E_{LT}^{eff} (or E_{LC}^{eff}) from earlier and E_{LT}^{lam} from the laminate analogy approach are all under 0.1%. In addition, the percent relative differences between E_{LF}^{eff} and E_{LF}^{lam} are all under 4.7%. E_{LT}^{lam} from the laminate analogy approach ranges from 5.61-7.57 GPa and E_{LF}^{lam} ranges from 6.63-9.38 GPa. Thus, the methods for predicting the stiffnesses are very comparable. In every case, the methodology of the author led to slightly more conservative estimates than the laminate analogy

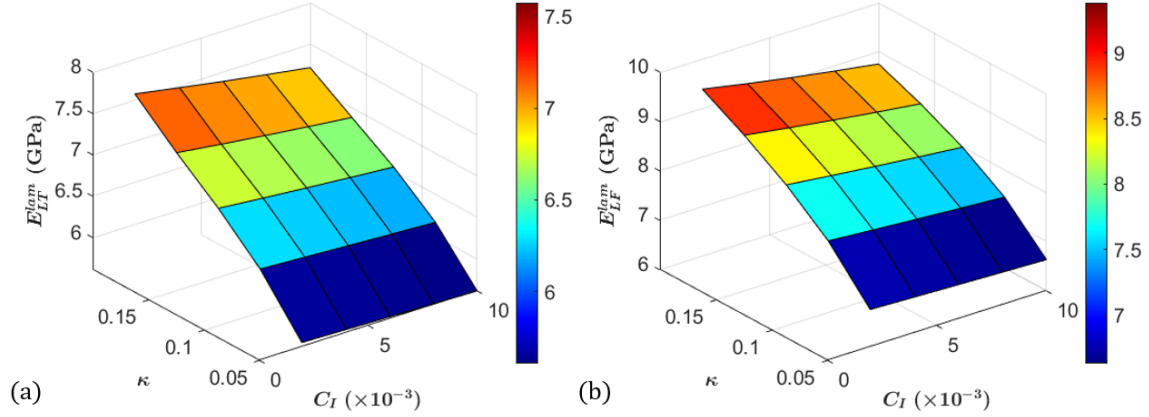


Figure 3.19: Laminate analogy approach: effective longitudinal (a) tensile/compressive stiffness and (b) flexural stiffness as functions of the RSC modeling parameters, C_I and κ . Used initial $A_{ij} = \frac{1}{3}\delta_{ij}$, $a_r = 38.8$, and $N_{x2} = N = 31$.

approach. An advantage to the laminate analogy approach, however, is that no FE simulation is required which greatly speeds up the calculations. However, the assumptions made by the laminate analogy approach, shown in Equations 2.43 and 2.44, are contrary to the non-symmetric orientation state calculated through the thickness of the printed bead shown in Figures 3.9b and d. In addition, the laminate analogy approach does not include strength predictions. Nevertheless, for quick prediction of the stiffness of a LAAM-printed SFRP bead, the laminate analogy approach can be useful.

3.3 A Unified Methodology

Advani's orientation-averaging approach to predicting properties of anisotropic SFRPs is advantageous for consistency reasons because it allows an entire suite of properties to be predicted in a similar manner, as demonstrated in the preceding sections of this dissertation. This makes predictive software development more straightforward. To demonstrate and solidify this point, a custom COMSOL application for predicting several different properties was made in-house by the author and is shown in Figure 3.20. There are five portions of this application that are to be run in consecutive order.

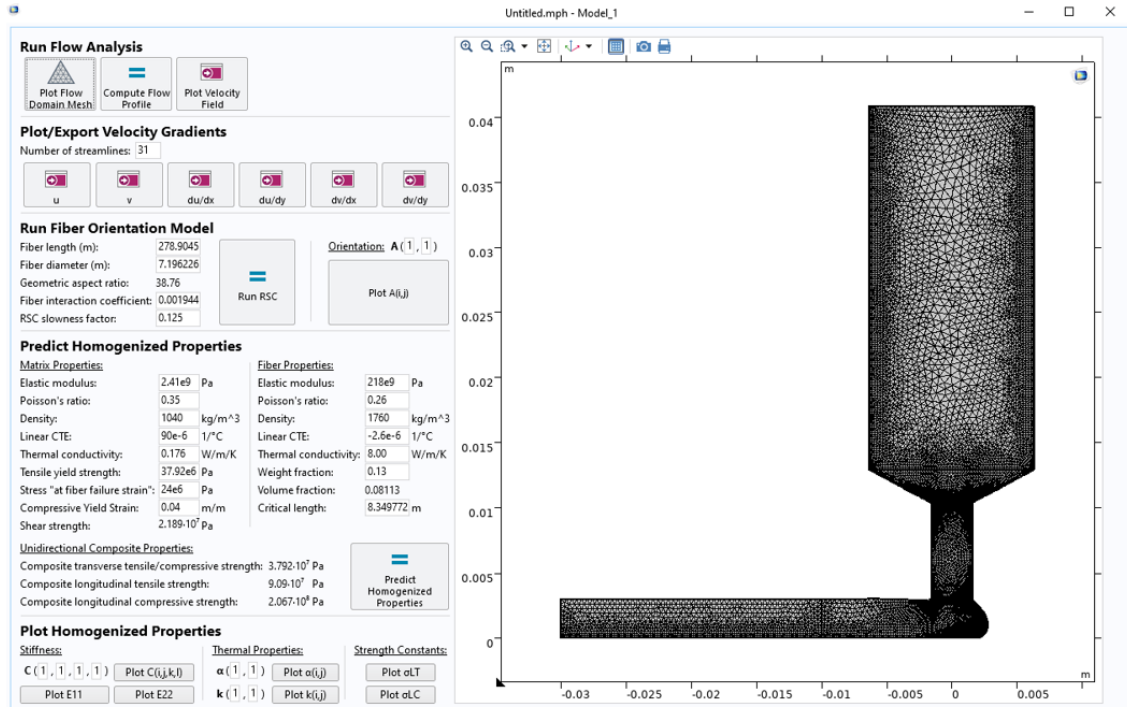


Figure 3.20: Custom COMSOL application for predicting anisotropic material properties of a 3D printed SFRP. An extremely fine mesh is used for the flow simulation, as shown.

The first portion of the application is entitled “Run Flow Analysis.” In this part of the application, the flow profile is computed using the boundary conditions given in Figure 3.3. The mesh for the flow model can also be plotted, as shown in Figure 3.20, along with the solved velocity magnitude shown in Figure 3.21a.

The next part of the COMSOL application, entitled “Plot/Export Velocity Gradients,” is where the velocities and velocity gradients along a user-specified number of streamlines are plotted and exported to externally-saved data files to be used as input for the flow model. Figure 3.21b shows the x -velocity, u , plotted along 31 streamlines.

The third section of the application, entitled “Run Fiber Orientation Model,” is where the RSC model is run. The user of the application can specify a fiber length and diameter, to get the fiber aspect ratio, a_r , used in the model, as well as the fiber interaction coefficient, C_I , and RSC slowness factor, κ . As mentioned earlier in

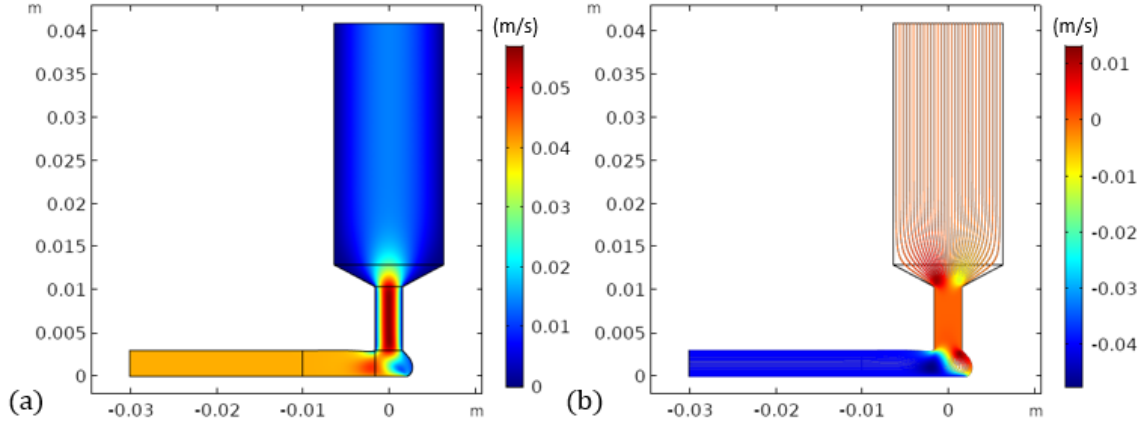


Figure 3.21: (a) Velocity magnitude (m/s) and (b) u velocity along 31 streamlines.

this dissertation, when $\kappa = 1$ the RSC model is equivalent to the IRD. Thus, this application can easily implement the IRD model as well. Once the fiber orientation state has been solved by clicking the “Run RSC” button, the components of the second order orientation tensor can be plotted as a function of space, \mathbf{x} , as shown in Figure 3.22. A_{ij} is plotted for user-specified values of i and j by clicking the “Plot A(i,j)” button.

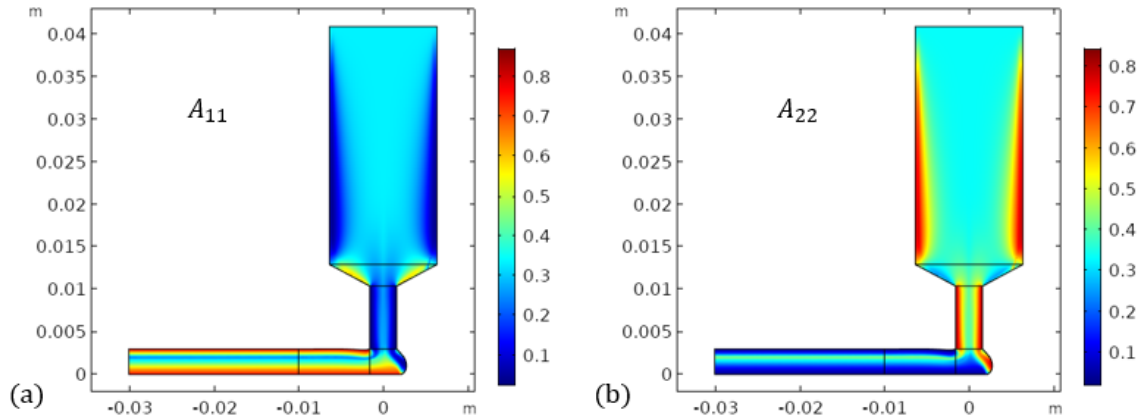


Figure 3.22: Spatially-varying orientation state in a LAAM nozzle: (a) amount of fiber alignment in x_1 represented by A_{11} and (b) amount of fiber alignment in x_2 represented by A_{22} . Used RSC with $C_I = 0.0019$, $\kappa = 0.125$, and $a_r = 38.8$.

The next section, “Predict Homogenized Properties,” provides material property input fields for the matrix and fiber, which are currently auto-filled with the properties from Table 3.1 but most of which can be edited (some cannot be directly

edited since they are functions of other properties). This section also displays the longitudinal tensile and compressive strength for the SFRP calculated using Equations 2.72a and 3.4 as well as the transverse tensile/compressive strength, currently taken to be equivalent to σ_m . After clicking the “Predict Homogenized Properties” button, several tensor properties are predicted at the \mathbf{x} locations where the orientation tensors are known and saved to external data files.

The components of the tensor properties along with the elastic constants and strength constants can be plotted across the entire flow domain in the next section of the application, “Plot Homogenized Properties.” Results are shown in Figures 3.23-3.27 for the 13% CF-ABS used in this study. In general it can be observed that if the fiber has a property that is higher than the corresponding property of the matrix, then the corresponding property of the SFRP will be higher in directions of higher fiber alignment, which happens to be along the nozzle walls and the top and bottom surfaces of the printed beads. This being the case, A_{11} , $\langle C \rangle_{1111}$, E_{11} , $\langle k \rangle_{11}$, σ_{LT} , and σ_{LC} all show similar trends. On the other hand, the transverse properties $\langle C \rangle_{2222}$, E_{22} , and $\langle k \rangle_{22}$ tend to follow the trends of A_{22} . The CTE shows the opposite trend as the orientation, stiffness, thermal conductivity, and strength since α_f is smaller than α_m . Non-diagonal components of the tensor properties can be easily plotted as well. It would be straightforward to add the capabilities to plot the moisture expansion, electrical conductivity, and mass diffusivity properties to the application as well if the corresponding properties of the fiber and matrix constituents were known, but this has been left for a future work.

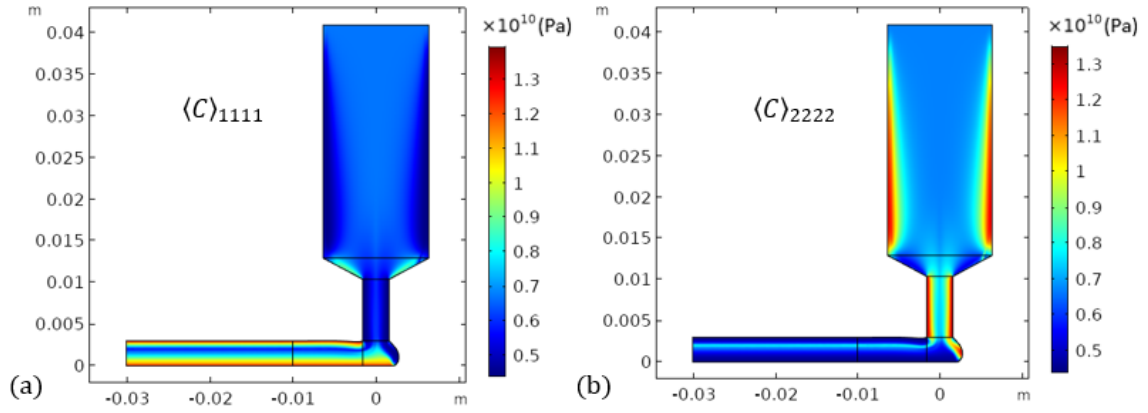


Figure 3.23: Spatially-varying stiffness as a function of the orientation state in Figure 3.22: (a) $\langle C \rangle_{1111}$ and (b) $\langle C \rangle_{2222}$.

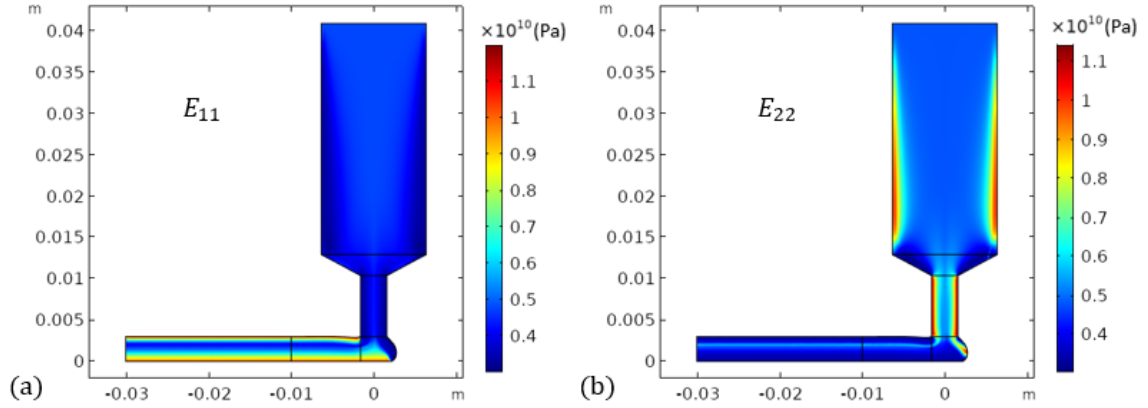


Figure 3.24: Spatially-varying elastic moduli as functions of the orientation state in Figure 3.22: (a) E_{11} and (b) E_{22} .

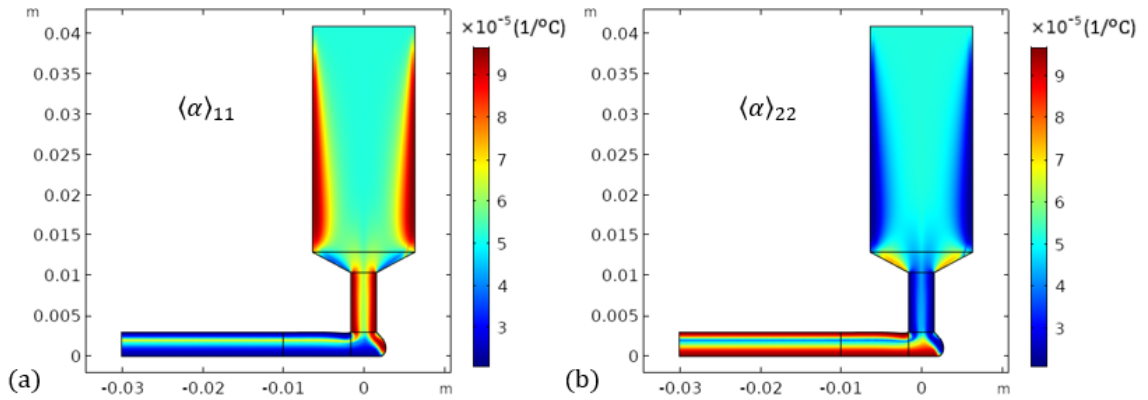


Figure 3.25: Spatially-varying CTE as a function of the orientation state in Figure 3.22: (a) $\langle \alpha \rangle_{11}$ and (b) $\langle \alpha \rangle_{22}$.

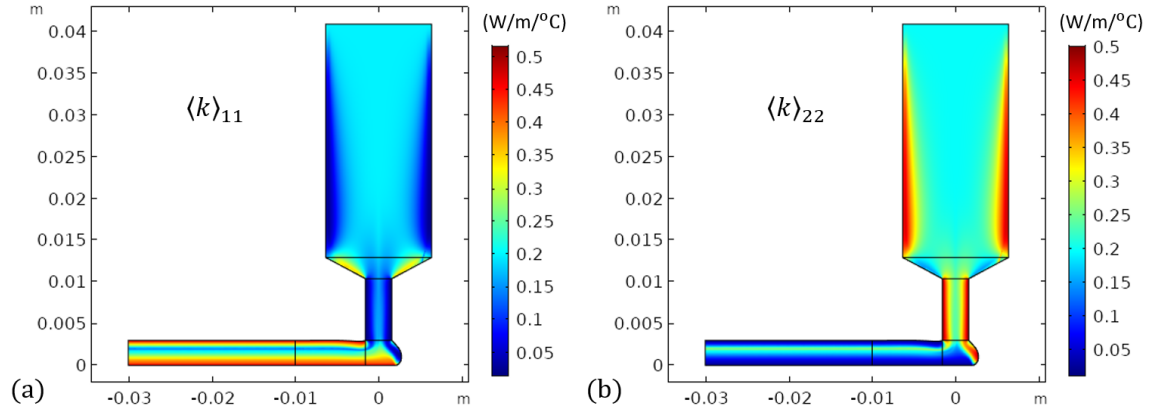


Figure 3.26: Spatially-varying thermal conductivity as a function of the orientation state in Figure 3.22: (a) $\langle k \rangle_{11}$ and (b) $\langle k \rangle_{22}$.

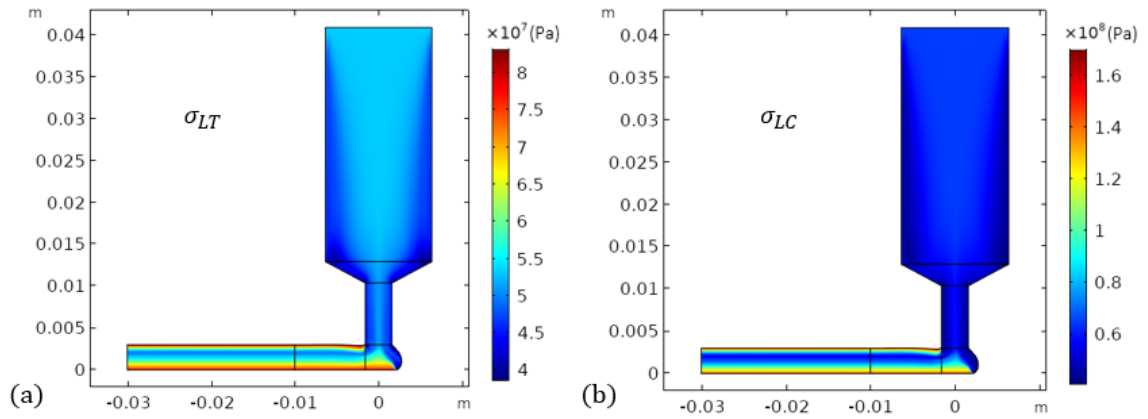


Figure 3.27: Spatially-varying strength constants as functions of the orientation state in Figure 3.22: (a) σ_{LT} and (b) σ_{LC} .

CHAPTER FOUR

Experimental Methods and Results

This chapter is devoted to describing the experiments performed as part of this dissertation. The chapter is divided into three subsections that cover the experimental methods used, the results of the experiments, and, finally, modifications to the modeling methodology based on the experimental findings.

4.1 Experimental Methodology

For fabricating test specimens for experimental purposes, the author of this dissertation led an undergraduate researcher and Baylor's machinist in constructing a miniature LAAM system at Baylor University. Along with this, the author led the development of a standard operating procedure including a list of troubleshooting tips, which is given in Appendix A. Several Baylor researchers have used this LAAM system for various research projects (e.g., [115,133,134]). After discussing the LAAM system in detail in the following subsection, the experiments performed are discussed and are divided into two main categories: measuring the fiber aspect ratio and measuring the strength, including the tensile, compressive, and flexural strength. Process specification documents written by the author for an aerospace company were used to inform the author on how to conduct the tensile, compressive, and flexural tests in this dissertation. The documents referred to were written for a Federal Aviation Administration material equivalency project and were based on ASTM D6272-17 [135], ASTM D2344/D2344M-16 [136], ASTM D695/SRM 1R-94 [137], and ASTM D3039 [138].

4.1.1 Baylor LAAM System

Shown in Figure 4.1, the Baylor LAAM system was built to fabricate LAAM specimens for experimental studies and has been used by several researchers in addition to the author. This system was described in detail by the present author in [37]. Thus, Section 4.1.1 closely follows [37]. The print area is approximately 4 feet \times 4 feet and the extruder has approximately 6 inches of travel in the z direction. The print bed has been bolted to perforated tubing and can therefore be manually unfastened, lowered, and re-fastened in case a person desires to print a part with a height greater than 6 inches, but this was not necessary for the specimens fabricated in this study. The materials for the main structure of the LAAM system were purchased locally and include cold-rolled steel railings, a 1/4 inch aluminum plate for the print bed, and 3 inch tubing for the frame which was cut and welded in-house. Currently, the operation of the system is controlled by three independent systems: the extruder, the gantry, and a heated print bed, each of which will be discussed next.

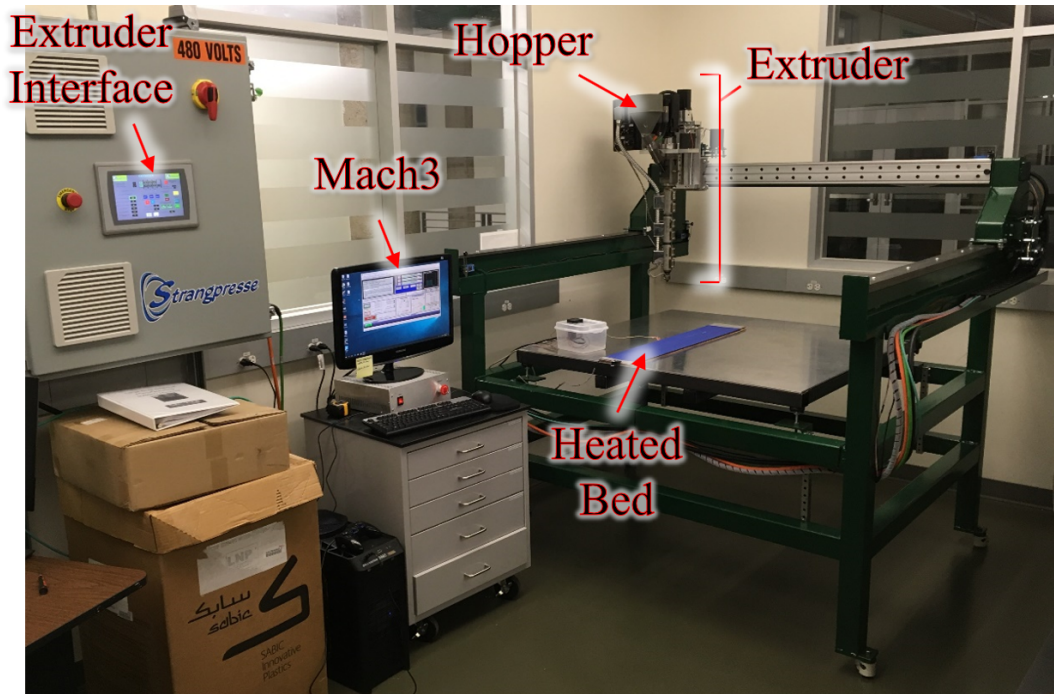


Figure 4.1: Baylor LAAM System.

4.1.1.1 *Gantry system.* The gantry system is a Magnum II system from Precision Plasma LLC. The Magnum II system was made as an assembly kit for CNC plasma cutters, but its ability to move in three dimensions make it suitable for custom LAAM systems as well. The components of the gantry system that were purchased include the aluminum track fastened to the top horizontal beam, the pieces on the sides that couple the cross beam to the rails, and the racks, pinions, and motors. The gantry system is controlled using Mach3 software managed on a local computer. The Mach3 standard user interface is shown in Figure 4.2. Mach3 allows for customization of the user interface as well, which can be done to improve simplicity and enhance visual features such as the print path. A custom Baylor-themed user interface was made for this purpose as displayed in Figure 4.3.

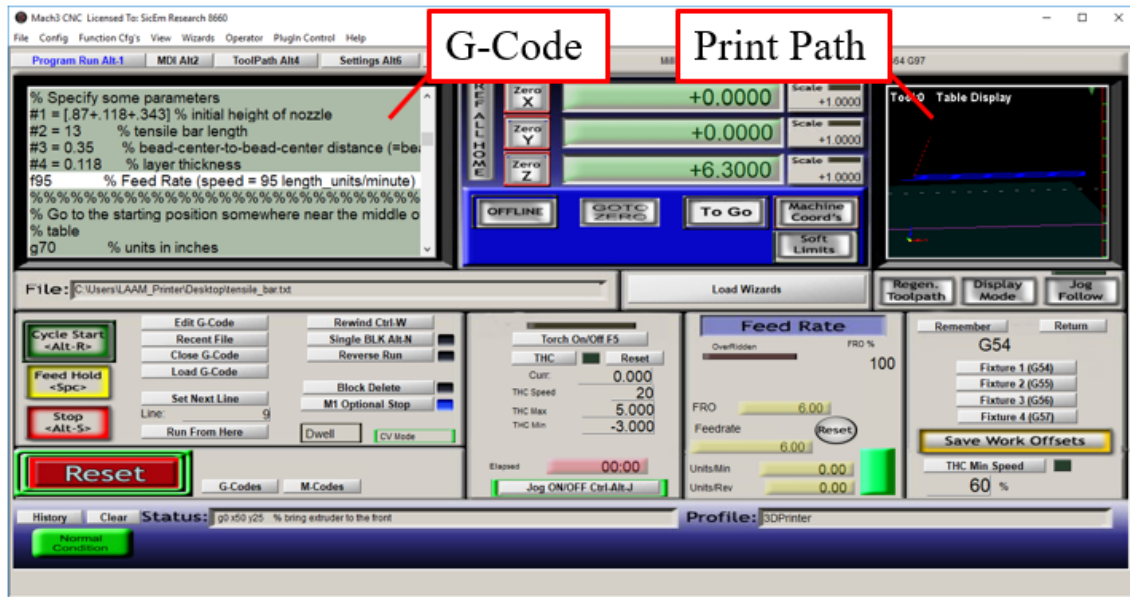


Figure 4.2: Mach3 standard user interface.

Mach3 instructs the movements of the extruder using G-Code. Although slicing software exists to automatically generate G-Code from a 3D object file, like a .stl file, this software often generates lines of code meant to control the temperature of the extruder nozzle and when the extruder should start or stop extruding. These lines are unnecessary for the Baylor LAAM system so it was therefore more conve-

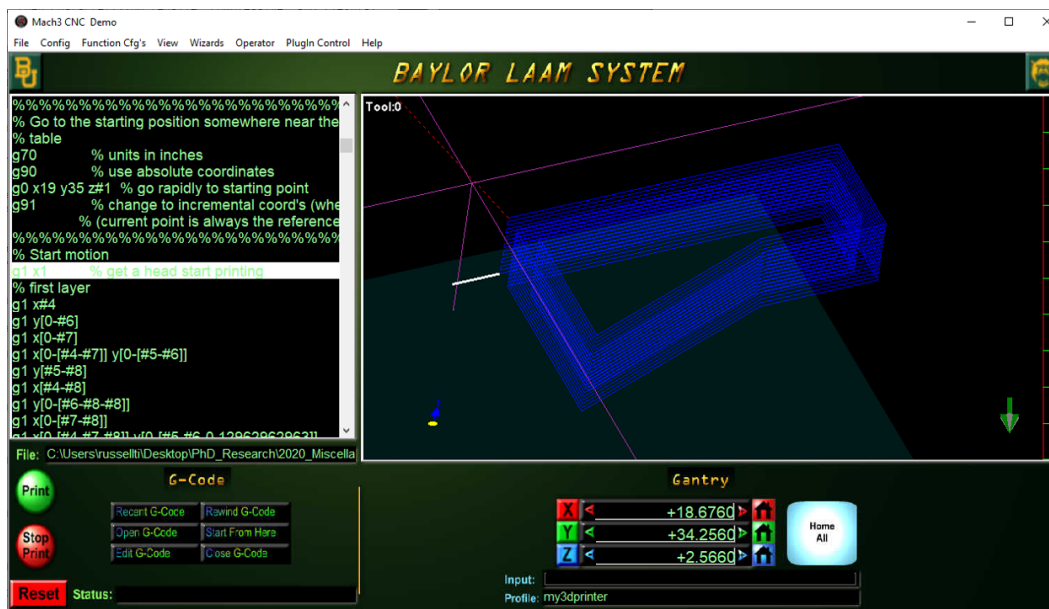


Figure 4.3: Custom Baylor-themed Mach3 user interface, designed in-house.

nient to manually create all the G-Codes. All the experimental specimens used for testing in this dissertation were thus fabricated using manually written G-Codes by the author.

4.1.1.2 Extruder system. A Strangpresse Extruder Model 19 is used on Baylor's LAAM system. The hopper at the top of the extruder was fabricated in-house by Baylor's machinist and takes polymer pellet feedstock rather than filament. The extruder with the hopper is about 3 feet in height and can be seen in Figure 4.4. The Strangpresse interface for controlling the extruder is pictured in Figure 4.4 and allows an operator to adjust the temperatures in three zones along the length of the extruder as well as the RPMs of the screw to control the deposition rate. A spigot on the upper part of the extruder allows for a hose to be attached so that coolant may be provided to the extruder to prevent overheating. An air hose was attached here at times to help mitigate early-onset melting of the polymer pellets so they would not conglomerate and clog the extruder, preventing it from extruding a steady bead of material.

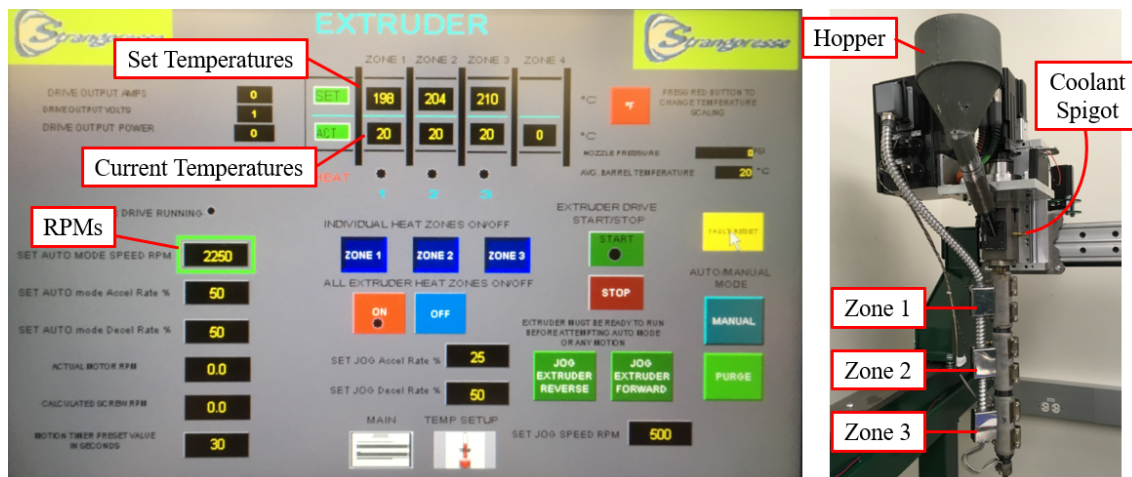


Figure 4.4: Strangpresse interface (left) and Strangpresse Extruder Model 19 (right).

4.1.1.3 Heated print bed. A heated print bed can reduce thermal gradients in a part as it is being printed, thereby mitigating warping of parts both during and after printing. As a preliminary setup for Baylor’s LAAM system, a 6”×36” heat sheet sandwiched between cork board and an aluminum plate was laid on the larger 4’×4’ build plate as is shown in Figure 4.1. Painters’ tape was taped to the top of the aluminum plate to improve adhesion between the printed material and the print surface. A thermocouple and temperature controller were used to measure and control the print bed temperature. This setup was used in the study described in Section 4.3.1 but was later upgraded. The upgraded system consists of four 6”×6” heat sheets, lined up, spaced about 6 inches apart, and placed underneath the 4’×4’ build plate itself. The heat sheets were placed in a line so that long strips could be printed above them. The heat sheets were also placed such that additional heat sheets could be added around them in the future as desired. The upgraded system is pictured in Figure 4.5. A video game controller is also shown in the figure and was connected to Mach3 to allow for manual control of the extruder’s position.

It should be noted that it was discovered that a significant amount of bowing in the aluminum print bed was induced while heating the print bed. A small amount of bowing, when dispersed across a large, 4’×4’ build plate, can cause sig-

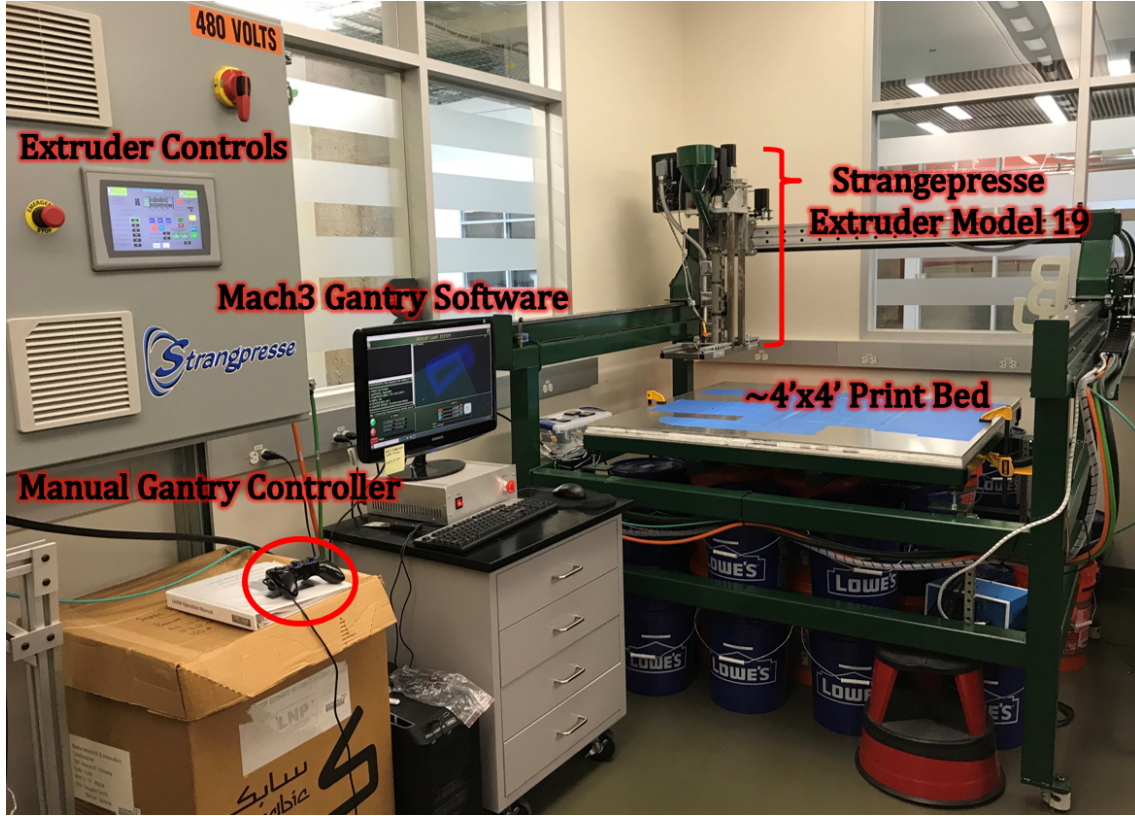


Figure 4.5: Upgraded Baylor LAAM System.

nificant discrepancy in nozzle-to-print-bed-distance across the build area, leading to inconsistent parts. Therefore, vice grips were added to the sides of the build plate to maintain flatness and sometimes the print bed was simply left at room temperature. An alternative design would be worth pursuing in future systems so that bed warpage is not so much of a problem. Nevertheless, this system was sufficient for the present studies.

4.1.2 Fiber Aspect Ratio Characterization

Predicting the material properties of LAAM-made SFRPs depends on knowledge of the fibers' aspect ratios. Furthermore, it has been shown that fibers may break during processing, which can have a significant impact on the fiber aspect ratio distribution and predicted mechanical properties (e.g., [134]). Thus, experimental measurement of the aspect ratio (L_f/d_f) in LAAM-made SFRPs is an important step

towards accurate material property prediction. Two fiber aspect ratio studies were conducted by the present author, one discussed in [36] and one being an internal study that was presented in a conference poster. Both sets of results indicate that the fiber aspect ratio significantly affects the property predictions.

The first study to characterize the fiber aspect ratio made use of two microscopes, a Keyence VR-3000 One-shot Measurement Macroscopic and a JEOL JSM-6610LV Scanning Electron Microscope (SEM). The SEM was used to image the fibers so their diameters could be measured, a feat which was difficult to perform using the optical microscope which had much lower magnification capabilities, but could be used to measure fiber length. The second study made use of a single, high-magnification microscope that could be used to measure both fiber length and fiber diameter so that the fiber measurement process could be more streamlined. A custom-written MATLAB code was written for the second study to aid in measuring the fibers. In addition, the second study examined fibers at several stages of the printing process so that the part of the printing process causing the most damage to the fibers could be identified and its effect on the material properties quantified.

4.1.2.1 Preparing the fibers for measurement - first study. To measure the carbon fibers in an SFRP, which are on the order of hundreds of μm in length and less than $10\ \mu\text{m}$ in diameter, the fibers need to be imaged under a microscope and clearly distinguishable from the polymer matrix. Perhaps the cheapest way of doing this effectively is by burning off the matrix material. Therefore, a pre-processed pellet of the 13% CF-ABS used in this study, along with a printed sample of the same material were put through burn-off tests. These tests had to be performed in an inert environment to avoid degrading the fibers.

The burn-off test of the pre-processed pellet was performed in a TA Instruments Q50 Thermogravimetric Analyzer (TGA) machine which is displayed in Fig-

ure 4.6a. This machine can measure the mass of very small samples (< 50 mg) in a furnace with an operator-selected atmosphere (like air or nitrogen) and be used to determine the thermal degradation temperature of a material. A typical pellet of the 13% CF-ABS is pictured in Figure 4.6b.

The burn-off testing procedure for the pellet was as follows: (1) $20^{\circ}\text{C}/\text{min}$ temperature ramp up to 600°C in an inert, nitrogen environment, (2) hold isothermal for 1 hour in nitrogen, and (3) hold isothermal for 5 minutes in non-inert air. Step 3 was introduced after several trial tests resulted in the fibers staying clumped together, likely due to remnants of the ABS. An early attempt at resolving this issue was to soak the fibers in acetone after burn-off, since acetone is known to corrode ABS (it is often used to treat 3D printed ABS parts, smoothing out their rough surface texture). This did not reliably result in the desired effect, however, even when boiling the acetone with the sample submerged in it. Thus, step (3) was introduced in the testing procedure. Carbon fiber will degrade at 600°C in air, so step (3) was limited to 5 minutes.

From the data in Figure 4.6c, the resulting sample weight percent was 8.8% at the start of step 3 and 8.2% at the end of the test. Assuming the fibers did not decompose in the nitrogen environment, the fiber weight fraction of the sample was thus approximately 8.8%, markedly lower than the 13% provided by the material supplier. It is possible that some fiber degradation may have occurred during the test if the nitrogen environment was not sufficiently pure, however. Thus, as a follow up study, more TGA burn-off tests were performed while making sure that the purity of the nitrogen source was tightly controlled. These tests are discussed in Section 4.1.3.4.

For the burn-off test of the 3D printed 13% CF-ABS material, individual beads (or strips) like those in Figure 4.7a were printed at 210°C on an 85°C heated print bed. After the beads were printed, a burn-off specimen was cut from one

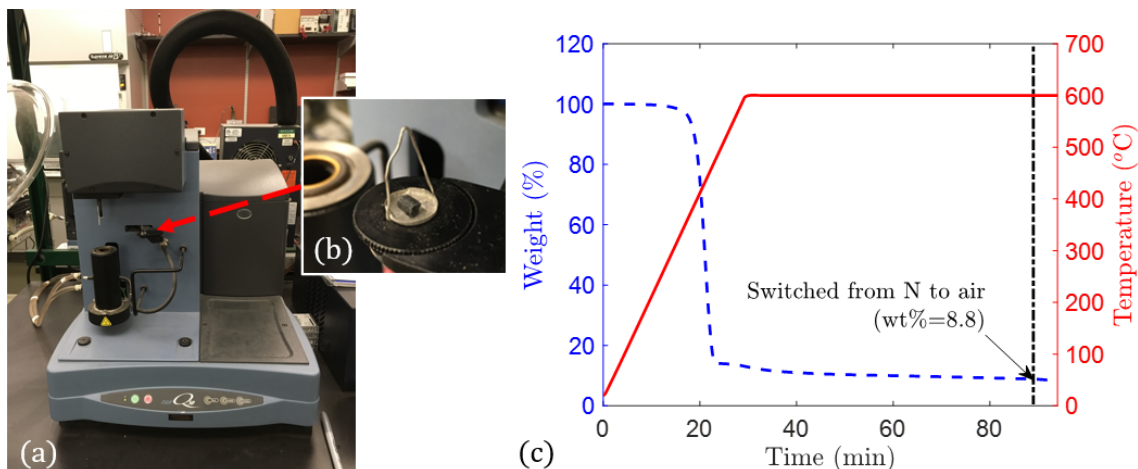


Figure 4.6: (a) TA Instruments Q50, TGA machine. (b) Typical pre-processed pellet of 13% CF-ABS. (c) Plot of TGA burn-off test data. The solid red curve indicates temperature change over time, the dashed blue curve indicates change in weight percent over time, and the black dash-dotted line indicates the point at which the environment was changed from nitrogen (N) to air.

bead. Since cutting a specimen from a bead involves potentially damaging the fibers, a large sample - large relative to the maximum fiber length - was needed to help minimize the effect damaged fibers might have on the measured fiber length distribution (FLD). A 2 inch specimen was used, which is diagrammed in Figure 4.7b. The hashed regions of the specimen in the diagram designate the ends where a fiber is at risk of being damaged by the cutting process. These regions make up 16% of the total specimen length, indicating that the effect of cut fibers on the measured FLD will be small. The length of these regions corresponds to the maximum fiber length, which is limited by the size of the pre-processed pellets. Therefore, after measuring 20 pellets and taking the average length, this length was determined to be approximately 0.16 inches.

While necessary to have a large specimen size for the 3D printed specimen, a 2 inch specimen was too large to fit into the TGA machine. Therefore the test setup depicted in Figure 4.8 was used. A Vulcan 3-1750 box furnace was used, shown in Figure 4.8a, and the sample was contained in a petri dish with a custom-made

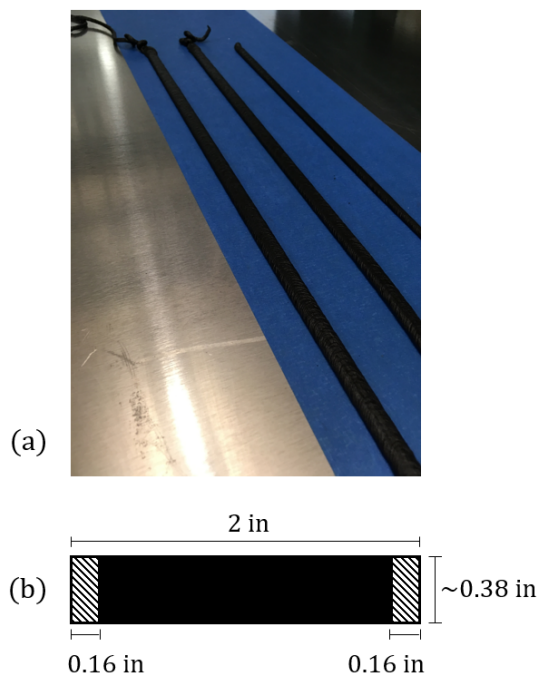


Figure 4.7: (a) Individual beads printed with Baylor's LAAM system. (b) Dimensions of the 3D printed specimen to be burn-off tested.

aluminum lid as shown in Figure 4.8b. The lid was milled to fit the petri dish and two holes were drilled and tapped on the top of it to connect to two steel tubes. The steel tubes were fit through the furnace vent to carry nitrogen in and out of the sample container during testing as shown in Figure 4.8a. In this way, the burn-off test could be performed in an inert, nitrogen environment. A gas bubbler was attached at the end of the outgoing nitrogen tube to prevent air from back-flowing into the sample container during testing. A similar test procedure as before was conducted: (1) 20°C/min temperature ramp up to 600°C in nitrogen, (2) hold isothermal for 1 hour in nitrogen, and (3) hold isothermal for 10 minutes in air. The time in step 3 was increased to 10 minutes since a larger specimen was being used. Figure 4.8c shows a 3D printed sample after going through a burn-off test.

After burn-off testing, the burn-off specimens were dropped into beakers of acetone and sonicated with a Branson Digital Sonifier 450, shown in Figure 4.9a. Sonication was typically done at 20% amplitude for a few minutes or less and the

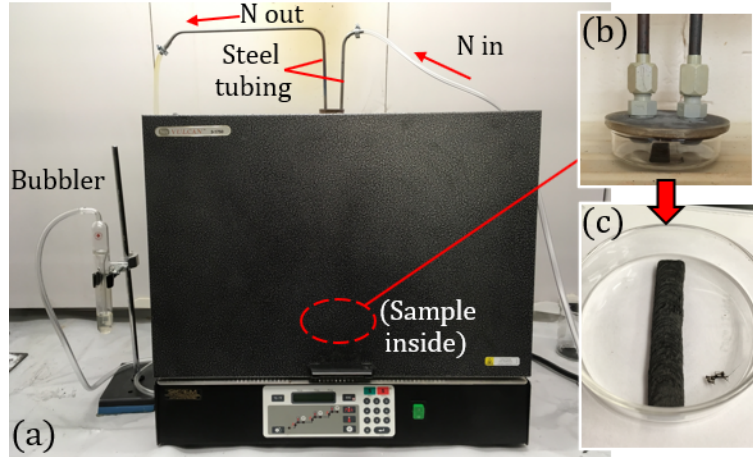


Figure 4.8: Burn-off testing setup for 3D printed specimen. (a) Ney Vulcan 3-1750 box furnace. (b) Specimen enclosed in a petri dish with custom aluminum lid, sitting inside the furnace. (c) Specimen after burn-off test.

fiber-acetone solutions were poured into petri dishes, as in Figure 4.9b, immediately after sonication before the fibers had time to settle at the bottom of the beakers. Sharma et al. found that after sonicating fibers from a long-fiber thermoplastic burn-off sample in water and pouring the water-fiber solution into several petri dishes, the petri dish selected for FLD measurement was of little consequence [139]. Therefore, only one petri dish for the pellet and one for the printed specimen were taken for the FLD measurements. One advantage of using acetone rather than water in the sonication process was that the acetone dried much faster, decreasing the wait-time needed before the fibers could be examined under a microscope and measured.

4.1.2.2 Measuring the fibers - first study. To characterize the fiber geometric aspect ratio ($a_r = L_f/d_f$), both fiber lengths and fiber diameters needed to be measured. The lengths were measured with a Keyence VR-3000 One-shot Measurement Macroscope which connects to a local computer as depicted in Figure 4.10a. The Keyence software displays a live micrograph and allows a user to measure a fiber by performing a mouse click on both of its ends. Figure 4.10b shows an example of what this looks like. The Keyence software also allows the user to stitch together up

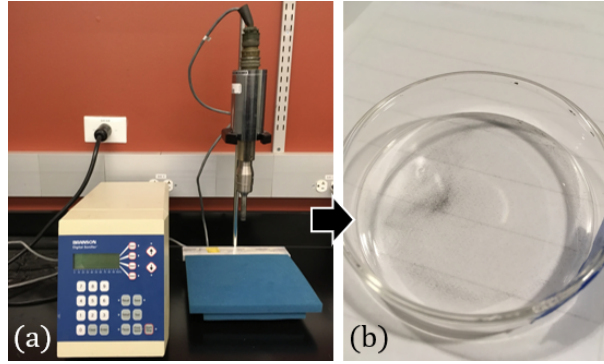


Figure 4.9: (a) Branson Digital Sonifier 450 used for dispersing fibers in a beaker of acetone. (b) Fiber-acetone mixture after sonication, in a petri dish. (The fibers are very small.)

to 100 images to create a larger, high magnification image. To image an entire petri dish, a magnification of 25x was used. This resulted in a poor resolution image, however, making it difficult to distinguish fiber ends in some areas where the fibers overlapped each other as shown in Figure 4.10b. It is difficult to quantify how much measurement error was caused by this problem, so this was one of the reasons a second aspect ratio study with more refined methods was warranted.

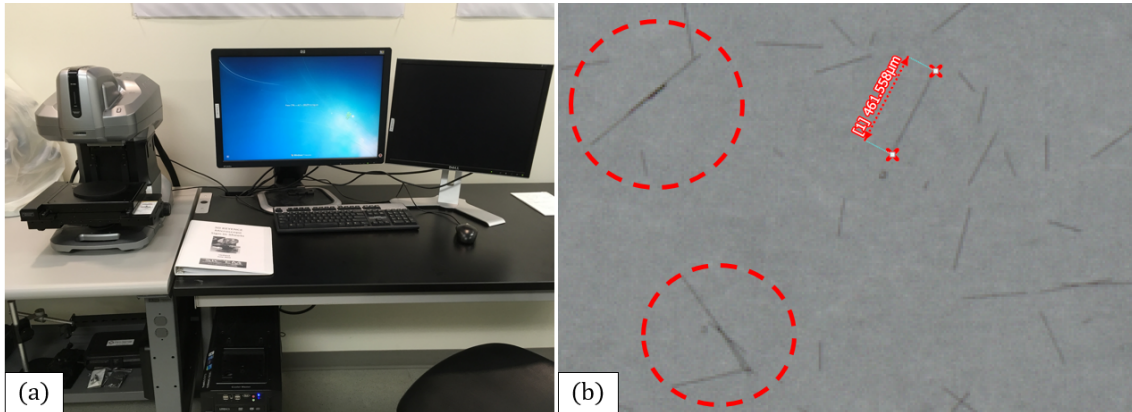


Figure 4.10: (a) Keyence VR-3000 One-shot Measurement Macroscope used for imaging fibers. (b) Keyence micrograph showing a typical fiber length measurement. Circles highlight areas where distinguishing between different fibers can be difficult when using the Keyence system.

Sharma et al. discovered that for long-fiber thermoplastic composites, a sample size of 800 fibers would yield a number-average and weight-average fiber length that

were less than 5% different from the number-average and weight-average length of a sample size of 2000 fibers [139]. Therefore, 800 fibers were measured in this study from both the pellet and 3D printed burn-off specimens.

To measure the diameters of the carbon fibers, a higher magnification microscope was needed. Thus, a JEOL JSM-6610LV Scanning Electron Microscope (SEM), pictured in Figure 4.11a, was used. Typical fiber diameter measurements are shown in Figure 4.11b at a magnification of 1100x.

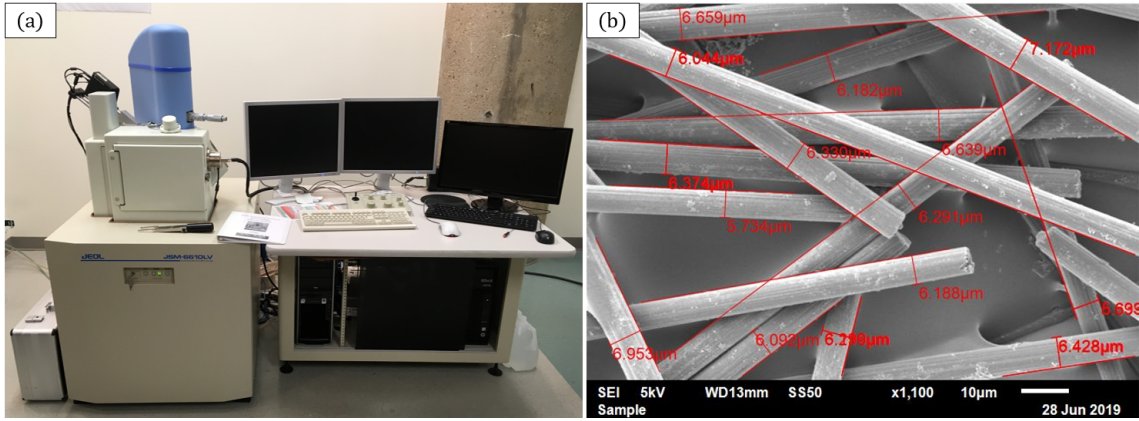


Figure 4.11: (a) JEOL JSM-6610LV Scanning Electron Microscope. (b) SEM micrograph with fiber diameter measurements.

4.1.2.3 Preparing and measuring the fibers - second study. For the second study, the carbon fibers were sampled from three stages of the printing process shown in Figure 4.12: the pellet, the extrudate (pre-deposition), and the printed bead (post-deposition). The deposited bead was printed at 250°C on a 95°C heated print bed. Burn-off specimens of 1 inch in length were sampled from the extrudate and printed bead and burn tested according to the following procedure: (1) 40°C/min temperature ramp up to 600°C, (2) hold isothermal 1 hour in nitrogen, and (3) hold isothermal for 10 minutes in air. The same burn-test configurations were used in this study as in the previous study. Thus, the TA Instruments TGA machine was used to burn-test the pellet, whereas the Ney Vulcan furnace with a nitrogen fed petri dish enclosure was used for the 1 inch extrudate and printed bead specimens.

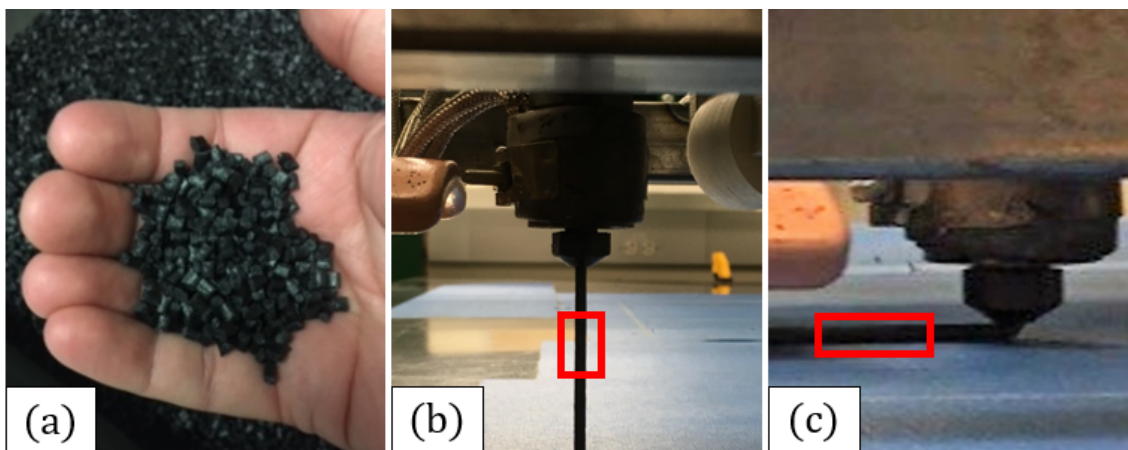


Figure 4.12: Sampling for second fiber aspect ratio characterization study.

After dispersing the fibers by sonication and pouring them into a petri dish as done in the previous study, the fibers were measured using an MZ7 microscope, shown in Figure 4.13a, and a custom MATLAB code written in-house. Micrographs were captured and stitched together in Adobe Photoshop CC 2017 before using the custom MATLAB analysis code. The custom MATLAB code allows a user to measure a fiber by performing two mouse-clicks on the ends of the fiber and automatically saves the data to a file to be added to or analyzed later. The correct length of the fiber is calculated by scaling the pixel distance between the two points that were clicked by using a known distance found from performing two mouse-clicks on a microscope ruler slide. Having the ability to use the MATLAB code to measure the fibers, as opposed to using software provided by a microscope manufacturer, allows a user to pause and resume measuring the fibers when desired rather than requiring the user to measure all the fibers in one sitting. It also allows the user to continue measuring fibers off-location while leaving the microscope open for others to use. A micrograph opened in MATLAB is displayed in Figure 4.13b to illustrate collecting the length measurement data. Clearly, it is much easier to see the fiber ends with the MZ7 microscope as opposed to the Keyence system (compare Figure 4.13b with Figure 4.10b).

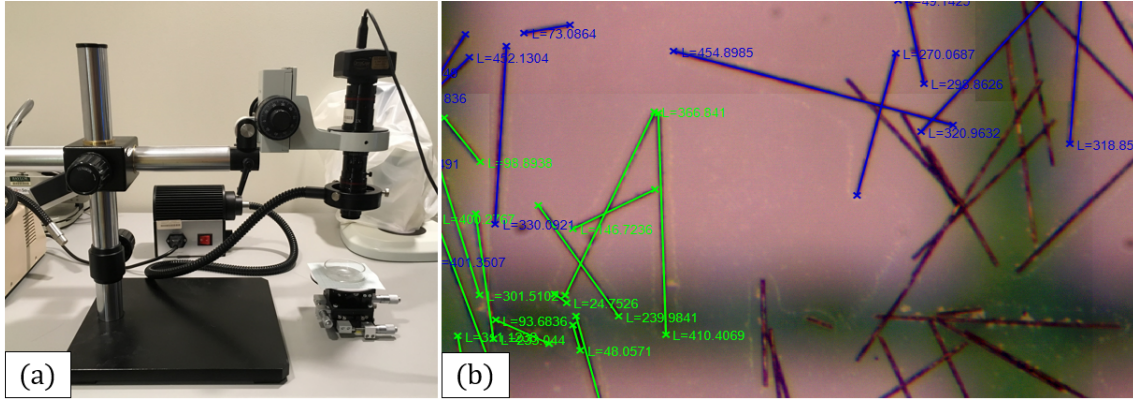


Figure 4.13: (a) MZ7 microscope used to capture micrographs of fibers in a petri dish. (b) Micrographs were stitched together in Adobe Photoshop CC 2017 to measure the fiber using a custom MATLAB code. The measurement data, shown in green, is saved from a previous measurement session, whereas the blue data is from the current measurement session.

4.1.3 Strength Testing

Prior to printing the test specimens for strength testing, the 13% CF-ABS was dried at 82°C for 4 hours and stored in an environmental chamber with a -40°C dew point to keep it dry until it was ready to be printed. Large (31"×6") rectangular prints were made according to the dimensions provided in Figure 4.14. These rectangular prints were printed and sectioned for the strength specimens. The heated bed was not turned on to print the rectangles because the bed bowed too much due to the heat. For a uniformly heated print bed, this would likely not have been as much of an issue.

For printing the samples, the extruder temperature zones were set to 200°C, 205°C, and 210°C and were observed to stay within $\pm 3^\circ\text{C}$ during printing. In addition, the extruder RPM was set to 2250 and the nozzle-to-bed distance was set to 0.1181 inches (3 mm), matching the distance in the COMSOL flow model presented earlier. Neat ABS samples were also printed using the same printing conditions.

After printing, the top of the printed material was wavy. Thus, before completing all of the cuts to obtain the strength specimens, the material was milled on the top surface to ensure a constant, rectangular cross section and dimensional

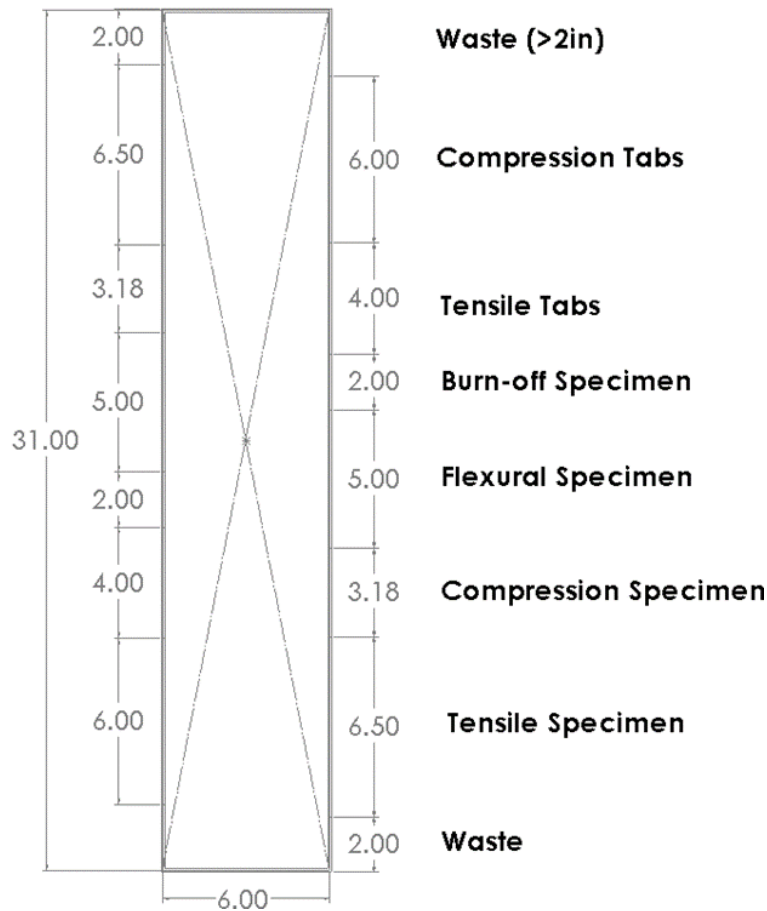


Figure 4.14: Printed rectangle from which strength specimens were cut. Dimensions are shown in inches.

consistency between the strength specimens. The strips of material tended to kick out from under the mill. Therefore, the strips were taped down with packing tape to a piece of flat, 8020 aluminum, as shown in Figure 4.15, to help keep them fixed during milling. After machining, the specimens were measured, cut, and labeled. To cut out the specimens, the Buehler IsoMetTM Low Speed Precision Cutter pictured in Figure 4.16 was used. After cutting, the strength specimens were cleaned and tabs were bonded to the tensile and compressive specimens using an adhesive. To cure the adhesive, the specimens were dried in an oven at 82°C for an hour.

Warping, as shown in Figure 4.17, was observed in the tensile specimens after their tab adhesive was cured, so an additional heating procedure was performed.

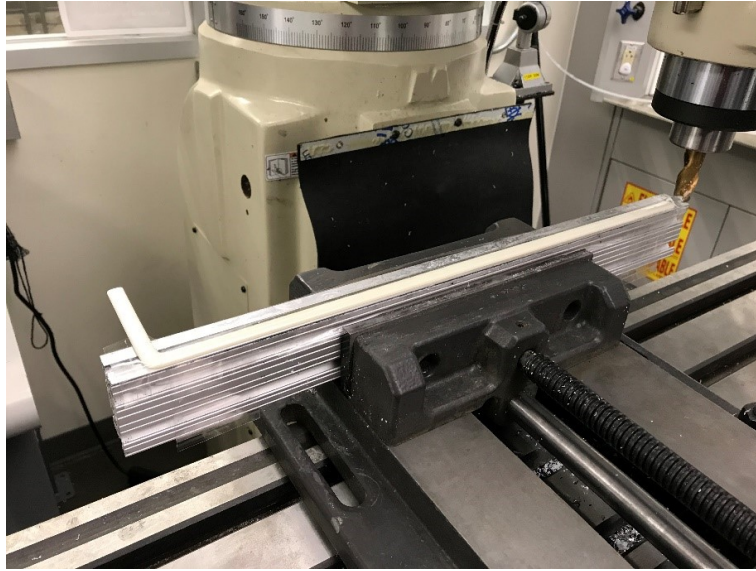


Figure 4.15: Strip of ABS taped with clear packing tape to 8020 aluminum for milling.

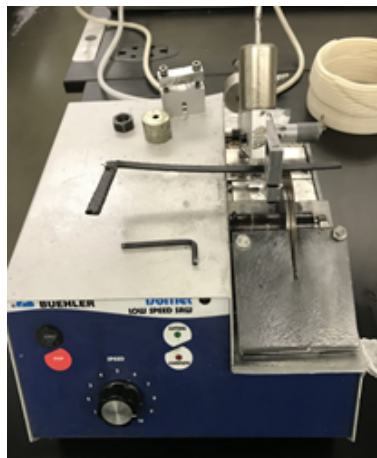


Figure 4.16: Buehler IsoMet™ Low Speed Precision Cutter used for cutting out specimens.



Figure 4.17: Warping of a tensile specimen after curing adhesive.

The specimens were heated at 110°C (slightly above the T_g of Neat ABS) between 10-15 minutes to take out the warp, although the time for this procedure was not well documented. It was discovered that care must be taken when performing a heat procedure like this so as to avoid overcorrecting the bow. The tensile specimens used for testing are shown in Figure 4.18. The compression specimens were not heat-treated since there was much less noticeable warping in them since they were considerably shorter than the tensile samples. After heat-treating the tensile specimens, the sides of the tensile, compressive, and flexural specimens were milled flat.

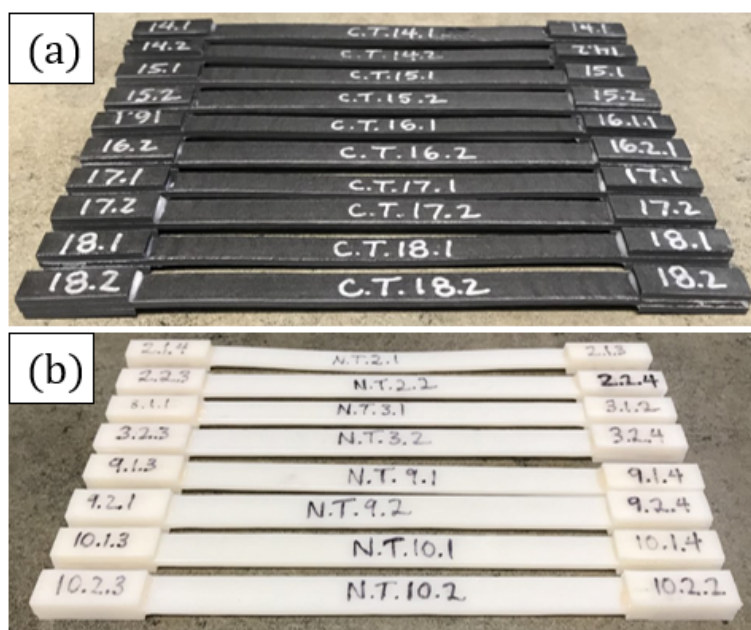


Figure 4.18: Tensile specimen tabbed, heat-treated, milled, and ready for testing: (a) 13% CF-ABS, (b) Neat ABS.

4.1.3.1 Tensile testing. For tensile testing, a Test Resources 810 Series fatigue tester with a F2500-B load cell was used as shown in Figure 4.19. Figure 4.20 shows a mounted tensile specimen with and without the extensometer used for measuring the strain. The specimens were tested at a speed of 0.059 in/min with a data collection rate of 20 Hz and at a temperature of approximately 21°C (70°F). Three width and three thickness measurements were taken for each specimen using micrometers in

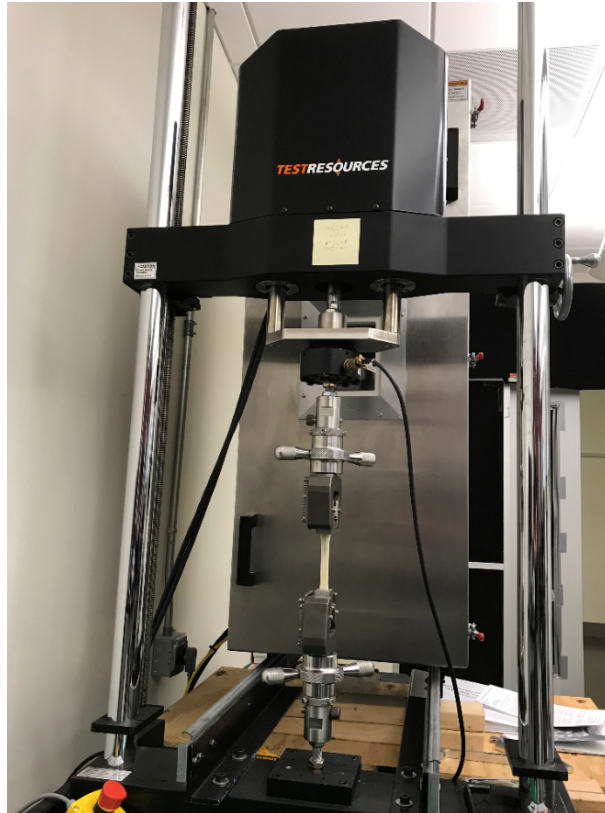


Figure 4.19: Test Resources 810 Series fatigue tester.

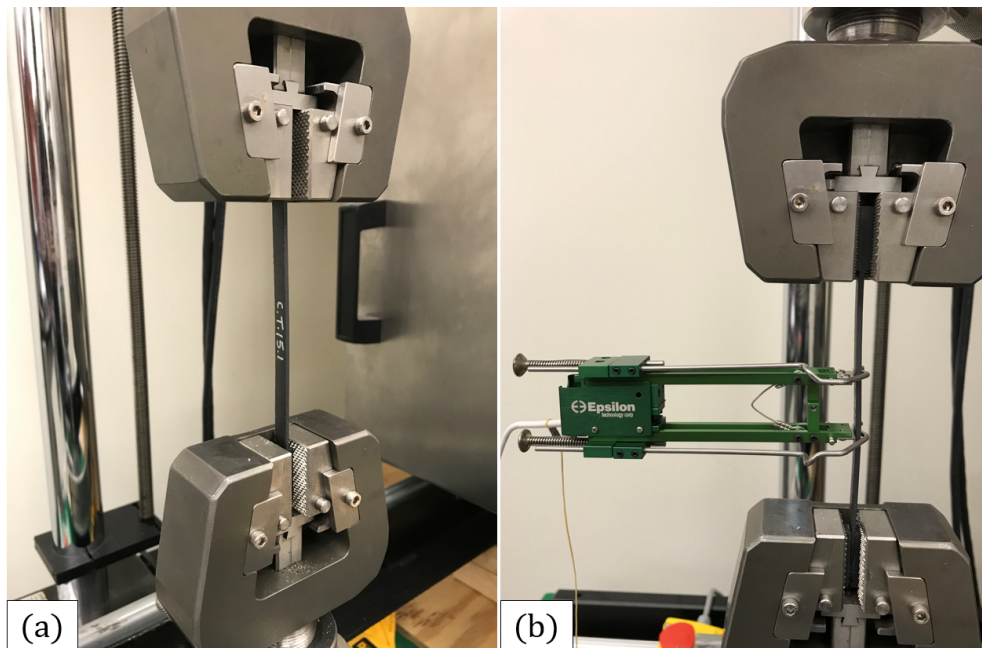


Figure 4.20: Tensile testing setup (a) without an extensometer and (b) with a 1 inch Epsilon 3542-0100-100-HT2 extensometer.

or near the gage region prior to testing. Prior to measuring the specimens' widths and thicknesses with micrometers, the micrometers' calibration was checked using a 0.125 in, a 0.135 in, and a 0.5 in NIST traceable gage block. The values measured for these blocks were, respectively, 0.125 in, 0.1350 in, and 0.50001 in. The width and thickness measurements were averaged to obtain the cross-sectional area of each specimen (average width \times average thickness), from which the stress was calculated (load divided by average initial cross-sectional area).

4.1.3.2 Compression testing. The same Test Resources 810 Series fatigue tester with the same F2500-B load cell was also used for compression testing. Figure 4.21 shows a mounted compression specimen. A confined compression test was done using a modified ASTM D695 compression test fixture (Boeing BSS 7260). Three width measurements were taken for each compression specimen, two on either end and one in the middle. Since the compression specimens had tabs covering most of their length, as can be seen in Figure 4.21b, only one thickness measurement was taken in the middle of the specimens and this was done with calipers since the micrometer anvils did not fit between the tabs. The average width and the thickness measurements were used to calculate the cross-sectional areas of the specimens, from which the stress was derived. The length of each specimen was also measured and used to calculate the approximate strain. The upper compression platen was lowered to be in contact with the compression specimen before initiating a test. Each compression test was conducted at 0.051 in/min (1.3 mm/min, as called for by ASTM D695) with a data collection rate of 20 Hz and an environmental temperature of about 21-22°C (70-71°F).

4.1.3.3 Flexural testing. A 100 Series Test Resources machine with a 1000 lbf force transducer was used for three-point bend, or flexural, testing. Figure 4.22

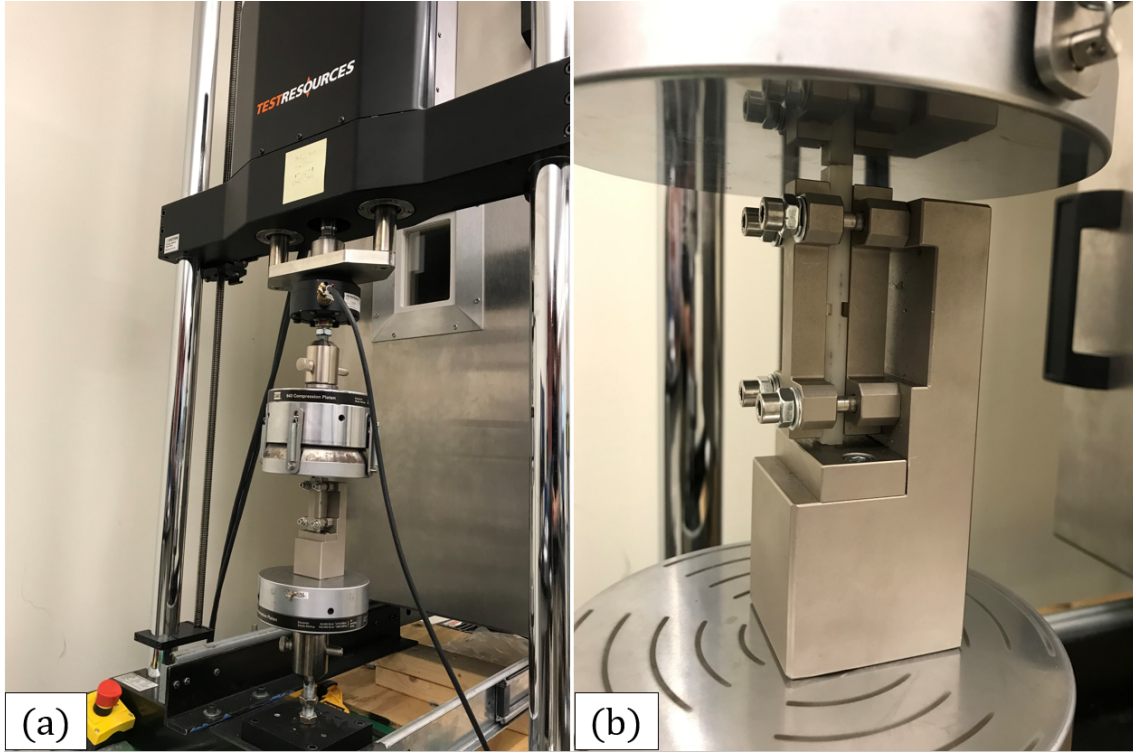


Figure 4.21: Compression testing setup (a) far view (b) close-up view of compression specimen inserted in the modified ASTM D695 compression test fixture (Boeing BSS 7260).

shows a mounted flexural specimen. Three width and three thickness measurements were made with micrometers for each flexural specimen and the averages taken to calculate the cross-sectional area and, subsequently, the stress for each test. The control rate for the crosshead was calculated according to the following equation from ASTM D790-17 [127] for each test:

$$R = 0.01L^2/6d \quad (4.1)$$

where R is crosshead rate, L is span length, and d is specimen thickness. According to the standard, a test is supposed to terminate at break or at a maximum strain of 0.05 mm/mm in the outer surface. This corresponds to a maximum deflection of

$$D = 0.05L^2/6d \quad (4.2)$$

where D is the deflection of the midspan, L is the span length, and d is the specimen

thickness [127]. Therefore, D was calculated for each specimen and used to define the termination setting for each test in case a specimen did not break during testing. For each test, the machined side of the flexural sample faced upward, as can be seen in Figure 4.22b. In addition, a data collection rate of 25 Hz was used and the environmental temperature was about 23°C (73°F) for each test.

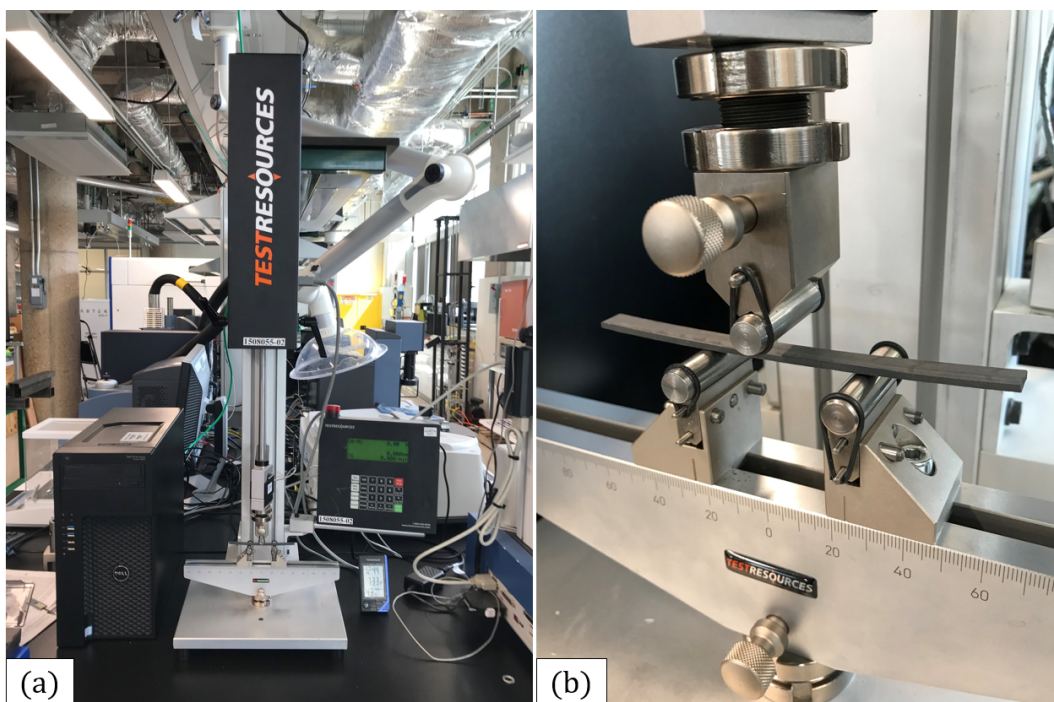


Figure 4.22: Flexural testing set up. (a) 100 Series Test Resources machine with a 1000 lbf load cell. (b) Close-up of testing specimen, ready for testing.

4.1.3.4 Additional TGA testing. Since the expected fiber volume fraction of the 13% CF-ABS was 13% but Figure 4.6 showed a considerably smaller weight percent at the end of a TGA test, more TGA testing was warranted to ascertain the actual fiber content in the 13% CF-ABS. Therefore, additional TGA tests were done using the aforementioned TA Instruments Q50 TGA machine. Testing based on ASTM E1131-20 [140] was performed on several pellet samples of both Neat ABS and the 13% CF-ABS, both from the same manufacturer, to determine the fiber content. In addition, for further confirmation, several samples of the Neat ABS and 13% CF-ABS were tested in the TGA based on ASTM D3171-15 [141].

For all of the tests based on ASTM E1131-20, the pellet samples weighed between 15-21 mg. In addition, the following test procedure was used for each: (1) in nitrogen, ramp 10°C/min up to 750°C, (2) switch to air and hold isothermal for 1 min, (3) ramp 10°C/min up to 800°C, (4) switch back to N before ending the test. The procedure was chosen to be similar to that for polyethylene as described in Table 2 of ASTM E1131-20. The amount of highly volatile matter, medium volatile matter, combustible matter, and ash were quantified for each test. Quantities from the tests of the Neat ABS were subtracted from the respective quantities of the tests of the 13% CF-ABS to obtain the fiber content. The results of the tests are given in Section 4.2.5.

For all of the tests based on ASTM D3171-15, the pellet samples weighed between 15-21 mg. In addition, the following test procedure was used for each: (1) in nitrogen, jump from ambient temperature to 560°C, (2) hold isothermal for 1 hour, (3) jump to 23°C and equilibrate. The procedure was chosen to be similar to Procedure H of ASTM D3171-15. The results are given in Section 4.2.5.

4.2 *Experimental Results*

4.2.1 *Fiber Aspect Ratio Characterization*

There are two items to note before presenting the fiber aspect ratio results. First, the methodology used in the fiber diameter measurements from the second study showed a large amount of error compared to the measurements from the first study. The measurements from the first study are more reliable since an SEM microscope was used and the fibers could be observed with a much higher resolution when they were measured. Thus, the average fiber diameter measurement from the first study was used to calculate the aspect ratios in both the first and second studies. This is acceptable since the fiber diameters do not shrink during processing

and therefore should be similar from one study to the next. Secondly, in the second study a correction factor, Δx , was introduced to account for fiber decomposition in the last step of the burn-off tests where the environment was switched from nitrogen to air. This idea is used to update the results of the first study that were published in [36] as well.

To obtain the fiber decomposition correction factor, Δx , it is assumed that the surface of the fiber decomposes the same amount, Δx , in both the length and width directions as shown in Figure 4.23. Thus, the final, measured fiber length and diameter are $L_m = L_o - \Delta x$ and $d_m = d_o - \Delta x$, respectively, where L_o and d_o are the initial fiber length and diameter, respectively.

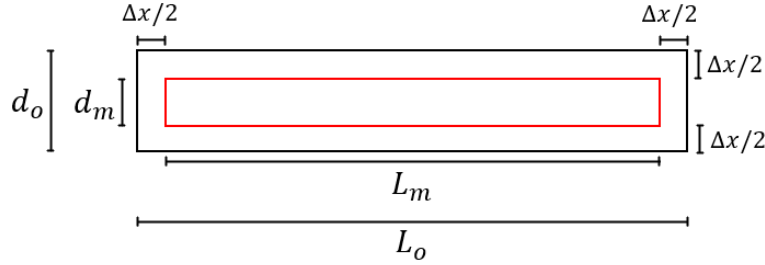


Figure 4.23: Fiber decomposition diagram.

To determine Δx , a burn-off test of carbon fiber alone was performed, the results of which are shown in Figure 4.24. There is a drop of $\Delta w_2 = 14.09\%$ in the weight of the carbon fiber from time $t=0$ to $t=t_2$ and a drop of $\Delta w_3 = 21.90\%$ from $t=0$ to $t=t_3$. Time $t=t_1$ is the time at which the environment is switched from nitrogen to air, t_2 is 5 minutes after t_1 , and t_3 is 10 minutes after t_1 . For an initial weight of w_o at $t=0$ and a weight of w_i at time $t=t_i$,

$$\Delta w_i = \frac{w_o - w_i}{w_o} \times 100\% \quad (4.3)$$

Using the fact that $w = mg = \rho V g$, where V is the volume and $g = 9.81 \text{ m/s}^2$ is the gravitational constant, and assuming the fibers are cylindrical, the above equation

can be re-written as

$$\Delta w_i = \frac{\rho_f \pi ((d_m + \Delta x)/2)^2 (L_m + \Delta x) g - \rho_f \pi (d_m/2)^2 L_m g}{\rho_f \pi ((d_m + \Delta x)/2)^2 (L_m + \Delta x) g} \times 100\% \quad (4.4)$$

Note, the terms ρ_f , π , and g cancel. Furthermore, since Δw_i comes from the TGA results given in Figure 4.24 and d_m and L_m are found experimentally, the above equation can be solved for the correction factor, Δx .

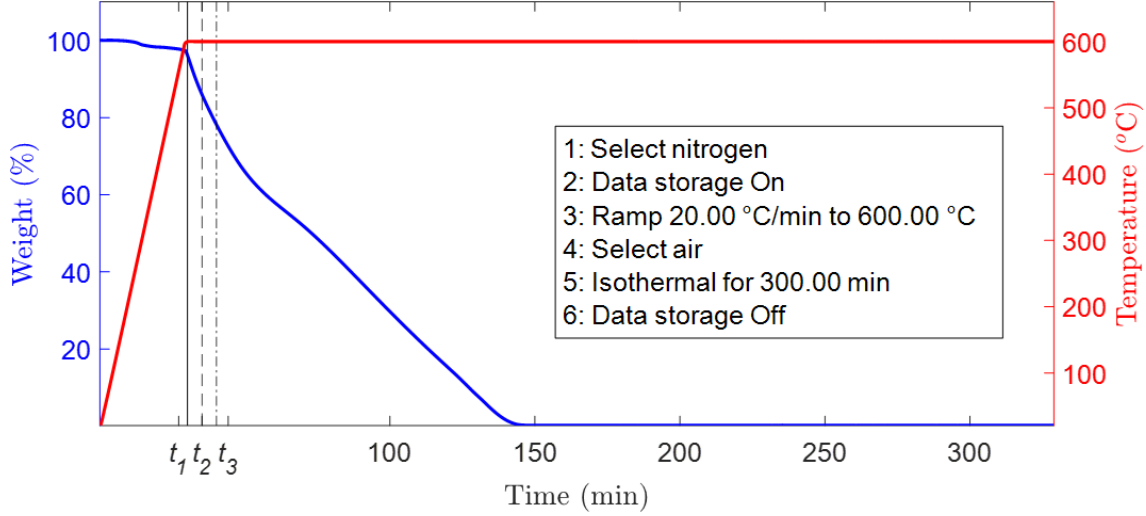


Figure 4.24: Burn-off test of carbon fiber.

For the pellet in the first study, the measured fiber diameter d_m was taken as the average of 14 fiber diameter measurements. For the printed bead in the first study, d_m was taken as the average of 24 fiber diameter measurements. For the second study, the same values are used for the pellet and bead, respectively, and their average is assigned to d_m for the extrudate specimen. These values are presented in Table 4.1. Next, the “measured” fiber length L_m is taken as the number-average and weight-average length given, respectively, by the following equations

$$L'_n = \frac{\sum N_i L_i}{\sum N_i} \quad (4.5)$$

$$L'_w = \frac{\sum N_i L_i^2}{\sum N_i L_i} \quad (4.6)$$

where N_i is the number of fibers in the i^{th} histogram bin and L_i is the length of the i^{th} fiber. These values are also presented in Table 4.1.

Table 4.1: Length and diameter measurements for fiber aspect ratio characterization.

Study	Property	Pellet	Extrudate	3D Printed Bead
Study 1	L'_n (μm)	342.36	-	272.66
	L'_w (μm)	462.79	-	341.23
	d_m (μm)	6.93	-	6.37
Study 2	L'_n (μm)	291.77	270.12	168.39
	L'_w (μm)	422.89	347.35	278.08
	d_m (μm)	6.93	6.65	6.37

The corrected forms of the values given in Table 4.1 are given by Equation 4.7 where the correction factor Δx_n is found by letting $L_m = L'_n$ in Equation 4.4 and the correction factor Δx_w is found by letting $L_m = L'_w$ in Equation 4.4.

$$d_n = d_m + \Delta x_n \quad (4.7a)$$

$$d_w = d_m + \Delta x_w \quad (4.7b)$$

$$L_n = L'_n + \Delta x_n \quad (4.7c)$$

$$L_w = L'_w + \Delta x_w \quad (4.7d)$$

In addition, the number-average and weight-average fiber aspect ratios are approximated by

$$a_{rn} = L_n/d_n \quad (4.8)$$

$$a_{rw} = L_w/d_w \quad (4.9)$$

All of the corrected values are given in Table 4.2. L_n and L_w are also indicated in Figures 4.25 and 4.26 which give the FLD histogram plots for the first and second aspect ratio studies, respectively.

Figures 4.25 and 4.26 show that the weight- and number-average fiber length decrease during processing, indicating process-induced breakage. The decrease in these average lengths is quite significant as well. In addition, interestingly, a bimodal fiber length distribution was measured in both studies.

Table 4.2: Corrected fiber aspect ratio measurements.

		Pellet	Extrudate	3D Printed Bead
Study 1	L_n (μm)	343	-	273
	L_w (μm)	463	-	342
	d_n (μm)	7.47	-	7.20
	d_w (μm)	7.47	-	7.20
	a_{rn} (μm)	45.9	-	38.0
	a_{rw} (μm)	62.0	-	47.5
Study 2	L_n (μm)	293	271	169
	L_w (μm)	424	348	279
	d_n (μm)	7.83	7.51	7.19
	d_w (μm)	7.83	7.51	7.20
	a_{rn} (μm)	37.4	36.1	23.5
	a_{rw} (μm)	54.1	46.3	38.8

Using the data from the second fiber aspect ratio study in Figure 4.26, one can gain insight into how much the different stages of the LAAM process reduce the properties of the printed SFRP material. Using the 2D flow model from Chapter Three, the RSC fiber orientation model with $C_I = 0.0019$ and $\kappa = 0.125$, and the laminate analogy approach, the tensile/compressive stiffness and flexural stiffness were predicted. For the pre-processed pellet, $a_r = 54.1$ from Table 4.2 and the predicted stiffnesses are $E_{LT}^{lam} = E_{LC}^{lam} = 7.38$ GPa from Equation 2.43 and $E_{LF}^{lam} = 9.30$ GPa from Equation 2.44. For the extrudate (pre-deposition) specimen, $a_r = 46.3$, $E_{LT}^{lam} = E_{LC}^{lam} = 7.10$ GPa and $E_{LF}^{lam} = 8.90$ GPa. For the printed bead (post-deposition), $a_r = 38.8$, $E_{LT}^{lam} = E_{LC}^{lam} = 6.74$ GPa and $E_{LF}^{lam} = 8.36$ GPa. These results indicate that E_{LT}^{lam} decreases by 3.75% during extrusion and 5.13% during deposition, leading to a total reduction of approximately 8.69%, which corresponds to about 0.64 GPa. The flexural stiffness drops by 4.37% during extrusion and 6.00% during deposition, leading to a total loss of 10.1%, or about 0.94 GPa. These results suggest the deposition stage, between when the material leaves the nozzle tip and ends up on the print bed, is more damaging than the extrusion stage of processing.

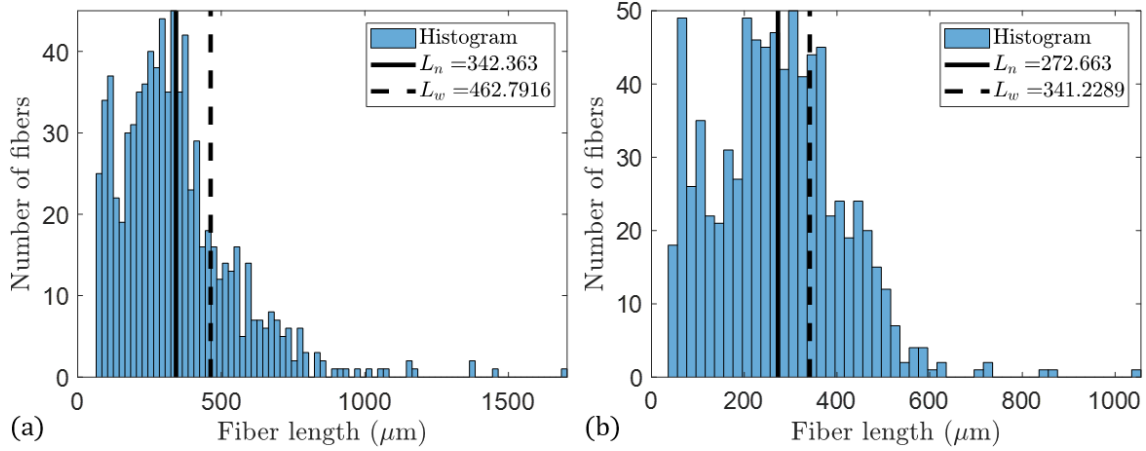


Figure 4.25: Study 1: fiber length distributions from, (a) the pre-processed pellet, and (b) the printed bead.

It would be interesting to examine this problem further to see if there are methods, perhaps adjusting nozzle height or the angle of the nozzle relative to the print bed, that could be used to mitigate fiber breakage and thereby retain the properties of the raw pellets.

4.2.2 Tensile Testing Results

Typical tensile stress-strain plots for LAAM-printed Neat ABS and 13% CF-ABS specimens are shown in Figures 4.27a and b, respectively. Five Neat ABS and four 13% CF-ABS tensile specimens were tested. The stiffness of the tensile specimens, E_{LT}^{eff} , was found over the strain range 0.003-0.005. In addition, the yield strength, σ_{LT}^{eff} , was determined by using a 0.2% strain offset. That is, a line parallel to the elastic region was extended from (0, 0.002) up to the stress-strain curve, and the stress at the intersection point was taken as σ_{LT}^{eff} . A toe region sometimes appeared at the beginning of the stress-strain curves for the 13% CF-ABS samples, as in Figure 4.27b. As noted in ASTM D638, this is due to taking up of slack in the system and does not represent a material property [142]. Therefore, the data was horizontally shifted so that the E_{LT}^{eff} lines would intersect the origin. Then the 0.2% offset was determined from the shifted data to obtain the yield strength.

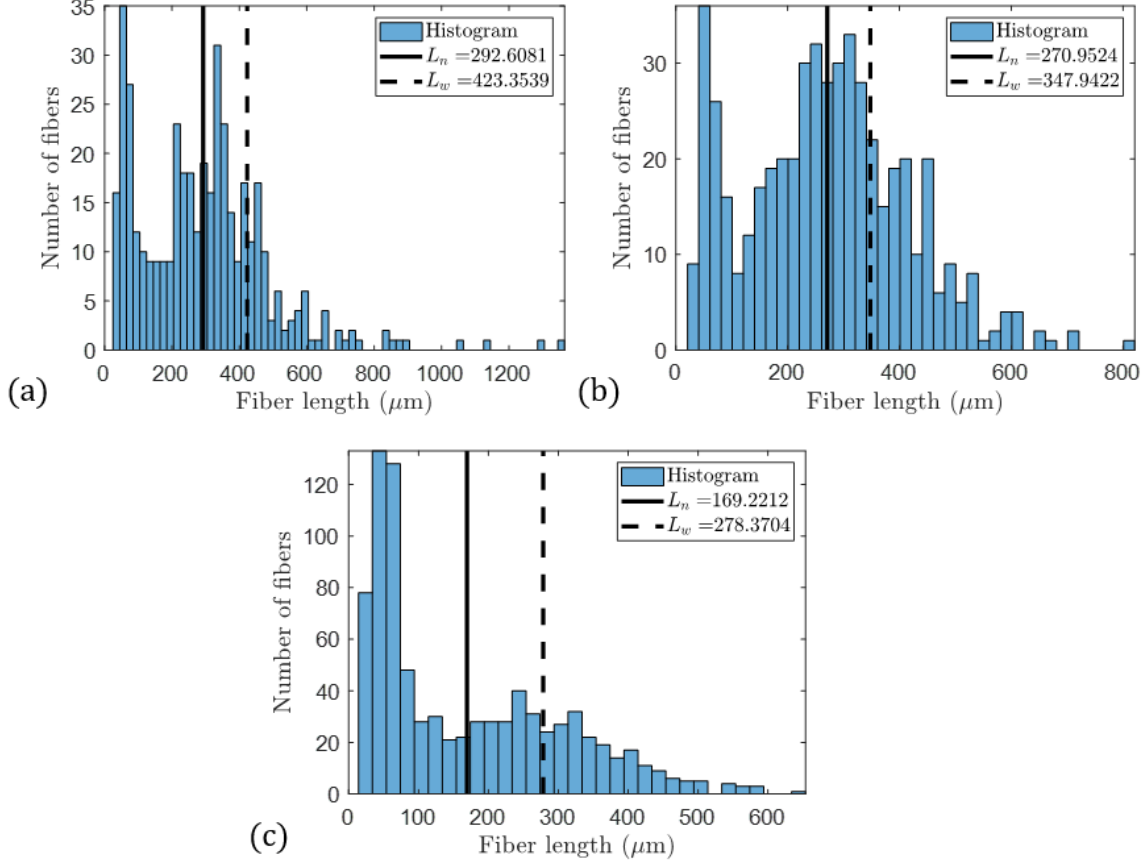


Figure 4.26: Study 2: fiber length distributions from, (a) the pre-processed pellet, (b) the extrudate (pre-deposition), and (c) the printed bead (post-deposition).

The statistics for the experimental results are given in Table 4.3 where \bar{x} is an average property, s_{n-1} is the standard deviation, and CV is the coefficient of variation defined in ASTM D3039, respectively, as

$$\bar{x} = \left(\sum_{i=1}^n x_i \right) / n \quad (4.10)$$

$$s_{n-1} = \sqrt{\left(\sum_{i=1}^n (x_i^2) - n\bar{x}^2 \right) / (n-1)} \quad (4.11)$$

$$CV = 100 \times s_{n-1} / \bar{x} \quad (4.12)$$

where x_i is a measured property and n is the number of specimens [138]. In addition, σ^{ult} is the ultimate tensile strength. The stress-strain curves for the remaining specimens are also provided in Appendix B.

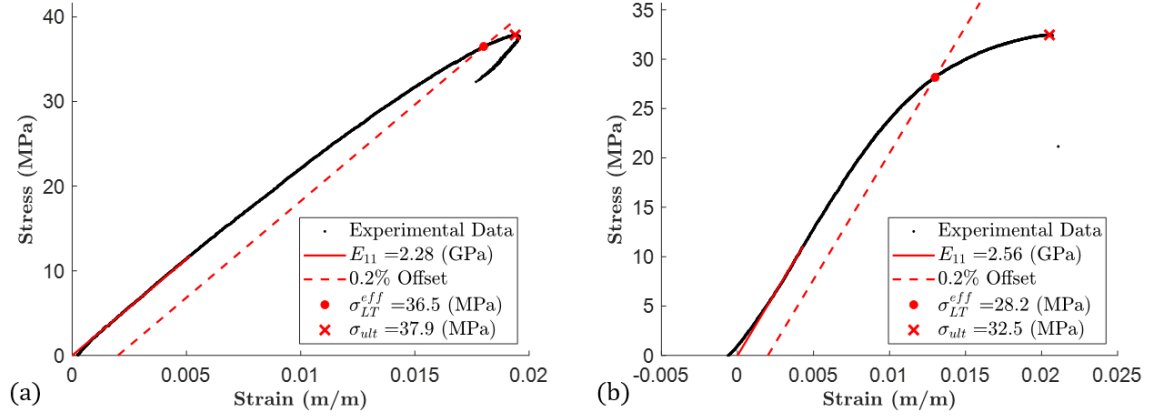


Figure 4.27: Tensile stress-strain plots: (a) Neat ABS and (b) 13% CF-ABS.

Table 4.3: Tensile testing statistics.

		Minimum	Maximum	\bar{x}	s_{n-1}	CV
Neat ABS	E_{LT}^{eff}	2.13 GPa	2.29 GPa	2.22 GPa	0.0672 GPa	3.03%
	σ_{LT}^{eff}	36.3 MPa	37.9 MPa	37.0 MPa	0.613 MPa	1.66%
	σ_{LT}^{ult}	37.5 MPa	38.8 MPa	38.0 MPa	0.465 MPa	1.22%
13% CF-ABS	E_{LT}^{eff}	2.56 GPa	2.88 GPa	2.71 GPa	0.163 GPa	6.04%
	σ_{LT}^{eff}	25.9 MPa	28.2 MPa	27.3 MPa	1.04 MPa	3.79%
	σ_{LT}^{ult}	30.5 MPa	32.8 MPa	32.0 MPa	1.04 MPa	3.24%

The 13% CF-ABS was stiffer than the Neat ABS as expected, but interestingly had a lower tensile yield strength, σ_{LT}^{eff} , and a smaller ultimate tensile strength, σ_{LT}^{ult} . The lower strength in the 13% CF-ABS is likely due, at least in part, to a higher void content which can knock down the mechanical properties of a material (e.g., [143]). In Section 4.3.3, corrections for void content are made to the modeling results presented earlier in this dissertation to achieve results that are closer to the experimental results. Another note, is that the properties of the Neat ABS are comparable to those that were used for the model inputs given in Table 3.1.

4.2.3 Compression Testing Results

Typical compressive stress-strain curves for the compression tests of LAAM-printed Neat ABS and 13% CF-ABS specimens are shown in Figures 4.28a and b,

respectively. A total of five compression tests were performed for the neat ABS and five for the 13% CF-ABS. The compressive stiffness was determined over the stress range 25-35 MPa, because the length of the toe region of each curve was not consistent. In addition, the effective longitudinal compressive yield strength, σ_{LC}^{eff} , was determined using a 0.2% strain offset. A distinct toe region appears in all of the compression stress-strain graphs, so all of the data was horizontally shifted before determining σ_{LC}^{eff} .

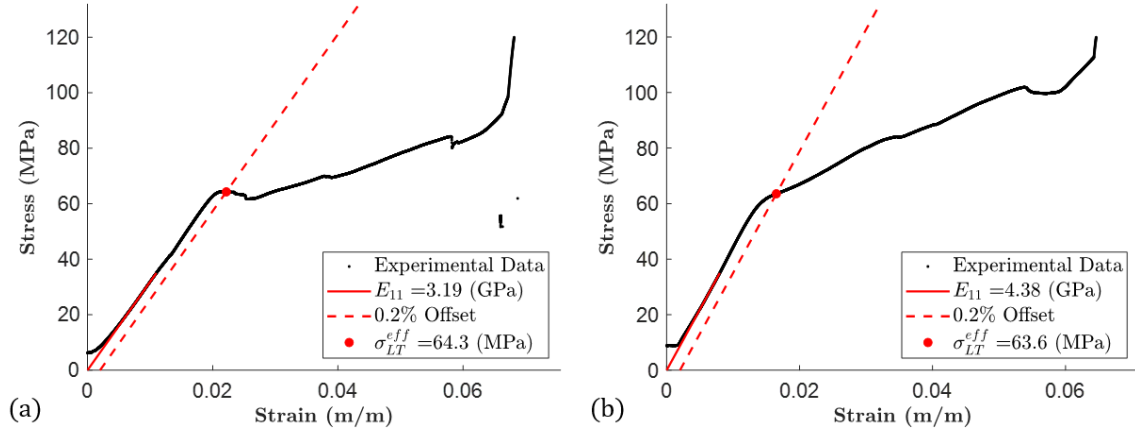


Figure 4.28: Compression stress-strain plots: (a) Neat ABS and (b) 13% CF-ABS.

The statistics for the compression tests are given in Table 4.4, where Equations 4.10-4.12 have been used. The ultimate compressive strength values are absent from the table because, in general, the compressive specimens did not fail catastrophically. Rather, the upper platen would come in contact with the top of the metal test fixture before complete failure of the specimen. This caused the stress data to shoot upwards at the end of the tests, which can be seen in Figure 4.28a. The stress data has been trimmed from the plots however, so that the physically meaningful regions of interest are visible. Once again, the experimental statistics reveal that the compressive stiffness of the 13% CF-ABS outperformed the compressive stiffness of the Neat ABS but, the compressive strength of the Neat ABS was higher than that of the 13% CF-ABS. It is likely that a higher void content in the 13% CF-ABS specimens is at least partially responsible for this unexpected result. It is also

noteworthy that the compressive stiffness and strength surpass the tensile stiffness and strength. The stress-strain plots for all of the compression tests are given in Appendix C and are summarized in Table 4.4.

Table 4.4: Compression testing statistics.

		Minimum	Maximum	\bar{x}	s_{n-1}	CV
Neat ABS	E_{LC}^{eff}	3.15 GPa	4.33 GPa	3.72 GPa	0.524 GPa	14.1%
	σ_{LC}^{eff}	56.1 MPa	69.1 MPa	65.3 MPa	5.52 MPa	8.44%
13% CF-ABS	E_{LC}^{eff}	3.65 GPa	4.42 GPa	4.06 GPa	0.336 GPa	8.28%
	σ_{LC}^{eff}	45.4 MPa	64.7 MPa	58.6 MPa	7.72 MPa	13.2%

4.2.4 Flexural Testing Results

Typical three-point bend test results are shown in Figures 4.29a-d for neat ABS and 13% CF-ABS. Two ways of measuring the deflection of the middle of the specimen are considered valid by ASTM D790-17, one using a deflectometer and the other using the displacement of the cross-head [127]. The second method is used in this study but required a data-correcting procedure to account for “slack” in the test setup, as stipulated in ASTM D790-17 [127]. The procedure involves performing a three-point bend test on a very stiff bar, such as a steel bar, with an identical control rate and termination setting as that used for the material being tested. This data is subtracted from the test data of the material in question to get corrected data from which the stiffness is determined. Figure 4.29a shows the load-deflection results from a steel bar and a specimen of neat ABS, along with corrected data for the neat ABS specimen. Figure 4.29b shows the stress-strain curve of the neat ABS after correcting the data, along with the stiffness and strength results. In addition, Figure 4.29c shows the load-deflection results from a 13% CF-ABS specimen and Figure 4.29d shows the corrected stress-strain curve for this specimen.

The stress and strain in Figures 4.29b and d were obtained from the load and deflection data in Figures 4.29a and c using Equations 4.13 and 4.14, which come

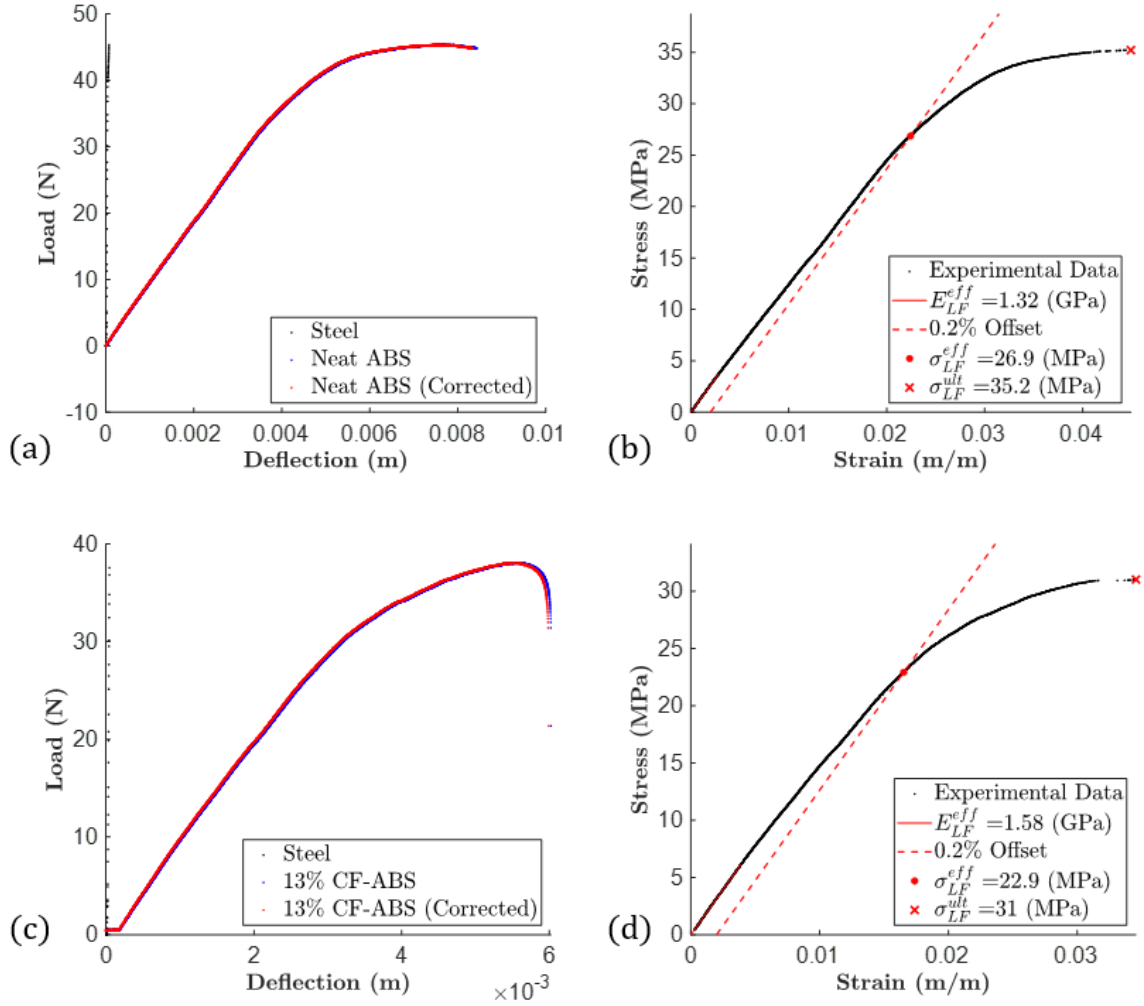


Figure 4.29: Flexural test results of Neat ABS, (a) load-deflection curve and (b) stress-strain curve, and of 13% CF-ABS, (c) load-deflection curve and (d) stress-strain curve.

from [127]:

$$\sigma = 3PL/2bd^2 \quad (4.13)$$

$$\varepsilon = 6Dd/L^2 \quad (4.14)$$

In the above equations, σ is stress, P is load, L is span length, b is specimen width, d is specimen thickness, and D is deflection. E_{LF}^{eff} was calculated as the chord modulus over the range $P=1.5$ - 4.7 N, which corresponds to a strain range of approximately 0.001-0.003 for the 13% CF-ABS. σ_{LF}^{eff} was found using a 0.2% strain offset and σ_{LF}^{ult}

was taken as the maximum stress. Note, ASTM D790-17 calls σ_{LF}^{ult} the flexural yield strength.

Five flexural tests were performed for the neat ABS and 13% CF-ABS. Every 13% CF-ABS specimen broke during testing, but each of the Neat ABS specimens deformed without breaking throughout the entirety of their tests. The data from one steel bar test was used to correct the data of all the other tests. The results of all the tests are summarized in Table 4.5 and the plots are in Appendix D.

The statistics in Table 4.5 reveal that the flexural stiffness of the 13% CF-ABS is higher than that of the Neat ABS, but the flexural strength is lower. This is similar to the results of the tensile and compressive tests. Once again, it is likely that a higher void content in the 13% CF-ABS specimens is at least partially responsible for this unexpected result.

Table 4.5: Flexural testing statistics.

		Minimum	Maximum	\bar{x}	s_{n-1}	CV
Neat ABS	E_{LF}^{eff}	1.23 GPa	1.32 GPa	1.29 GPa	0.0382 GPa	2.97%
	σ_{LF}^{eff}	26.9 MPa	31.6 MPa	29.1 MPa	1.78 MPa	6.14%
	σ_{LF}^{ult}	35.2 MPa	35.8 MPa	35.6 MPa	0.286 MPa	0.802%
13% CF-ABS	E_{LF}^{eff}	1.54 GPa	1.79 GPa	1.67 GPa	0.108 GPa	6.48%
	σ_{LF}^{eff}	22.9 MPa	26.8 MPa	25.0 MPa	1.71 MPa	6.86%
	σ_{LF}^{ult}	30.6 MPa	33.9 MPa	32.3 MPa	1.45 MPa	4.49%

4.2.5 Additional TGA Testing Results

Five tests of Neat ABS pellet samples and five tests of 13% CF-ABS pellet samples were performed based on ASTM E1131-20 [140]. Two of the five Neat ABS samples and two of the five 13% CF-ABS samples were conditioned in laboratory temperature and humidity conditions for over two years. In addition, three of the five Neat ABS samples and three of the five 13% CF-ABS samples were dried at 60°C for 10-15 hours. Figure 4.30 shows typical results for a dried Neat ABS sample and a dried 13% CF-ABS sample.

By examining the mass and temperature data, the amounts of several types of matter can be quantified as shown in Figure 4.30. These include highly volatile matter (V), which decomposes in nitrogen between the start of the test up to the point where the temperature reaches 150°C; medium volatile matter (O), which decomposes in nitrogen between 150-600°C; combustible matter (C), which decomposes in air between 600-800°C; and ash (A), which is matter that does not decompose. Highly volatile matter consists of materials such as small traces of water or other foreign content that will decompose at relatively low temperature and in an inert, nitrogen environment. Medium volatile matter includes Neat ABS, which decomposes in the inert nitrogen environment at high temperature. Combustible matter includes such substances as ABS residue and carbon fibers. The ash content includes leftover matter from both ABS and carbon fiber that never fully decomposes.

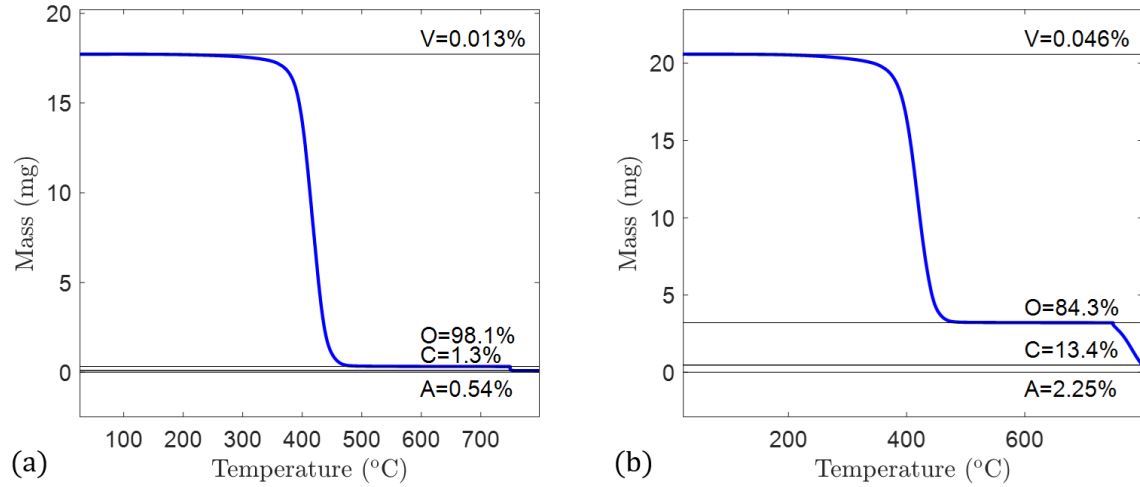


Figure 4.30: Additional TGA burn-off test results showing the amount of highly volatile matter (V), medium volatile matter (O), combustible matter (C), and ash (A). Figure (a) is for a dried Neat ABS pellet sample, and figure (b) is for a dried 13% CF-ABS pellet sample.

Letting the fiber weight fraction and matrix weight fraction in the 13% CF-ABS be called W_f and W_m , respectively, the following can be stated:

$$(C_{13CFABS} + A_{13CFABS}) = W_f + (C_{ABS} + A_{ABS})W_m \quad (4.15)$$

where $C_{13CFABS}$ and $A_{13CFABS}$ are, respectively, the combustible matter and ash from the 13% CF-ABS sample, both of which consist of contents from both the fiber and matrix, and C_{ABS} and A_{ABS} are, respectively, the combustible matrix content and matrix ash from the Neat ABS sample. In addition, we have

$$W_f + W_m = 1 \quad (4.16)$$

Equations 4.15 and 4.16 make a system of two equations with two unknowns, W_f and W_m , and can thus be solved. For example, taking numbers from Figure 4.30, the fiber weight and matrix weight fractions are

$$\begin{bmatrix} W_f \\ W_m \end{bmatrix} = \begin{bmatrix} 1 & (0.013 + 0.0054) \\ 1 & 1 \end{bmatrix}^{-1} \begin{bmatrix} (0.134 + 0.0225) \\ 1 \end{bmatrix} = \begin{bmatrix} 0.14 \\ 0.86 \end{bmatrix}$$

The average V , O , C , and A for the ABS tests were calculated, as were those of the 13% CF-ABS. These average values were then used to determine the fiber weight fraction, W_f . The results for the dried and non-dried samples were similar so both were included in calculating the average V , O , C , and A values. However, one of the dried 13% CF-ABS samples produced outlying test results and was therefore excluded from the average calculations. The results of all the tests are given in Appendix F and the fiber weight fraction was found to be approximately $W_f = 13.3\%$ for the tests based on ASTM E1131-20. This is reasonably close to the 13% that was expected. The matrix weight fraction was found to be $W_m = 86.7\%$.

In addition to running tests based on ASTM E1131-20, three tests of Neat ABS pellet samples and three of 13% CF-ABS pellet samples were performed based on ASTM D3171-15 [141]. These samples were dried at 80°C for approximately 5 hours before being tested. Using equations 6-11 from ASTM D3171-15 and the fiber and matrix densities from Table 3.1, as well as the density of the 13% CF-ABS composite given in [117], the fiber weight fraction was determined to be approximately 13.6%, which is reasonably close to 13%. Figure 4.31 shows the TGA plots for (a) a Neat

ABS pellet sample and (b) a 13% CF-ABS pellet sample. The rest of the plots and a report of the test data is given in Appendix F. The fact that both the tests based on ASTM E1131-20 and ASTM D3171-15 resulted in fiber weight fractions near 13% gives us confidence that this weight fraction was correctly used in the modeling portion of this dissertation.

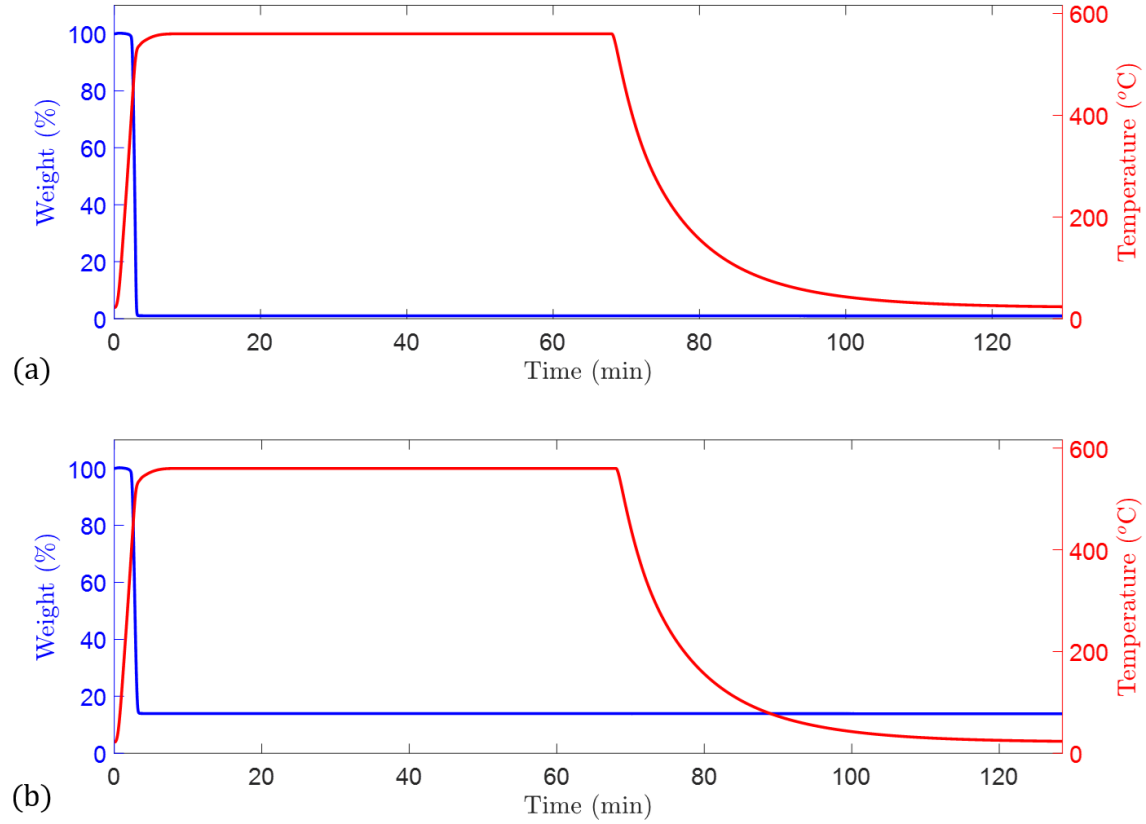


Figure 4.31: Additional TGA burn-off test results for (a) a dried Neat ABS pellet sample, and (b) a dried 13% CF-ABS pellet sample.

4.3 Modeling Modifications Based on Experimental Data

In this section, modifications based on experimental data have been made to the proposed modeling methodologies to improve their accuracy. The first subsection deals with extending the FE tensile model to 3D to obtain the tensile stiffness and strength and uses the actual geometry from the physical specimen. The next subsection addresses making tensile stiffness predictions based on the actual fiber

orientation state data measured in a laboratory setting. This enables the models used herein to be judged independently of a fiber orientation model. The last subsection finally incorporates porosity considerations into the models to obtain a better sense of how accurate the modeling methodology proposed in this dissertation can be.

4.3.1 Considering a Realistic Tensile Bar Geometry

Tensile specimens that were two beads wide and three beads thick were fabricated as shown in Figure 4.32 and tested for stiffness. In addition, a realistic tensile bar geometry was built in COMSOL and simulations were performed to see the effect this realistic geometry might have on the predicted tensile stiffness and strength as compared to using a rectangular geometry. The stiffness part of this study in Section 4.3.1 runs parallel with the study performed in [37], but some of the modeling inputs have been updated so the results do not exactly coincide. In addition, strength prediction has been added.

The tensile specimens for this study were made of the same 13% CF-ABS stock mentioned earlier in this dissertation (see Section 3.1). Strips that were two beads in width, three beads in height, and with dimensions of approximately 19 mm (0.75 in) wide, 9 mm (0.37 in) thick, and 337 mm (13.25 in) long were printed. Two 152.4 mm (6 in) tensile specimens were sectioned out of each strip using the Buehler IsoMetTM Low Speed Precision Cutter pictured in Figure 4.16. As far as the print parameters were concerned, the extruder was set to 198°C, 204°C, and 210°C for temperature zones 1-3, respectively, and the print bed was heated at 85°C. Figure 4.32a shows the Baylor LAAM system printing a strip, and some tensile bars that were cut from a strip are shown in Figure 4.32b.

A photograph of a tensile specimen's cross-section was taken, as shown in Figure 4.33a. A custom MATLAB program, written in-house, was then used to capture the outline of the specimen in the photograph, the results of which are

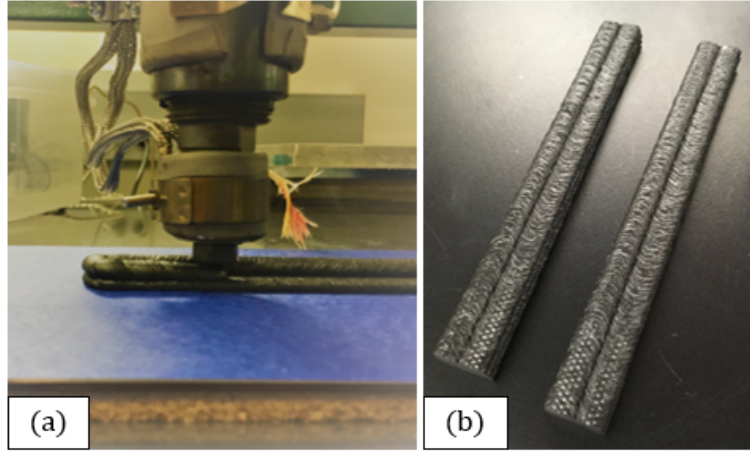


Figure 4.32: (a) Baylor LAAM extruder, printing a strip (photograph filtered for better lighting). (b) Tensile specimens.

shown in Figure 4.33b. This program allows a user to capture the spatial point data by performing mouse-clicks along the edge of the cross-section in the photograph. This coordinate data, which is defined by pixel location, is scaled using caliper measurements of the physical tensile specimen width and thickness.

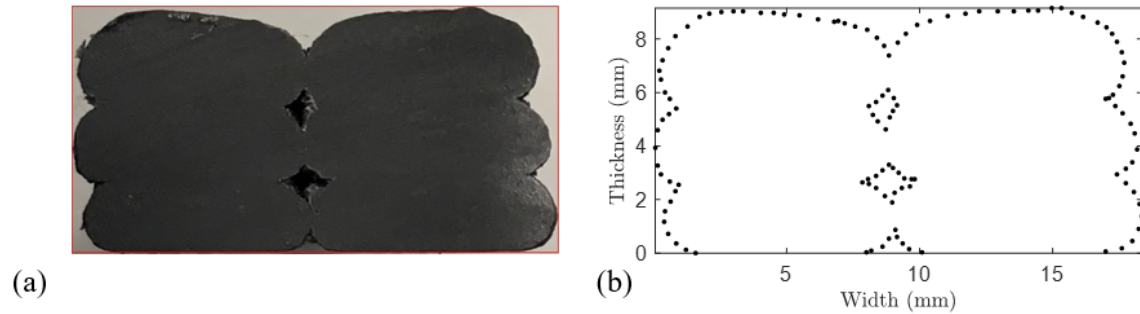


Figure 4.33: Cross-section of a tensile specimen: (a) photograph taken with an iPhone SE (model A1662) and (b) points captured along the edges of the specimen, used to define the cross-section of the tensile specimen geometry in COMSOL.

The coordinate data is loaded in COMSOL to define the cross-section of the COMSOL tensile specimen shown in Figure 4.34, which has been extruded to 152.4 mm (6 in). The boundary conditions are also shown in the figure and include fixing the entire rear surface in the x_1 (longitudinal) direction and applying a displacement to the front surface some amount δ in the $-x_1$ direction. Moreover, a point close to the center of the base of the backside is fixed in every direction to prevent translation

in the x_2 - x_3 plane and a point on the left side of base is fixed in the x_2 direction, preventing rotation. A rectangular tensile specimen with the same overall width, thickness, and length and similar boundary conditions is also considered, as shown in Figure 4.35. Since the real LAAM-printed beads were not all exactly 3 mm tall, the $\langle C \rangle_{ijkl}$ that is found from the flow model over the range $0 \leq x_2 \leq 3$ mm is linearly mapped to the range $0 \leq x_2 \leq h$ mm, where h is the height of a bead. This linear mapping is performed for each bead in both the realistic and rectangular models.

A mesh of 8550 elements was used for the more realistic specimen and a mesh of 8736 elements was used for the rectangular specimen as shown in Figures 4.36a and b. These meshes, which are too coarse to take advantage of the full resolution

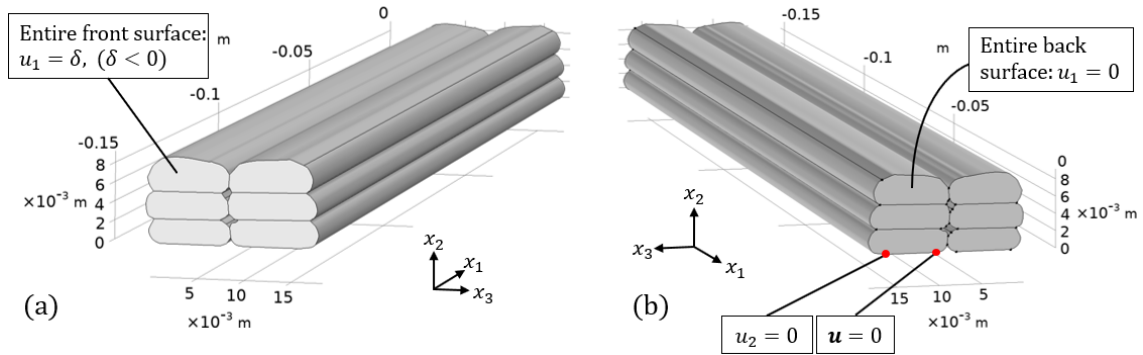


Figure 4.34: FE tensile specimen geometry in COMSOL with boundary conditions: (a) front view and (b) back view.

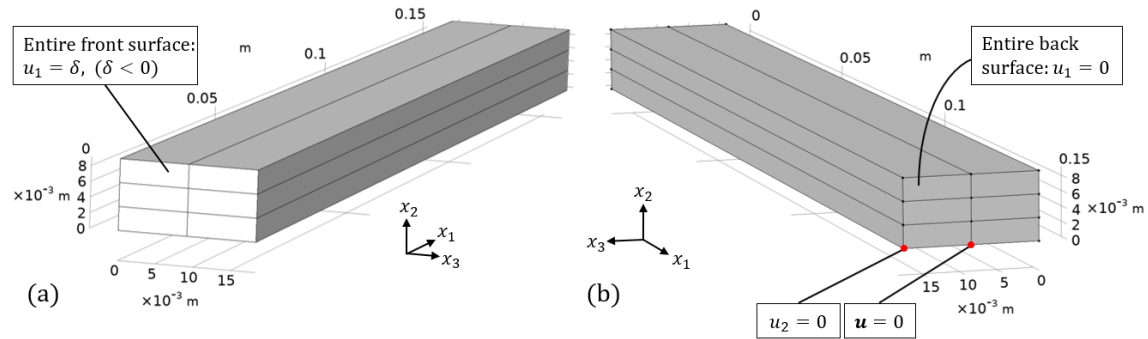


Figure 4.35: FE idealized rectangular tensile specimen geometry in COMSOL with boundary conditions: (a) front view and (b) back view.

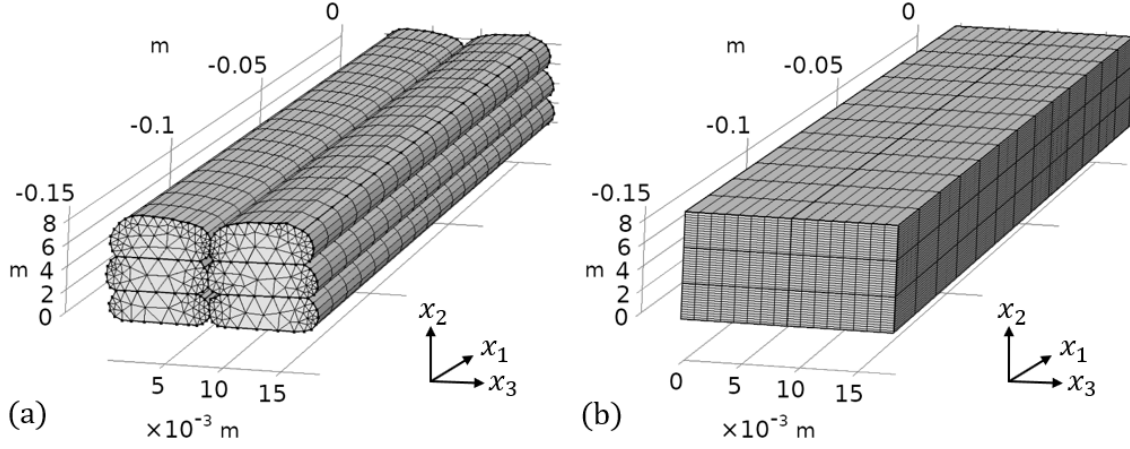


Figure 4.36: FE meshes for (a) the realistic geometry and (b) the rectangular geometry.

of the flow solution for the orientation state, were used to save on computational expense, since each simulation takes at least 13 minutes to run using a computer system with 32.0 GB of RAM and an Intel Core i7-3930K processor operating at 3.20 GHz. Part of the reason why these simulations take a while is that COMSOL must call custom-made MATLAB files while running. These MATLAB files, themselves, also call on externally saved data files. In addition, while the 2D simulations give insight into the δ values that will produce failure, there is no guarantee that multiple simulations will not have to be run until the correct δ values are found to obtain the strength of each model.

To gain a sense of the refinement of the solution, meshes of 2574 elements and 2509 elements were also used for the rectangular and realistic geometries, respectively. For the rectangular geometry, the percent relative difference (PRD) in the E_{LT}^{eff} predictions is less than 0.1% when the 2574 element mesh is used compared to when the 8736 element mesh is used. This seems to indicate that the solution is reasonably stable as the number of elements is increased up to 8736 elements, and that not much more accuracy could be gained if the mesh were to be refined even more. The PRD for the σ_{LT}^{eff} predictions for the rectangular geometry is less than 1% as well. For the realistic geometry when the mesh is increased from 2509 elements

to 8550, the PRD for the E_{LT}^{eff} predictions is less than 0.1% and the PRD for the σ_{LT}^{eff} predictions is 4.0%. Thus, the 8736-element mesh and the 8550-element mesh were used for the rectangular and realistic geometries in this section, respectively.

Several simulations were run using the above 3D tensile FE models. Figure 4.37 gives stiffness predictions over $C_I = 0.0019$ -0.03 and $\kappa = 1/30$ -1/8. The results are in the range seen earlier in Figure 3.17 for the 2D models. In addition, the tensile strength was predicted for each model using $C_I = 0.0019$ and $\kappa = 0.125$. For the rectangular specimen, failure occurs at $\delta = 967\mu\text{m}$ and $\sigma_{LT}^{eff} = 43.3$ MPa. For the realistic specimen, failure occurs at $\delta = 950\mu\text{m}$ and $\sigma_{LT}^{eff} = 40.7$ MPa.

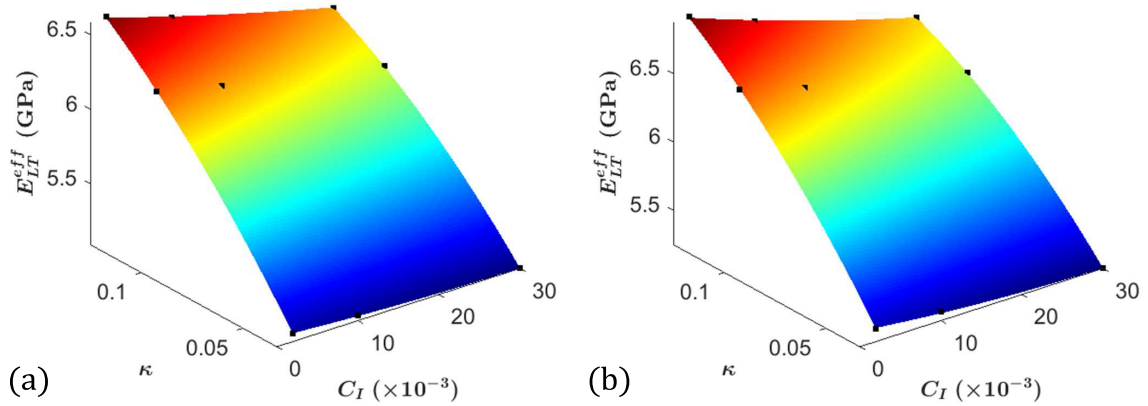


Figure 4.37: Stiffness predictions for 3D FE COMSOL models: (a) used realistic tensile specimen geometry and (b) used rectangular tensile specimen geometry.

Figures 4.38a and b show the Von Mises stress at failure for both specimens. The stress can be seen to be a function of x_2 due to the stiffness being a function of x_2 . Figures 4.38c and d are failure plots for the realistic and rectangular geometries. These indicate weakness at the top of the specimens, near the interfaces, and at the bottom. It should be noted that the present methodology assumes ideal bonding between beads, when in reality the interfacial bond between beads could be the limiting factor of the tensile strength of LAAM-printed material. Nevertheless, the plots provide insight into the microstructural properties of the LAAM-made SFRP material. It is also interesting to note that, if we use a laminate analogy, the beads do

not have an orientation state through their thickness that is balanced and symmetric. This means that a small amount of bending-extension coupling is taking place, and that the beads, and consequently the overall tensile samples, twist a small amount as they are extended.

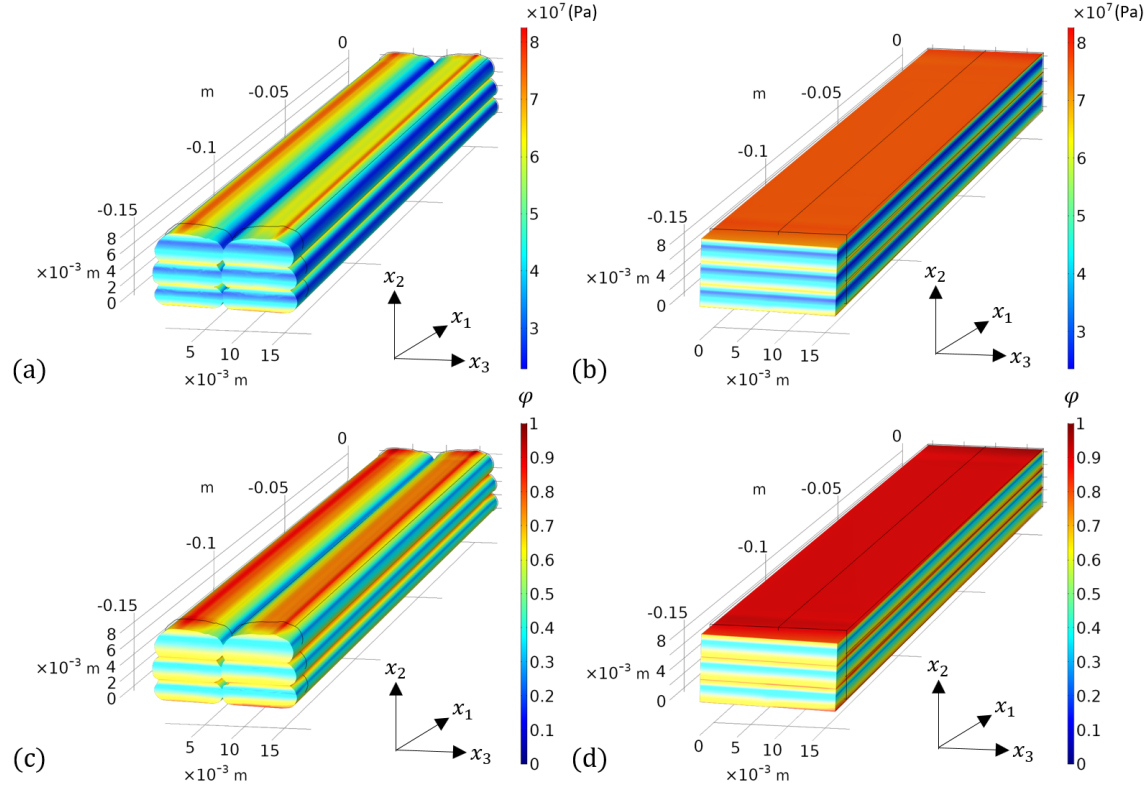


Figure 4.38: FE tensile simulations. Von Mises stress (deformation scale factor=6) for (a) the realistic geometry and (b) the rectangular geometry. Also, failure plots (deformation scale factor=6) for (c) the realistic geometry and (d) the rectangular geometry.

Tensile testing was performed on several of the actual tensile specimens using a MTS QTest/100 machine and a 100 kN load cell, pictured in Figure 4.39a. In addition, an MTS 25 mm gage extensometer (Model 634.11F-24) was used and is pictured in Figure 4.39b. The test procedure consisted of a 2 mm/min displacement control rate up to 4000 kN with a 25 Hz data acquisition rate. Stress-strain results from a typical test are given in Figure 4.40. The stress data for each test was found by dividing the load data by the tensile specimen's cross-sectional area, found

with the help of the tracing procedure discussed earlier. Data from five tests were found in this way, the figures for which are given in Appendix E, and the effective stiffness was calculated over the strain range 0.001-0.003 for each test. The data was shifted to correct for the toe region such that the E_{LT}^{eff} line would pass through the origin. The stiffness results are summarized in Table 4.6, where \bar{x} , s_{n-1} , and CV are, respectively, the mean E_{LT}^{eff} , the standard deviation, and the coefficient of variation.

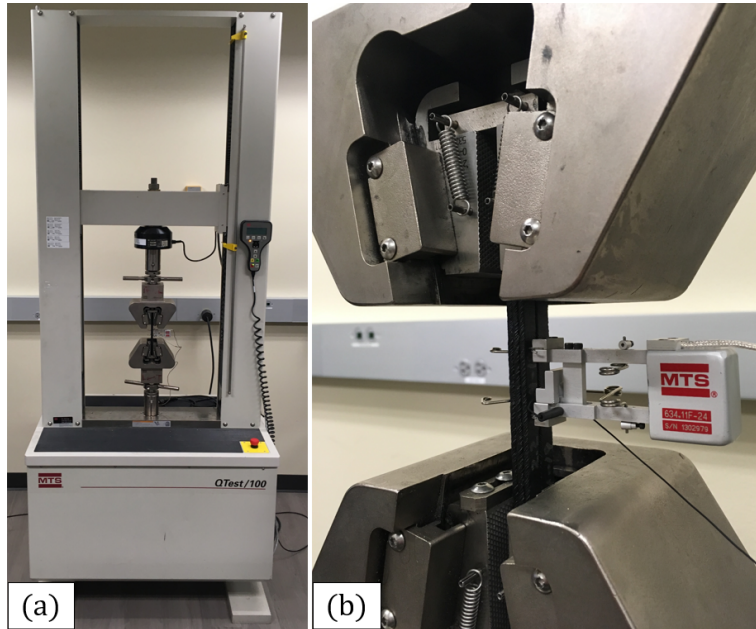


Figure 4.39: Tensile test setup: (a) MTS QTest/100 tensile testing machine with 100 kN load cell; (b) MTS 25 mm gage extensometer (Model 634.11F-24) mounted to a specimen.

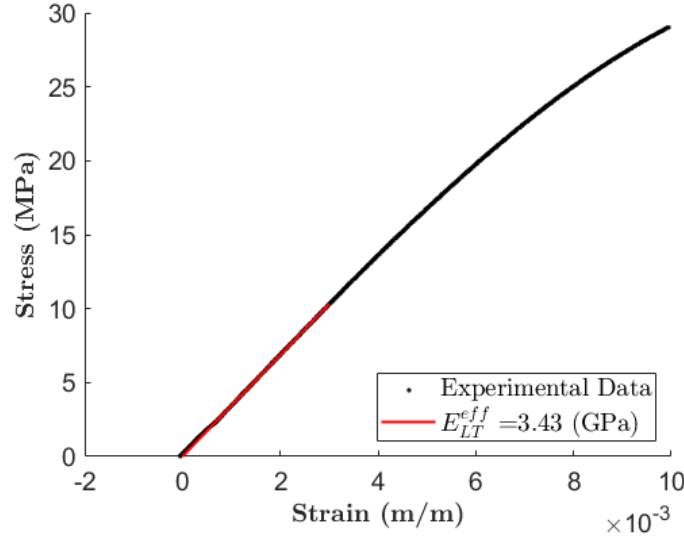


Figure 4.40: Typical stress-strain response of a 6-bead tensile specimen like that shown in Figure 4.32b.

Table 4.6: Tensile stiffness experimental results for tensile specimens made of 13%CF-ABS.

Minimum	Maximum	\bar{x}	s_{n-1}	CV
3.26 GPa	3.43 GPa	3.36 GPa	0.0716 GPa	2.13%

4.3.2 Considering Fiber Orientation Measurement Data

By physically measuring the internal fiber orientation state in a LAAM-printed SFRP bead, one can bypass any errors from a fiber orientation model and judge the stiffness model directly by inserting the orientation information into the model. Nargis [133] measured the spatially varying fiber orientation state in the same 13% CF-ABS material that was used in this study and printed with Baylor’s LAAM system. The orientation measurements were found using a method similar to that of Vélez-García et al. [58, 60], using a polishing procedure, plasma etching, and analyzing elliptical fiber cross-sections and their shadows under a microscope. Nargis [133] divided the cross section of a printed bead into nine regions, measuring the orientation state in each region. Her results give the approximate value of \mathbf{A} at the

centroid of each region. Figure 4.41 shows a diagram of a bead cross section with the nine regions numbered.

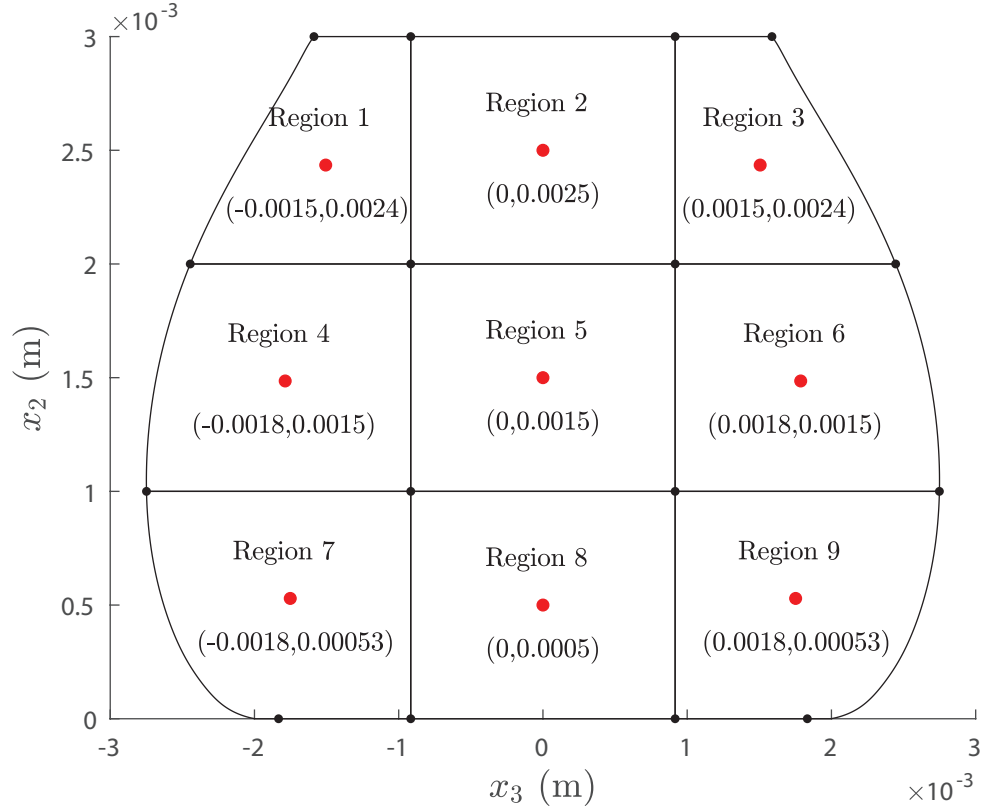


Figure 4.41: Printed bead cross section, divided into nine regions where the orientation has been found by Nargis [133]. The red dots indicate the centroids of each region.

The results of Nargis have been plotted as surface plots across the cross section of a hypothetical LAAM-printed bead in Figures 4.42a-c. In these plots, along with the rest of the plots in Figure 4.42, A_{ij} has been linearly interpolated between the centroid points and extrapolated beyond the centroid points by using the value of the nearest neighbor. Figures 4.42d-f show the results obtained by using the RSC model to predict the orientation state at each region's centroid with $C_I = 0.0019$ and $\kappa = 0.125$. The geometry of the flow domain used for the orientation predictions in this section is shown in Figure 4.43. This geometry was made by revolving the nozzle geometry from the 2D FE flow model (see Figure 3.3) around the x_2 axis

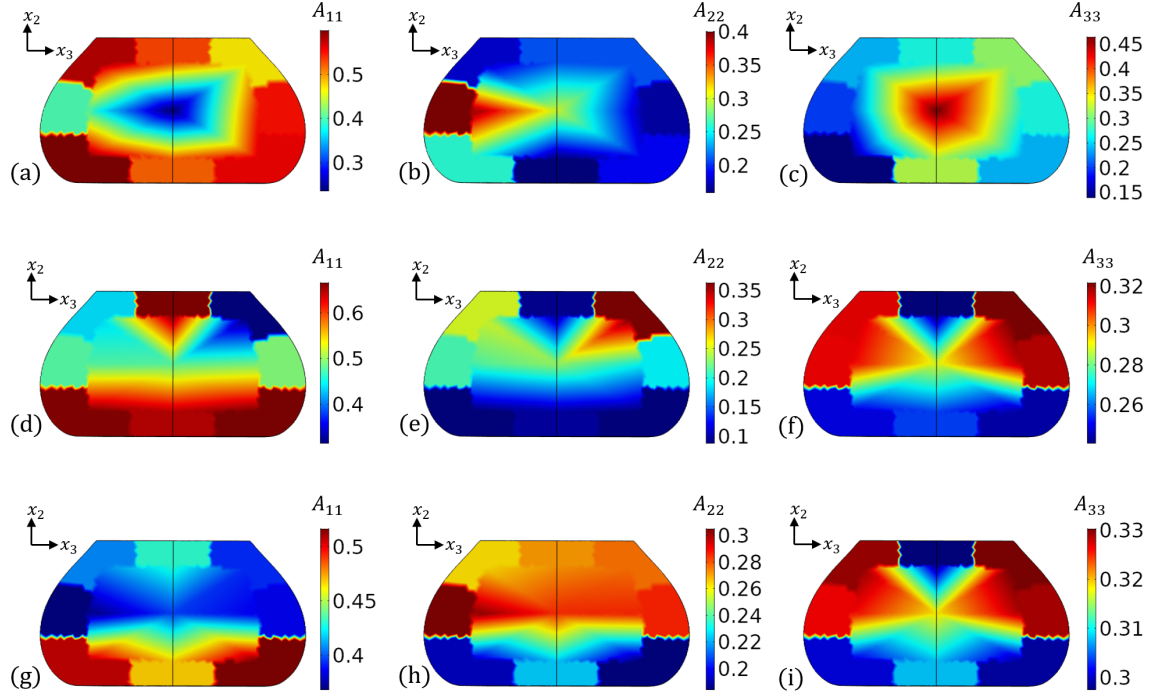


Figure 4.42: Spatially varying components of A_{ij} across the cross section of a LAAM-printed bead. Measurement data from Nargis [133]: (a) A_{11} , (b) A_{22} , (c) A_{33} . RSC prediction using $a_r = 38.8$, $C_I = 0.0019$, $\kappa = 0.125$: (d) A_{11} , (e) A_{22} , (f) A_{33} . RSC prediction using $a_r = 38.8$, $C_I = 0.0019$, $\kappa = 0.05$: (g) A_{11} , (h) A_{22} , (i) A_{33} .

to make a 3D nozzle geometry. The right side of the die-swell curve in the 2D model was also revolved around the x_2 axis and extruded to create the printed bead. As in the 2D model, the printed bead is 3 mm tall in the 3D model. A fine mesh and 9 streamlines, spaced such that they end at the regions' centroids, were also used. The shape of the 3D deposited bead was not generated using a shape-optimization procedure like that of Heller where he minimized the surface normal velocity [125]. Thus, this 3D FE model is a simple first pass at corroborating 3D fiber orientation state predictions with experimental data and needs improvement in the future. Furthermore, a separate 3D FE model of a single bead was also made for stiffness predictions as shown in Figure 4.44.

As shown in Table 4.7, the alignment in the flow direction is overpredicted by the RSC model compared to Nargis' results, therefore an additional run of the RSC model was performed with a lower value of the slowness parameter, $\kappa = 0.05$. The

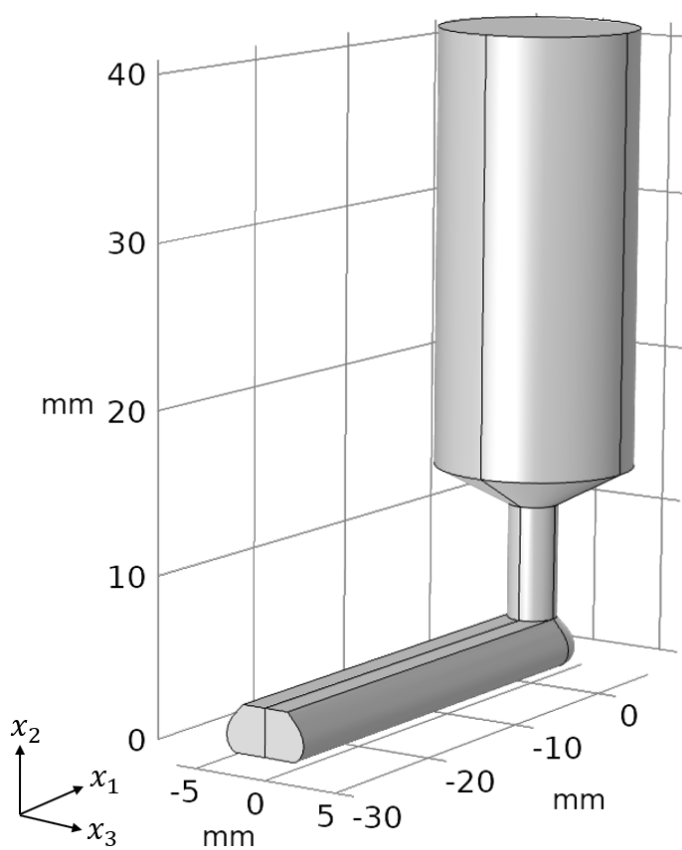


Figure 4.43: 3D finite element COMSOL flow model.

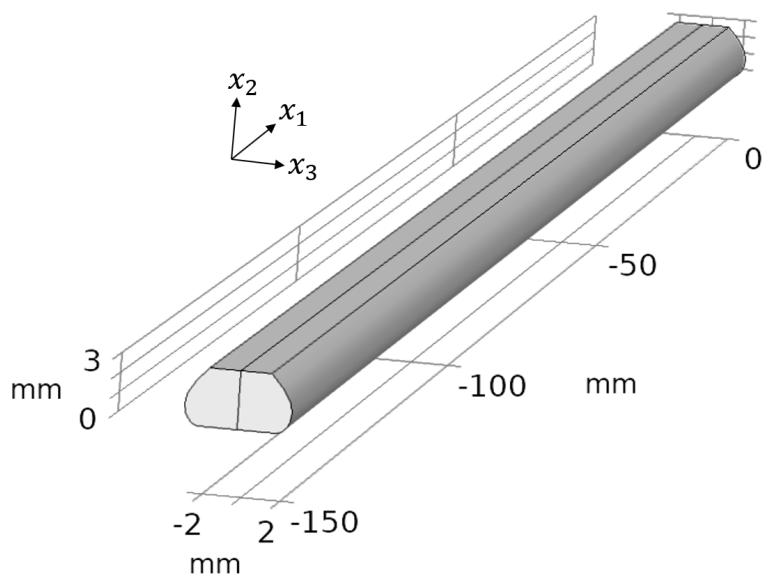


Figure 4.44: 3D finite element COMSOL tensile simulation geometry.

Table 4.7: Measured vs. predicted A_{ij} data in a LAAM-printed bead. “Measured” values are from Nargis [133]. Region numbers come from Figure 4.41. Percentage errors are given in parentheses.

Region	Method	A_{11}	A_{22}	A_{33}
1	Measured	0.58	0.18	0.24
	RSC ($\kappa=0.125$)	0.44 (25%)	0.25 (39%)	0.31 (30%)
	RSC ($\kappa=0.05$)	0.41 (30%)	0.26 (46%)	0.33 (37%)
2	Measured	0.53	0.21	0.27
	RSC ($\kappa=0.125$)	0.66 (25%)	0.09 (55%)	0.24 (11%)
	RSC ($\kappa=0.05$)	0.43 (19%)	0.27 (29%)	0.30 (10%)
3	Measured	0.47	0.21	0.31
	RSC ($\kappa=0.125$)	0.31 (33%)	0.36 (73%)	0.32 (4%)
	RSC ($\kappa=0.05$)	0.39 (16%)	0.28 (32%)	0.33 (7%)
4	Measured	0.4	0.4	0.2
	RSC ($\kappa=0.125$)	0.48 (19%)	0.21 (47%)	0.31 (56%)
	RSC ($\kappa=0.05$)	0.37 (8%)	0.31 (24%)	0.33 (63%)
5	Measured	0.23	0.3	0.47
	RSC ($\kappa=0.125$)	0.48 (108%)	0.23 (22%)	0.29 (38%)
	RSC ($\kappa=0.05$)	0.40 (72%)	0.29 (5%)	0.32 (32%)
6	Measured	0.55	0.17	0.27
	RSC ($\kappa=0.125$)	0.49 (10%)	0.19 (12%)	0.32 (17%)
	RSC ($\kappa=0.05$)	0.39 (30%)	0.29 (68%)	0.33 (22%)
7	Measured	0.6	0.26	0.14
	RSC ($\kappa=0.125$)	0.66 (10%)	0.09 (66%)	0.25 (78%)
	RSC ($\kappa=0.05$)	0.51 (15%)	0.19 (26%)	0.30 (115%)
8	Measured	0.52	0.16	0.32
	RSC ($\kappa=0.125$)	0.65 (24%)	0.10 (39%)	0.26 (20%)
	RSC ($\kappa=0.05$)	0.47 (10%)	0.22 (40%)	0.31 (4%)
9	Measured	0.56	0.19	0.24
	RSC ($\kappa=0.125$)	0.67 (19%)	0.09 (53%)	0.24 (2%)
	RSC ($\kappa=0.05$)	0.52 (8%)	0.18 (3%)	0.30 (25%)

results for this are given in Figures 4.42g-i. It can be seen in the figure, as well as in the table, that the RSC with $\kappa=0.05$ still overpredicts the amount of alignment in the print direction but the results are closer to that of Nargis than when $\kappa=0.125$. Nargis' results indicate higher alignment in the print direction on the top and bottom surface of the printed bead than in the core. This trend is also captured by the fiber orientation models.

Part of the reason for the discrepancy between the fiber orientation modeling results and the measured orientation data can be attributed to porosity in the printed material. In Section 4.3.3, porosity will be considered as to its effect on mechanical property predictions but it will not be taken into account in any of the flow models in this dissertation even though it certainly could have an effect on the final fiber orientation state. As was already mentioned, the 3D flow model was not shape-optimized, so this is another factor that could explain some of the error in the fiber orientation modeling results. In addition, Nargis found that the fiber orientation results actually varied to some extent along the length of a printed bead [133], which is not considered in the tensile geometry shown in Figure 4.44. Thus, the amount of agreement between the predictions and the measurements is also dependent on the location where the physical samples were taken out of the printed bead.

A mesh of 34,900 elements was used in the tensile test simulations. Using the orientation data predicted by the RSC model with $C_I=0.0019$ and $\kappa=0.125$, $E_{LT}^{eff} = 6.88$ GPa. Using the orientation data predicted by the RSC model with $C_I=0.0019$ and $\kappa=0.05$, $E_{LT}^{eff} = 6.57$ GPa. Finally, using the measured orientation results from Nargis [133], $E_{LT}^{eff} = 6.37$ GPa. Clearly the orientation state plays a role in the stiffness predictions.

4.3.3 Considering Porosity

In her thesis, Nargis [133] utilized the Baylor LAAM system to print the same 13% CF-ABS used in this study and found there to be significant void formation in the deposited material. For an RPM of 2250, temperatures 200/205/210°C, and a gantry speed set to generate a bead with cross sectional area of approximately 27 mm², Nargis found the void areal fraction to be 13.84% [133]. The void areal fraction was calculated as the ratio of the area of the voids seen on a cross section of the bead divided by the whole cross sectional area. Nargis also found that the void areal fraction can be used to approximate the void volume fraction. Therefore, a void volume fraction of 13.84% is considered in this part of the dissertation. This was a much larger void volume fraction than originally anticipated, and it has a significant impact on predictions as this section will show.

Zhang et al. presented simple models for both the yield strength and the elastic modulus of a foam material:

$$\frac{\sigma_{yf}}{\sigma_{ym}} \approx \frac{E_f}{E_m} \approx (1 - V_v)^n \quad (1.93 \leq n \leq 2.01) \quad (4.17)$$

where σ_{yf} is the yield strength of the foam, σ_{ym} is the yield strength of the matrix, E_f is the elastic modulus of the foam, E_m is the elastic modulus of the matrix, V_v is the void volume fraction, and n is a power index [143]. Since the material in question in this study is a fiber-filled material rather than a neat polymer, σ_{ym} and E_m are replaced with properties of the composite material, as done by Pulipati and Jack [144]. In addition, the power index is related to the Poisson's ratio of the composite, which in this case can be calculated by the rule of mixtures:

$$\nu_c = V_f \nu_f + (1 - V_f) \nu_m \approx 0.34 \quad (4.18)$$

The above equation was evaluated using the fiber and matrix properties from Table 3.1. According to the table provided by Zhang et al. in [143], a Poisson's ratio of 0.34 results in a power index of 2.00. Thus, the stiffness and strength properties

corrected for void volume fraction are

$$E_{corrected} = E(1 - 0.1384)^{2.00} \quad (4.19)$$

$$\sigma_{corrected} = \sigma(1 - 0.1384)^{2.00} \quad (4.20)$$

where E is some stiffness value such as E_{LT}^{eff} , E_{LC}^{eff} , or E_{LF}^{eff} , and σ is some strength value such as σ_{LT}^{eff} , σ_{LC}^{eff} , or σ_{LF}^{eff} .

Using Equations 4.19 and 4.20, the results from Figure 3.17 have been corrected and represented in Figure 4.45. The exact same trends in the data can be seen as in Figure 3.17 since Equations 4.19 and 4.20 are effectively reducing the properties by a multiplication factor less than one. Summarizing all the predictions, E_{LT}^{eff} and E_{LC}^{eff} are both in the range 4.16-5.62 GPa, E_{LF}^{eff} is 4.78-6.65 GPa, σ_{LT}^{eff} is 30.4-38.4 MPa, σ_{LC}^{eff} is 55.9-74.0 MPa, and σ_{LF}^{eff} is 38.5-50.2 MPa.

In general, the models over predict the properties found in Tables 4.3-4.5. One possible explanation for this is that in the specimen preparation process for the tensile, compressive, and flexural tests, the top surface of the specimens were machined down 10-20% of the specimen height to eliminate waviness and to ensure a uniform cross-section along the specimens' length. The top and bottom of a printed bead are where the fibers tend to align the most however, and removing a part of this highly aligned material could have an effect on the properties, especially the flexural properties.

Correcting the results of Figure 4.37, which were found using 3D FE tensile bar geometries in COMSOL, the results shown in Figure 4.46 are obtained. For the rectangular tensile bar, $E_{LT}^{eff} = 3.90$ -5.11 GPa. For the realistic tensile bar, $E_{LT}^{eff} = 3.78$ -4.89 GPa. The realistic tensile geometry yields slightly better results than the rectangular geometry when compared to the average E_{LT}^{eff} from the experimental results in Table 4.6. The best prediction is the lower bound produced by the realistic tensile bar which has an error of 12.6%.

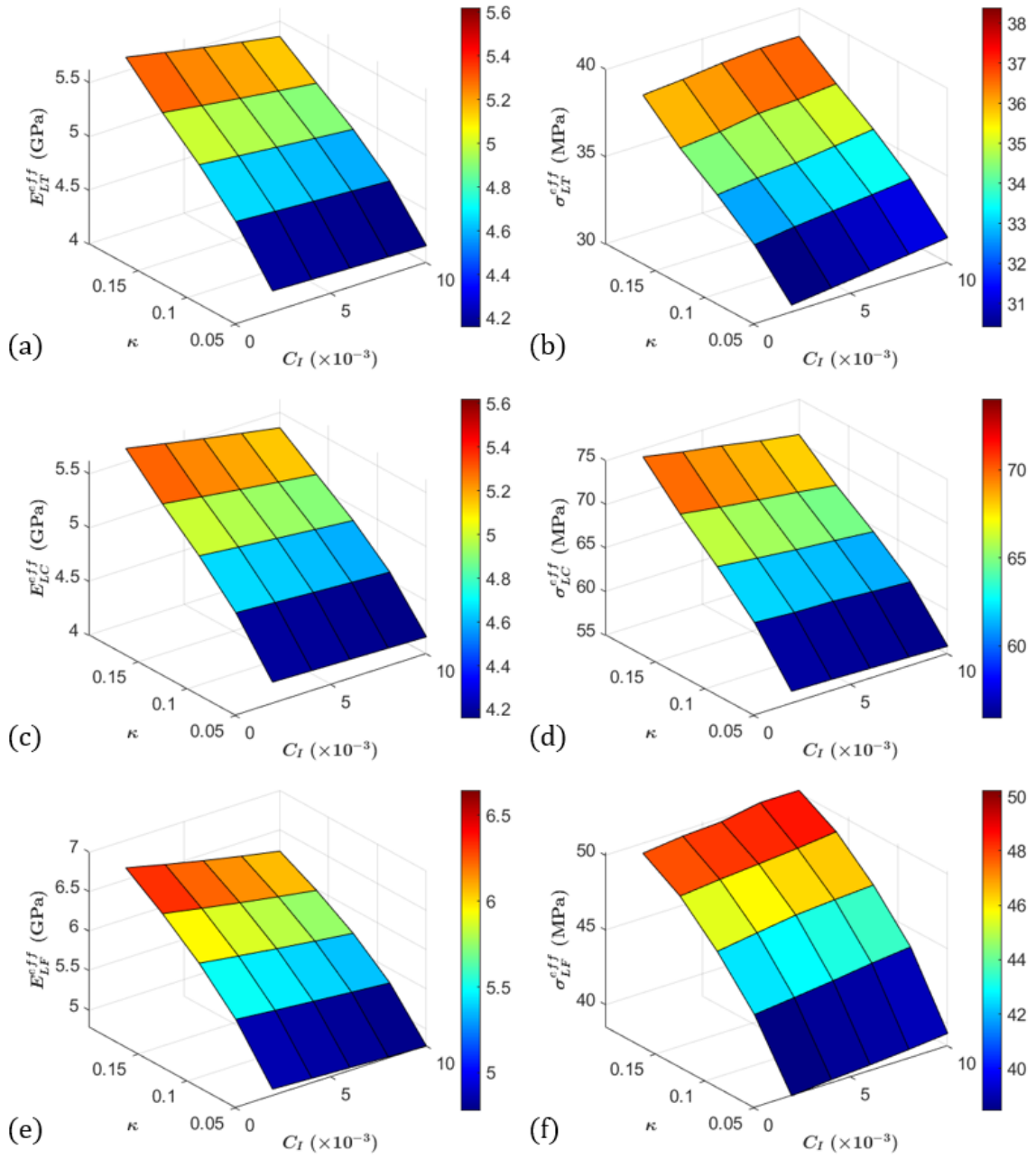


Figure 4.45: Effective longitudinal stiffness and strength predictions, *corrected for void volume fraction*, as functions of RSC modeling parameters, C_I and κ : (a) tensile stiffness, (b) tensile strength, (c) compressive stiffness, (d) compressive strength, (e) flexural stiffness, and (f) flexural strength. Used initial $A_{ij} = \frac{1}{3}\delta_{ij}$, $a_r = 38.8$, and $N = 31$.

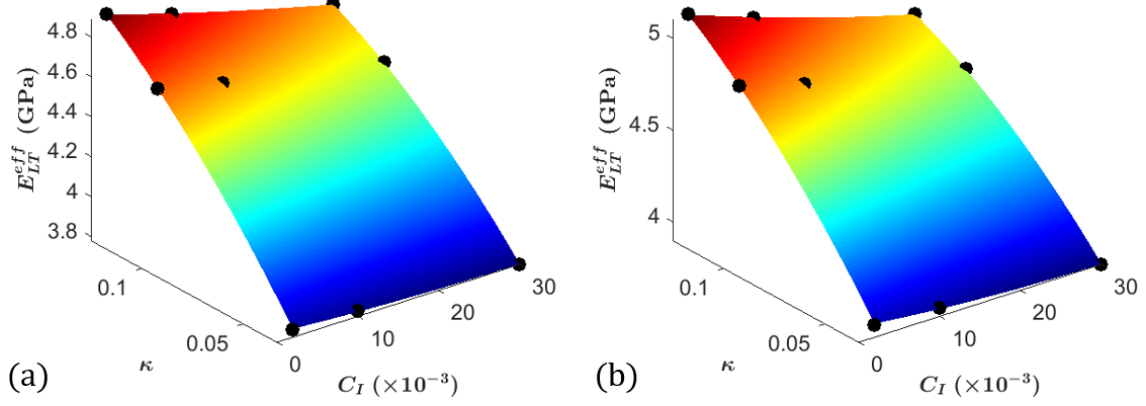


Figure 4.46: Stiffness predictions for 3D FE COMSOL models, *corrected for void volume fraction*: (a) used realistic tensile specimen geometry and (b) used rectangular tensile specimen geometry.

The strength predictions were also updated with $\sigma_{LT}^{eff} = 33.2$ MPa for the rectangular tensile geometry and $\sigma_{LT}^{eff} = 30.4$ MPa for the realistic tensile geometry. In comparison to the average σ_{LT}^{eff} from the experimental results in Table 4.3, the realistic tensile geometry yields better results with a percent error of 11.4%. The rectangular geometry results in an error of 21.6%. The orientation data for both the rectangular and realistic geometries was obtained using the RSC with $C_I = 0.0019$ and $\kappa = 0.125$.

The corrected results of Section 4.3.2 are the following. For the RSC with $C_I = 0.0019$ and $\kappa = 0.125$, $E_{LT}^{eff} = 6.20$ GPa. For the RSC with $C_I = 0.0019$ and $\kappa = 0.05$, $E_{LT}^{eff} = 5.27$ GPa. Using the results of Nargis [133], $E_{LT}^{eff} = 4.73$ GPa. Comparing these results to the average stiffness, E_{LT}^{eff} , from Tables 4.3 and 4.6, the results are not very accurate. Part of the reason for this may have to do with the poor resolution of the \mathbf{A} solution across the cross-section of the geometry using only nine data points.

It should be noted that while porosity was used to correct the final stiffness and strength predictions in a LAAM-printed bead in this section, it was not included in the flow modeling from which the fiber orientation state is obtained and input

into the predictions. It is possible that the presence of porosity in the printed SFRP material reduces the amount of fiber alignment in the print direction. This would explain some of the discrepancy between the **A** predictions and those presented by Nargis [133]. Porosity has been entirely ignored when predicting the fiber orientation state in this dissertation though. Furthermore, porosity may effect the fiber-matrix bond strength and thus, L_c . While L_c does not have a strong influence on σ_{LT}^{eff} and σ_{LF}^{eff} as demonstrated in Figure 3.18, it is possible that porosity could have a more noticeable impact on σ_{LC}^{eff} .

4.4 Comparison of Modeling and Experimental Results

The following section summarizes the modeling and experimental results presented in this dissertation for comparison purposes. A random initial orientation state, $A_{ij} = \frac{1}{3}\delta_{ij}$ was used for all of the following models along with $a_r = 38.8$, except for when a range of L_w values was considered. Tables 4.8 and 4.9 give, respectively, the tensile/compressive and flexural stiffness predictions. The values corrected for porosity, Cor. E_{LT}^{eff} and Cor. E_{LF}^{eff} , are found by Equation 4.19 and are also given in these tables. Tables 4.10-4.12 give the predicted tensile, compressive, and flexural strength values along with their corrected values. In addition, Table 4.13 gives a summary of the experimentally characterized stiffness and strength properties.

The compressive property predictions seem to fit best with the experimental data, followed by the tensile property predictions, and finally the flexural property predictions. In general, the models overpredict the experimental results, but the predictions are susceptible to the effects of many factors. It is evident from the results in the tables that the choice of fiber orientation model can make a significant difference. Overall, the RSC produces lower, more accurate predictions for stiffness than the IRD. A realistic, 3D FE tensile bar geometry produces moderately more accurate results than a rectangular one too. Interestingly, the 3D rectangular and

Table 4.8: Tensile/Compressive Stiffness - Predictions.

Section	Model	Parameters	E_{LT}^{eff} (GPa)	Cor. E_{LT}^{eff} (GPa)
3.2.4	IRD, 2D flow; nozzle exit; 2D tensile geometry	$C_I = 0.0019-0.01$	10.1-12.1	7.48-8.99
3.2.4	IRD, 2D flow; 2D tensile geometry	$C_I = 0.0019-0.01$	9.59-11.6	7.12-8.65
3.2.4	RSC, 2D flow; nozzle exit; 2D tensile geometry	$C_I = 0.0019-0.01$, $\kappa = 1/30-1/8$	5.60-7.37	4.16-5.47
3.2.4	RSC, 2D flow; 2D tensile geometry	$C_I = 0.0019-0.01$, $\kappa = 1/30-1/8$	5.28-6.73	3.92-5.00
3.2.5.2	RSC, 2D flow; 2D tensile geometry	$C_I = 0.0019-0.01$, $\kappa = 0.05-0.2$	5.60-7.57	4.16-5.62
3.2.5.2	RSC, 2D flow; 2D tensile geometry	$L_w = 100-1100 \mu\text{m}$	4.40-8.33	3.27-6.19
3.2.6	RSC, 2D flow; laminate analogy	$C_I = 0.0019-0.01$, $\kappa = 0.05-0.2$	5.61-7.57	4.16-5.62
4.3.1	RSC, 2D flow; 6-bead, 3D realistic tensile geometry	$C_I = 0.0019-0.03$, $\kappa = 1/30-1/8$	5.09-6.59	3.78-4.89
4.3.1	RSC, 2D flow; 6-bead, 3D rect. tensile geometry	$C_I = 0.0019-0.03$, $\kappa = 1/30-1/8$	5.25-6.88	3.90-5.11
4.3.2	RSC, 3D flow; 1-bead, 3D tensile geometry	$C_I = 0.0019$, $\kappa = 0.125$	6.88	5.11
4.3.2	RSC, 3D flow; 1-bead, 3D tensile geometry	$C_I = 0.0019$, $\kappa = 0.05$	6.57	4.88
4.3.2	A from [133]; 1-bead, 3D tensile geometry	N/A	6.37	4.73

Table 4.9: Flexural Stiffness - Predictions.

Section	Model	Parameters	E_{LF}^{eff} (GPa)	Cor. E_{LF}^{eff} (GPa)
3.2.5.2	RSC, 2D flow; 2D flexural geometry	$C_I=0.0019-0.01$, $\kappa=0.05-0.2$	6.44-8.95	4.78-6.65
3.2.5.2	RSC, 2D flow; 2D flexural geometry	$L_w=100-1100 \mu\text{m}$	4.86-10.2	3.61-7.55
3.2.6	RSC, laminate analogy	$C_I=0.0019-0.01$, $\kappa=0.05-0.2$	6.63-9.38	4.92-6.96

Table 4.10: Tensile Strength - Predictions.

Section	Model	Parameters	σ_{LT}^{eff} (MPa)	Cor. σ_{LT}^{eff} (MPa)
3.2.5.2	RSC, 2D flow; 2D tensile geometry	$C_I=0.0019-0.01$, $\kappa=0.05-0.2$	41.0-51.7	30.4-38.4
3.2.5.2	RSC, 2D flow; 2D tensile geometry	$L_w=100-1100 \mu\text{m}$	31.3-103	23.2-76.1
4.3.1	RSC, 2D flow; 6-bead, 3D realistic tensile geometry	$C_I=0.0019$, $\kappa=0.125$	40.7	30.2
4.3.1	RSC, 2D flow; 6-bead, 3D rect. tensile geometry	$C_I=0.0019$, $\kappa=0.125$	43.3	32.1

Table 4.11: Compressive Strength - Predictions.

Section	Model	Parameters	σ_{LC}^{eff} (MPa)	Cor. σ_{LC}^{eff} (MPa)
3.2.5.2	RSC, 2D flow; 2D compressive geometry	$C_I=0.0019-0.01$, $\kappa=0.05-0.2$	75.3-99.7	55.9-74.0
3.2.5.2	RSC, 2D flow; 2D compressive geometry	$L_c=300-1100 \mu\text{m}$	82.9-98.3	61.6-73.0
3.2.5.2	RSC, 2D flow; 2D compressive geometry	$L_w=100-1100 \mu\text{m}$	61.0-119	45.3-88.0

Table 4.12: Flexural Strength - Predictions.

Section	Model	Parameters	σ_{LF}^{eff} (MPa)	Cor. σ_{LF}^{eff} (MPa)
3.2.5.2	RSC, 2D flow; 2D flexural geometry	$C_I=0.0019-0.01$, $\kappa=0.05-0.2$	51.8-67.7	38.5-50.2
3.2.5.2	RSC, 2D flow; 2D flexural geometry	$L_w=100-1100 \mu\text{m}$	37.6-167	27.9-124

Table 4.13: Experimental Results Summary.

Section	Sample Type	Property	Average Property
4.2	1-bead, milled, tabbed	E_{LT}^{eff}	2.71 GPa
4.3.1	6-bead, unaltered	E_{LT}^{eff}	3.36 GPa
4.2	1-bead, milled, tabbed	E_{LC}^{eff}	4.06 GPa
4.2.4	1-bead, milled, tabbed	E_{LF}^{eff}	1.67 GPa
4.2.2	1-bead, milled, tabbed	σ_{LT}^{eff}	27.3 MPa
4.2.3	1-bead, milled, tabbed	σ_{LC}^{eff}	58.6 MPa
4.2.3	1-bead, milled, tabbed	σ_{LF}^{eff}	25.0 MPa

2D rectangular tensile bar models yield very similar results for the tensile stiffness as well.

The weight-average fiber length (or, alternatively, the fiber aspect ratio) also plays a significant role and can significantly affect the predictions. Including porosity effects into the models makes a large difference as well and greatly increases accuracy. However, the porosity modeling consideration that was made effectively only knocks down the predicted properties by a scaling factor and does not make a difference in the predicted orientation state. Porosity likely *does* reduce the amount of fiber alignment in reality, thus, this may be one reason why the predictions are currently too high. Real fiber orientation measurement data [133] shows the fiber alignment is indeed lower than what is predicted. Thus, this data is also used in a model and it can be seen that it leads to a better prediction of the tensile stiffness than most of the other model-parameter combinations.

As discussed earlier, the initial orientation state is also very important when using the RSC model and thus this factor can also significantly affect the predictions. Furthermore, many of the constituent material properties used in the models were drawn from online sources. These will have a strong affect on the predictions, so if they are slightly off, this could be part of the reason why the models are overpredicting the stiffness and strength properties. Other factors such as using a fiber aspect ratio distribution rather than a single-value aspect ratio could lead to moderately improved accuracy as well. Coupling the flow and orientation problems will also make a difference.

Having so many variables increases the difficulty to fully validate all of the models used in this dissertation. However, it has been demonstrated that correct order of magnitude predictions can be made for the stiffness and strength of LAAM-printed SFRP beads using the computational methodology demonstrated in this dissertation. In addition, a framework has been developed upon which others can improve by using more accurate model inputs, as they are measured, and by using more accurate equations for the properties of underlying unidirectional composites, if they are invented.

CHAPTER FIVE

Conclusions and Recommendations

This dissertation has contributed to the general understanding of Large Area Additive Manufacturing (LAAM) and its effects on the effective tensile stiffness, strength, and CTE of LAAM-printed SFRPs. Background information on the state of the art in additive manufacturing and additive manufactured composites was covered. In addition, modern methods of fiber orientation modeling used in the injection and compression molding industries were applied to the newer industry of additive manufacturing, specifically, with LAAM in mind. The computational methodology utilized in Chapter Three gave insight into the fiber orientation state in a single bead of LAAM-printed short fiber filled polymer, predicting that the fibers will align highly on the bottom and top surfaces of the bead and more randomly in the core of the bead. This pattern was confirmed by experimental results from Nargis [133].

It was also discovered that the selection of the model used to predict the fiber orientation state could have a strong influence on the orientation predictions. In addition, when using the Reduced Strain Closure (RSC) fiber orientation model [44], it was discovered that it is important to define the initial orientation conditions accurately if the final orientation state within the printed bead is to be determined accurately. However, the initial orientation conditions are not so impactful when using the Folgar-Tucker Isotropic Rotary Diffusion model.

The computational methodology developed in this dissertation can be used to determine many orientation-dependent, anisotropic material properties of LAAM-printed short fiber reinforced polymers (SFRPs). These spatially varying properties, which are functions of the spatially varying fiber orientation state, are first deter-

mined on a microstructural level and then the effective, bulk response of the material is determined using finite element analysis. Such properties that can be predicted in this way include thermal properties, such as thermal conductivity and coefficient of thermal expansion (CTE), mechanical properties, such as tensile, compressive, and flexural stiffness and strength, and other properties such as electrical conductivity, mass diffusivity, and coefficient of moisture expansion. The equations for all these properties are provided in this dissertation in chapters 2 and 3, but the main focus of this dissertation is on thermal and mechanical properties. This work allowed the first representation of the spatially varying CTE, stiffness, and strength behavior in an AM fabricated SFRP material that could then be used for predicting bulk thermo-mechanical behavior. In addition, the computational methodology developed in this dissertation and presented in Figures 3.1 and 3.2 are not restricted to AM, but can be used in other applications involving the processing of SFRPs.

Much work was put into visuals in this dissertation, and methods were developed to give the reader immediate insight into the spatially varying properties in a processed SFRP material. In Section 3.3, a custom-made application created in-house in COMSOL Multiphysics is presented. This application demonstrates the versatility of the computational methodology developed in this dissertation by allowing a user to predict the spatially varying fiber orientation state in a polymer melt flow through a LAAM nozzle, and then predict the spatially varying elastic moduli, CTE, thermal conductivity, and tensile and compressive strength properties as functions of the underlying orientation state. In addition, the Van Hattum-Bernardo failure criterion can be used to generate failure plots that give immediate insight into potential weak areas of a part.

It was also discovered that the laminate analogy approach to predicting stiffness provides very similar results as the method used by the author of this dissertation. The laminate analogy approach bypasses finite element analysis, making it

much more efficient. Thus, if stiffness prediction is the only item of interest, the laminate analogy approach is recommended. However, the methods developed by the author are more versatile in that they can also be used to predict the strength constants and thermal properties as well. We note that these are not the only methods that have been attempted to predict effective properties of anisotropic SFRPs though. For example, Wang and Smith [126] used an integration method to obtain average elastic moduli through an extrudate. Methods that bypass the use of finite elements like this could be a route for future work.

The strength theory used in this dissertation was originally posed by Van Hattum and Bernardo [87], but the Hill criterion, which was originally used by Van Hattum and Bernardo, was relaxed, allowing the methods developed herein to be used for SFRPs that do not have equal tensile and compressive yield strength. While Van Hattum and Bernardo were aware of the full form of their model, it was explicitly demonstrated here in the prediction of tensile, compressive, and flexural strength. An advantage of their form is that it allows the anisotropic strength of an SFRP to be readily determined in any direction. In addition, the failure characteristics of a part can be examined under *any* loading condition using their model.

From the computational analyses, it was found that the RSC slowness parameter κ can have a profound impact on the final CTE and mechanical property predictions given the LAAM-nozzle flow model that was studied. The fiber interaction coefficient C_I apparently does not have as strong of an effect though when using the RSC model. Furthermore, the weight-average fiber length can have a significant impact on the mechanical property predictions, but the critical fiber length not so much. Incorporating porosity considerations into the models can have a significant effect on the predictions as well, and make them considerably more accurate. Using a realistic tensile bar geometry also helped increase accuracy in the mechanical property predictions.

A couple of comments on the computational methodology for predicting yield strength are worth mentioning. First, though it was not given much discussion in this dissertation, caution must be exercised when selecting a mesh to use in the yield strength predictions since these predictions are sensitive to areas of stress concentration. If stress concentrations are predicted due to a poor mesh selection, this may drastically change the amount of deformation that is needed to produce yielding according to the models. Secondly, in this study, tensile, compressive, and flexural strength were found by adjusting a deformation parameter, δ , until a failure parameter, φ , was equal to unity. This may take a while if a person must adjust δ by hard coding it before each simulation. Thus, an optimization technique to automate this process would be helpful. This is left for future work. It is, however, worth noting that failure plots can still be plotted even when φ does not equal unity. Thus, immediate insight into a material's weak points can be gained before δ is determined.

There are multiple ways in which the presented computational methodology can be improved. Perhaps the main contributions of this dissertation were articulating a modeling framework and giving visuals, but the underlying equations of the modeling methodology can be updated with newer, more accurate models as they are developed. For example, the CTE, stiffness, and strength models are all dependent on \mathbf{A} , the orientation state described by the second order orientation tensor. As newer, more accurate models for obtaining \mathbf{A} as a function of space are developed, they can readily be incorporated into the modeling methodology. Furthermore, if more accurate models are developed for getting the transversely isotropic longitudinal tensile and compressive strength, $\bar{\sigma}_{LT}$ and $\bar{\sigma}_{LC}$, and transverse tensile and compressive strength, $\bar{\sigma}_{TT}$ and $\bar{\sigma}_{TC}$, these can also be readily inserted into the strength tensors and used to predict the anisotropic strength properties of an SFRP in any direction.

Another area in which there is room for improvement is in predicting progressive damage failure. Polymers generally exhibit plastic deformation, but the focus of this dissertation has been on elastic properties. Predicting yield strength, as is demonstrated in this dissertation, is a good starting point, but predicting ultimate strength poses a bigger challenge. Nguyen and Kunc have utilized Van Hattum and Bernardo's model to predict elastic-plastic behavior in long fiber thermoplastics [145] and their insights could be useful in developing the current work even further.

Wang and Smith also studied viscoelastic behavior of SFRPs [146] using representative volume elements, but their analysis was restricted to unidirectional SFRPs. Further work on understanding the viscoelastic response of SFRPs would be helpful.

Other researchers have looked into ways to improve the Tsai-Wu criterion as well. Since Van Hattum and Bernardo's strength theory is built on the Tsai-Wu criterion, these improvements could potentially be made to the current modeling methodology too. For example, the researchers in [147] have attempted to improve the Tsai-Wu failure criterion in such a way that it allows the failure mode to be identified, a capability that was lacking in the original Tsai-Wu theory.

In addition to advancing the development of microstructural property prediction, insight into LAAM technology was also gained during the course of this dissertation. This work encompassed the building of a miniature LAAM system to fabricate test specimens, which has been used by several researchers at Baylor for various research projects since its construction. In addition, tied to this work, process specification documents were written for tensile, compression, and flexural testing as well as standard operating procedures for the LAAM system itself.

The experimental characterization of fiber aspect ratio in a LAAM-processed SFRP was also performed in this dissertation and it was confirmed that fiber breakage occurs during LAAM-processing and that the predicted, effective stiffness is significantly effected by changes in the weight-average fiber aspect ratio. The part

of the LAAM process that caused the most reduction in stiffness was the deposition stage after the material had left the nozzle already. However, it was noted that this problem could potentially be mitigated by adjusting the nozzle height and/or orientation. Further research on this topic is left for future work.


While the LAAM process offers the advantage of being able to process polymer pellets that have not been converted into filament, saving time and money, the 13% CF-ABS material printed with the LAAM system in this study contains a large amount of void content which can have a negative affect on the properties of the final product. Not only does void content directly decrease mechanical properties, but it may also reduce the amount of fiber alignment that is achievable in the printed SFRP material, thereby decreasing properties indirectly as well. Therefore, for LAAM-printed SFRPs to live up to their full potential, more research on void formation and how to mitigate it would be helpful.

APPENDICES

APPENDIX A

Standard Operating Procedure for Baylor LAAM System


The Standard Operating Procedure for the Baylor LAAM System is included in the following pages. The primary author of this procedure is the author of this dissertation, however, it is an evolving document and may have seen edits and additions by other Baylor researchers as well who saw areas where it could be improved. The author of this dissertation, while referring to this document, has trained several students on the operation of this system and updated it over time.

	PROCESS SPECIFICATION	PS-LAAM
	Revision:	Date Created: 10/08/21
	LAAM Machine	

PROCESS SPECIFICATION

PS-LAAM

Large Area Additive Manufacturing (LAAM) Machine Operation

	PROCESS SPECIFICATION	PS-LAAM
	Revision:	Date Created: 10/08/21
	LAAM Machine	

LIST OF REVISIONS

Rev.	Description	Date	Approval
IR	Initial Release	10/08/21	



	PROCESS SPECIFICATION	PS-LAAM
	Revision:	Date Created: 10/08/21
	LAAM Machine	


TABLE OF CONTENTS

Title Page	1
List of Revisions	2
Table of Contents	3
1.0 - Introduction	4
2.0 - Material List	5
3.0 - Procedure	6

	PROCESS SPECIFICATION	PS-LAAM
	Revision:	Date Created: 10/08/21
	LAAM Machine	

1.0 – Introduction


This is a large scale 3D printing machine that takes as input, thermoplastic material pellets. Mach3 software is used for controlling the gantry system of the machine whereas the extruder is controlled using the Strangpresse extruder control box. These do not work in conjunction and thus must be operated separately by the user(s) at the same time. Mach3 runs G-Code and thus to print a specific design, a print file must be written in G-Code syntax. A print file may be written in Notepad, saved as a *.txt file, and uploaded into the Mach3 software.

	PROCESS SPECIFICATION	PS-LAAM
	Revision:	Date Created: 10/08/21
	LAAM Machine	

2.0 – Materials List

You will need the materials as follows:


- ___ Material pellets
- ___ Painter's tape
- ___ Putty knife

	PROCESS SPECIFICATION	PS-LAAM
	Revision:	Date Created: 10/08/21
	LAAM Machine	


3.0 – Procedure

The following steps shall be followed when printing parts with the LAAM system:

1. Start the computer. Log into the computer using the following:
Username: drdj-siberian\laam_printer
Password: LAAM_Printer
2. Set up the extruder.
 - a. Turn on the extruder by turning the big red rotary switch on the Strangpresse control box clockwise 90° (the switch handle should be vertical).
 - b. After giving the extruder a moment to turn on, a message, `Extruder Drive Fault`, may appear on the control box interface. If it does, press `Close`.
 - c. Press `Extruder` to go to the extruder settings.
 - d. There may be a red, flashing `FAULT` ● message on the right side of the screen. If so, press the `FAULT RESET` button just beneath the message (the message should then disappear).
 - e. Temperature settings. There are three temperature zones and both their set temperatures (top row, to the right of the `SET` label) and their current (actual) temperatures (second row, to the right of the `ACT` label) should appear at the top of the screen. Make sure appropriate temperatures for processing your material are entered in the `SET` boxes. To adjust one of these temperatures, press it and enter the desired temperature in the pop-up window. After entering the desired temperature, press `↵` to return to the main extruder page.
 - f. Turn the extruder heating zones on. After all of the desired extruder settings are set, press the red `ON` button in the middle of the main extruder screen under `ALL EXTRUDER HEAT ZONES ON/OFF`. A light will come on the `ON` button and you should see the `ACT` temperatures approaching the `SET` temperatures. (If an error message pops up, check the thermocouples on the extruder. If they appear in working order, press `Close` and proceed with caution, by keeping a close eye on the `ACT` temperatures.)
 - g. Extrusion rate. On the main extruder page to the left, you should see a box entitled `SET AUTO MODE SPEED RPM`. This displays the extruder screw RPM which can be changed to adjust the extrusion rate. To change it, press the box and enter the desired RPM in the pop-up window and then press `↵`.
3. Set up gantry system.
 - a. Turn the gantry system on by flipping on the power switch on the silver box.
 - b. Double-click the “Mach3” shortcut on the desktop.

	PROCESS SPECIFICATION	PS-LAAM
	Revision:	Date Created: 10/08/21
	LAAM Machine	

- c. "Session Profile" window will appear. Make sure "3DPrinter" is selected and click "OK."
- d. "Reset" button should be flashing - you must click it before you will be able to move the extruder.
- e. "Soft Limits" button should be highlighted with green border – if it isn't, click it so it is.
- f. You may use the PlayStation controller to move the extruder: L1 (or R1) trigger + left joystick to move in the x-y plane and L1 (or R1) trigger + right joystick to move up and down in the z direction. (You can also use the arrow keys on the keyboard.)
- g. You may also go to a specific, hard-coded coordinate. Do this by going to the "MDI Alt2" tab and entering an appropriate command in the "Input" line.
NOTE: Make sure you know what you are coding before you execute any commands! Consult the G-Code manual for help!
- h. In the "Program Run Alt-1" tab, you may also upload a G-Code written for printing a specific part. Click "Load G-Code," opening the desired code. You should see the file appear in the upper left of Mach3. The highlighted line shows which line is being executed. You may edit the G-Code by clicking "Edit G-Code." If you edit a file, you must save it. To change to a different G-Code, click "Close G-Code" and then load the new G-Code.
NOTE: BE CAREFUL ABOUT CLICKING "CYCLE START" IN THE MIDDLE OF THE G-CODE FILE SINCE THE FIRST HALF OF THE FILE (WHICH MIGHT DEFINE THE STARTING POINT AND THE UNIT SYSTEM) WILL NOT RUN!!! CLICK REWIND TO START A G-CODE FILE FROM THE BEGINNING!!!

	PROCESS SPECIFICATION	PS-LAAM
	Revision:	Date Created: 10/08/21
	LAAM Machine	

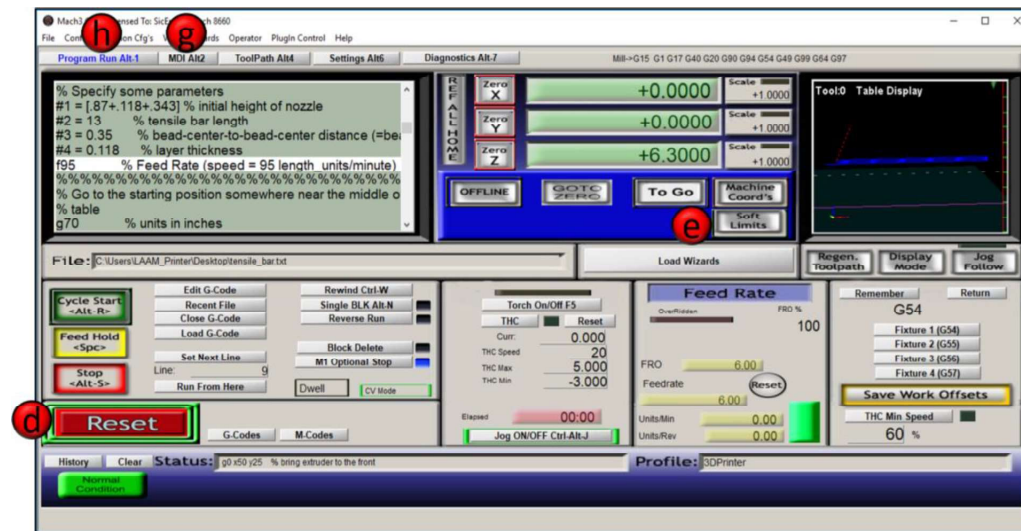




Figure 1. Mach3 Software. Steps d, e, g, and h refer to the buttons labeled.

4. If using, turn on the heated bed.
 - a. To use the 3 foot heat sheet, plug in both of its cords (black and grey) into the wall outlet.
 - b. The top number (green) on the temperature controller display is the current temperature (°C) and the bottom number (red) is the set temperature (°C). Make sure you adjust the thermocouple as necessary to get an accurate reading of the temperature of the bed. (You will see the current temperature jumping around as you move the thermocouple around. I generally adjust the thermocouple till I find the position where it gives its maximum temperature reading and then carefully leave it there. If the thermocouple is reading a temperature much lower than the actual temperature, the heater will try to compensate and get way too hot! Beware!)
5. Air hose.
 - a. Turn on the air nozzle with the attached, long, flexible hose. Don't turn it on too high – you should see the hose segment before the regulator start to swell a bit but not a lot. You may check the air pressure by blocking the end of the hose with your thumb. It should be ~10-15 psi. Attach the hose to the top of the extruder (one of the two brass colored nozzles). Hot air should come out of the other nozzle.
6. Print a part.

	PROCESS SPECIFICATION	PS-LAAM
	Revision:	Date Created: 10/08/21
	LAAM Machine	

- a. Make sure the extruder is in a proper starting position and that it will be clear from running into anything during execution of the G-Code made for printing the part.
 - b. Start extruding, then immediately run G-Code. To start extruding, press the green button titled EXTRUDER DRIVE START/STOP. It should light up and the extruder should start. To run the G-Code, click the “Cycle Start <Alt-R>” button (highlighted in green).
 - c. Should a problem occur during the print.
 - a. **Stop the extruder** – push EXTRUDER DRIVE START/STOP
 - b. **Stop the gantry** – push “Stop <Alt-S>” or the red “EMERGENCY” stop button on the silver box
7. Finishing up.
- a. After the part is done printing, let it cool for a moment, then pry it up. You can use a putty knife if you like.
 - b. Return the extruder to the home position – go to the “MDI Alt2” tab and type G28+enter in the text box
 - c. Turn off all of the equipment.

	PROCESS SPECIFICATION	PS-LAAM
	Revision:	Date Created: 10/08/21
	LAAM Machine	

Trouble Shooting

Resetting X-Y Home Position

1. Start with the gantry power box off.
2. Manually push the extruder to the back, left corner of the system.
3. Push the extruder in the -x direction so that it meets the limit switch. Push it a little further until the limit switch clicks, then back it up. Back it up until the limit switch clicks again and then stop. The gantry system should now be putting pressure on the limit switch but not enough to trigger it (see Figure 2(a)). Repeat the same process for the y direction.

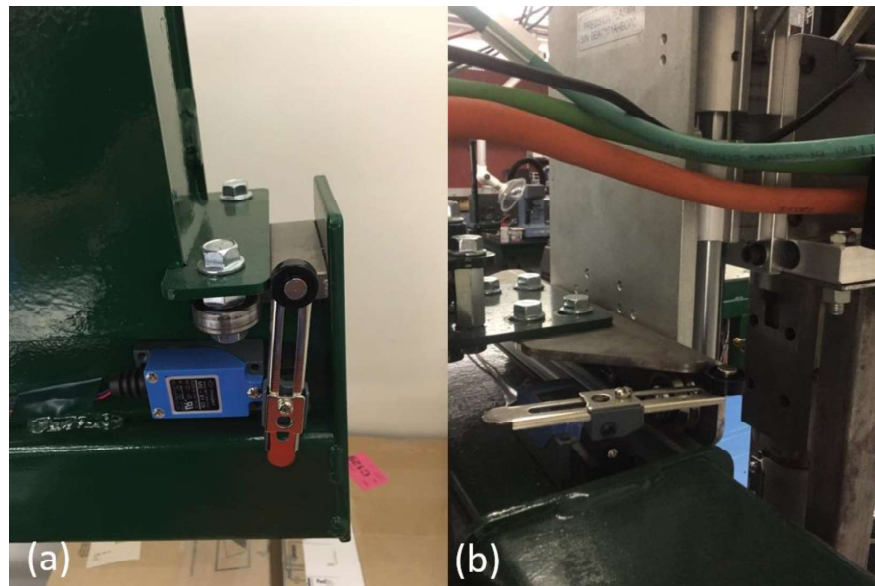


Figure 2. Gantry system in contact with limit switches but not pressing hard enough to trigger them. (a) x limit switch; (b) y limit switch.

4. Open Mach3.
5. Select 3DPrinter and click OK.
6. If the Status box says Limit Switch Triggered:
 - a. Go to the Settings Alt6 tab and click OverRide Limits (Figure 3). A red light should start flashing.
 - b. Click the flashing Reset button.


	PROCESS SPECIFICATION	PS-LAAM
	Revision:	Date Created: 10/08/21
	LAAM Machine	



Figure 3. Where to override the limits.

7. Go to the Config tab and click Homing/Limits.
8. Confirm that the G28 home location coordinates have X=0 and Y=0 (see Figure 3) and click OK.

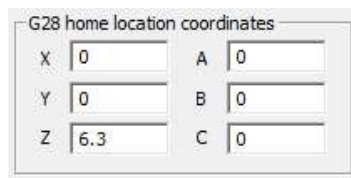


Figure 4. Where to set home location coordinates.

9. Go to the MDI Alt2 tab and type G0 X0 Y0+Enter in the Input box.
10. Confirm that the X-Y home position has been reset:
 - a. Turn on the gantry power box.
 - b. Restart Mach3, go to the MDI Alt2 tab and type G28+Enter in the Input box. The extruder should go to the correct X-Y home position and read the coordinates X=+0.0000 and Y=+0.0000 on the digital readout (DRO) display.

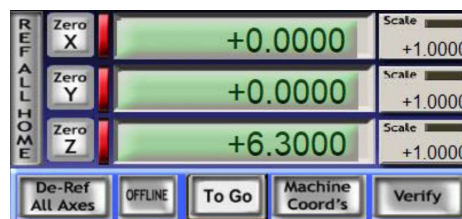



Figure 5. Digital Readout (DRO) of (X,Y,Z) coordinates.

	PROCESS SPECIFICATION	PS-LAAM
	Revision:	Date Created: 10/08/21
	LAAM Machine	

Resetting Z Home Position

1. Turn the gantry power box on.
2. Open Mach3.
3. Select 3DPrinter and click OK.
4. If the Reset button is flashing, click it.
5. Use the PlayStation controller to adjust the Z-height of the extruder until it is at its maximum height. Leave a small gap above the plate on which the extruder is mounted as shown in Figure 6.

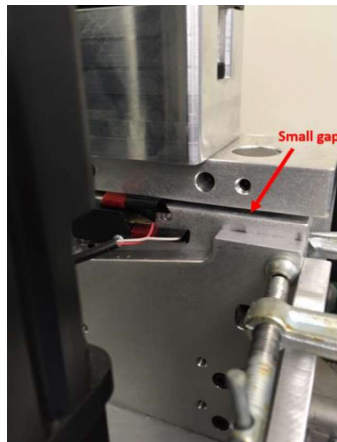



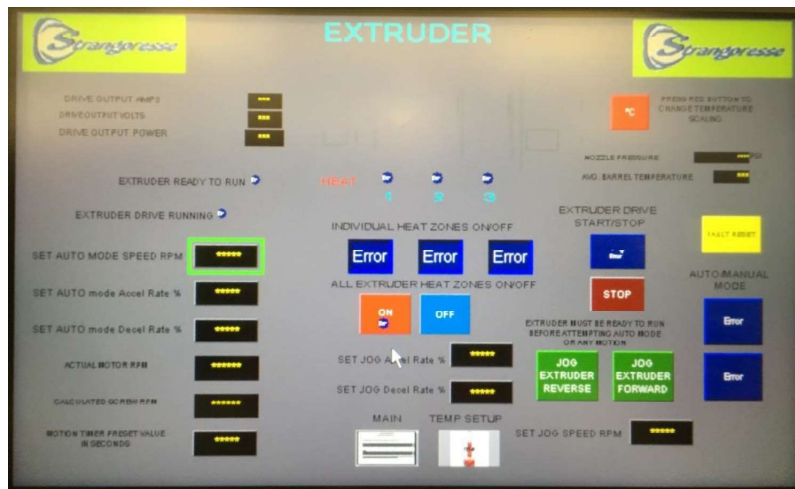
Figure 6. Correct Z-height position.


6. Switch off the gantry power box.
7. If the Status box says Limit Switch Triggered:
 - a. Go to the Settings Alt6 tab and click OverRide Limits (Figure 3). A red light should start flashing.
 - b. Click the flashing Reset button.
8. Go to the Config tab, click Homing/Limits, and confirm that Z=6.3 as shown in Figure 4.
9. Go to the MDI Alt2 tab and type G0 Z6.3+Enter in the Input box.
10. Confirm that the Z home position has been reset:
 - a. Turn on the gantry power box.
 - b. Restart Mach3, go to the MDI Alt2 tab and type G28+Enter in the Input box. The extruder should go to the correct Z home position and read the coordinate Z=+6.3000 on the digital readout (DRO) display as shown in Figure 5.

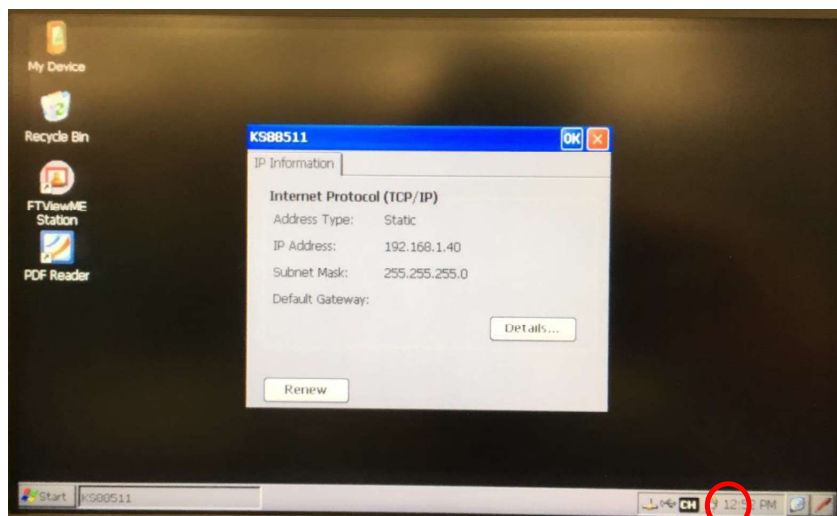
	PROCESS SPECIFICATION	PS-LAAM
	Revision:	Date Created: 10/08/21
	LAAM Machine	


Extruder Error

If you get a screen that looks like the one below, it is likely an issue with the IP address.

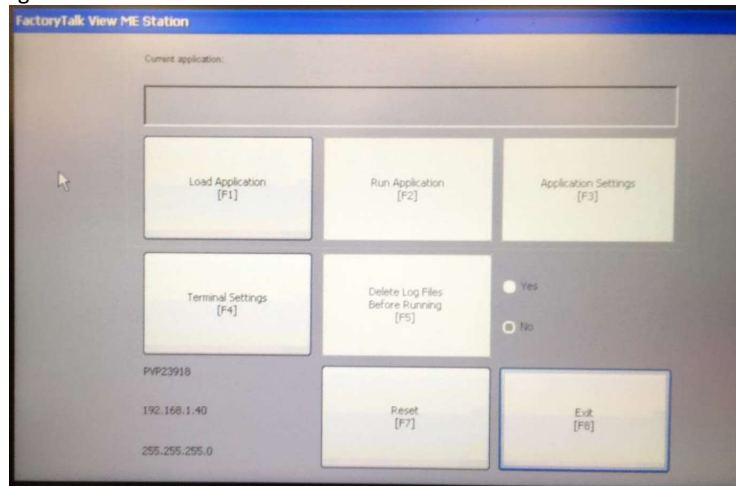


1. Go to the desktop and click the  button in the bottom right. The IP Address and Subnet Mask are 192.168.1.40 and 255.255.255.0, respectively, as given in the figure below.

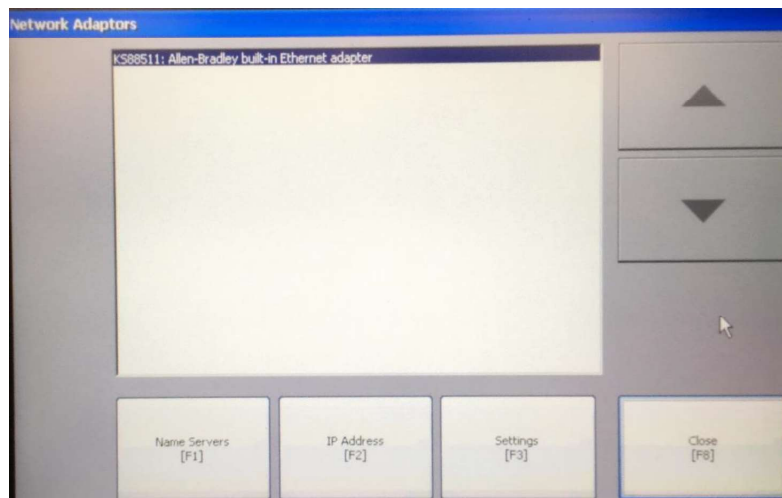


	PROCESS SPECIFICATION	PS-LAAM
	Revision:	Date Created: 10/08/21
	LAAM Machine	


- Double-tap the FTViewME Station icon on the desktop to open up FactoryTalk. You should see the following screen.



- Tap Terminal Settings. You should see the following screen next.
- Go to Network and Communications > Network Connections > Network Adaptors. You should see the following screen next.



- Tap IP Address [F2]. You should have the following information displayed on the screen:
IP Address [F1]: 192.168.1.40
Subnet Mask [F2]: 255.255.255.0

	PROCESS SPECIFICATION	PS-LAAM
	Revision:	Date Created: 10/08/21
	LAAM Machine	

Gateway [F3]: 0.0.0.0

6. Tap OK.
7. If there's another box that pops up, accept it.
8. Cancel out of everything and restart the Strangepresse computer.
9. If the computer opens to the desktop screen, double-tap FTViewME Station.
10. Tap Load Application [F1].
11. Once the application is done loading, tap Run Application [F2].
12. Open the Extruder interface.

APPENDIX B

Tensile Testing Results

Five Neat ABS and four 13% CF-ABS tabbed tensile specimens were tested. The stress-strain responses for the Neat ABS specimens are shown in Figure B.1. The stress-strain responses for the 13% CF-ABS specimens are shown in Figure B.2.

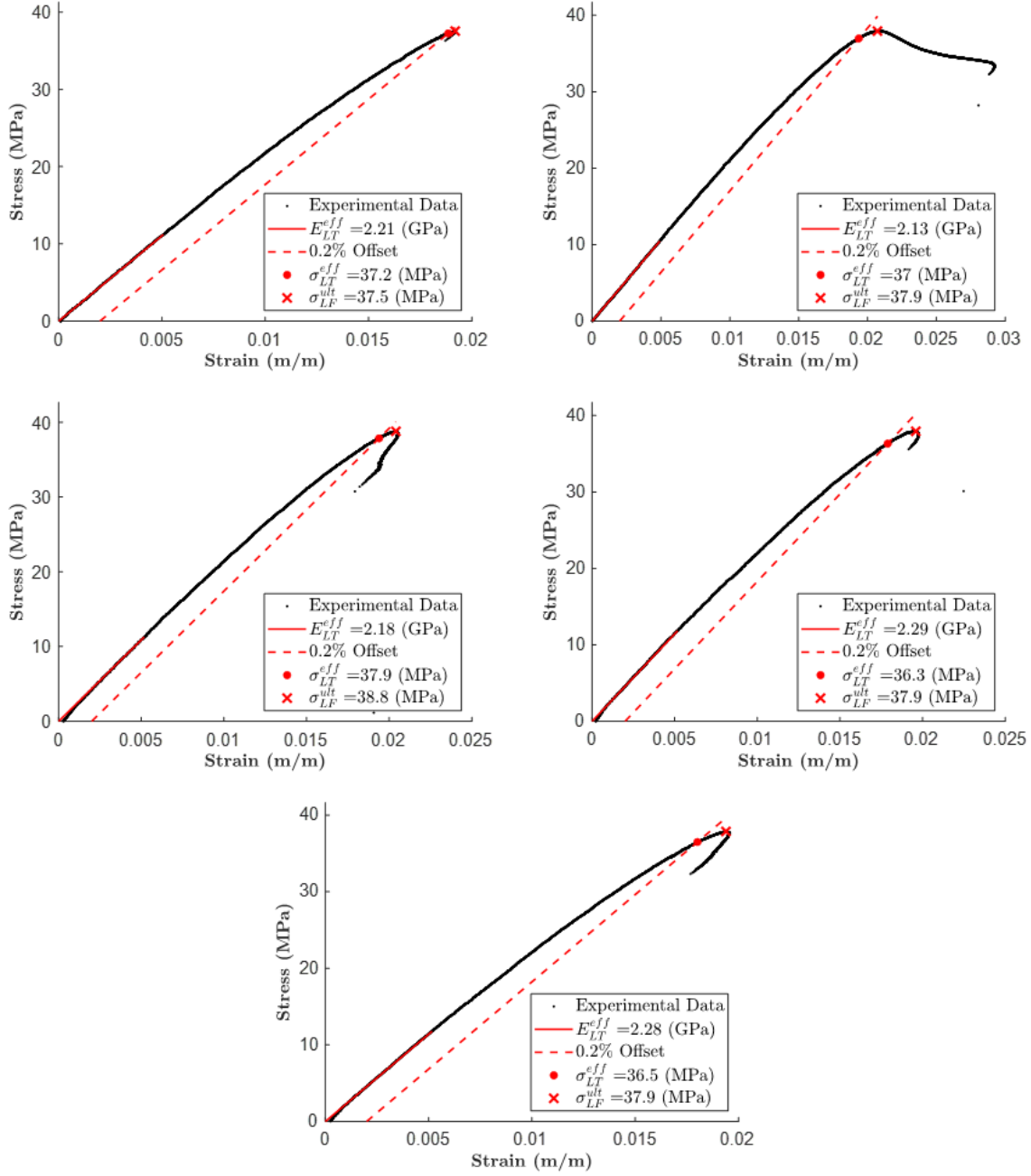


Figure B.1: Tensile testing stress-strain curves for Neat ABS.

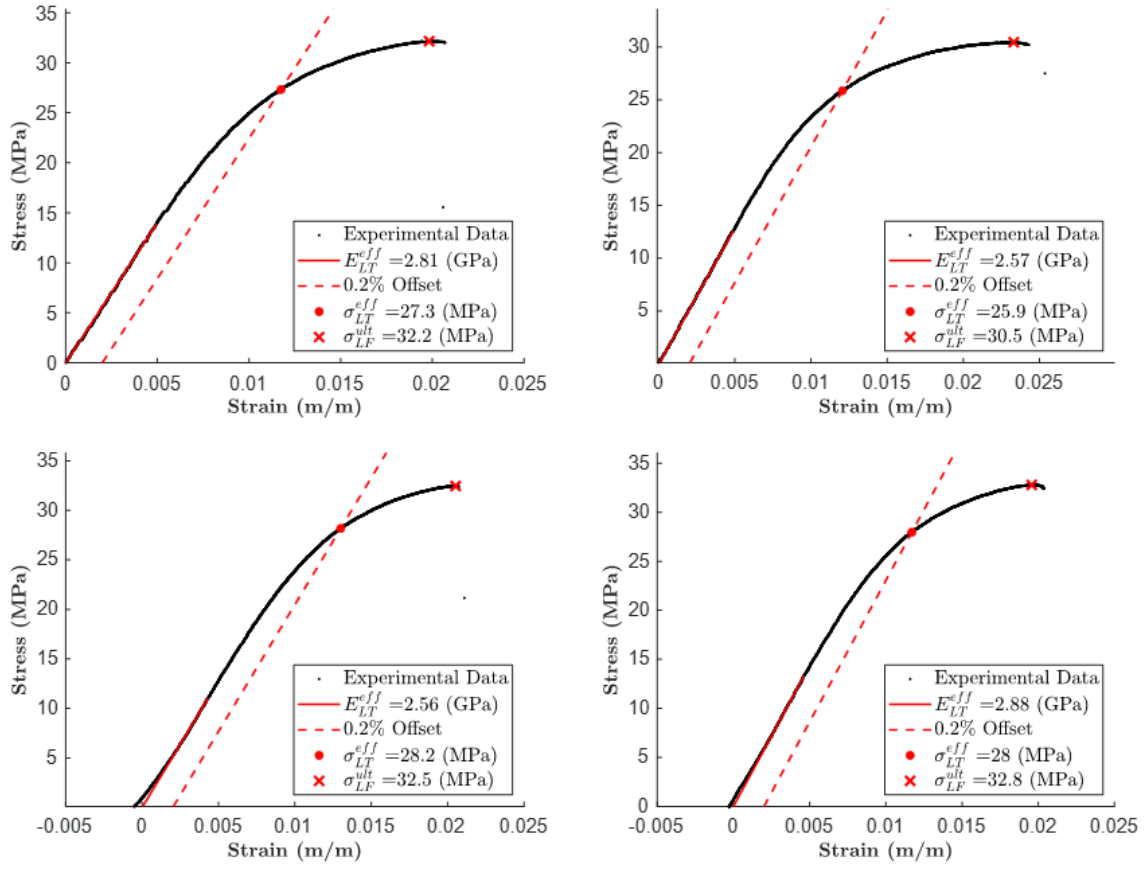


Figure B.2: Tensile testing stress-strain curves for 13% CF-ABS.

APPENDIX C

Compression Testing Results

Five Neat ABS and five 13% CF-ABS tabbed compression specimens were tested. The stress-strain responses for the Neat ABS specimens are shown in Figure C.1. The stress-strain responses for the 13% CF-ABS specimens are shown in Figure C.2.

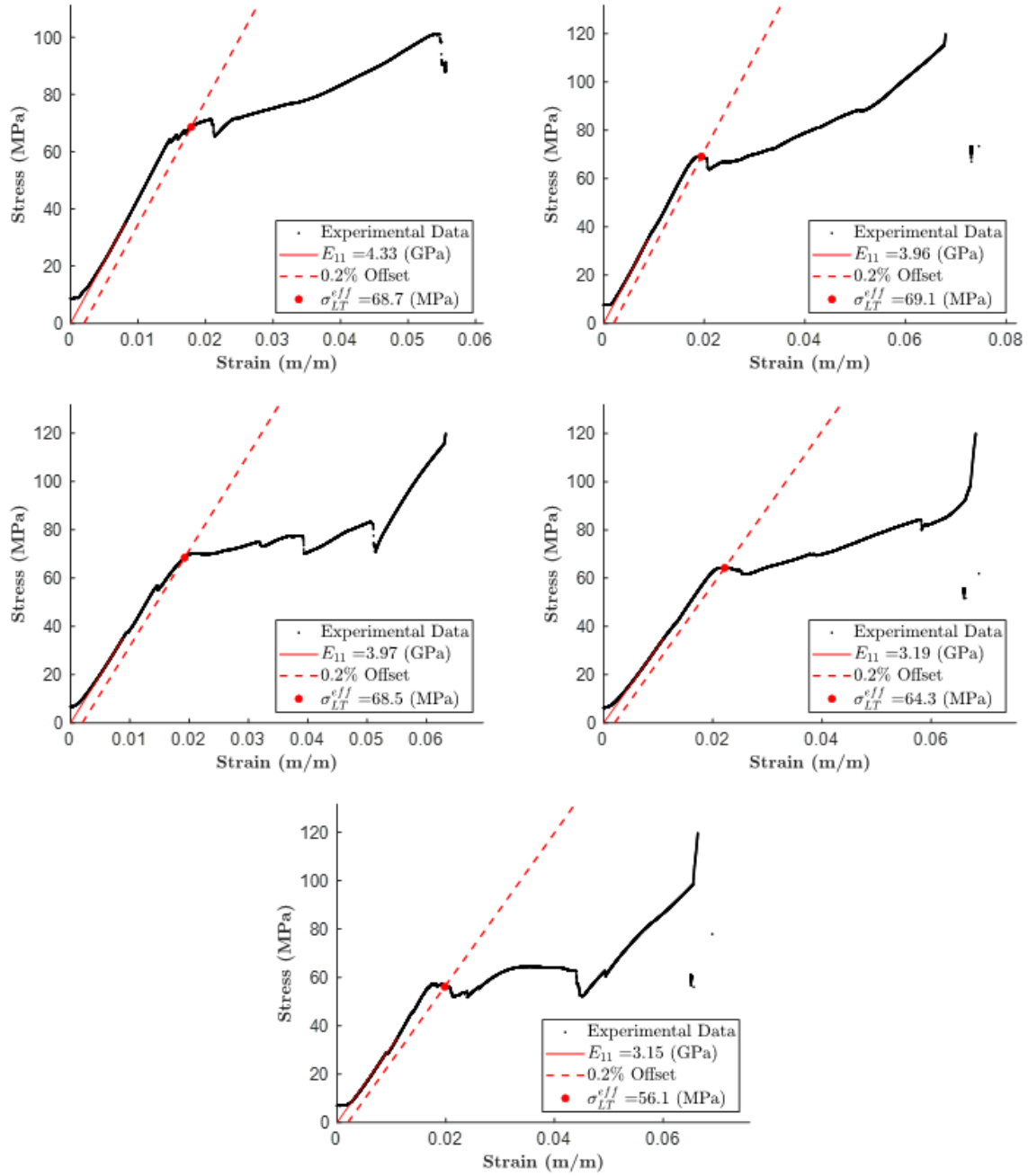


Figure C.1: Compression testing stress-strain curves for Neat ABS.

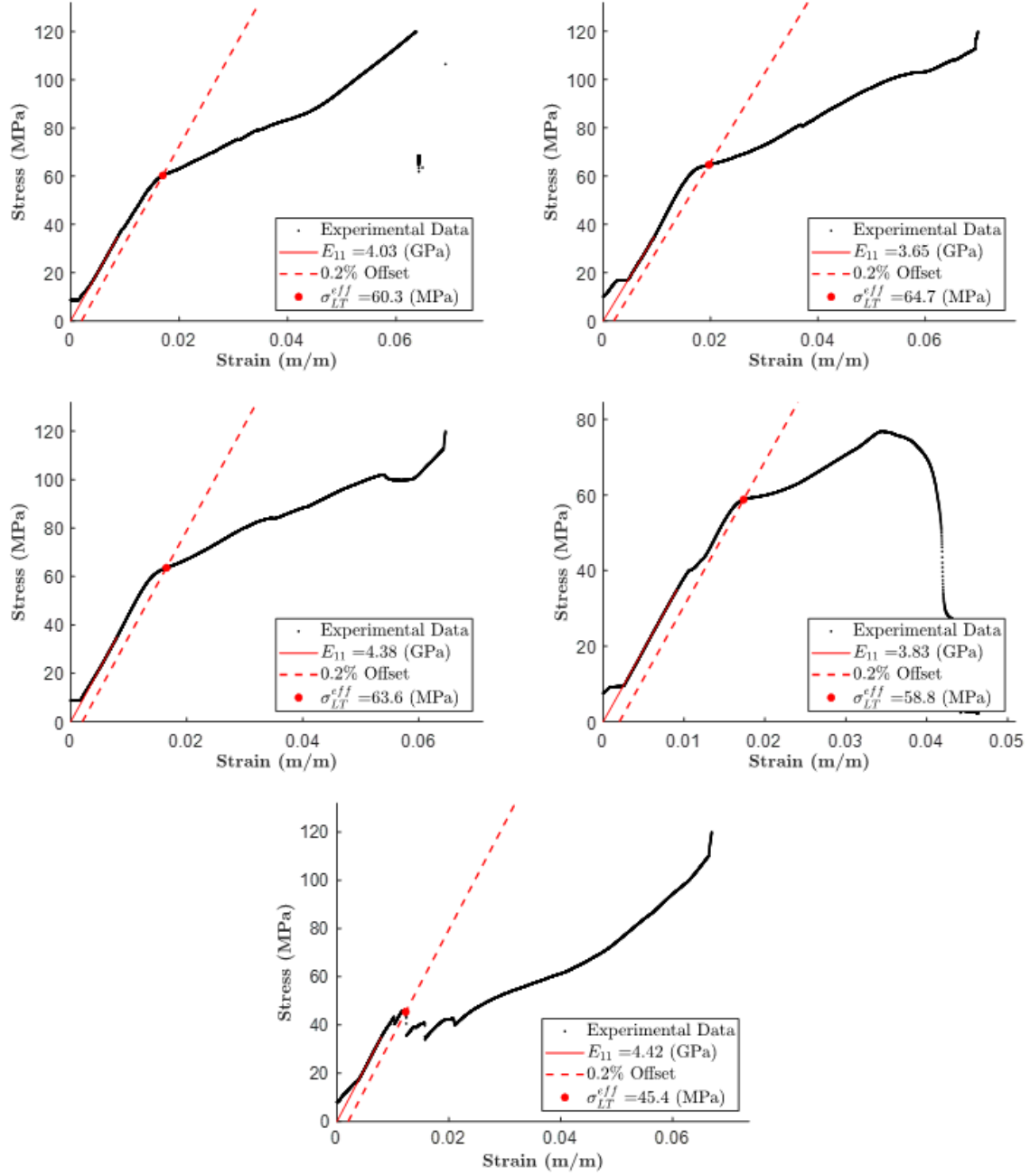


Figure C.2: Compression testing stress-strain curves for 13% CF-ABS.

APPENDIX D

Flexural Testing Results

Five Neat ABS and five 13% CF-ABS three-point bend test specimens were tested. The load-deflection and stress-strain responses for the Neat ABS specimens are shown in Figures D.1 and D.2. The load-deflection and stress-strain responses for the 13% CF-ABS specimens are shown in Figures D.3 and D.4.

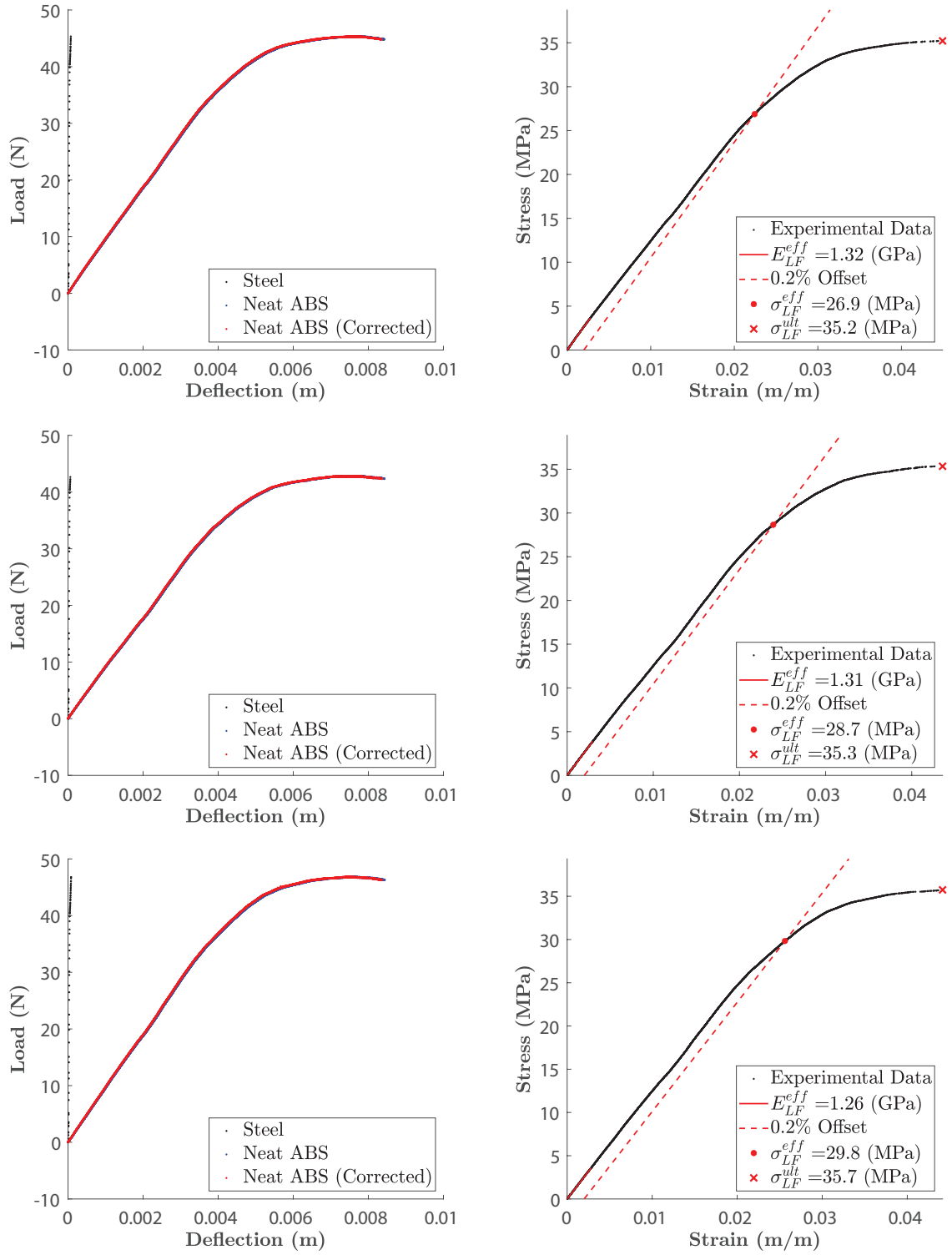


Figure D.1: Flexural testing results for Neat ABS. The load-deflection plots for each sample are presented on the left, while the corresponding stress-strain plots are plotted to the right.

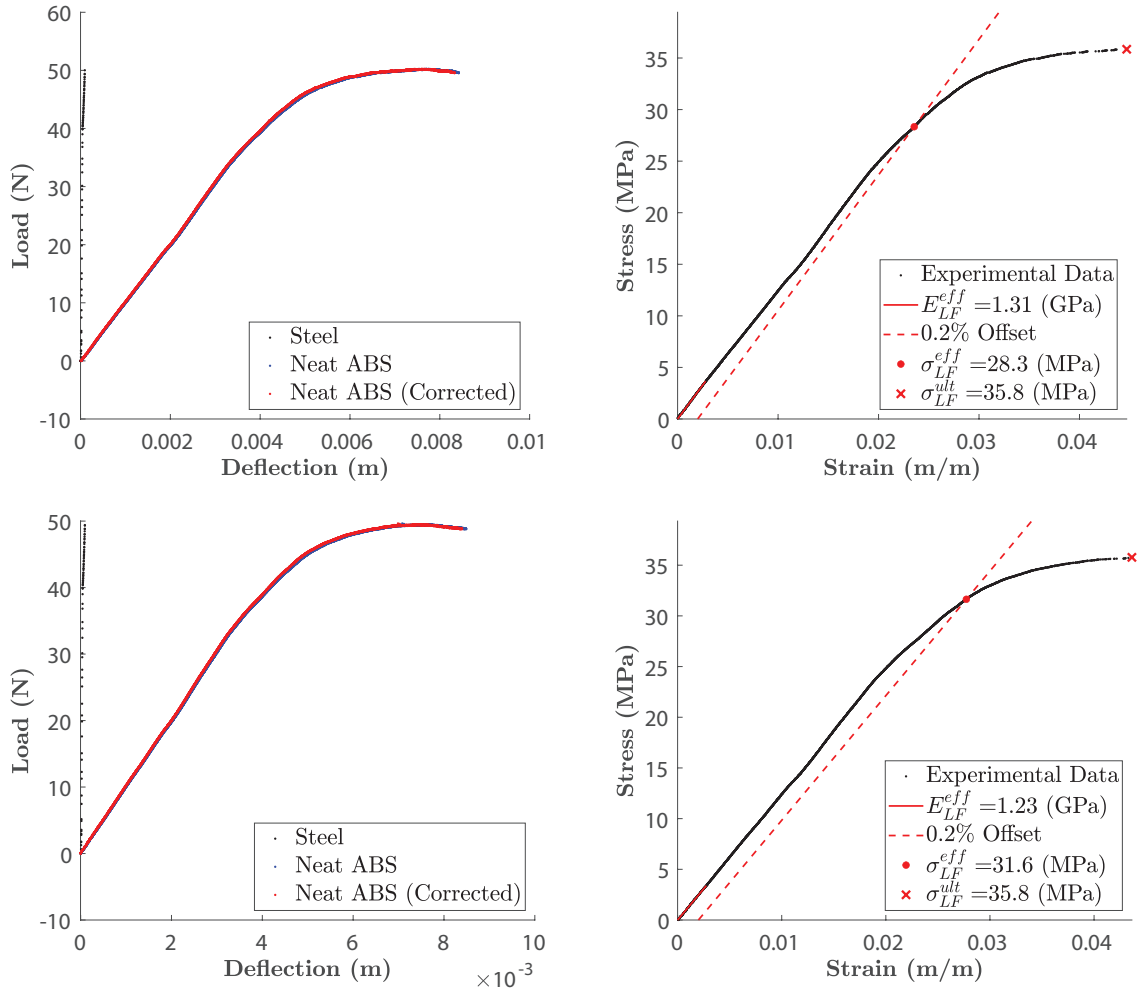


Figure D.2: Flexural testing results for Neat ABS. The load-deflection plots for each sample are presented on the left, while the corresponding stress-strain plots are plotted to the right.

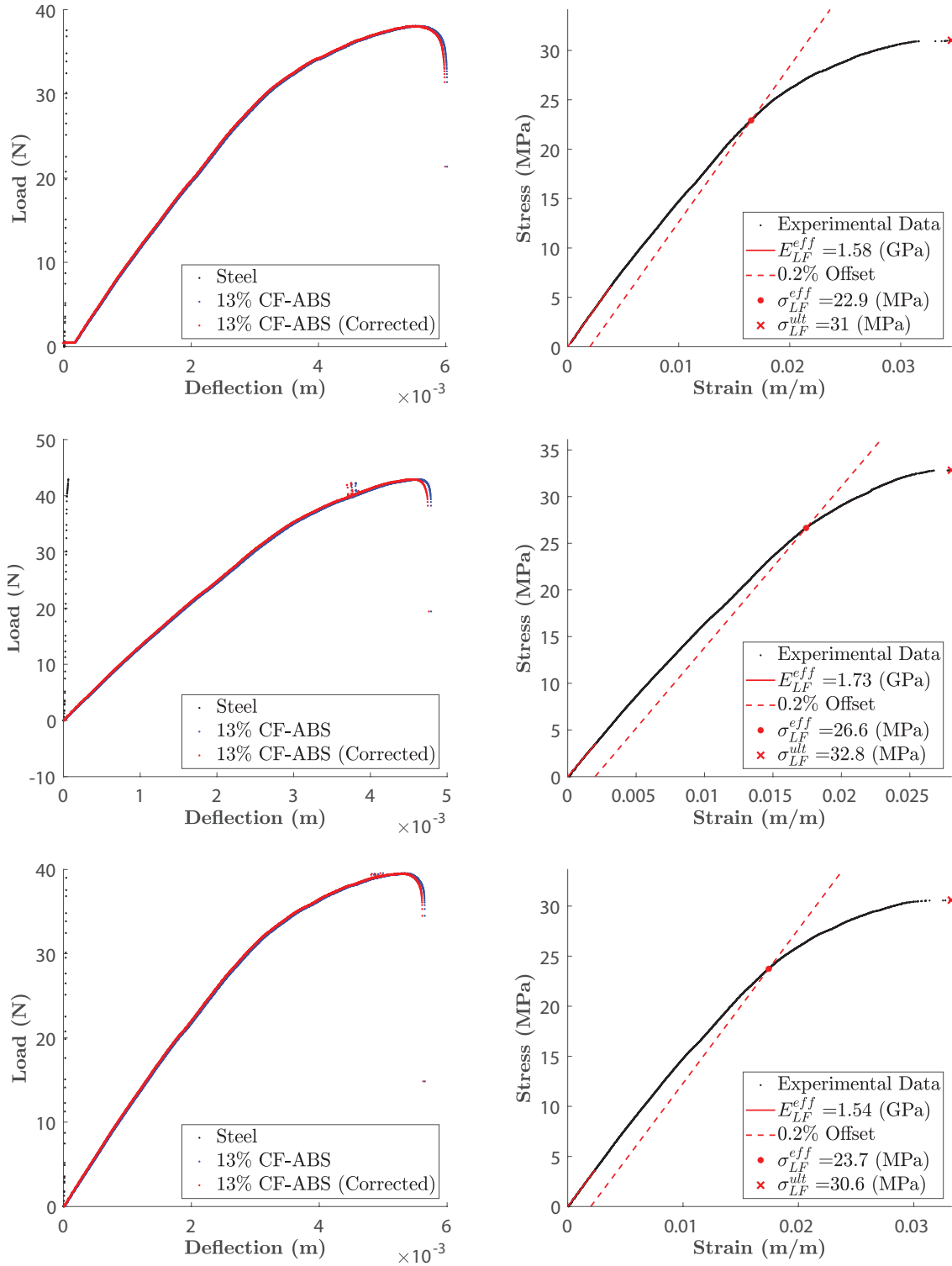


Figure D.3: Flexural testing results for 13% CF-ABS. The load-deflection plots for each sample are presented on the left, while the corresponding stress-strain plots are plotted to the right.

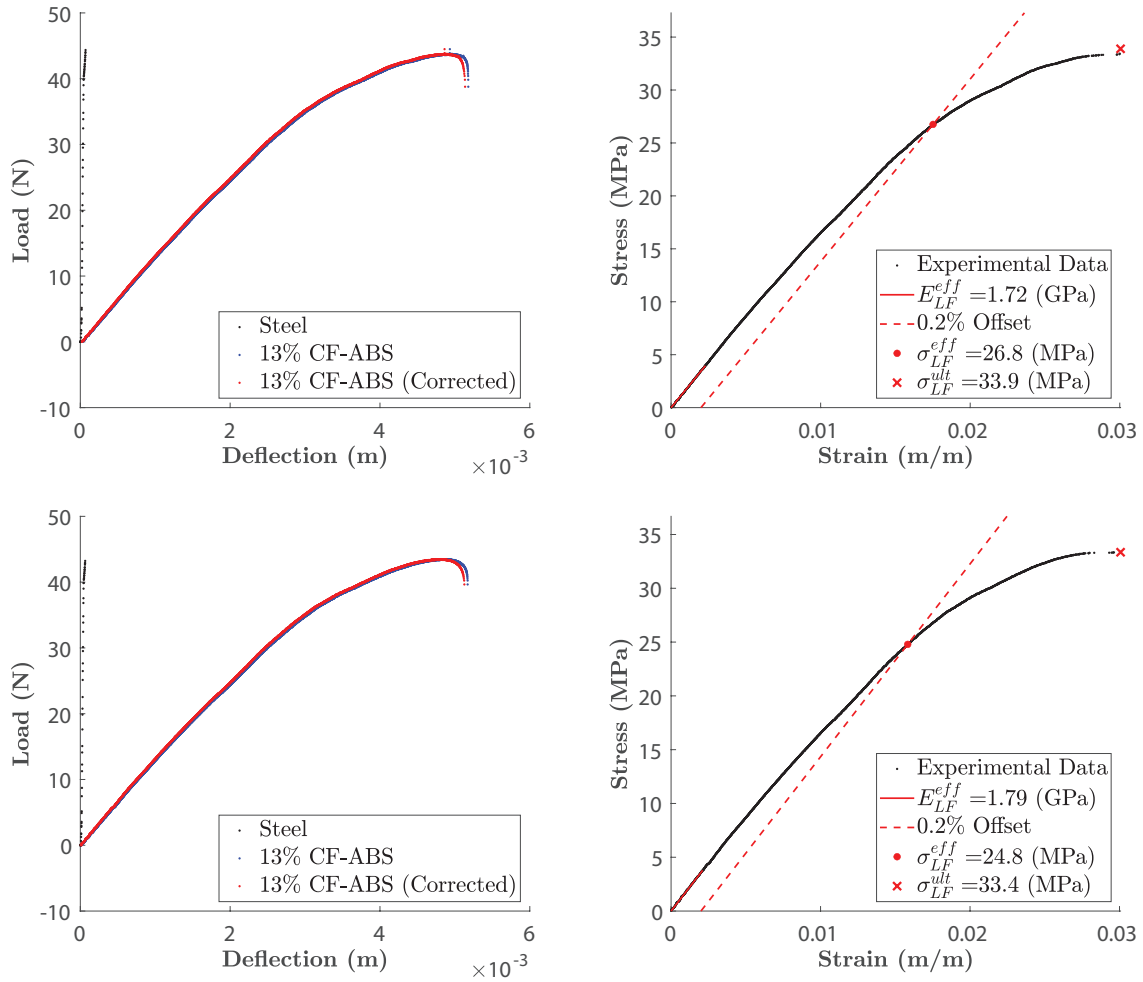


Figure D.4: Flexural testing results for 13% CF-ABS. The load-deflection plots for each sample are presented on the left, while the corresponding stress-strain plots are plotted to the right.

APPENDIX E

Tensile Testing Results from SAMPE Study

Five 13% CF-ABS tabbed tensile specimens were tested by the author for the study presented in [37]. These have been reused in this dissertation. The stress-strain responses for the 13% CF-ABS specimens are shown in Figure E.1.

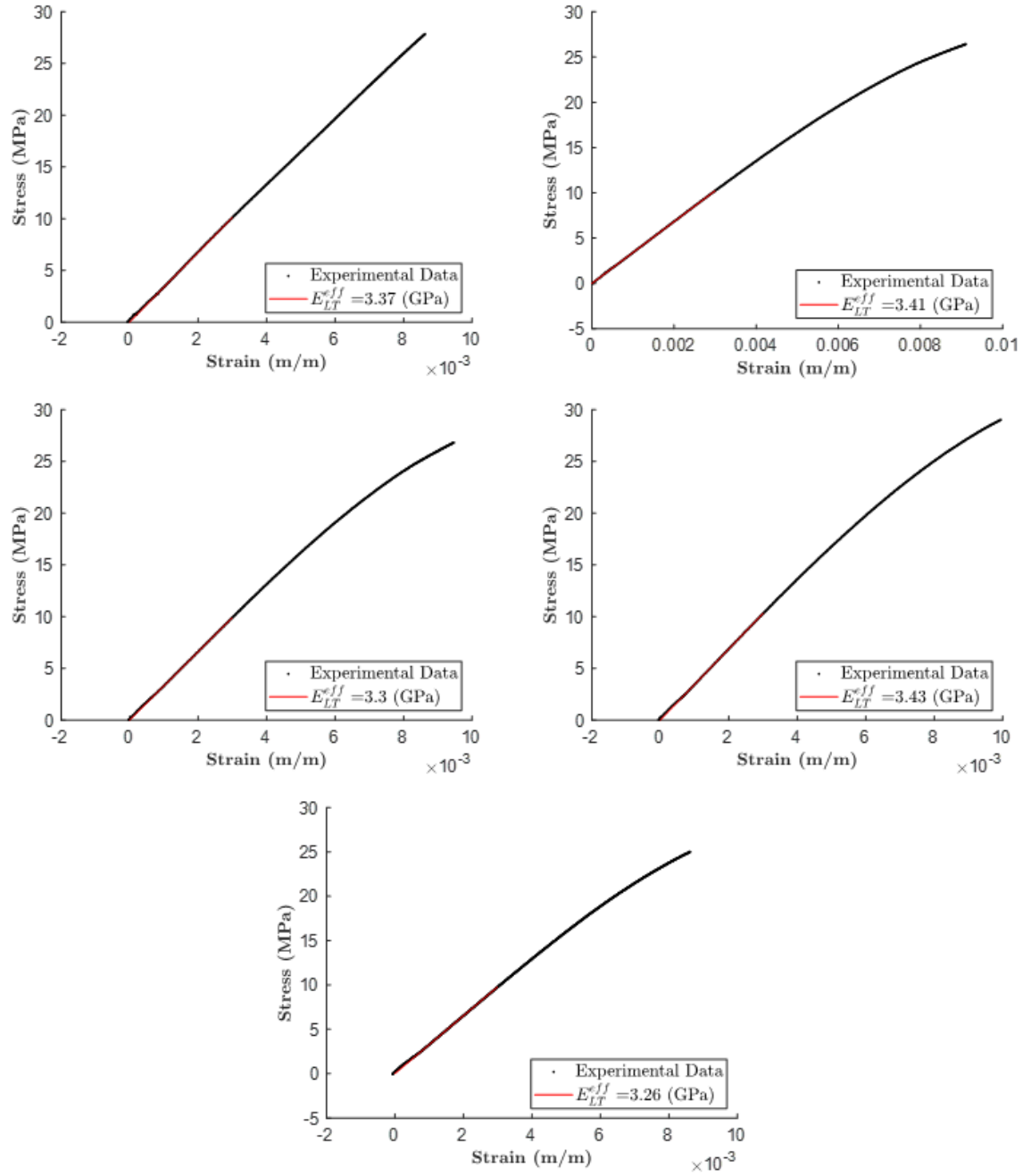


Figure E.1: Tensile testing stress-strain curves for 13% CF-ABS from the study conducted in [37].

APPENDIX F

Additional TGA Testing Results

Five Neat ABS and five 13% CF-ABS pellet samples from PolyOne were tested in a TA Instruments Q50 TGA machine based on ASTM E1131-20. The mass-temperature curves for the Neat ABS samples are shown in Figure F.1 and the mass-temperature curves for the 13% CF-ABS samples are shown in Figure F.2. Reports of the tests are also given in Table F.1 and Table F.2. In addition, three Neat ABS and three 13% CF-ABS samples were tested based on ASTM D3171-15, and the results of these tests are given in Figure F.3 and Figure F.4. A report on the test data for these tests, which includes the calculated fiber volume fraction, is also given in Table F.3.

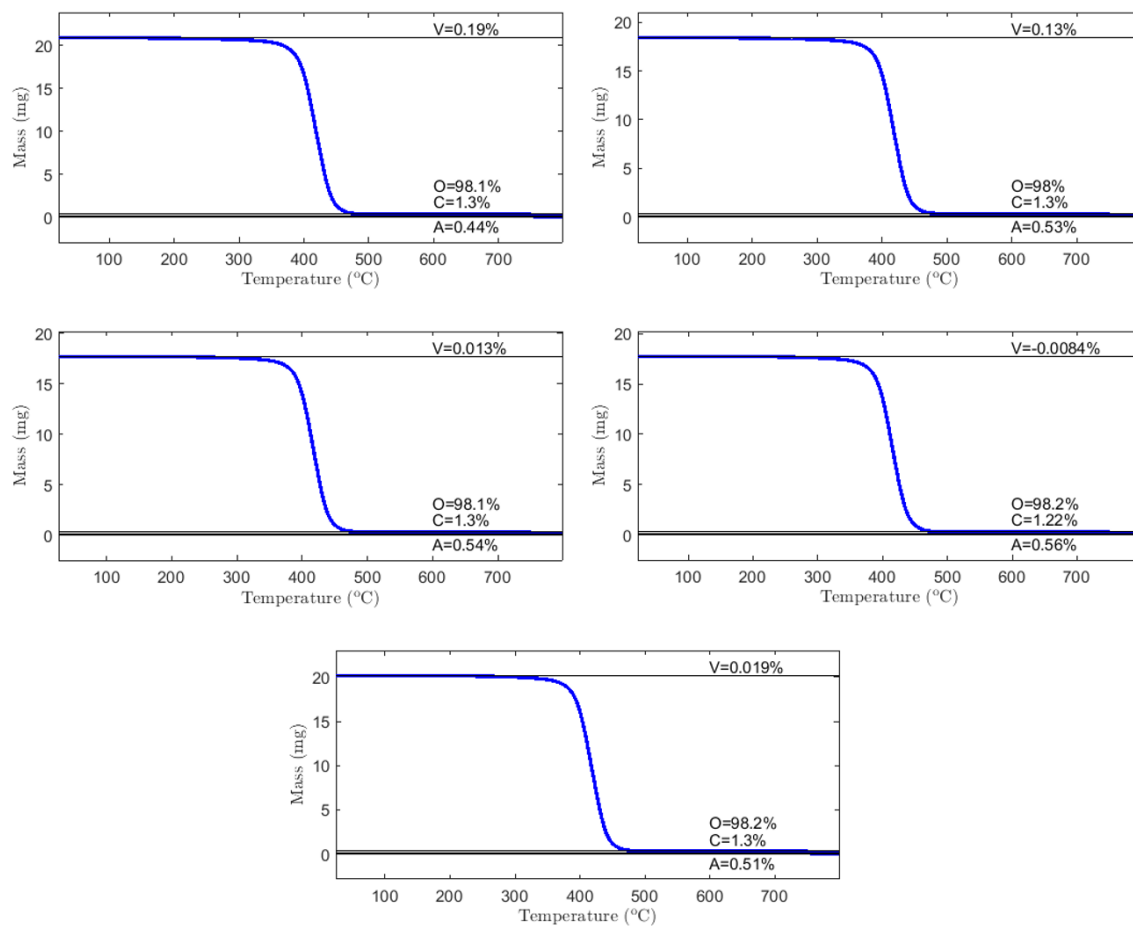


Figure F.1: Mass-temperature curves for five Neat ABS pellet samples tested based on ASTM E1131-20.

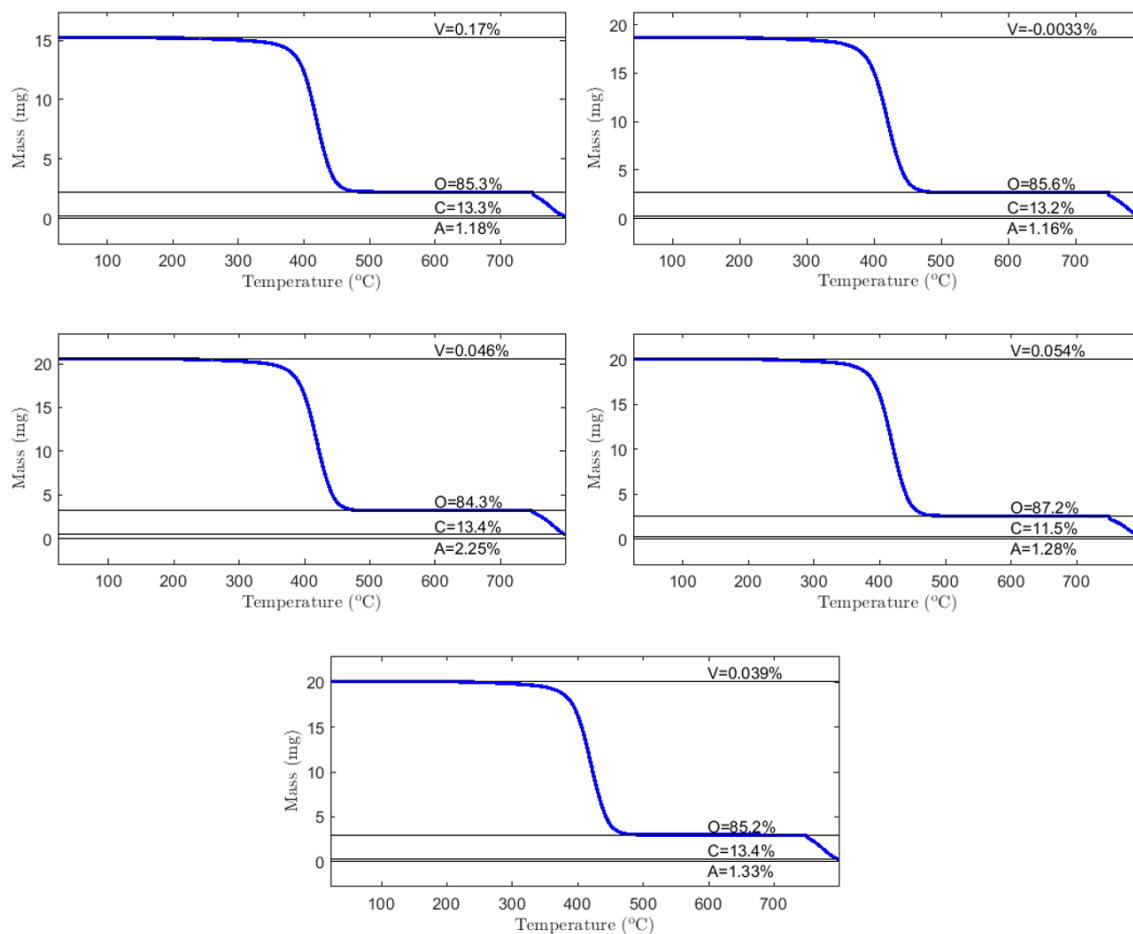


Figure F.2: Mass-temperature curves for five 13% CF-ABS pellet samples tested based on ASTM E1131-20.

Table F.1: Report on TGA burn-tests of PolyOne Neat ABS samples based on ASTM E1131-20.

Standards Used	ASTM E1131-20				
Procedure Used	Compositional Analysis by Thermogravimetry				
Date of specific dated version of the standard used	E1131 - March 15, 2020				
Testing performed by	David Jack, Timothy Russell				
Location	BRIC 2148				
Date	10/21-22/2021				
Test material Information					
Product number (if applicable)	N/A				
Material Description	PolyOne Neat ABS				
Environmental Conditioning Summary	Sample 1-2 - Room for 2+ years, Samples 3-5 dried at 60°C for 10-15 hours				
Test Equipment					
Test machine number/description	TA Instruments Q50 - TGA				
Temperature calibration date	Tuesday, May 4, 2021				
Weight calibration date	Tuesday, May 4, 2021				
Room Temperature (°F)	~73				
Room humidity (%RH)	~41				
Pan type	Platinum				
Total number of tests	5				
Pre-Test Check					
Mass of sample before test start using TGA (mg)	21		17	17	19
Test Parameters					
Balance Purge Flow (mL/min)	40.0	40.0	40.0	40.0	40.0
Sample Purge Flow (mL/min)	40.0	40.0	40.0	40.0	40.0
Nitrogen Purity (%)	99.9	99.9	99.9	99.9	99.9
Start Temperature (°C)	21.42	23.59	26.63	22.16	24.24
Highly volatile mass plateau (i.e., Temperature X in °C)	150	150	150	150	150
Hold prior to ramp to temperature X (min)	0.0	0.0	0.0	0.0	0.0
Ramp rate to Temperature X (°C/min)	10.0	10.0	10.0	10.0	10.0
Gas used during ramp from start to X	N2	N2	N2	N2	N2
Medium volatile mass plateau (i.e., Temperature Y in °C)	600	600	600	600	600
Hold prior to ramp to temperature Y (min)	0.0	0.0	0.0	0.0	0.0
Ramp rate to Temperature Y (°C/min)	10.0	10.0	10.0	10.0	10.0
Gas used during ramp from X to Y	N2	N2	N2	N2	N2
Purge air temperature	750	750	750	750	750
Hold prior to initiating purge ramp (min)	0.0	0.0	0.0	0.0	0.0
Ramp rate to purge temperature (°C/min)	10.0	10.0	10.0	10.0	10.0
Gas used during ramp from Y to purge	N2	N2	N2	N2	N2
Combustible mass plateau (i.e., Temperature Z in °C)	800	800	800	800	800
Hold prior to ramp to Z (min)	1.0	1.0	1.0	1.0	1.0
Ramp rate to Temperature Z (°C/min)	10.0	10.0	10.0	10.0	10.0
Gas used during ramp during purge and ramp to Z	Air	Air	Air	Air	Air
Test Results - Measured Values					
W - Original Specimen mass (mg)	20.891	18.436	17.719	17.736	20.179
R - Mass measured at Temperature X (mg)	20.851	18.412	17.716	17.737	20.176
S - Mass measured at Temperature Y (mg)	0.362	0.337	0.326	0.316	0.366
Mass measured prior to purge (mg)	0.127	0.127	0.134	0.133	0.149
T - Mass measured at Temperature Z (mg)	0.091	0.098	0.096	0.099	0.103
Test Results - Calculated Values					
V - Highly volatile matter content (%)	0.189	0.129	0.013	-0.008	0.019
O - Medium volatile matter content (%)	98.077	98.042	98.146	98.229	98.170
C - Combustible matter content (%)	1.297	1.297	1.303	1.222	1.302
A - Ash content (%)	0.436	0.532	0.539	0.557	0.510
Test Results - Calculated Value Statistics					
	Average	Standard Deviation	Coefficient of Variation		
V - Highly volatile matter content (%)	0.07	0.09	126.50		
O - Medium volatile matter content (%)	98.13	0.07	0.08		
C - Combustible matter content (%)	1.28	0.03	2.70		
A - Ash content (%)	0.51	0.05	9.14		

Table F.2: Report on TGA burn-tests of PolyOne 13% CF-ABS samples based on ASTM E1131-20.

Standards Used	ASTM E1131-20				
Procedure Used	Compositional Analysis by Thermogravimetry				
Date of specific dated version of the standard used	E1131 - March 15, 2020				
Testing performed by	David Jack, Timothy Russell				
Location	BRIC 2148				
Date	10/21/2021				
Test material Information					
Product number (if applicable)	N/A				
Material Description	PolyOne ABS with 13% Carbon Fiber				
Environmental Conditioning Summary	Sample 1-2 - Room for 2+ years, Samples 3-5 dried at 60°C for 10-15 hours				
Test Equipment					
Test machine number/description	TA Instruments Q50 - TGA				
Temperature calibration date	Tuesday, May 4, 2021				
Weight calibration date	Tuesday, May 4, 2021				
Room Temperature (°F)	~73				
Room humidity (%RH)	~41				
Pan type	Platinum				
Total number of tests	5				
Pre-Test Check					
Mass of sample before test start using TGA (mg)	15	18.8	20	19	20
Test Parameters					
Balance Purge Flow (mL/min)	40.0	40.0	40.0	40.0	40.0
Sample Purge Flow (mL/min)	40.0	40.0	40.0	40.0	40.0
Nitrogen Purity (%)	99.9	99.9	99.9	99.9	99.9
Start Temperature (°C)	24.75	42.01	22.13	24.81	22.07
Highly volatile mass plateau (i.e., Temperature X in °C)	150	150	150	150	150
Hold prior to ramp to temperature X (min)	0.0	0.0	0.0	0.0	0.0
Ramp rate to Temperature X (°C/min)	10.0	10.0	10.0	10.0	10.0
Gas used during ramp from start to X	N2	N2	N2	N2	N2
Medium volatile mass plateau (i.e., Temperature Y in °C)	600	600	600	600	600
Hold prior to ramp to temperature Y (min)	0.0	0.0	0.0	0.0	0.0
Ramp rate to Temperature Y (°C/min)	10.0	10.0	10.0	10.0	10.0
Gas used during ramp from X to Y	N2	N2	N2	N2	N2
Purge air temperature	750	750	750	750	750
Hold prior to initiating purge ramp (min)	0.0	0.0	0.0	0.0	0.0
Ramp rate to purge temperature (°C/min)	10.0	10.0	10.0	10.0	10.0
Gas used during ramp from Y to purge	N2	N2	N2	N2	N2
Combustible mass plateau (i.e., Temperature Z in °C)	800	800	800	800	800
Hold prior to ramp to Z (min)	1.0	1.0	1.0	1.0	1.0
Ramp rate to Temperature Z (°C/min)	10.0	10.0	10.0	10.0	10.0
Gas used during ramp during purge and ramp to Z	Air	Air	Air	Air	Air
Test Results - Measured Values					
W - Original Specimen mass (mg)	15.233	18.685	20.586	20.065	20.119
R - Mass measured at Temperature X (mg)	15.207	18.685	20.576	20.054	20.111
S - Mass measured at Temperature Y (mg)	2.212	2.691	3.213	2.566	2.973
Mass measured prior to purge (mg)	2.034	2.413	3.042	2.365	2.772
T - Mass measured at Temperature Z (mg)	0.180	0.217	0.462	0.257	0.269
Test Results - Calculated Values					
V - Highly volatile matter content (%)	0.170	-0.003	0.046	0.054	0.039
O - Medium volatile matter content (%)	85.306	85.601	84.347	87.158	85.186
C - Combustible matter content (%)	13.339	13.241	13.361	11.506	13.440
A - Ash content (%)	1.185	1.161	2.246	1.282	1.335
Test Results - Calculated Value Statistics*					
	Average	Standard Deviation		Coefficient of Variation	
V - Highly volatile matter content (%)	0.06	0.06		103.16	
O - Medium volatile matter content (%)	85.11	1.03		1.21	
C - Combustible matter content (%)	13.35	0.83		6.19	
A - Ash content (%)	1.48	0.46		30.72	

*Note: sample 4 was an outlier and thus left out of calculations for average, standard deviation, and coefficient of variation

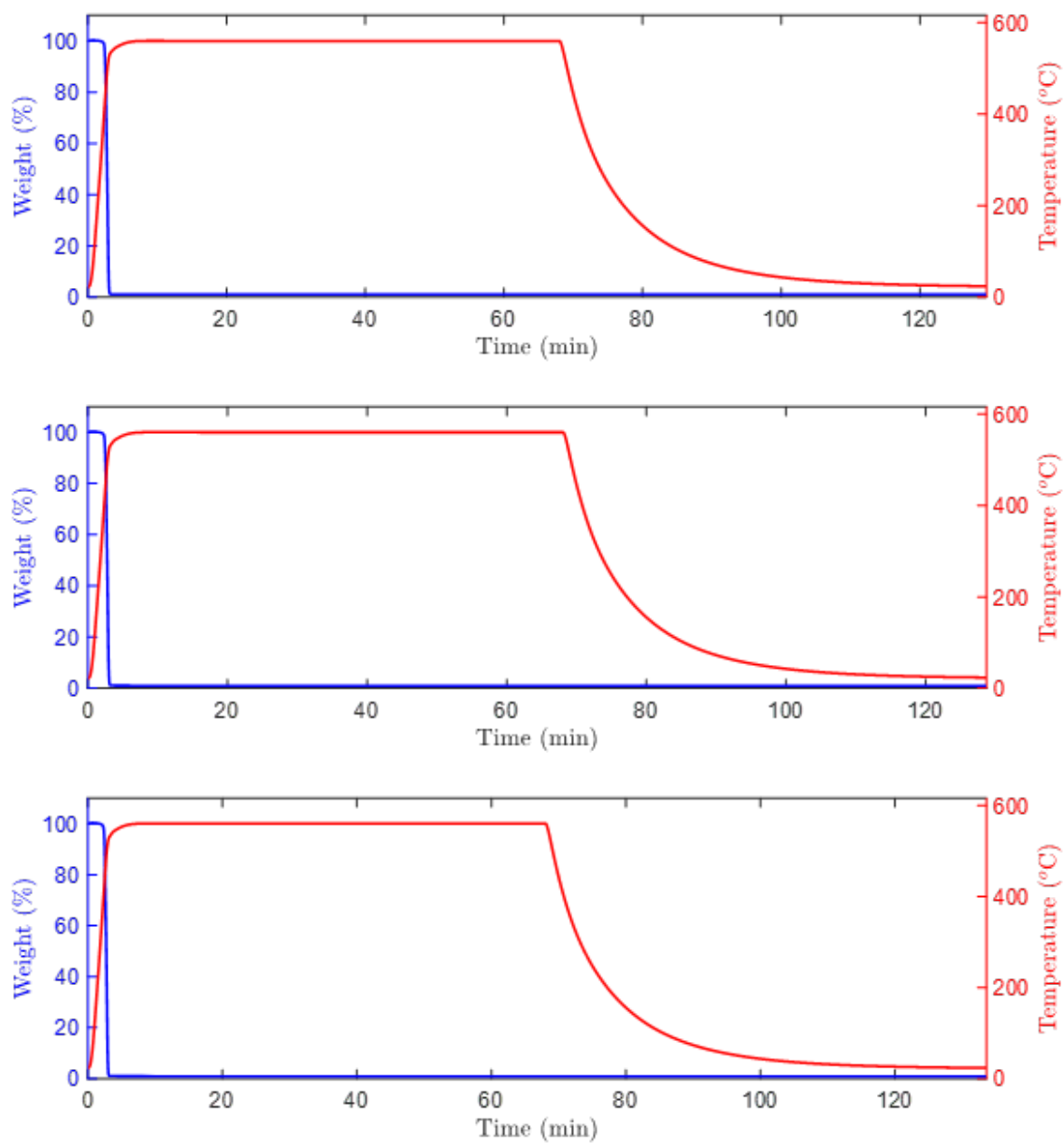


Figure F.3: TGA data for three Neat ABS pellet samples tested based on ASTM D3171-15.

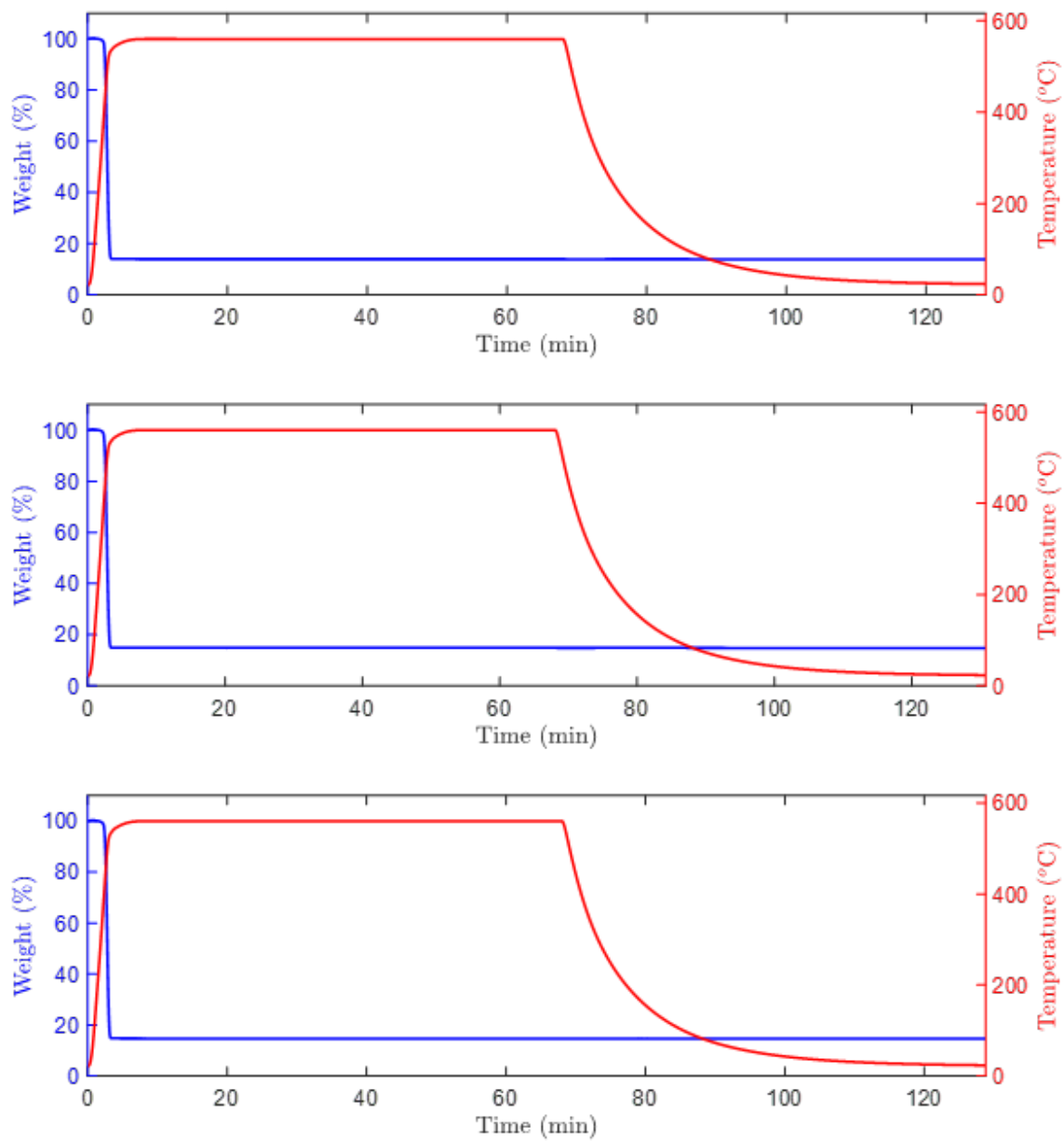


Figure F.4: TGA data for three 13% CF-ABS pellet samples tested based on ASTM D3171-15.

Table F.3: Report on TGA burn-tests of PolyOne Neat ABS and 13% CF-ABS tested based on ASTM D3171-15.

Standards Used	ASTM D3171 - 15, Procedure H		
Procedure Used	Constituent Content of Composite Materials		
Date of specific dated version of the standard used	D3171 - April 1, 2015		
Testing performed by	Timothy Russell		
Location	BRIC 2148		
Date	10/20/2021		
Test material Information			
Product number (if applicable)	N/A		
Material 1 Description	PolyOne Neat ABS		
Material 2 Description	PolyOne ABS with 13% Carbon Fiber		
Environmental Conditioning Summary	Samples 1 - 3 dried at 80 degC for 5 hr and 10 min		
Test Equipment			
Test machine number/description	TA Instruments Q50 - TGA		
Temperature calibration date	Tuesday, May 4, 2021		
Weight calibration date	Tuesday, May 4, 2021		
Room Temperature (degF)	~72.4		
Room humidity (%RH)	~42		
Pan type	Platinum		
Total number of tests	6 (3 of Neat ABS, 3 of 13% CF-ABS)		
Pre-Test Check			
Mass of Neat ABS samples before test start (g)	0.02	0.018	0.017
Mass of 13% CF-ABS samples before test start (g)	0.019	0.019	0.015
Test Parameters			
pr = density of the reinforcement (g/cm^3)	1.76	1.76	1.76
pm = density of the matrix (g/cm^3)	1.04	1.04	1.04
pc = density of the composite specimen (g/cm^3)	1.11	1.11	1.11
Test Results - Measured Values			
mi = initial mass of the neat resin specimen (g)	0.021	0.019	0.017
md = Final mass of the neat resin residue after carbonization (g)	0.000	0.000	0.000
Mi = initial mass of the composite specimen (g)	0.020	0.018	0.015
Md = final residue mass of the composite specimen (g)	0.003	0.003	0.002
Test Results - Measured Value Statistics			
	Average	Standard Deviation	Coefficient of Variation
mi = initial mass of the neat resin specimen (g)	0.019	0.002	10.633
md = Final mass of the neat resin residue after carbonization (g)	0.000	0.000	14.999
Mi = initial mass of the composite specimen (g)	0.018	0.003	15.817
Md = final residue mass of the composite specimen (g)	0.003	0.000	14.075
Test Results - Calculated Values			
CR = carbonization ratio of the neat resin	0.009		
Mm = mass of the resin matrix in the composite specimen (g)	0.015		
Wr = fiber (reinforcement) content, weight (%)	13.599		
Vr = fiber (reinforcement) volume fraction (%)	8.577		
Wm = matrix content, weight (%)	86.401		
Vm = matrix content, volume (%)	92.216		
Vv = void volume (%)	-0.793		

BIBLIOGRAPHY

- [1] U. Gandhi, S. Goris, T. Osswald, and Y. Song. *Discontinuous Fiber-Reinforced Composites: Fundamentals and Applications*. Hanser Publications, Cincinnati, December 2019.
- [2] S. Advani. *Prediction of fiber orientation during processing of short fiber composites*. Ph.D., University of Illinois at Urbana-Champaign, United States – Illinois, 1987.
- [3] 3DPrinting.com. “What is 3D printing?,” from <https://3dprinting.com/what-is-3d-printing/>.
- [4] L. Love, V. Kunc, O. Rios, C. Duty, A. Elliott, B. Post, R. Smith, and C. Blue. The importance of carbon fiber to polymer additive manufacturing. *Journal of Materials Research*, 29(17):1893–1898, September 2014.
- [5] C. Hull. Apparatus for production of three-dimensional objects by stereolithography, March 1986.
- [6] J. Stansbury and M. Idacavage. 3D printing with polymers: Challenges among expanding options and opportunities. *Dental Materials*, 32(1):54–64, January 2016.
- [7] M. Fey. *3D printing and international security: risks and challenges of an emerging technology*. Number 144 in PRIF Reports. Hessische Stiftung Friedens- und Konfliktforschung, Frankfurt am Main, 2017.
- [8] N. Guo and M. Leu. Additive manufacturing: technology, applications and research needs. *Frontiers of Mechanical Engineering*, 8(3):215–243, September 2013.
- [9] X. Wang, M. Jiang, Z. Zhou, J. Gou, and D. Hui. 3D printing of polymer matrix composites: A review and prospective. *Composites Part B: Engineering*, 110:442–458, February 2017.
- [10] B. Brenken, E. Barocio, A. Favaloro, V. Kunc, and R. Pipes. Fused filament fabrication of fiber-reinforced polymers: A review. *Additive Manufacturing*, 21:1–16, May 2018.
- [11] J. Fallon, S. McKnight, and M. Bortner. Highly loaded fiber filled polymers for material extrusion: A review of current understanding. *Additive Manufacturing*, 30:100810, December 2019.

- [12] C. Duty, V. Kunc, B. Compton, B. Post, D. Erdman, R. Smith, R. Lind, P. Lloyd, and L. Love. Structure and mechanical behavior of Big Area Additive Manufacturing (BAAM) materials. *Rapid Prototyping Journal*, 23(1):181–189, January 2017.
- [13] A. Hassen, R. Springfield, J. Lindahl, B. Post, L. Love, C. Duty, U. Vaidya, R. Pipes, and V. Kunc. The Durability of Large-Scale Additive Manufacturing Composite Molds. In *CAMX Conference Proceedings*, page 11, Anaheim, CA, September 2016.
- [14] V. Kunc, J. Lindahl, R. Dinwiddie, B. Post, L. Love, M. Matlack, R. Fahy Jr, and A. Hassen. Investigation of In-Autoclave Additive Manufacturing Composite Tooling. In *CAMX Conference Proceedings*, page 9, Anaheim, CA, September 2016.
- [15] L. Love. Utility of Big Area Additive Manufacturing (BAAM) for the Rapid Manufacture of Customized Electric Vehicles. Technical Report ORNL/TM-2014/607 CRADA/NFE-14-04988, Oak Ridge National Laboratory, Oak Ridge, TN, October 2014.
- [16] B. Post, B. Richardson, P. Lloyd, L. Love, S. Nolet, and J. Hannan. Additive Manufacturing of Wind Turbine Molds. Technical Report ORNL/TM-2017/290, CRADA/NFE-16-06051, 1376487, Oak Ridge National Laboratory, Oak Ridge, TN, July 2017.
- [17] M. Nikzad, S. Masood, and I. Sbarski. Thermo-mechanical properties of a highly filled polymeric composites for Fused Deposition Modeling. *Materials & Design*, 32(6):3448–3456, June 2011.
- [18] D. Klosterman, R. Chartoff, G. Graves, N. Osborne, and B. Priore. Interfacial characteristics of composites fabricated by laminated object manufacturing. *Composites Part A: Applied Science and Manufacturing*, 29(9-10):1165–1174, January 1998.
- [19] T. Kellner. “The Blade Runners: This Factory Is 3D Printing Turbine Parts For The World’s Largest Jet Engine,” from [https://www.ge.com/news/reports/future-manufacturing-take-look-inside-factory-3d-printing-jet-engine-parts.](https://www.ge.com/news/reports/future-manufacturing-take-look-inside-factory-3d-printing-jet-engine-parts), March 2018.
- [20] Relativity Space Inc. “Relativity Space,” from <https://www.relativityspace.com/stargate>.
- [21] K. Wong and A. Hernandez. A Review of Additive Manufacturing. *ISRN Mechanical Engineering*, 2012:1–10, August 2012.
- [22] Icon Technology Inc. “Home,” from <https://www.iconbuild.com/>.

- [23] S. Ford and T. Minshall. Invited review article: Where and how 3D printing is used in teaching and education. *Additive Manufacturing*, 25:131–150, 2018.
- [24] A. Vanderploeg, S. Lee, and M. Mamp. The application of 3D printing technology in the fashion industry. *International Journal of Fashion Design, Technology and Education*, 10(2):170–179, May 2017.
- [25] E. Barbero. *Introduction to Composite Materials Design*. CRC Press, Boca Raton, 3rd edition edition, October 2017.
- [26] N. van de Werken, H. Tekinalp, P. Khanbolouki, S. Ozcan, A. Williams, and M. Tehrani. Additively manufactured carbon fiber-reinforced composites: State of the art and perspective. *Additive Manufacturing*, 31:100962, January 2020.
- [27] S. Goris, S. Simon, C. Montoya, A. Bechara, M. Candal, D. Brands, and T. Osswald. Experimental Study on Fiber Attrition of Long Glass Fiber-Reinforced Thermoplastics under Controlled Conditions in a Couette Flow. In *Proceedings of the Technical Conference & Exhibition*, page 7, Anaheim, CA, 2017.
- [28] K. Shon, D. Liu, and J. White. Experimental Studies and Modeling of Development of Dispersion and Fiber Damage in Continuous Compounding. *International Polymer Processing*, 20(3):322–331, September 2005.
- [29] F. Ning, W. Cong, Y. Hu, and H. Wang. Additive manufacturing of carbon fiber-reinforced plastic composites using fused deposition modeling: Effects of process parameters on tensile properties. *Journal of Composite Materials*, 51(4):451–462, February 2017.
- [30] H. Pierson, E. Celik, A. Abbott, H. De Jarnette, L. Sierra Gutierrez, K. Johnson, H. Koerner, and J. Baur. Mechanical Properties of Printed Epoxy-Carbon Fiber Composites. *Experimental Mechanics*, 59(6):843–857, July 2019.
- [31] O. Rios, W. Carter, B. Post, P. Lloyd, D. Fenn, C. Kutchko, R. Rock, K. Olson, and B. Compton. 3D printing via ambient reactive extrusion. *Materials Today Communications*, 15:333–336, June 2018.
- [32] S. Romberg, C. Hershey, J. Lindahl, W. Carter, B. Compton, and V. Kunc. Large-scale Additive Manufacturing of Highly Exothermic Reactive Polymer Systems. In *SAMPE 2019 - Charlotte, NC*. SAMPE, April 2019.
- [33] D. Karalekas. Study of the mechanical properties of nonwoven fibre mat reinforced photopolymers used in rapid prototyping. *Materials & Design*, 24(8):665–670, December 2003.

- [34] R. Goodridge, M. Shofner, R. Hague, M. McClelland, M. Schlea, R. Johnson, and C. Tuck. Processing of a Polyamide-12/carbon nanofibre composite by laser sintering. *Polymer Testing*, 30(1):94–100, February 2011.
- [35] B. Compton, B. Post, C. Duty, L. Love, and V. Kunc. Thermal analysis of additive manufacturing of large-scale thermoplastic polymer composites. *Additive Manufacturing*, 17:77–86, October 2017.
- [36] T. Russell and D. Jack. Fiber Aspect Ratio Characterization and Stiffness Prediction in Large-Area, Additive Manufactured, Short-Fiber Composites. Novi, Michigan, September 2019.
- [37] T. Russell and D. Jack. Stiffness Prediction and Validation of Large Volume 3D Printed, Short-Fiber-Filled Polymer Composites. Charlotte, NC, April 2019. SAMPE.
- [38] P. Chesser, B. Post, A. Roschli, C. Carnal, R. Lind, M. Borish, and L. Love. Extrusion control for high quality printing on Big Area Additive Manufacturing (BAAM) systems. *Additive Manufacturing*, 28:445–455, August 2019.
- [39] Cincinnati Incorporated. “BAAM - Big Area Additive Manufacturing,” from <https://www.e-ci.com/baam>.
- [40] Thermwood Corporation. “Thermwood LSAM - Large Scale Additive Manufacturing,” from http://www.thermwood.com/lam_home.htm.
- [41] H. Tekinalp, V. Kunc, G. Velez-Garcia, C. Duty, L. Love, A. Naskar, C. Blue, and S. Ozcan. Highly oriented carbon fiber–polymer composites via additive manufacturing. *Composites Science and Technology*, 105:144–150, December 2014.
- [42] D. Jiang and D. Smith. Anisotropic mechanical properties of oriented carbon fiber filled polymer composites produced with fused filament fabrication. *Additive Manufacturing*, 18:84–94, December 2017.
- [43] D. Zhang, D. Smith, D. Jack, and Stephen Montgomery-Smith. Numerical Evaluation of Single Fiber Motion for Short-Fiber-Reinforced Composite Materials Processing. *Journal of Manufacturing Science and Engineering*, 133(5), October 2011.
- [44] J. Wang, J. O’Gara, and C. Tucker. An objective model for slow orientation kinetics in concentrated fiber suspensions: Theory and rheological evidence. *Journal of Rheology*, 52(5):1179–1200, September 2008.
- [45] G. Jeffery. The Motion of Ellipsoidal Particles Immersed in a Viscous Fluid. *Proceedings of the Royal Society of London. Series A, Containing Papers of a Mathematical and Physical Character*, 102(715):161–179, 1922. Publisher: The Royal Society.

- [46] B. Trevelyan and S. Mason. Particle motions in sheared suspensions. I. Rotations. *Journal of Colloid Science*, 6(4):354–367, August 1951.
- [47] S. Mason, R. Manley, and O. Maass. Particle motions in sheared suspensions: orientations and interactions of rigid rods. *Proceedings of the Royal Society of London. Series A. Mathematical and Physical Sciences*, 238(1212):117–131, December 1956. Publisher: Royal Society.
- [48] S. Advani and C. Tucker. The Use of Tensors to Describe and Predict Fiber Orientation in Short Fiber Composites. *Journal of Rheology*, 31(8):751–784, November 1987.
- [49] D. Jack and D. Smith. Assessing the use of Tensor Closure Methods with Orientation Distribution Reconstruction Functions. *Journal of Composite Materials*, 38(21):1851–1871, November 2004.
- [50] D. Jack. *Advanced analysis of short-fiber polymer composite material behavior*. Ph. D., University of Missouri–Columbia, December 2006.
- [51] K. Breuer, M. Stommel, and W. Korte. Analysis and Evaluation of Fiber Orientation Reconstruction Methods. *Journal of Composites Science*, 3(3):67, July 2019.
- [52] A. Sillem. *Fundamental Theory and Implementation of the Wang-O’Gara-Tucker Model for the Modeling of Fiber Orientation in Fiber Filled Injection Molded Thermoplastics*. PhD thesis, Delft University of Technology, Delft, the Netherlands, March 2010.
- [53] R. Hogg, J. McKean, and A. Craig. *Introduction to Mathematical Statistics*. Pearson, 6th edition edition, June 2004.
- [54] E. Onat and F. Leckie. Representation of Mechanical Behavior in the Presence of Changing Internal Structure. *Journal of Applied Mechanics*, 55(1):1–10, March 1988.
- [55] D. Jack and D. Smith. Elastic Properties of Short-fiber Polymer Composites, Derivation and Demonstration of Analytical Forms for Expectation and Variance from Orientation Tensors. *Journal of Composite Materials*, 42(3):277–308, February 2008.
- [56] F. Van Hattum, J. Nunes, and C. Bernardo. A theoretical and experimental study of new towpreg-based long fibre thermoplastic composites. *Composites Part A: Applied Science and Manufacturing*, 36(1):25–32, January 2005.
- [57] J. Cintra and C. Tucker. Orthotropic closure approximations for flow-induced fiber orientation. *Journal of Rheology*, 39(6):1095–1122, November 1995.

- [58] G. Vélez-García, P. Wapperom, D. Baird, A. Aning, and V. Kunc. Unambiguous orientation in short fiber composites over small sampling area in a center-gated disk. *Composites Part A: Applied Science and Manufacturing*, 43(1):104–113, January 2012.
- [59] C. Huang, J. Chu, W. Fu, C. Hsu, and S. Hwang. Flow-induced Orientations of Fibers and Their Influences on Warpage and Mechanical Property in Injection Fiber Reinforced Plastic (FRP) Parts. *International Journal of Precision Engineering and Manufacturing-Green Technology*, 8(3):917–934, May 2021.
- [60] G. Vélez-García, P. Wapperom, V. Kunc, D. Baird, and A. Zink-Sharp. Sample preparation and image acquisition using optical-reflective microscopy in the measurement of fiber orientation in thermoplastic composites: Sample Preparation and Image Acquisition. *Journal of Microscopy*, 248(1):23–33, October 2012.
- [61] T. Konicek. *A method to determine three-dimensional fiber orientation in fiber reinforced polymers*. PhD thesis, University of Illinois at Urbana-Champaign, 1987.
- [62] A. Clarke and C. Eberhardt. *Microscopy Techniques for Materials Science | ScienceDirect*. CRC, Boca Raton, 2002.
- [63] F. Folgar and C. Tucker. Orientation Behavior of Fibers in Concentrated Suspensions. *Journal of Reinforced Plastics and Composites*, 3(2):98–119, April 1984.
- [64] J. Phelps and C. Tucker. An anisotropic rotary diffusion model for fiber orientation in short- and long-fiber thermoplastics. *Journal of Non-Newtonian Fluid Mechanics*, 156(3):165–176, February 2009.
- [65] R. Bay and C. Tucker. Stereological measurement and error estimates for three-dimensional fiber orientation. *Polymer Engineering & Science*, 32(4):240–253, 1992. eprint: <https://onlinelibrary.wiley.com/doi/pdf/10.1002/pen.760320404>.
- [66] A. Favaloro, H. Tseng, and R. Pipes. A new anisotropic viscous constitutive model for composites molding simulation. *Composites Part A: Applied Science and Manufacturing*, 115:112–122, December 2018.
- [67] X. Fan, N. Phan-Thien, and R. Zheng. A direct simulation of fibre suspensions. *Journal of Non-Newtonian Fluid Mechanics*, 74(1-3):113–135, January 1998.
- [68] N. Phan-Thien, X. Fan, R. Tanner, and R. Zheng. Folgar–Tucker constant for a fibre suspension in a Newtonian fluid. *Journal of Non-Newtonian Fluid Mechanics*, 103(2-3):251–260, March 2002.

- [69] B. Verweyst and C. Tucker. Fiber Suspensions in Complex Geometries: Flow/Orientation Coupling. *The Canadian Journal of Chemical Engineering*, 80(6):1093–1106, December 2002.
- [70] Zhaogui Wang and Douglas E. Smith. A Fully Coupled Simulation of Planar Deposition Flow and Fiber Orientation in Polymer Composites Additive Manufacturing. *Materials*, 14(10):2596, May 2021.
- [71] Zhaogui Wang and Douglas E. Smith. Finite element modelling of fully-coupled flow/fiber-orientation effects in polymer composite deposition additive manufacturing nozzle-extrudate flow. *Composites Part B: Engineering*, 219:108811, August 2021.
- [72] K. Ortman, D. Baird, P. Wapperom, and A. Whittington. Using startup of steady shear flow in a sliding plate rheometer to determine material parameters for the purpose of predicting long fiber orientation. *Journal of Rheology*, 56(4):955–981, July 2012.
- [73] K. Ortman, D. Baird, P. Wapperom, and A. Aning. Prediction of fiber orientation in the injection molding of long fiber suspensions. *Polymer Composites*, 33(8):1360–1367, August 2012.
- [74] U. Strautins and A. Latz. Flow-driven orientation dynamics of semiflexible fiber systems. *Rheologica Acta*, 46(8):1057–1064, September 2007.
- [75] L. Switzer and D. Klingenberg. Rheology of sheared flexible fiber suspensions via fiber-level simulations. *Journal of Rheology*, 47(3):759–778, May 2003.
- [76] C. Zhang. *Modeling of Flexible Fiber Motion and Prediction of Material Properties*. Thesis, Baylor University, Waco, Texas, 2011.
- [77] E. Bertevas, J. Férec, B. Khoo, G. Ausias, and N. Phan-Thien. Smoothed particle hydrodynamics (SPH) modeling of fiber orientation in a 3D printing process. *Physics of Fluids*, 30(10):103103, October 2018.
- [78] E. Wetzel. *Modeling Flow-induced Microstructure in Inhomogeneous Liquid-Liquid Mixtures*. PhD Thesis, University of Illinois at Urbana-Champaign, Urbana, IL, 1999.
- [79] B. VerWeyst. *Numerical Predictions of Flow-induced Fiber Orientation in 3-D Geometries*. PhD Thesis, University of Illinois at Urbana-Champaign, Urbana, IL, 1998.
- [80] R. Jones. *Mechanics Of Composite Materials*. CRC Press, Philadelphia, PA, 2nd edition edition, July 1998.
- [81] C. Tucker III and E. Liang. Stiffness predictions for unidirectional short-fiber composites: Review and evaluation. *Composites Science and Technology*, pages 655–671, 1999.

- [82] J. Halpin and J. Kardos. The Halpin-Tsai equations: A review. *Polymer Engineering and Science*, 16(5):344–352, May 1976.
- [83] R. Hewitt and M. De Malherbe. An Approximation for the Longitudinal Shear Modulus of Continuous Fibre Composites. *Journal of Composite Materials*, 4(2):280–282, February 1970. Publisher: SAGE Publications Ltd STM.
- [84] G. Lielens, P. Pirotte, A. Courniot, F. Dupret, and R. Keunings. Prediction of thermo-mechanical properties for compression moulded composites. *Composites Part A: Applied Science and Manufacturing*, 29(1-2):63–70, January 1998.
- [85] G. Tandon and G. Weng. The effect of aspect ratio of inclusions on the elastic properties of unidirectionally aligned composites. *Polymer Composites*, 5(4):327–333, 1984. _eprint: <https://onlinelibrary.wiley.com/doi/pdf/10.1002/pc.750050413>.
- [86] J. Eshelby. The Determination of the Elastic Field of an Ellipsoidal Inclusion, and Related Problems. *Proceedings of the Royal Society of London. Series A, Mathematical and Physical Sciences*, 241(1226):376–396, 1957. Publisher: The Royal Society.
- [87] F. Van Hattum and C. Bernardo. A model to predict the strength of short fiber composites. *Polymer Composites*, 20(4):524–533, August 1999.
- [88] H. Cox. The elasticity and strength of paper and other fibrous materials. *British Journal of Applied Physics*, 3(3):72–79, March 1952.
- [89] H. Fukuda and T. Chou. A probabilistic theory of the strength of short-fibre composites with variable fibre length and orientation. *Journal of Materials Science*, 17(4):1003–1011, April 1982.
- [90] R. Bajracharya, A. Manalo, W. Karunasena, and K. Lau. Experimental and theoretical studies on the properties of injection moulded glass fibre reinforced mixed plastics composites. *Composites Part A: Applied Science and Manufacturing*, 84:393–405, May 2016.
- [91] P. Chen. Strength properties of discontinuous fiber composites. *Polymer Engineering & Science*, 11(1):51–56, 1971. _eprint: <https://onlinelibrary.wiley.com/doi/pdf/10.1002/pen.760110109>.
- [92] W. Bowyer and M. Bader. On the re-inforcement of thermoplastics by imperfectly aligned discontinuous fibres. *Journal of Materials Science*, 7(11):1315–1321, November 1972.
- [93] K. Jayaraman and M. Kortschot. Correction to the Fukuda-Kawata Young’s modulus theory and the Fukuda-Chou strength theory for short fibre-reinforced composite materials. *Journal of Materials Science*, 31(8):2059–2064, April 1996.

- [94] S. Fu and B Lauke. Effects of fiber length and fiber orientation distributions on the tensile strength of short-fiber-reinforced polymers. *Composites Science and Technology*, 56(10):1179–1190, 1996.
- [95] R. Kuriger, M. Alam, and D. Anderson. Strength prediction of partially aligned discontinuous fiber-reinforced composites. *Journal of Materials Research*, 16(1):226–232, January 2001.
- [96] T. Hayashi and K. Koyama. Theory and experiments of compressive strength of unidirectionally fiber-reinforced composite materials. *Mechanical Behavior of Materials*, pages 104–12, 1972.
- [97] B. Rosen. Mechanics of composite strengthening. January 1965. NTRS Author Affiliations: NTRS Document ID: 19660035520 NTRS Research Center: Legacy CDMS (CDMS).
- [98] R. Christensen. Failure criteria for fiber composite materials, the astonishing sixty year search, definitive usable results. *Composites Science and Technology*, 182:107718, September 2019.
- [99] A. Kaddour and M. Hinton. Maturity of 3D failure criteria for fibre-reinforced composites: Comparison between theories and experiments: Part B of WWFE-II. *Journal of Composite Materials*, 47(6-7):925–966, March 2013.
- [100] R. Christensen. The World Wide Failure Exercise II Examination of Results. *Journal of Reinforced Plastics and Composites*, 32(21):1668–1672, November 2013.
- [101] Z. Hashin. Failure Criteria for Unidirectional Fiber Composites. *Journal of Applied Mechanics*, 47(2):329–334, June 1980.
- [102] S. Tsai and E. Wu. A General Theory of Strength for Anisotropic Materials. *Technical Report AFML-TR-71-12*, August 1972.
- [103] S. Li, E. Sitnikova, Y. Liang, and A. Kaddour. The Tsai-Wu failure criterion rationalised in the context of UD composites. *Composites Part A: Applied Science and Manufacturing*, 102:207–217, November 2017.
- [104] E. Wu. Optimal Experimental Measurements of Anisotropic Failure Tensors. *Journal of Composite Materials*, October 1972.
- [105] R. Narayanaswami and H. Adelman. Evaluation of the Tensor Polynomial and Hoffman Strength Theories for Composite Materials. *Journal of Composite Materials*, October 1977.
- [106] S. Tsai and H. Hahn. *Introduction to composite materials*. Technomic Publishing Company, Westport, CT, 1980.

- [107] S. DeTeresa and G. Larsen. Derived Interaction Parameters for the Tsai-Wu Tensor Polynomial Theory of Strength for Composite Materials. Technical Report UCRL-JC-145041, Lawrence Livermore National Lab. (LLNL), Livermore, CA (United States), August 2001.
- [108] J. Andersons, E. Spārniņš, and R. Joffe. Stiffness and strength of flax fiber/polymer matrix composites. *Polymer Composites*, 27(2):221–229, April 2006.
- [109] S. Stair and D. Jack. Comparison of experimental and modeling results for cure induced curvature of a carbon fiber laminate. *Polymer Composites*, 38(11):2488–2500, 2015.
- [110] J. Halpin. Stiffness and Expansion Estimates for Oriented Short Fiber Composites. *Journal of Composite Materials*, 3(4):732–734, October 1969.
- [111] C. Wright. Prediction of Elastic Properties and Thermal Expansion for Multi-Component Composites. Master’s thesis, University of Illinois, Urbana-Champaign, 1988.
- [112] R. Schapery. Thermal Expansion Coefficients of Composite Materials Based on Energy Principles. *Journal of Composite Materials*, 2(3):380–404, July 1968. Publisher: SAGE Publications Ltd STM.
- [113] C. Camacho, C. Tucker, S. Yalvaç, and R. McGee. Stiffness and thermal expansion predictions for hybrid short fiber composites. *Polymer Composites*, 11(4):229–239, August 1990.
- [114] S. Tsai and H. Hahn. *Introduction to Composite Materials*. Technomic, Lancaster, PA, 1980.
- [115] B. Heller. *Non-Isothermal Non-Newtonian Flow and Interlayer Adhesion in Large Area Additive Manufacturing Polymer Composite Deposition*. PhD thesis, Baylor University, Waco, Texas, 2019.
- [116] B. Agarwal and L. Broutman. *Analysis and Performance of Fiber Composites*. Wiley, New York, NY, 2nd edition, 1990.
- [117] MatWeb LLC. “Avient Stat-Tech™ AS-13CF/000 Black Acrylonitrile Butadiene Styrene (ABS),” from <http://www.matweb.com/search/datasheet.aspx?matguid=59f0e0a398da4c99b6039a46bfcf93d1&ckck=1>.
- [118] Polyhedron Laboratories Inc. “ABS Plastics Testing Services - ABS Testing - ABS Plastic Strength Test,” from <https://www.polyhedronlab.com/service/plastics-testing/abs-plastics-testing.html>.

- [119] Engineers Edge LLC. “Specifications for Common Plastic Molding Design Material,” from https://www.engineersedge.com/plastic/materials_common_plastic.htm.
- [120] M. Minus and S. Kumar. The processing, properties, and structure of carbon fibers. *JOM*, 57(2):52–58, February 2005.
- [121] T. Russell, B. Heller, D. Jack, and D. Smith. Prediction of the Fiber Orientation State and the Resulting Structural and Thermal Properties of Fiber Reinforced Additive Manufactured Composites Fabricated Using the Big Area Additive Manufacturing Process. *Journal of Composites Science*, 2(2), April 2018.
- [122] J. Wang, D. Xu, W. Sun, S. Du, J. Guo, and G. Xu. Effects of nozzle-bed distance on the surface quality and mechanical properties of fused filament fabrication parts. *IOP Conference Series: Materials Science and Engineering*, 479, March 2019.
- [123] B. Banjanin, G. Vlastic, M. Pál, S. Balos, M. Dramicanin, M. Rackov, and I. Knezevic. Consistency analysis of mechanical properties of elements produced by FDM additive manufacturing technology. *Matéria (Rio de Janeiro)*, 23(4), December 2018.
- [124] J. Crosby. Long-Fiber Molding Materials. In *Thermoplastic Composite Materials*, pages 139–168. Elsevier, Amsterdam, 1991.
- [125] B. Heller, D. Smith, and D. Jack. Simulation of Planar Deposition Polymer Melt Flow and Fiber Orientation in Fused Filament Fabrication. In *Proceedings of the 28th Annual International Solid Freeform Fabrication Symposium – An Additive Manufacturing Conference*, Austin, TX, August 2017.
- [126] Z. Wang and D. Smith. Rheology Effects on Predicted Fiber Orientation and Elastic Properties in Large Scale Polymer Composite Additive Manufacturing. *Journal of Composites Science*, 2(1):10, February 2018.
- [127] ASTM. Standard Test Method for Flexural Properties of Unreinforced and Reinforced Plastics and Electrical Insulating Materials. ASTM D790 - 17, ASTM International, West Conshohocken, PA, 2017.
- [128] T. Russell and D. Jack. Initial Fiber Orientation Effects on Predicting Thermo-Mechanical Properties of Large Volume, Fused Filament Composites. Novi, Michigan, September 2018.
- [129] Z. Wang and D. Smith. Numerical analysis of screw swirling effects on fiber orientation in large area additive manufacturing polymer composite deposition. *Composites Part B: Engineering*, 177:107284, November 2019.

- [130] T. Russell. *The Effects of Fiber Orientation on Stiffness and Thermal Expansion of Large Volume, Anisotropic, Short-Fiber, Composite Material Fabricated by Fused Filament Fabrication*. PhD thesis, Baylor University, Waco, Texas, 2017.
- [131] T. Russell and D. Jack. Strength Prediction in Single Beads of Large Area Additive Manufactured Short-Fiber Polymers. *Polymer Composites*, 2021.
- [132] Z. Quan, Z. Larimore, A. Wu, J. Yu, X. Qin, M. Mirotznik, J. Suhr, J. Byun, Y. Oh, and T. Chou. Microstructural design and additive manufacturing and characterization of 3D orthogonal short carbon fiber/acrylonitrile-butadiene-styrene preform and composite. *Composites Science and Technology*, 126:139–148, April 2016.
- [133] R. Nargis. Internal Fiber Orientation Measurements and Void Distribution for Large Area Additive Manufactured Parts Using Optical and SEM Imaging Techniques. Master’s thesis, Baylor University, Waco, Texas, 2021.
- [134] Z. Wang, D. Smith, and D. Jack. A statistical homogenization approach for incorporating fiber aspect ratio distribution in large area polymer composite deposition additive manufacturing property predictions. *Additive Manufacturing*, 43:102006, July 2021.
- [135] ASTM. Standard Test Method for Flexural Properties of Unreinforced and Reinforced Plastics and Electrical Insulating Materials by Four-Point Bending. ASTM D6272-17, ASTM International, West Conshohocken, PA, 2017.
- [136] ASTM. Standard Test Method for Short-Beam Strength of Polymer Matrix Composite Materials and Their Laminates. ASTM D2344/D2344M-16, ASTM International, West Conshohocken, PA, 2016.
- [137] ASTM. Standard Test Method for Compressive Properties of Rigid Plastics. ASTM D695-15, ASTM International, West Conshohocken, PA, 2015.
- [138] ASTM. Standard Test Method for Tensile Properties of Polymer Matrix Composite Materials. ASTM D3039/D3039M - 17, ASTM International, West Conshohocken, PA, 2017.
- [139] B. Sharma, S. Kijewski, L. Fifield, Y. Shin, C. Tucker, and M. Sangid. Reliability in the characterization of fiber length distributions of injection molded long carbon fiber composites. *Polymer Composites*, 39(12):4594–4604, 2018.
- [140] ASTM. Standard Test Method for Compositional Analysis by Thermogravimetry. ASTM E1131-20, ASTM International, West Conshohocken, PA, 2020.

- [141] ASTM. Standard Test Method for Constituent Content of Composite Materials. ASTM D3171-15, ASTM International, West Conshohocken, PA, 2015.
- [142] ASTM. Standard Test Method for Tensile Properties of Plastics. ASTM D638-14, ASTM International, West Conshohocken, PA, 2014.
- [143] Y. Zhang, D. Rodrigue, and A. Ait-Kadi. High density polyethylene foams. III. Tensile properties. *Journal of Applied Polymer Science*, 90(8):2130–2138, November 2003.
- [144] D. Pulipati and D. Jack. Characterization and Model Validation for Large Format Chopped Fiber, Foamed, Composite Structures Made from Recycled Olefin Based Polymers. *Polymers*, 12(6):1371, June 2020.
- [145] B. Nguyen and V. Kunc. An Elastic-plastic Damage Model for Long-fiber Thermoplastics. *International Journal of Damage Mechanics*, 19(6):691–725, August 2010.
- [146] Z. Wang and D. Smith. Numerical analysis on viscoelastic creep responses of aligned short fiber reinforced composites. *Composite Structures*, 229:111394, December 2019.
- [147] X. Chen, X. Sun, P. Chen, B. Wang, J. Gu, W. Wang, Y. Chai, and Y. Zhao. Rationalized improvement of Tsai–Wu failure criterion considering different failure modes of composite materials. *Composite Structures*, 256:113120, January 2021.